Investigation of Transition Signals from Single-Cell to Multicell Thunderstorms based on Vertical Vorticity and Polarimetric Structure Analysis using Polarimetric Doppler Radar Observation

Fauziana Ahmad

2022

Investigation of Transition Signals from Single-Cell to Multicell Thunderstorms based on Vertical Vorticity and Polarimetric Structure Analysis using Polarimetric Doppler Radar Observation

Fauziana Ahmad

A dissertation submitted in partial fulfillment
of the requirement for the degree of
Doctoral of Philosophy

2022

ACKNOWLEDGEMENT

First and foremost, I would like to express my deepest gratitude to my supervisors, Prof. Eiichi Nakakita and Assoc. Prof. Kosei Yamaguchi, for their good supervision, advice, and moral support all along the way of my study. A lot of appreciation goes to Prof. Kenji Tanaka for sharing his knowledge and supporting the research. I especially thank Dr. Shingo Shimizu (NIED) for the information and knowledge about dual-Doppler analysis. I'd like to thank Dr. Naka Yukari, Dr. Satoshi Watanabe, and Dr. Wu Ying Hsin for all the help and encouragement they've given me.

My special thanks to the Malaysian Meteorological Department (MMD) for giving me the precious opportunity to learn about disasters and radar meteorology adapted from Japanese technology. I especially want to thank the Radar and Satellite Department for the data supply and for providing information. The most appreciation goes to Mr. Yip Weng Sang, Mr. Diong Jeong Yik, Mr. Noor Azam Shaari, Ms. Dayang Norazila, and other MMD members for their guidance and assistance. It is my pleasure to express sincere gratitude to the Malaysian Public Service Department Training (HLP JPA) for the financial support and scholarship throughout my studies and my family in Japan. I am very grateful for this opportunity to study in Japan and will keep it as an unforgettable memory.

I wish to give big thanks to my lab members in DPRI, especially Akiyuki Ono (thank you for helping me with translation), Aoi Nakamura (my beloved tutor), Mayumi Tsuji (thank you for everything), and others whose names are not mentioned here for their great contributions in assisting me in daily life, research, and my successful dissertation. I am also very proud to have the best lab members for the continuous encouragement, guidance, and unconditional support during this learning.

A big thanks go to my family and in-law in Malaysia. I am blessed to have such a close and loving family. Thank you for the continuous prayers for us abroad. Most importantly, I want to express my thanks and love to my husband, Abdul Mutalib, and my children, Fateen Afiqah, Fayyadh Amsyar, and Fateh Ammar, for their endless support and understanding. I am grateful to Allah s.w.t. for realizing my dream and easing the journey.

ABSTRACT

The localized heavy rainfall induced by the single-cell could be more hazardous if the single-cell merged into the multicell thunderstorms. Flash floods and landslides are common disasters with a lifespan of multicell more than one hour and a scale of an area larger than a single-cell. To mitigate the flood risk, the short-term precipitation forecast is suggested as one of the observation tools to disseminate early warnings for the flood forecasting systems. Therefore, the study of the transition from single-cell to multicell was proposed by utilizing the vertical vorticity and polarimetric parameter characteristics. These methods were employed in single-cell and supercell storms but did not evolve into multicell storms, and such techniques had proved successful in the detection of hazardous clouds. The novelty of this study was the investigation of transition signals from single-cell merged into the multicell, which focused on the evolution of single-cell and multicell in terms of characteristics and mechanism analysis. In addition, the polarimetric characteristics of the Z_{dr} column and K_{dp} column were emphasized, including the case study of non-merging. The mechanisms studied using dual-Doppler analysis (DDA) were further reviewed to quantify their relationships between vertical vorticity and polarimetric characteristic patterns. The study events were focused on the multicell broken-aerial type formation in the Kinki region of Japan, as well as the selected radar station, which was chosen based on the target areas.

In this finding, the core vorticity was examined between each single-cell and multicell by applying the pseudo-vorticity and DDA methods, in which the core vorticity was defined as the maximum of positive vorticity and the minimum of negative vorticity. In the preliminary analysis, the changing position of core vorticity was indicated as the signature pattern of transition; however, it was presented as a combination of a new vortex tube and an existing vortex tube. The new proposal of selection in core vorticity at the same position to construct the vertical vortex tube was proposed. The results showed the average of core vorticity in the single-cell before merging was 0.002 s^{-1} for DDA, and 0.02 s^{-1} for pseudo-vorticity analysis. This technique revealed the peak of core vorticity intensity was mainly discovered after the cells merged. Both DDA and pseudo-vorticity found these patterns, and the study showed that the average core vorticity intensity of single-cell to multi-cell was 0.004 s^{-1} and 0.04 s^{-1} for DDA and pseudo-vorticity, respectively.

The characteristics of single-cell could be characterized using vertical vorticity, where the formation height of the peak of core pair vorticity occurred at 4.4 km, and their peak of vortices developed at the same time of occurrence using pseudo-vorticity. Meanwhile, DDA observed its formation height at 3.8 km and 3.7 km for positive and negative vorticity, respectively, which occurred in the same period. It was assumed that the period of peak intensity occurred at a similar time for single-cell, which was related to the initial formation of the updraft. The pseudo-vorticity method was able to differentiate between the single-cell and multicell characteristics in terms of the formation height and the time occurrence of peak core vorticity owing to the high spatial and temporal resolution. However, the first detection of both pseudo-vorticity and DDA vorticity could forecast the peak of rainfall after cells merged with a 17-minute and 13-minute lead time, respectively.

The distance analysis was suggested in this study to investigate the relationship of characteristic patterns between single-cell and multicell. The same sign of core vorticity was analyzed with the comparison of core vorticity intensity. From the analysis, the DDA technique revealed the correlation between distance and core vorticity intensity by the separation of single-cell and multicell due to the highest estimation resolution. It was discovered that the multicell affects the strength of the core vorticity of a single-cell at the optimal distance in the range of 5-10 km, owing to the effect of downdraft and divergence from the multicell development. The multicell development is influenced by the periodic strong updrafts associated with a low-level southwesterly inflow that supplied warm, moist air to the precipitation cells.

The results of mechanisms analysis from the evolution of cells development were mainly affected on the increment of core vorticity intensity. The convergence, updraft, and stretching of the vortex tube were influenced on the increment of core vorticity intensity, especially at the lower level, and the tilting of the vortex tube was mostly affected at the middle-level height. At the later stage of multicell formation, the mature vortex was discovered with the core vorticity maxima boundary remaining due to the existence of updraft and convergence in the development of multicell.

The verification from vertical vorticity analysis was further explored by investigating the case of single-cell transition to multicell by emphasizing their first development of formation and comparing them with the non-merged of single-cell. This study was focused on the polarimetric characteristics based on the Z_{dr} column and K_{dp} column with the new approach concentrated on

the maximum columns' depth after the melting level. The upper maximum of column depth indicated the strength of the updraft, related to the transition of single-cell to multicell. The peak of core vorticity for single-cells merged was observed to be at 0.008 s^{-1} and 0.002 s^{-1} before merging into the multicell, whereas the single-cells not merged were identified at less than 0.003 s^{-1}. The results revealed that the transition signals of single-cells did not merge and showed a strength of less than 0.004 s^{-1}. This new finding of peak core vorticity intensity could be referred to as an indicator of transition signals from single-cell to multicell with the support of environmental conditions.

In the case of single-cells merged, the maximum column of K_{dp} was identified during the transition of a single-cell with 1 km in height. The Z_{dr} column was discovered after 5 minutes of cells merging, indicating the strong updraft remained in the multicell development. The single-cell not merged case was presented with a 1 km maximum column compared with the case of merging, which showed an average of 3.5 km column depth. These patterns were discovered to distinguish between single-cell merged and non-merged cases. On the other hand, the study quantified the relationship between vertical vorticity and maximum K_{dp} column with a correlation coefficient of 0.88, compared with Z_{dr} with a moderate correlation of 0.58. The K_{dp} column is a representation of deep convection updrafts since the life stages of multicell formation are controlled by the strength of the updraft and inflow from the warm and moist low-level wind. In particular, Z_{dr} above melting height is a useful indicator of the early appearance of deep convection. Cells merged are mainly related to the existence of weak vertical wind shear, convergence, updraft, and downdraft of moist air in the presence of precipitation.

In conclusion, the transition signals from single-cell to multicell were newly discovered by utilizing the vertical vorticity method and polarimetric analysis with the combination of mechanisms analysis that was quantified as crucial in the transition to multicell development. The outcome of this study could assist in determining the characteristics of single-cells developed in the multicell and their early transition patterns for the single-cell merged into the multicell. In the short-term forecast of precipitation, both methods were found to be useful in figuring out the stage of change from single-cell to multicell.

TABLE OF CONTENTS

ACKNOWLEDGEMENT i

ABSTRACT ii

TABLE OF CONTENTS v

LIST OF FIGURES viii

LIST OF TABLES xv

LIST OF ABBREVIATIONS xvi

CHAPTER 1

1 Introduction 1

1.1 Background of Study 1

1.2 Objectives of Study 4

1.3 Motivation of Study 5

1.4 Literature Review 6

1.4.1 Life cycle of thunderstorms 6

1.4.2 Characteristics of thunderstorms 8

1.4.3 Vertical vorticity in the supercell thunderstorm 10

1.4.4 Multi-parameter radar analysis 13

1.5 Structure of Dissertation 14

CHAPTER 2

2 Data and Study Area 17

2.1 Radar Observation and Data Acquisitions 17

2.1.1 Radar parameters 19

2.1.2 Dual-Doppler radar 22

2.2 Vertical Vorticity Analysis 26

2.2.1 Dual-Doppler Analysis 26

2.2.2 Pseudo-Vorticity Analysis 27
2.3 Study Area and Synoptic Conditions 28
2.3.1 Event 1 - September 10, 2014 29
2.3.2 Event 2 – August 13, 2018 31
2.3.3 Event 3 – July 25, 2019 33
CHAPTER 3
3 Preliminary Investigation of Single-cell to Multicell in the Cluster Thunderstorms using Pseudo-Vorticity Analysis 36
3.1 Overview 37
3.2 Methodology 38
3.2.1 Classification of cells 38
3.2.2 Radar reflectivity and vertical vorticity analysis 39
3.3 Results and Discussion 40
3.3.1 Event 1 - 10th September 2014 40
3.3.2 Event 2 - 13th August 2018 45
3.3.3 Discussion 48
3.4 Conclusions 50
CHAPTER 4
4 Investigation of Transition Signals from Single-cell to Multicell Thunderstorms Using Pseudo-Vorticity, Dual-Doppler Vorticity, and Mechanism Analysis 53
4.1 Overview 54
4.2 Methodology 56
4.2.1 Classification of cells 56
4.2.2 Pseudo-vorticity analysis 56
4.2.3 DDA vorticity analysis 57
4.2.4 Analysis of transition signals and mechanisms effect 59

4.3 Results and Discussion 61
4.3.1 Detailed kinematic and cells distribution 61
4.3.2 Vertical vorticity analysis 66
4.3.3 Mechanisms analysis 78
4.3.4 Theoretical discussion on vortex merger in the transition from single-cell to multicell 93
4.3.5 Comparison between DDA and pseudo-vorticity analysis 100
4.4 Conclusions 102
CHAPTER 5
5 Polarimetric Characteristics of Transition from Single-cell to Multicell Thunderstorms with Vertical Vorticity Analysis 105
5.1 Overview 106
5.2 Methodology 107
5.2.1 Classification of cells 107
5.2.2 Kinematic mechanism analysis 109
5.2.3 Multi-parameter radar analysis 109
5.3 Results and Discussion 110
5.3.1 Kinematic mechanism analysis 110
5.3.2 Z_{dr} column and K_{dp} column analysis 115
5.3.3 Discussion of characteristics and mechanisms 117
CHAPTER 6
6 Conclusions and Future Work 121
6.1 Conclusions 121
6.2 Future Work in Malaysia 128
REFERENCES 132
APPENDICES 137

LIST OF FIGURES

Figure 1.1(a) The residential areas flooded by the Chikuma River due to Typhoon Hagibis (b) Hiroshima sediment disaster occurred in 2014 due to the back-building type precipitation system. (Source: japantimes.co.jp). 1
Figure 1.2 The monitoring video of the Toga River basin showed the rapid increase of water level in a 10-minute duration caused five people died. (Source: Nakakita et al.,2017) 2
Figure 1.3 Radar distributions and their coverage of MLIT X-band MP radar networks. 3
Figure 1.4 The conceptual of stage development of thunderstorms (Source: NOAA). 6
Figure 1.5 The illustration of three stages in the multicell thunderstorms that were observed as one single cloud by the observer at the ground. 9
Figure 1.6 Conceptual model of tilting mechanism that leads to updraft rotation. The pink ribbons represent the vertical flow associated with the vortex lines. The black arrows represent the ambient vertical wind profile. (Source: Dahl, J. M. L.,2017). 11
Figure 1.7 Schematic figure of the creation of a vertical vortex tube. Circular arrows depict horizontal vortex tube circulations. (a) The horizontal wind shear forms a vortex tube with a horizontal orientation. (b) An updraft tilts a horizontal vortex tube into a vertical vortex tube. (Source: Nakakita et al.,2017) 12
Figure 1.8 Information of dual polarization parameters observed from MP radars (Source: Japan Meteorology Agency (JMA)). 13
Figure 1.9 The outline of thesis chapter with its own objectives. 16
Figure 2.1 Four radar stations in the Kinki region, Japan, were used for the observation of the cell merging of the radar reflectivity. The dashed black arrow shows the maximum range of 80 km between the radar stations. 17
Figure 2.2 The XRAIN radar observation schedule in the Kinki region, Japan using 4 radar stations to acquire entire volume scan data. 18
Figure 2.3 Example of horizontal distribution of the (a) radar reflectivity, (b) Doppler velocity 19
Figure 2.4 The signatures from point of radar based on velocity products. 19
Figure 2.5 Schematic illustration of the location of dual-Doppler lobes for two Doppler radars (Ronald E., 2004). 24

Figure 2.6 (a) The illustration of the calculated baseline from two radars with a crossing angle of 30 degrees. (b) The blockage area is shown at the target area when used two radars as mentioned in (a). 25
Figure 2.7 The observation domain for the dual-Doppler radar study was conducted within the two solid circles, but not within the hatched area, as shown on the map for (a) event 1 and (b) event 2. 26
Figure 2.8 Schematic illustration of DDA vertical vorticity analysis. 26
Figure 2.9 Illustration of pseudo-vorticity estimation using single radar. 27
Figure 2.10(a) Rainfall accumulation map with red box indicated target area (b) MSM relative humidity (shaded), red contour (surface temperature) (c) Surface weather map of Japan at 9:00 JST (d) MSM wind level analysis. Images are based on data obtained on 10 September 2014... 29
Figure 2.11 Hodograph obtained at Shionomisaki Station at 21:00 JST on 10 September 2014. 30
Figure 2.12 (a) Horizontal distribution of radar reflectivity at 1700JST with red box indicated target area (b) MSM relative humidity(shaded), red contour (surface temperature) (c) Surface weather map of Japan at 9:00 JST (d) MSM wind level analysis. Images are based on data obtained on 13 August 2018. 32
Figure 2.13 Hodograph obtained at Shionomisaki Station at 0900 JST on 13 August 2018. 33
Figure 2.14 (a) Horizontal distribution of radar reflectivity at 1200JST with red box indicated target area (b) MSM relative humidity(shaded), red contour (surface temperature), (c) Surface weather map of Japan at 0900 JST, and (d) MSM wind level analysis. Images are based on data obtained on 25 July 2019. 34
Figure 2.15 Hodograph obtained at Shionomisaki Station at 0900 JST on 25 July 2019. 35
Figure 3.1 The schematic illustrations of (a) merging single-cell A and B to multicell B and (b) merging single-cell C with multicell B to cluster B. 38
Figure 3.2 The methodology used in the analysis. 39
Figure 3.3 The comparison of the initial stage of vorticity and after 10-minute development using radar reflectivity. A black solid circle indicates the example of the investigated cell. 40
Figure 3.4 (a) The storm cluster history of Z_h at 2 km CAPPI height (b) One illustrative example of radar reflectivity images when single-cell A merge with single-cell B. 41
Figure 3.5 One illustrative example of the selection of the initial stage of cells A and B. 42

Figure 3.6(a) The time-longitude distribution of (a) each cell in cluster A at latitude 34.7654°N, (b) selected latitude at 34.79°N. 43
Figure 3.7 The vertical vortex tube structure of single-cell A. 44
Figure 3.8 The vertical vortex tube structure of single-cell B. 44
Figure 3.9(a) The target area in the Kinki region, Japan (b) The storm cluster Z_h history at 2 km CAPPI height. 45
Figure 3.10 The time distribution of each cells in cluster A. 46
Figure 3.11 The vertical vortex tube structure of single-cell A. 47
Figure 3.12 The vertical vortex tube structure of single-cell C. 47
Figure 3.13 The relationships between the lifetime of cells and (a) core positive vorticity and (b) core negative vorticity. (c) Distribution of height of changing the position of single-cells before merged. 48
Figure 3.14 Schematic illustration relating downdraft interaction to bridging and merger in case of light wind and weak shear (Adapted from Simpson et al.,1980). 49
Figure 3.15 (a) The probability of changing the position of the vortex tube might be indicated the existence of a vortex tube at the middle-level and a new ingested vortex tube at the lower-level. The schematic illustration is shown in (b). 51
Figure 4.1 Schematic of vortex tilting at the early stage of initiation of the meso-convective vortex with purple lines representing vortex filaments. Adapted from (Montgomery. MT, et al., 2006). 54
Figure 4.2(a) The comparison of PPI images of pseudo-vorticity and radar reflectivity. The red box referred to the boundary of single-cell and multicell. (b) The vertical vortex tube construction which circle indicated the core vorticity position. The red and blue lines referred to the vertical vortex tube of core positive and negative. 57
Figure 4.3 Dual-Doppler radar analysis map on 13th August 2018 with the target area shown on the red dashed line 57
Figure 4.4(a) Storm-relative horizontal wind at 3 km height. The color scale determined the vertical vorticity from DDA, the contoured line indicated radar reflectivity in the interval of 10 dBZ. (b) In the vertical vortex tube construction, plus indicated the core vorticity position, red and blue lines referred to the vertical vortex tube of core positive and negative. All red color boxes referred to the boundary of cells. 58

Figure 4.5 Schematic illustration of (a) height calculation from the pseudo-vorticity analysis and (b) distance analysis for the same sign of core vorticity for both methods. The red anticlockwise arrow indicates positive vorticity; the blue clockwise arrow specifies negative vorticity. 60
Figure 4.6 Storm propagation including the labels of the single-cells and multicell at a height of 2 km above the ground level. The black arrow indicates the storm motion movement. 62
Figure 4.7 Core vorticity, maximum reflectivity, and updraft during the entire storm at 2 km and 4 km. The circle indicated the peak of vorticity that happened in the multicell development. 62
Figure 4.8 Vertical cross-section images of single-cell transformed into multicell respected with the time of developing stage and merged cells. 63
Figure 4.9 Storm-relative horizontal wind distribution at a height of 2 km in the interval of 5 minutes from the dual-Doppler analysis. In the horizontal distribution, the wind vectors denote 5 m s^{-1}. The color scale showed the vertical vorticity derived from DDA. The green contours indicate radar reflectivity at an interval of 10 dBZ. The data from 2205 until 2220 was excluded due to the non-existence of single-cells developed near the storm. 65
Figure 4.10 The wind profile from DDA for cell A investigated with the schematic illustration of the position of the vortex tube existed at low-level and middle-level. 66
Figure 4.11 Horizontal distribution of radar reflectivity and vertical vorticity from pseudo-vorticity 67
Figure 4.12 Time series of the core vorticity between (a) single-cell A and multicell α and (b) single-cell F and multicell ε for positive and negative vorticity for pseudo-vorticity at each elevation angle. The black dashed line indicates the cell merging before and after cells merging. 68
Figure 4.13 The vortex tube of single-cell A and multicell α at the early stage of multicell formation before merging (left figure), and updraft position and strength using the Z_{dr} column (right figure). 70
Figure 4.14 Core vorticity analysis in terms of the distance and correlation between the core vorticity and distance. 71
Figure 4.15 The distribution of merged cells at the shortest distance. 72
Figure 4.16 Time series of the core vorticity between (a) single-cell A-multicell α, and (b) single-cell F-multicell η for positive and negative vorticity at each CAPPI height. 73

Figure 4.17 Distribution of maximum updraft for each height for (a) single-cell (b) multicell, and (c) distribution of maximum downdraft in multicell. 75
Figure 4.18 Analysis of the core vorticity in terms of the distance and correlation between the core vorticity and distance. 76
Figure 4.19 Downdraft effect from cell α to single-cell A on the vertical vorticity intensity increment. This figure showed at a height of 3 km AGL. 77
Figure 4.20 The horizontal distribution of updraft (top figure) and vertical vorticity (below figure) at 2 km height CAPPI. 78
Figure 4.21 Kinematic analysis of cell A and multicell α. (a) Top figure indicates radar reflectivity with wind vector, below figure shows vertical vorticity. (b) Top figure indicates convergence (red color), and divergence (blue color), below figure shows updraft (red shaded color) and downdraft (green shaded color). See Figure 4.20 for the cross-line. 80
Figure 4.22 Dynamic analysis of cell A and multicell α. (a) Top figure indicates stretching term (b) below figure shows the tilting term. 81
Figure 4.23 The horizontal distribution of updraft and vertical vorticity at 2 km height CAPPI. 82
Figure 4.24 Kinematic analysis of cell F and multicell η. (a) Top figure indicates radar reflectivity with wind vector, below figure shows vertical vorticity. (b) Top figure indicates convergence (red color), and divergence (blue color), below figure shows updraft (red shaded color) and downdraft (green shaded color). See Figure 4.24 for the cross-line. 83
Figure 4.25 Dynamic analysis of cell F and multicell η. (a) Top figure indicates stretching term (b) below figure shows the tilting term. 84
Figure 4.26 Lead time detection of the first detection of vertical vorticity between the peak of core Z_h after cells merged. 85
Figure 4.27 The time investigation of formation height and time occurrence of peak core vorticity. 86
Figure 4.28 The spatial changes of vertical vorticity from 3.5 km to 5.0 km with positive vorticity(red color), and negative vorticity (blue color) shaded region. The solid black contour indicated updraft with an interval of 0.5 m s^{-1}. The dashed black contour specified the downdraft. 88

Figure 4.29 (a) Scatterplot relationship between distance and single-cell(blue color) and multicell (orange color). (b) Box-and-whisker plots of core vorticity intensity for new cells and multicell at each distance interval for positive vorticity. 89
Figure 4.30 (a) The time-series of new cell A for positive vorticity (blue line color) related to the downdraft (orange color column) and divergence (grey line color) from cell α. (b)Vertical cross sections of DDA vorticity with wind vector taken along line Z1-Z2 for single-cell A (dashed purple color) and cell α. The red box indicated the downdraft happened in cell α. Radar reflectivity in interval 10 dBZ is in the green contour line. 90
Figure 4.31 (a)The time-series of single-cell F for positive vorticity (blue line color) related to the downdraft (orange color column) and divergence (grey line color) from cell η. (b) Vertical cross sections of DDA vorticity with wind vector taken along line Z1-Z2 for new cell F (dashed purple color) and cell η. The red box indicated the downdraft happened in cell η. Radar reflectivity in interval 10 dBZ is in the green contour line. 91
Figure 4.32 The correlation coefficient of core positive vorticity intensity to the height between mechanisms using DDA vorticity. 93
Figure 4.33 Schematic illustration of the same sign of vorticities between single-cell and multicell. 99
Figure 4.34 Probability density distribution of single-cell and multicell core vorticity intensity for (a) DDA vertical vorticity (b) pseudo vertical vorticity. 100
Figure 5.1 The development of SC1 and SC2 were observed at 1530JST and 1535JST. 107
Figure 5.2 The horizontal wind distribution of (a) Target area of cells investigated for SC1 and SC2 after the transition to multicell (b) After 5-min cells merged into multicell (c) Illustration of multicell development with a cross-section of at line AA'. 108
Figure 5.3 Horizontal distribution of radar reflectivity at 2 km CAPPI height for single-cell not merged (SCNM) at the target location and time of the first cell developed. Time is shown in JST. 108
Figure 5.4 Illustration of **(a)** Z_{dr} column depth **(b)** K_{dp} column depth referred to solid arrow, above the melting level indicated by red solid line. 110
Figure 5.5 Horizontal distribution at 1555JST for SC1 and SC2 for **(a)** Z_{dr} **(b)** K_{dp} at 5 km height, and **(c)** Z_h **(d)** Vertical vorticity at 2 km height. Line BB' gives the location of the vertical cross-section shown in Figure 5.10. 111

Figure 5.6 Vertical cross-section of SC1 at (a) 1545JST before transition into multicell (b) at 1605 JST after the transition. See Figure 5.5(d) for location. 112
Figure 5.7 Time-series of averaged maximum reflectivity, updraft, and convergence for entire storm volume and of maximum vertical vorticity **(a)** for SC1 **(b)** for SC2. 113
Figure 5.8 Example of time-height distribution of SCNM2 indicated the duration of cells investigated. 114
Figure 5.9 Time-series of averaged maximum reflectivity, updraft, and convergence for entire storm volume and of maximum vertical vorticity **(a)** for SCNM2 **(b)** for SCNM3. 114
Figure 5.10 Vertical cross-section of updraft (shaded) and vertical vorticity (contoured line), $Z_{dr,}$ and K_{dp} through SC1 and SC2 at 1600JST and 1605JST. The red solid line showed the melting height (See Figure 5.5(c) for location). 115
Figure 5.11 The maximum column depth of Z_{dr} and K_{dp} for SCNM1. 116
Figure 5.12 Distribution of the calculated height of maximum column depth of Z_{dr} and K_{dp} 118
Figure 5.13 Calculated zonal vertical wind shear existed on the case of cells merged. 119
Figure 5.14 Schematic illustration of (a) K_{dp} column depth (b) Z_{dr} column depth in the process of transition stage from single-cell to multicell formation. 120
Figure 6.1 Schematic illustration of transition stage from single-cell to multicell in terms of vertical vorticity and mechanisms influence such as updraft, convergence, and downdraft. 125
Figure 6.2 The floods inundated at the city center of Kuala Lumpur on March 7, 2022. (Source: Berita Harian) 129
Figure 6.3 The prolonged heavy rainfall hit east coast of Peninsular Malaysia in 2014. 130
Figure 6.4 Green shaded areas indicate the flood prone areas in Peninsular Malaysia, and Sabah Sarawak (Source: DID) 130
Figure 6.5 The weather radar observations in Malaysia region. 131

LIST OF TABLES

Table 2.1 Specification of MLIT X-band Multi-Parameter Radars 18
Table 2.2 Several Z-R relationships are used depending on the type of clouds 20
Table 2.3 Advantages and disadvantages of vertical vorticity methods 27
Table 3.1 Initial stage of single-cell 42
Table 3.2 Initial stage of each cell 46
Table 4.1 Peak of core vorticity intensity before merging into multicell 66
Table 4.2 Peak of core vorticity intensity and its formation height. 69
Table 4.3 Core vorticity intensity and its height formation 74
Table 4.4 Correlation coefficient (R^2) between the core vorticity intensity and mechanisms 92
Table 4.5 The comparison of vertical vorticity analysis from pseudo-vorticity and vertical vorticity 101
Table 5.1 Characteristics of cells investigated 117
Table 6.1 The summary of methods used for the transition signals analysis based on positive vorticity 123

LIST OF ABBREVIATIONS

AGL	: Above Ground Level
BRN	: Bulk Richardson Number
CAPE	: Convective Available Potential Energy
CAPPI	: Constant Altitude Plan Position Indicator
DID	: Department of Irrigation and Drainage
DDA	: Dual-Doppler Analysis
DSD	: Drop Size Distribution
EL	: Equilibrium Level
JMA	: Japan Meteorology Agency
JST	: Japan Standard Time
LCL	: Liquid Condensation Level
LFC	: Level of Free Convection
LFD	: Left Flank Downdraft
LWC	: Liquid Water Content
MMD	: Malaysian Meteorological Department
MLIT	: Ministry of Land, Infrastructure, Transport, and Tourism
MP	: Multi-Parameter
MSM	: Meso-scale Model
NOAA	: National Oceanic and Atmospheric Administration
NWP	: Numerical Weather Prediction
PPI	: Plan Position Indicator
VIL	: Vertical Integrated Liquid
XRAIN	: Extended Radar Information Network

CHAPTER 1

1 Introduction

1.1 Background of Study

Recently, attention has been drawn to the flood and sediment disasters in Japan caused by heavy rain due to the typhoons and localized heavy rainfall brought by the quasi-stationary band-shaped precipitation systems. Ministry of Land, Infrastructure, Transport, and Tourism (MLIT) reported the total damages induced by Typhoon Hagibis that occurred in October 2019 was 1.88 trillion yen and the casualties or missing person was 108 people (MLIT, 2021). The reported flood disaster that happened in Nagano is described in Figure 1.1(a) due to Typhoon Hagibis. In the meantime, the localized heavy rainfall events producing accumulated three-hour precipitation amount larger than 200 mm often caused the severe flood and sediment disasters. These events are mainly caused by the back-building type precipitation systems or well-known as “senjo-kousuitai” in Japanese (Kato, 2020). Senjo-kousuitai is classified as a band-shaped area of intense rainfall with dimensions of 500–300 km in length and 20–50 km in width. It is caused by convective cells that consecutively form and develop, align to create multicell clusters, and remain nearly stationary for a few hours. Figure 1.1(b) presented the sediment disaster in Hiroshima due to the continuous localized heavy rainfall in August 2014. Within three-hour, the rainfall exceeded 200 causing 44 injuries and 74 deaths.

Figure 1.1(a) The residential areas flooded by the Chikuma River due to Typhoon Hagibis (b) Hiroshima sediment disaster occurred in 2014 due to the back-building type precipitation system. (Source: japantimes.co.jp).

Figure 1.2 The monitoring video of the Toga River basin showed the rapid increase of water level in a 10-minute duration caused five people died. (Source: Nakakita et al.,2017)

In addition, the localized heavy rainfall from cumulonimbus clouds commonly occurred in the summer season also potential to be a hazardous cloud. In 2008, a flash flood occurred in the Toga River Basin located in Kobe, Japan due to the downpour of Guerilla-heavy rainfall from the development of isolated cumulonimbus clouds (Nakakita et al.,2013; Nakakita et al.,2017). The rapid rise of the water level in the river basin caused the death of five people. The snapshot from the monitoring video of the Toga River camera at the site is displayed in Figure 1.2. The dissemination of early warnings could not be delivered promptly since the flood came rapidly. Furthermore, the single-cell clouds could be merged into multicell clouds, which have a common lifetime of more than an hour and greater aerial coverage than a single-cell. Small-to-medium-sized hail, small tornadoes, and heavy precipitation are all risks linked with multicell. Heavy precipitation from multicell thunderstorms also can intensify flash flood events, especially in urban areas. For example, the multicellular storm brought localized heavy rain near Zoshigaya, Tokyo on August 5, 2008, causing five sewage workers to be washed away by a flash flood (Kato and Maki 2009; Hirano and Maki 2010; Kim, et al. 2012).

As a result, the short-term precipitation forecast system is essential to predict the initiation and peak precipitation contribute to the accurate heavy rainfall alerts for the dissemination to the public and related disasters agency. The prediction of typhoon and back-building precipitation systems could be established several days before using Numerical Weather Prediction (NWP) in terms of movement and intensity. However, the localized heavy rainfall on a smaller scale is difficult to predict due to the intense development of the cumulonimbus cloud. Due to increment flood disaster events caused by localized heavy rainfall in Japan, MLIT deployed an extended

radar information network (XRAIN) consisting of 39 X-band multi-parameter (MP) radars as illustrated in Figure 1.3 for the detection of localized heavy rainfall, especially in the urban areas. The solid circles indicate the radar locations, and circles indicate the observation ranges (r = 80 km). The performance of volume scans every 5 minutes for the composite radars at different elevation angles and the distribution of rainfall intensity at the surface every one minute could be utilized in the short-term precipitation forecast.

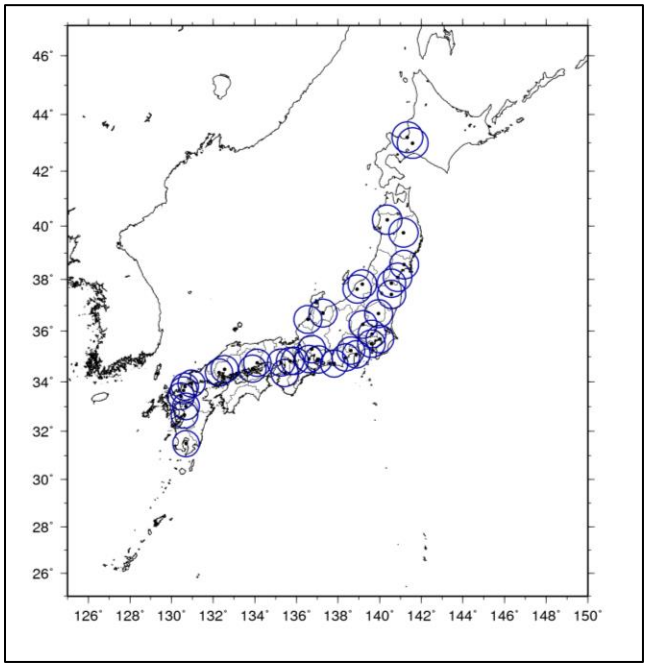

Figure 1.3 Radar distributions and their coverage of MLIT X-band MP radar networks.

Numerous researchers have developed the forecast for the detection of convective cell development using various radar parameters by deploying X-band radar. For instance, based on a case of localized heavy rainfall in Tokyo, Hirano and Maki (2010, 2018) proposed the vertically integrated liquid (VIL) water content method using three methods: (1) horizontal reflectivity (Z), (2) specific differential phase (K_{dp}); and (3) Z and K_{dp}. They proved that the combination method of Z and K_{dp} were the best approach to VIL estimation, and this method could detect 5-10 minutes before the rainfall reached the ground surface. Referred to the case of the Toga River basin, Nakakita et al, (2013, 2017) developed prediction methods on the first radar echo aloft that was described as a “baby-rain-cell” in a single cumulonimbus cloud using Doppler weather radar observation. According to the studies, the vertical vorticity values should be greater or equal to 0.03 s^{-1} to identify the hazardous rain cell in the initiation stage before it developed to the cumulus

stage. This criterion is currently used in weather radar observation data of the XRAIN operated by MLIT to deliver early warnings to local governments. It focused only on the vertical vortex tube of a single-cell that connected at different altitudes and did not evolve into multicell development.

Rather than forecasting the detection of localized heavy rainfall, multicell formation studies in Japan are mostly investigated to understand the characteristics and its stage of formation. Previous research has focused on radar reflectivity (Nishiwaki et al., 2013; Shusse et al., 2005; Geng et al., 1997) based on the stage of multicell development. Kim et al. (2012) analyzed the precipitation core development and its structure by combining liquid water content (LWC) and K_{dp}. Furthermore, the multi-parameter radars in Japan are commonly investigated for the detection of hazardous clouds (Adachi et al., 2013) and developed a technique to identify the stage of the storm life cycle using polarimetric radar parameters (Masuda et al.,2014). The detection of the supercell storm that generated the tornado in Ibaraki also revealed the Z_{dr} signature of the supercell storm which persisted approximately for approximately half an hour (Suzuki et al., 2018). Consequently, the detection of hazardous clouds using polarimetric radar parameters and short-term precipitation forecasts have been successfully developed in Japan to assist the forecasters to analyze the stages of cloud development and disseminate the early warnings to the public and flood warning system.

1.2 Objectives of Study

This study utilizes the X-band multi-parameter radar observation using vertical vorticity and polarimetric radar parameters to identify the potential of cell merging related to heavy precipitation in multicell thunderstorms. The objectives of the study are as follows:

1) To examine the availability of vertical vorticity to characterize the potential of cell merging related to heavy rain in a hazardous storm.
2) To discover the characteristic patterns of vertical vorticity during cell merging for distinguishing the severity of thunderstorms.
3) To investigate the characteristic patterns during the transition from single-cell to multicell by utilizing polarimetric radar parameters.
4) To quantify the mechanisms effect on the characteristic based on vertical vorticity and polarimetric radar analysis.

1.3 Motivation of Study

Severe thunderstorms that induced heavy precipitation could contribute to disaster occurrences such as flash floods, especially in urban areas. The development of single-cell, multicell, and supercells could be observed by the weather radar which is performed well in terms of spatial and temporal resolutions. In this study, we emphasized multicell development because the potential of cells merging related to the severity of thunderstorms is also important in the dissemination of early warnings. The investigation of the characteristics of the cells merging and its mechanisms effect helped the forecasters in analyzing the hazardous cells.

Numerous research on multicell studies focused on the structure of the precipitation core and its formation height. The study on the multicell thunderstorm from the initiation stage of convective cells involved in merging echo cores has been established to examine the factors that influenced the frequency of merging cells, the characteristics, and their effects based on radar reflectivity. Since the successful lead time in the detection of "baby-rain-cell" in localized Guerilla heavy rainfall, the vertical vorticity method is a novel approach to discover the potential of cell merging in the multicell thunderstorm analysis. Therefore, the purpose of this study is to examine the availability of vertical vorticity to forecast the potential of cell merging related to heavy rain in the hazardous storm. The intensity of vertical vorticity indicated the development of convective cells such as a tornado, supercell, and hazardous single-cell. We are also interested to determine the transition index from single-cell to multicell and the longevity of storms using the vertical vorticity criterion.

Many researchers analyzed the mechanisms that supported multicell development such as wind shear, convergence, updraft, and downdraft. These mechanisms are important to the stages of development of thunderstorm clouds. The vertical vorticity analysis is mostly investigated in supercell thunderstorms owing to the exhibition of updraft rotation. In addition, a vorticity pair in the baby-rain-cells was detected, which was related to the existence of an updraft in the single-cell. Therefore, the characteristics and mechanisms for the development from single-cell to multicell thunderstorms which are contributed to localized heavy rainfall motivated the author to discover the significant criteria related to the severity of thunderstorms.

In addition, the detection of potentially hazardous convective clouds using polarimetric radar parameters is widely utilized in Japan based on the analysis of the Z_{dr} column and K_{dp} column. The Z_{dr} column and K_{dp} column also indicated the strength and the location of updraft

which were beneficial in the detection of hazardous clouds. Therefore, the study on polarimetric for detection of potential heavy rainfall in multicell thunderstorms could provide insight into the understanding of the multicell characteristics from the initiation stage to the development stage of occurrence of heavy rainfall. The quantification of the mechanisms that influence the interaction between cell merging in promoting the generation of strong heavy rainfall also contributes to the enhancement of knowledge in the transition process from single-cell to multicell development.

1.4 Literature Review

1.4.1 Life cycle of thunderstorms

Mostly thunderstorm is related to the convective cloud which is categorized into three types of cells (single-cell, multicell, and supercell). A single-cell is usually analyzed in detail related to its development which can be categorized into three stages (developing, maturing, and dissipating stage). Supercells are mostly investigated in the mid-latitude to understand their characteristics and development since their largest scale of areas and could be persisted for six hours. Multicell are the most common appeared in the atmosphere that could contribute to the severe thunderstorm and their lifetime could be more than one hour but the areas of multicell are smaller than supercells.

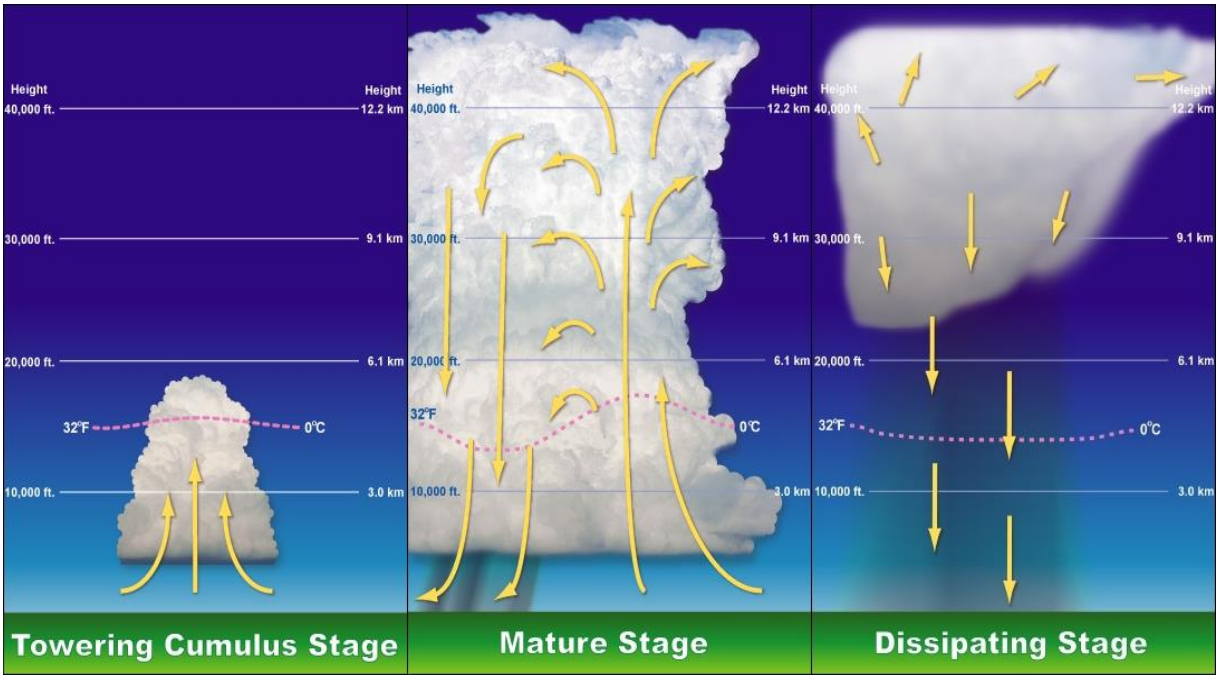

Figure 1.4 The conceptual of stage development of thunderstorms (Source: NOAA).

A critical concept that has emerged from past research on thunderstorms is that thunderstorms are composed of one or more dynamical building components known as cells. A cell is a small area of rather an intense upward air movement that has its life cycle. The characteristic complex structure and evolution of radar echoes may be simply understood in terms of the storm's constituent cells. The life cycle of thunderstorm cells divides into three stages determined by the magnitude and direction of the predominating vertical motions. The three stages are shown in Figure 1.4 namely developing or cumulus stage, mature stage, and dissipating stage.

a) Developing stage

The first stage of the lifecycle of thunderstorms is characterized by an updraft throughout the cell. In this stage, the cumulus clouds form when parcels of warmer air are lifted to the liquid condensation level (LCL). If the atmosphere is conditionally unstable, it is lifted to the level of free convection (LFC). After this point, parcels are free to rise beyond the equilibrium level (EL). In the cumulus stage, the significant concentration of rain or ice (or both) is suspended within the updraft at or slightly above the freezing level.

b) Mature stage

The mature stage begins when the precipitation starts falling from the cloud base. It usually reaches the ground, and the updraft continues and often reaches its strength in this stage. The precipitation is driven by the drops or ice particles that could be no longer supported by the updraft. In this stage, it is characterized by the existence of both updraft and downdraft. The mature stage encompasses the most intense period of the thunderstorm’s life cycle. Updraft and downdraft are at their maximum strength, and the precipitation is most intense. The maximum radar reflectivity is observed, and the cross-section of radar echoes at the top of the cloud could reach more than 10 km.

c) Dissipating stage

In this stage, it is dominated by the downdraft. The downdraft at the low-level outflow spreads out and undercuts the updraft, cutting off its source of warm and moist air. As rain partly evaporates during its fall, the air underneath the thunderstorm cloud is cooled and sinks, forming a downdraft that diverges horizontally and nearly uniformly in all directions as it reaches the surface. In the absence of significant vertical wind shear, the lifetime of thunderstorms typically lasts about 30 minutes (Doswell, 1985).

1.4.2 Characteristics of thunderstorms

A single-cell storm is developed with one main precipitation shower and its lifecycle as shown in Figure 1.4. The significance of single-cell storms in terms of precipitation or storm damage is relatively small when developing in a short time, usually 20 minutes - 30 minutes. The characteristics of single-cell thunderstorms usually indicate the small vertical wind shear and move with the mean environmental wind over 5 km to 7 km from ground level. The single-cell thunderstorms did not influence the storm and its structure depends on the storm cores and updraft (Benjamin et al., 2019). The cumulonimbus cloud mainly could bring a short localized heavy rainfall which was suddenly generated aloft and developed rapidly in a very short time was investigated (Nakakita et al.,2013; 2017). However, the single-cell of cumulonimbus takes on more importance when it serves as a building block of a larger multicell storm (Robert A.Houze, 2014). The study of the transition from single-cell to multicell is more concentrated on radar reflectivity in which the merging of echo cores involved the merger of updrafts (Wescott, 1994). They discovered that the enhancement of low-level convergence by storm outflows was essential in initiating the growth of new echo cores and increased the likelihood of a merger. In addition, the core motion, wider spacing between new and older core echoes, and differential speed of about 10 m s^{-1} were primarily found as factors of the merger.

Many researchers investigated the transition from multicell to supercell thunderstorm due to the adverse weather induced by the supercell. According to research by Vasiloff et al. (1986), the size and intensity of subsequent cells and updrafts increased due to a storm-environment feedback process involving updraft-downdraft interactions, as well as increased ambient vertical winds shear and buoyancy. Multicell storms often contain several cells in different stages of evolution. These storms move more rapidly because of the stronger wind and bring heavy precipitation and wind damage. The air mass thunderstorm, which occurs apart from frontal systems or other synoptic-scale disturbances, is a frequent and mostly non-severe event. They develop in areas of the atmosphere where there are moist and unstable conditions. Typically, locations with less shear produce air mass thunderstorms. However, when the change in wind velocity (speed and direction), it may produce high winds, hail, and heavy precipitation which develop because of high instability. Within the multicell storm, the pattern of cells is continuously changing as the downdraft air spreading out in the boundary layer triggers new cells.

The multicell has been defined as a group of cells, that behaves as a single unit. Each cell is in a different stage of the thunderstorm life cycle. The stages of a multicell are similar to those of a convective cell and can typically be divided into the developing stage, mature stage, and dissipation stage (Byers and Braham, 1949), with the life stages controlled by the source of updraft (Vasiloff et al., 1986). These stages could be referred to as illustrated in Figure 1.5. The weather radar could observe the patterns of cells in various stages of maturity which are enveloped in a single mass of cloud that the observer on the ground sees only one large cloud. The presence of vertical wind shear results in the tilting of the updraft and downdraft. Due to the tilting, the less buoyant downdraft air will not destroy the updraft and hence created the new updraft that converged with the region of strong low-level convergence.

The environmental conditions are required to maintain a line of a convective system which typically has a longer lifetime than the individual cells. The wind shear is an important role in the environment ahead of the line in sustaining the line's organization. As wind shear organizes the convection, new thunderstorms emerge due to the convergence of parent thunderstorm outflows and warm, moist inflow, which creates new updrafts. Multicell storms can develop along a line known as a squall line when continuous updrafts develop at the leading edge of the outflow, or gust front. Multicell clusters, on the other hand, signify the formation of new updrafts when the low-level convergence is strongest on the right or right-rear flank of existing cells. Multicell storms also need to be watched carefully for signs of one of the cells evolving into a slow-moving supercell.

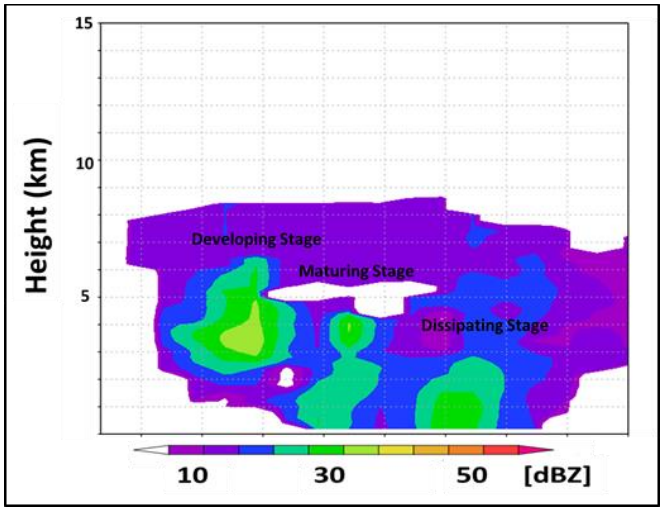

Figure 1.5 The illustration of three stages in the multicell thunderstorms that were observed as one single cloud by the observer at the ground.

1.4.3 Vertical vorticity in the supercell thunderstorm

The study of thunderstorm rotation is mostly related to the pattern of updraft and downdraft and this theory is investigated in supercell thunderstorms. A supercell thunderstorm is mostly investigated in the mid-latitude region due to its strength and associated adverse weather such as large hail and strong tornadoes. The supercell storm is a single-cell storm scale circulation consisting of one giant updraft-downdraft pair that dominates its cloud structure, air motion, and precipitation processes (Robert A.Houze, 2019).

The air motion associated with clouds are particularly prone to rotation, and fluid rotation is most helpful in understanding the dynamics of cloud. The local measure of the rotation is the vorticity, which is defined as the curl of the wind velocity:

$$\frac{\partial \omega}{\partial t} = \underset{\text{A}}{-\nu \cdot \omega} + \underset{\text{B}}{\omega \cdot \nu} + \underset{\text{C}}{\nabla \times \mathrm{B}k} \qquad (1.1)$$

where ω = curl ν is the vorticity vector.

Equation 1.1 expresses that the vorticity at a location can be changed by (A) advection of vorticity, changes in the orientation and length of vortex tubes (B), and baroclinicity (C). A quantitative study of the evolution of storm rotation considers the vertical component of (1.1),

$$\frac{\partial \zeta}{\partial t} = -\nu \cdot \nabla \zeta + \omega \cdot \nabla w \qquad (1.2)$$

that the baroclinic terms do not appear in this equation is a consequence of Boussinesq approximation. The second term on the right-hand side of (1.2) is often written as

$$\omega \cdot \nabla w = k \cdot \left(\frac{\partial \nu_H}{\partial z} \times \nabla_H w \right) + \zeta \frac{\partial w}{\partial z} \qquad (1.3)$$

where the first and second terms on the right-hand side are tilting and stretching terms, respectively; the subscript *H* denoted the horizontal component of a vector. The vortex stretching terms express the concentration of vorticity that occurs when vortex tubes are elongated, whilst the tilting terms indicate the conversion of vorticity parallel to one coordinate axis to vorticity around another axis as the orientations of vortex tubes change (Robert A.Houze, 2019).

The vorticity has been examined using Doppler analysis to determine the common formation mechanisms of supercells, tropical cyclones, and tornadoes. The formation of counter-rotating vortices surrounding the updraft is a universal characteristic of all convective clouds in the early stage of development. Commonly, the core of the updraft is located between the vorticity

pair (Franklin et al., 2006). It is well known that the counter-rotating couplet plays an important role in cloud dynamics, affecting the entrainment of ambient air into convective clouds as well as the pressure field on the cloud. In the early stage of supercell formation, a pair of positive (generated along the southern flank of updraft) and negative (produced on the northern flank of updraft) vertical vortex tubes appeared in the rain cell when the horizontal vortex tube meets an updraft. Based on studies of thunderstorm rotation, the lower-level vorticity pair extrema increase after the initial stage due to vortex stretching and convergence on the updraft and downdraft sides (Rotunno, 1981). It has been discovered that tilting and stretching mechanisms are required for the dynamic formation of vorticity.

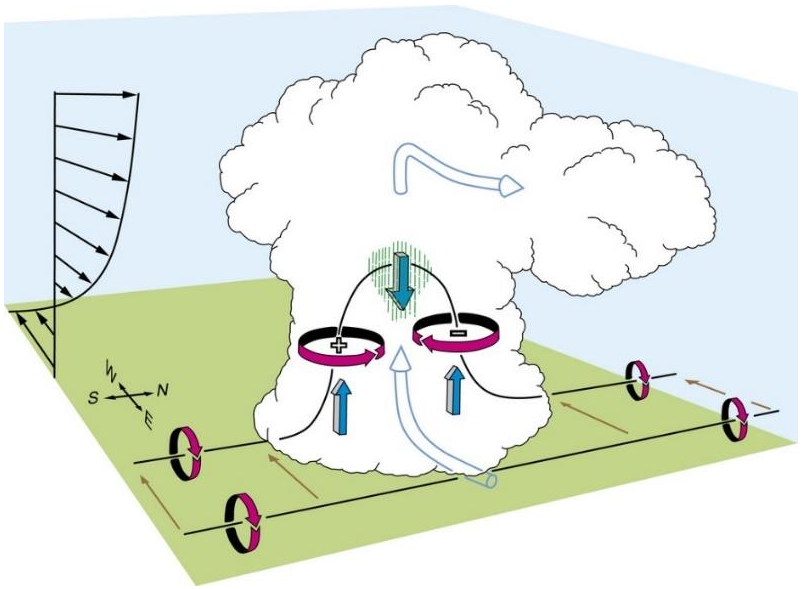

Figure 1.6 Conceptual model of tilting mechanism that leads to updraft rotation. The pink ribbons represent the vertical flow associated with the vortex lines. The black arrows represent the ambient vertical wind profile. (Source: Dahl, J. M. L.,2017).

As illustrated in Figure 1.6, the vertical vorticity arises in a cloud by tilting crosswise horizontal vorticity from the environment by considering a large-scale environment in which the mean flow u is unidirectional in the x-direction and increases with height. The environment has crosswise horizontal vorticity which is illustrated schematically by the north-south aligned vortex tubes outside the cloud. When the updraft of the convective cloud is superimposed on the vortex tube, the tube is deformed upward then exists vorticity around vertical axes in the form of counter-rotating vortices on either side of the updraft.

The research of vertical vorticity in the evolution of thunderstorm rotation by Rotunno (1981) revealed that the convergence in the updraft and divergence in the downdraft at the lower level height substantially enhanced the cyclonic or anticyclonic of the vortex pair in the rightward or leftward moving storm. Initial maximal vorticity occurred at the largest gradient of vertical velocity. In addition, the analysis of vertical vorticity in single-cell thunderstorms for identifying hazardous rain cells was established, and the vorticity within baby rain cells was investigated (Nakakita et al., 2017). They confirmed the presence of a pair of positive and negative vertical vortex tubes as well as an updraft in the early stage of a rain-cell. The schematic figure of the formation of a vertical vortex tube as illustrated in their research is presented in Figure 1.7.

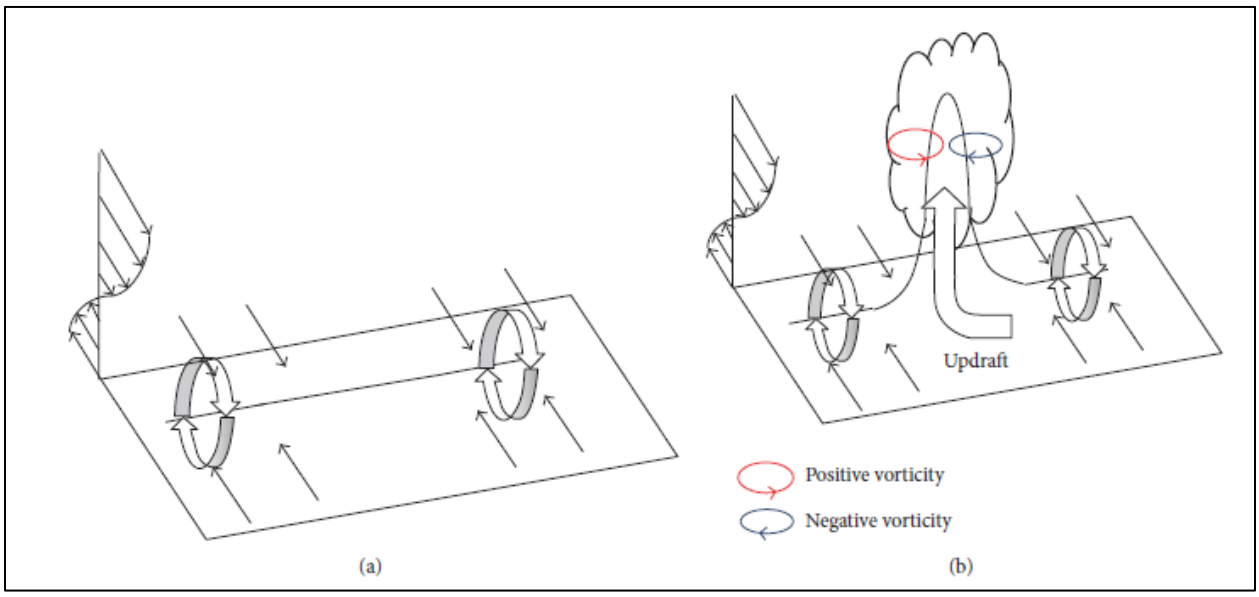

Figure 1.7 Schematic figure of the creation of a vertical vortex tube. Circular arrows depict horizontal vortex tube circulations. (a) The horizontal wind shear forms a vortex tube with a horizontal orientation. (b) An updraft tilts a horizontal vortex tube into a vertical vortex tube. (Source: Nakakita et al.,2017)

1.4.4 Multi-parameter radar analysis

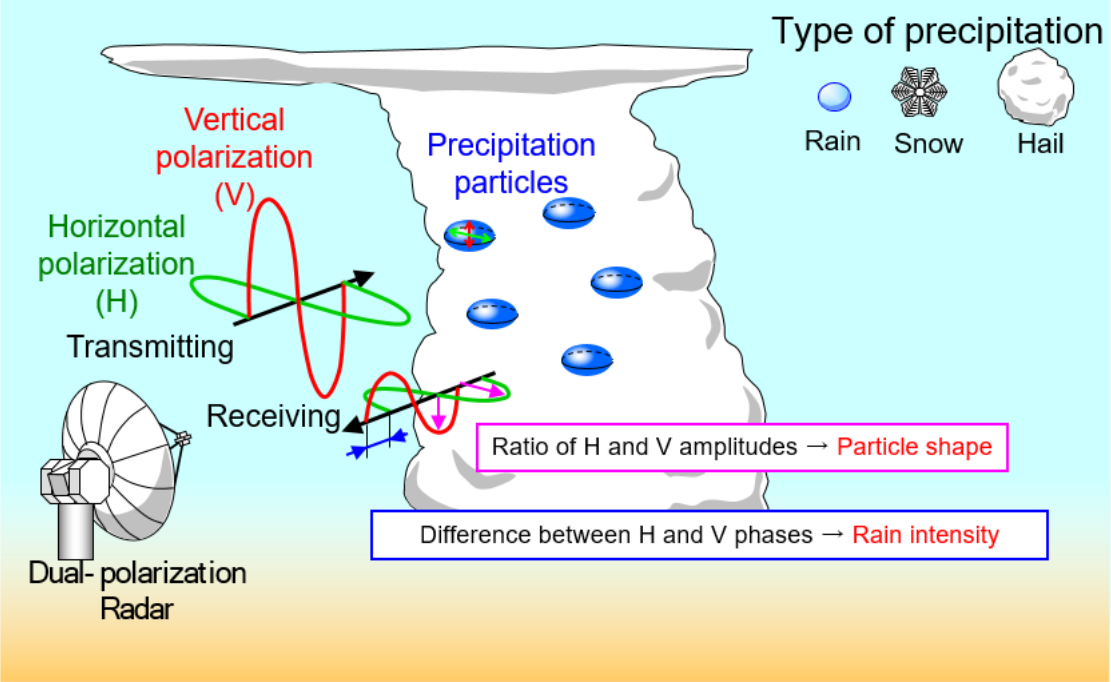

Figure 1.8 Information of dual polarization parameters observed from MP radars (Source: Japan Meteorology Agency (JMA)).

Dual-polarization radars are radars that transmit and receive radiation in both horizontal and vertical polarizations. Polarimetric parameters reveal the predominant ice particle types involved in precipitation processes. The dual-polarization or MP radars parameters are widely used for rainfall estimation, supercell signatures, and radar echoes classification. Instead of utilizing horizontal polarization (Z_h), other radar parameters such as differential reflectivity (Z_{dr}), specific differential phase (K_{dp}), and the magnitude of the copular cross-correlation coefficient (ρ_{HV}) are also mainly used in the detection of severe thunderstorms. Information on these dual polarization parameters is described in Figure 1.8. The polarimetric parameters can provide information on the severity in terms of rainfall intensity, updraft strength, and locations which would be able to forecast the severity of storm structures. These benefits could improve the early warnings of the dissemination of severe weather and assist the forecasters in arbitrating the termination of issuance warnings. In the meantime, these products provide more information about the microphysical processes in the storm, which can help in improving the numerical weather prediction models. The non-meteorological targets also could be differentiated such as bugs and birds, from the meteorological data.

Research on polarimetric radars has often observed a narrow of enhanced Z_{dr} values about the ambient 0℃ level near the region of thunderstorms updraft as the signature in short-term thunderstorm forecast, labeled as Z_{dr} column. This signature appears to be associated with rising motion within thunderstorms. Z_{dr} column analysis is strongly suggested in the operational and research application due to its identification of updraft location and strength (Kumjian et al.,2008). The strength of prominence of Z_{dr} columns in multicellular convection may allow forecasters to distinguish between the decaying cells and intensifying cells. The changes in appearances of the Z_{dr} column can give forecasters a prognosis of storm behavior and improve the lead time for increases in storm severity. The Z_{dr} columns may also aid in tracking dominant updrafts in multicell storms or storm-merger situations.

In addition, the positive values of K_{dp} observed above the melting level, which is labeled as the K_{dp} column, are usually associated with deep convection updraft cells. Many studies proved that K_{dp} volumes with the updraft mass flux, lightning flash, and intense rainfall. Moreover, K_{dp} columns also reveal signatures of changing updraft properties in the evolution of storm events (van Lier-Walqui, M. et al., 2016). As dual polarization research currently is more investigated due to its advantages of discrimination of rainfall distribution and intensity, the K_{dp}-R relationship also is used in the intensity conversion owing to the less susceptible to drop size distribution (DSD) variations, especially in heavy rain. The characteristics of the supercell thunderstorm were developed by using the parameters. The feature of the Z_{dr} arc at low levels reduced ρ_{HV} in the storm-inflow region at low levels and in the updraft commonly existed in the supercell storms. It was also discovered that Z_{dr} and K_{dp} columns, as well as midlevel rings of enhanced Z_{dr} and depressed ρ_{HV} are commonly detected around the main rotating updraft and in the rear-flank downdraft (Kumjian, et al., 2008).

1.5 Structure of Dissertation

This dissertation consists of six chapters. The outline of this dissertation is illustrated in Figure 1.9. A brief explanation of each chapter is as followed:

Chapter 2 briefly explains the data used in the analysis using radar parameters in detail. It includes data acquisition used for the pseudo-vorticity analysis and dual-Doppler analysis. The Doppler radial velocity is used for the extraction of vertical vorticity. The multi-parameter radar

distribution and analysis are discussed in quantifying the mechanisms and cell features. Dual-Doppler analysis used two radars is described in detail to investigate the kinematic mechanisms. The study area and synoptic condition of each event are discussed using radiosonde observation data and hodograph to visualize the synoptic condition of multicell formation for related events.

Chapter 3 presents the preliminary analysis of single-cell to multicell using pseudo-vorticity analysis. The cell merging boundary of single-cell and multicell are defined based on radar reflectivity and compared with core vorticity. The definition for each cell is explained in detail in this chapter. In this preliminary analysis, pseudo-vorticity is utilized to identify the structures of cell merging based on the vertical vortex tube analysis. To determine the lifetime of cell development, the initial stage of vorticity is examined until their dissipation stages of core reflectivity.

Chapter 4 proposes the improvement of vertical vorticity analysis by introducing the criteria of characteristics to be investigated. The analysis is divided into two methods, pseudo-vorticity, and dual-Doppler vorticity analysis. The characteristic is emphasized in the time-series of intensity evolution before and after cell merging, the formation height of the peak of core vorticity, and distance analysis with the same sign of core vorticity. The kinematic and dynamic mechanisms estimated from the dual-Doppler analysis will be investigated for more understanding of multicell development. The Pearson correlation coefficient for each height is investigated to identify the relationship of core vorticity intensity with the mechanisms.

Chapter 5 enhances the investigation of the transition from the first development of single-cell to multicell thunderstorms in the different events and synoptic conditions. The multi-parameter radar analysis is emphasized by focusing on the columns of Z_{dr} and K_{dp} that are widely utilized in the research. The single-cell that is not merged is also included in this study by investigating each characteristic of polarimetric radar parameters and core vorticity intensity. The updraft strength and formation height of updraft from dual-Doppler analysis also are compared to quantify the mechanisms with the polarimetric characteristic and vertical vorticity analysis.

Chapter 6 concludes the research study throughout the analysis and summarizes the transition signals from single-cell to multicell. The criteria of vertical vorticity characteristics and comparison of utilization from the two methods will be explained in detail. The study of multi-parameter radar analysis and kinematics mechanisms provide insight into the understanding of

multicell thunderstorms development as well as the synoptic conditions that influence the formation, transition, and characteristics of single-cell and multicell. The research contributions, limitations, and further works relevant to this study are included in this chapter.

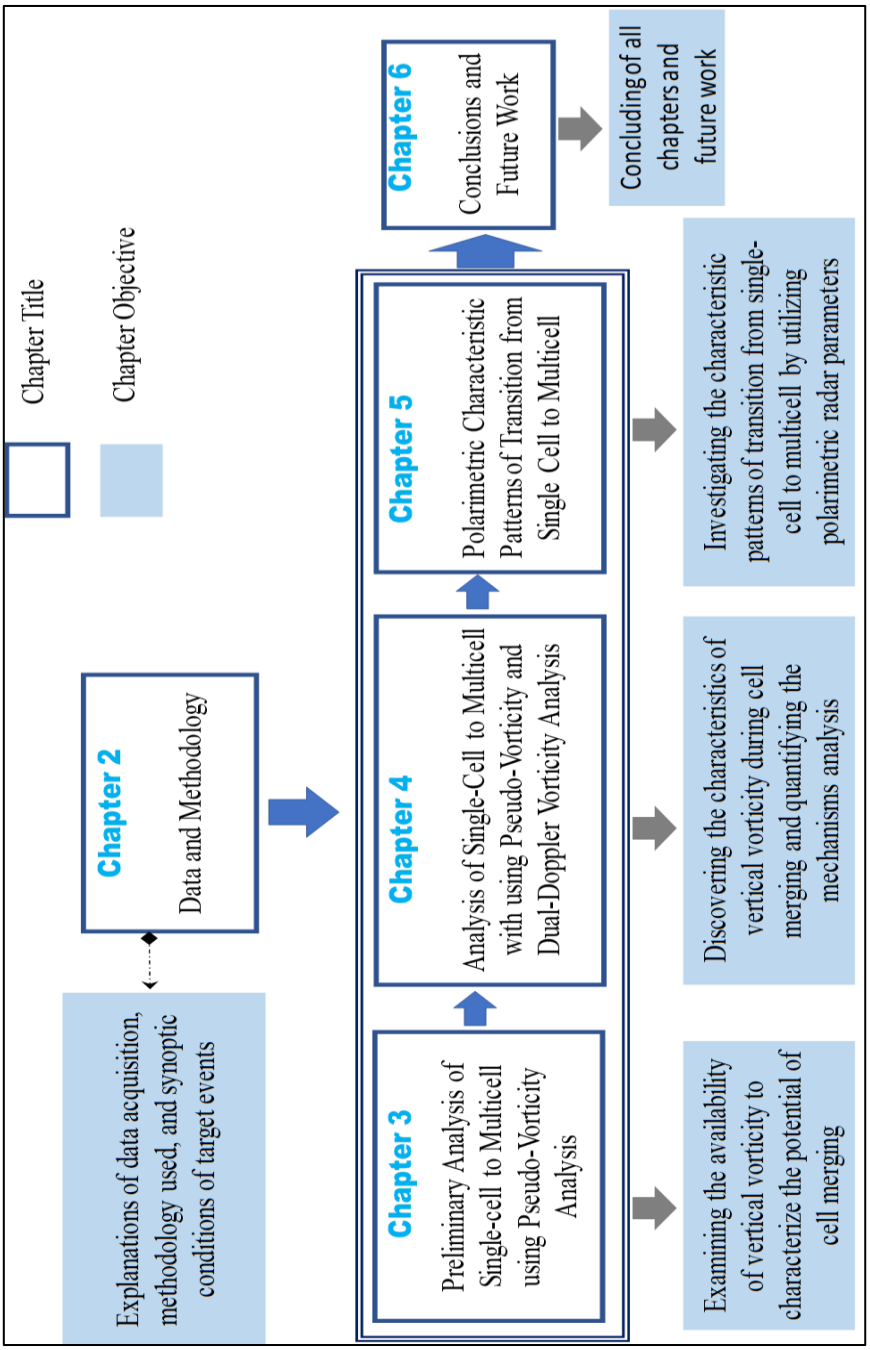

Figure 1.9 The outline of thesis chapter with its own objectives.

CHAPTER 2

2 Data and Study Area

2.1 Radar Observation and Data Acquisitions

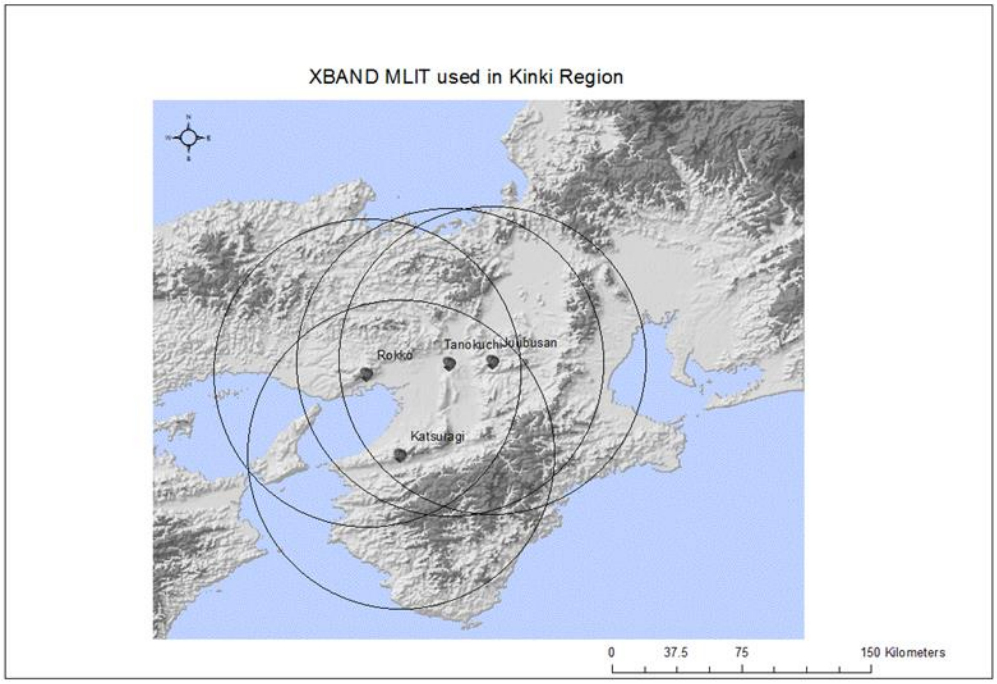

Figure 2.1 Four radar stations in the Kinki region, Japan, were used for the observation of the cell merging of the radar reflectivity. The dashed black arrow shows the maximum range of 80 km between the radar stations.

The XRAIN operated by MLIT was used in this study. In this analysis event, X-band polarimetric radar with parabolic antenna namely Tanokuchi, Rokko, Juubusan, and Katsuragi radar stations was selected, as illustrated in Figure 2.1. The radars cover an 80-km radius. All radars have a sampling resolution of 150 m, and the azimuth resolution is 1.2 degrees in the radial direction based on 12 elevation angles. The detailed radar specification is presented in Table 2.1. Each radar scans for 20 seconds for one rotation, which means that one minute can be used for three rotations of varied angle scanning. The scanning strategies for every one minute included scanning from a low angle and two scans at a higher angle to acquire entire volume scan data as illustrated in Figure 2.2. The Kinki region XRAIN radar observation schedule generates composite radar images every minute and entire volume scan data every five minutes.

Table 2.1 Specification of MLIT X-band Multi-Parameter Radars

Features	Specifications
Microwave amplifier	Klystron or solid-state device
Wavelength	3 cm
Frequency	9700 MHz- 9800MHz
Transmit Power	100 kW
Pulse Width	1.0 μ sec
Antenna	Parabola, $\phi \leq$ 2.2 m
Antenna gain	$\geq$ 42 dBi
Beam width	$\leq$ 1.2°
Elevation Angle	12
Data resolution	150 m (range) 1.2 º (azimuth)
Observation Range	80 km
Parameters	Horizontal Polarization (Z_H), Doppler velocity (V), Differential Reflectivity (ZDR), Copolar Correlation Coefficient (ρ_{hv}), Differential phase shift (Φ_{DP}), and Spectrum Width (W)

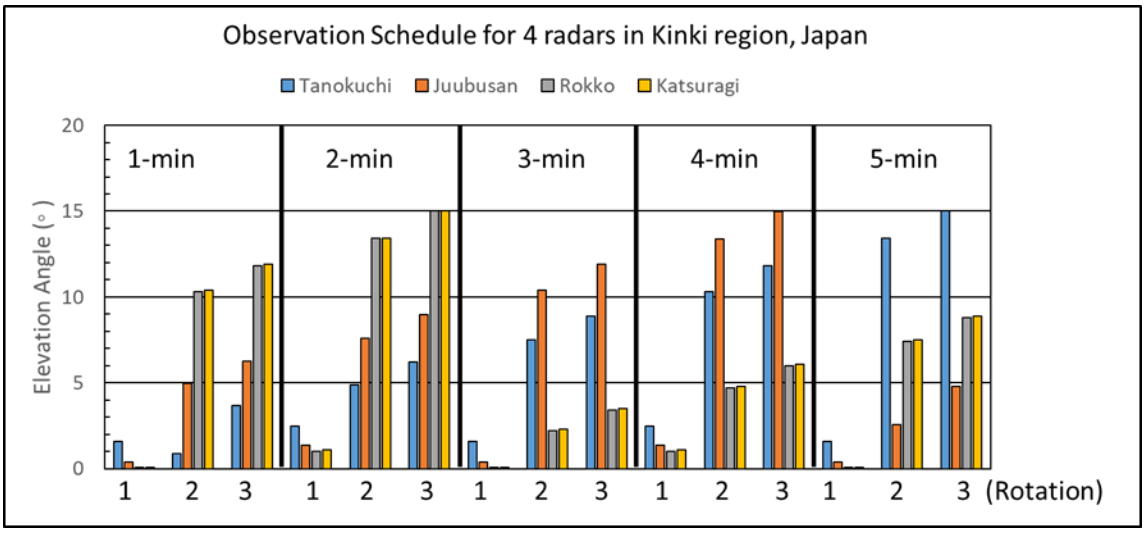

Figure 2.2 The XRAIN radar observation schedule in the Kinki region, Japan using 4 radar stations to acquire entire volume scan data.

2.1.1 Radar parameters

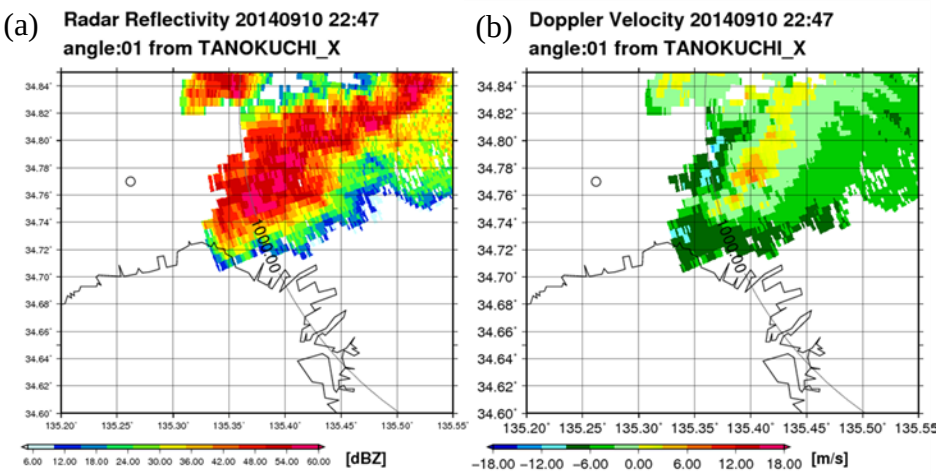

Figure 2.3 Example of horizontal distribution of the (a) radar reflectivity, (b) Doppler velocity

The Doppler single polarization radar provided only parameters such as Doppler velocity and radar reflectivity (Z_h). The example of these radar parameters is shown in Figure 2.3. The Doppler velocity is the radial velocity that moves towards and away from the radar. Doppler radar is mainly utilized in the identification of cyclonic and anti-cyclonic rotation, divergence, and convergence signatures related to the severity of the weather. The divergence signature is indicated as the downburst happens at the areas, meanwhile, convergence is specified as the initial stage of updraft at the lower-level elevation angles. Cyclonic signatures are dependent on the circulation of air motion of radar clouds that reveals the meso-cyclone is occurring during severe weather. Figure 2.4 shows the signature patterns that are used in the detection of severe weather.

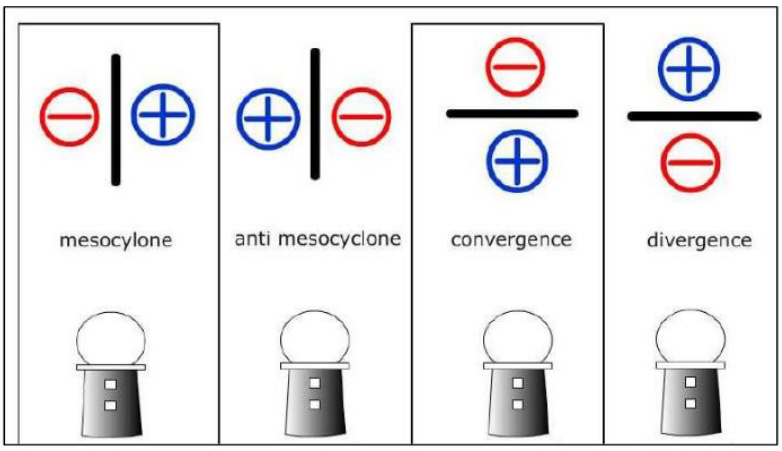

Figure 2.4 The signatures from point of radar based on velocity products.

If a radar signal is transmitted with an initial phase of ϕ_0 in the distance in radians, then the phase of the returned signal will be

$$\phi = \phi_0 + \frac{4\pi r}{\lambda} \qquad (2.1)$$

Furthermore, the time rate of change of phase from one pulse to the next pulse is given by

$$\frac{d\phi}{dt} = \frac{4\pi r}{\lambda}\frac{dr}{dt} \qquad (2.2)$$

where ($V_D = dr/dt$) is the Doppler velocity.

The radar reflectivity provides useful information on the position of storms, their movement, and their development. It is mainly used to estimate the rainfall rate (R) with the relationship between radar reflectivity (Z) and R using the Z-R relationship. Z is the radar reflectivity factor in a unit ($mm^6\ m^{-3}$) and is defined as follows:

$$Z = \int_0^\infty N(D)D^6 dD \qquad (2.3)$$

where D is the diameter of a raindrop (m), N(D) is the number distribution of diameter. The relationship between rain rate (R) and radar reflectivity (Z) is commonly described as the empirical power-law relationship

$$Z = aR^b \qquad (2.4)$$

where *a* and *b* are empirically derived constant.

There are various Z-R relationships used in the radar research study, as listed in Table 2.2. Conventional radars can underestimate rainfall rates because their signals are weakened by intense precipitation. Therefore, multi-parameter radars currently use the specific differential phase K_{dp} to estimate rainfall rate using the K_{dp}-R relationship owing to the less sensitivity to DSD, and K_{dp} is not affected by rain attenuation.

Table 2.2 Several Z-R relationships are used depending on the type of clouds

$Z=aR^b$	**Relationship**	**Type of cloud**
$Z=200R^{1.6}$	Marshall Palmer	General stratiform precipitation
$Z=250R^{1.2}$	Rosenfeld	Tropical convective system
$Z=400R^{1.4}$	Laws and Parsons	General stratiform precipitation
$Z=300R^{1.5}$	Joss and Waldvogel	General stratiform precipitation

The distinction between Z_h and Z_v is known as the differential radar reflectivity (Z_{dr}). Z_{dr} displays the ratio of scattering targets in relation to particle form. For spherical targets, it ranges from close to zero to values as high as 5 dB for echoes from oblate targets like huge raindrops. Z_{dr}, on the other hand, responds negatively to vertically long objects like significant hail. Z_{dr} is helpful for classifying hydrometeors and estimating the rate of rainfall. Z_{dr} formula is given by:

$$Z_{dr}=10\log_{10}\left(\frac{Z_H}{Z_V}\right) \qquad (2.5)$$

The differential phase (ϕ_{dp}) is defined as the phase difference between horizontal and vertical signals. The phase of the horizontal signal begins to lag earlier than the vertically polarized signal because falling raindrops are not spheres. The signals' phases slightly shift as a result. The magnitude is influenced by the direction in which hydrometeors fall and the total path length to the target. In general, ϕ_{hh} is greater than ϕ_{vv} due to the flattening of raindrops as they fall. ϕ_{dp} can be defined by the following equation:

$$\phi_{dp} = \phi_{hh} - \phi_{vv} \qquad (2.6)$$

Since ϕ_{dp} is path accumulated value, it is not clear the occurrence of heavy rainfalls. Therefore, the rate of change of the differential phase ϕ_{dp} is called a specific differential phase or K_{dp}. K_{dp} is often used for heavy rainfall detection, especially in high amounts of liquid precipitation. K_{dp} can be defined as the equation below:

$$K_{dp} = \frac{\phi_{dp}(r_2) - \phi_{dp}(r_1)}{2(r_2 - r_1)} \qquad (2.7)$$

In the observation of drop size distribution (DSD), Maki et al. (2005), revealed that the maximum contribution of raindrops to rainfall was closer to K_{dp} and Z_h, and useful in studying the weak rainfall events using X-band radar owing to larger scattering simulations. Numerous studies have demonstrated that K_{dp} is also largely resistant to beam obstruction, irrespective of radar power calibrations, and unaffected by attenuation caused by heavy rain. (Bringi et al., 1990). The example of the radar-rainfall R-K_{dp} relationship developed by Maki et al. (2005) is as follows:

$$R(Z_h; K_{dp}) = \begin{cases} 0.229Z_H^{0.673} \\ 19.63K_{DP}^{0.823} \end{cases} \begin{matrix} for\ K_{DP} \le 0.3\ degkm^{-1}\ or\ Z_h \le 35\ dBZ \\ for\ K_{DP} > 0.3\ degkm^{-1} \end{matrix}$$

The correlation coefficient ρ_{hv} is the correlation coefficient between horizontal and vertical signals which is very useful for hydrometeor classification and quality control. ρ_{hv} reflects the diversity of scattering targets within a bin with a possible range of values is 0 to 1, but mostly the data is within the range of 0.7 to 1.0. In the detection of uniform particles such as drizzle, light rain, or oriented ice particles, ρ_{hv} values are close to 1, meanwhile, for not uniform particles such as melting snow, and hail with rain, the values are typically between 0.85 to 0.95. For the non-meteorological target such as ground clutter or biological targets, ρ_{hv} less than 0.85. ρ_{hv} is defined as follows:

$$\rho_{hv} = \frac{< s_{vv} s_{hh}^{*} >}{< |s_{hh}|^2 >^{1/2} < |s_{vv}|^2 >^{1/2}} \qquad (2.8)$$

where, s and s* are scattering matrices, and subscripts *h* and *v* represent the received and transmitted polarizations for horizontal and vertical signals, respectively.

2.1.2 Dual-Doppler radar

The most essential and extensively used approach for determining air movements within precipitating cloud systems is dual-Doppler synthesis. A dual-Doppler analysis also presented an analysis of the horizontal and vertical motion in the storms. The study of kinematics and precipitation structure could be established by utilizing dual-Doppler analysis in terms of convergence or divergence, updraft or downdraft, and wind field motion. Doppler radar studies have clarified airflow patterns in convective systems by investigating radar evolution, and vertical air motions inside air volumes occupied by hydrometeors (Robert A.Houze, 2014).

A single Doppler radar can measure the radial component of a target but cannot produce the complete three-dimensional velocity. Therefore, dual-Doppler processing is beneficial in retrieving the three-dimensional wind fields by the combination of radial velocity from two Doppler radars. The dual-Doppler radar analysis is helpful in understandings of the weather phenomena such as in mesoscale convective system analysis and mechanism influenced in cloud development (Kim et al., 2012). The continuity equation is employed in most dual Doppler radar studies, and in recent years, a variational technique has been applied to minimize a cost function, defined as the distance between the analysis and the observation, to yield optimal *u*, *v*, and *w*

components. The variational method proposed by Gao et al. (1999) is a procedure that minimizes the cost function J and is defined as the sum of squared errors due to the misfit between observations and analyses subject to constraints. In this study, the constraints used in Protat et al. (1999) are adapted. When the analysis was performed, the simplified Shimizu and Maesaka (2006) cost function is used as shown in Appendix-B.

Using the mass continuity equation and assuming the terminal velocity is a function of the radar reflectivity, the four unknowns could be solved. The four unknowns are *u*, *v*, *w*, and w_t where these are the component of velocity in the *x*, *y*, and *z* directions, and w_t is the terminal velocity of the precipitation. The horizontal winds (*u*, *v*) are then used to compute the vertical velocity (*w*) using a mass continuity equation by considering the terminal fall velocities of rain, snow, and graupel. This latter relationship is based on Marshal-Palmer drop size distribution and the laboratory measurement by Gunn and Kinzer (1949). In this study, the terminal velocities relationship of rain, snow, and graupel reported by Shimizu et al. (2008) are shown in Equation 2.9:

$$W = \begin{cases} -0.75\left(\frac{\rho}{\rho_0}\right)^{0.4} Z_e^{0.0714} \; for\; snow \\ -3.80\left(\frac{\rho}{\rho_0}\right)^{0.4} Z_e^{0.0714} \; for\; rain \\ -1.23\left(\frac{\rho}{\rho_0}\right)^{0.4} Z_e^{0.103} \; for\; graupel \end{cases} \qquad (2.9)$$

where ρ and ρ_0 indicate the air density and surface density respectively, and Z_e $(mm^6\, mm^{-3})$ indicates the equivalent reflectivity factor.

The additional assumption of boundary condition is also required, in which the vertical wind component of the wind is zero at the bottom of the surface by considering the earth's surface is not porous (Ronald E., 2004). The sounding data is needed for reducing errors in estimating vertical velocity near the storm top and filling in the data-void regions between successive elevation angles (Shimizu et al., 2008). The dual-Doppler analysis (hereafter termed as "DDA"), using the variational technique proposed by Shimizu et al. (2008) and Protat and Zawadzki (1999) method was used in this study. Previously, the Gao et al. (1999) method was applied with an approach that suppressed the iterative process typically associated with the Cartesian retrieval algorithm. However, using Protat and Zawadzki (1999) method, an improved method by considering both upward and downward integrations using zero velocity at ground level and 750

m above the radar echo as boundary conditions were proposed to limit the errors in the vertical component. For the three-dimensional (3D) wind field retrieval, the adjustment of the particle fall velocity along the vertical axis and integrating both the ground- and upper-level boundaries should be taken into account to obtain more realistic upward and downward motions inside the cell (Protat and Zawadzki,1999; Shapiro et al., 2009; Shimizu, 2012).

The other important element in considering DDA is the crossing angle, which its function as minimizing the variation of the cross-baseline component of wind. Its effect is maximum close to the radar baseline, and weak in the properly conditioned areas. As illustrated in Figure 2.5, useful data would be limited to the shaded area within the larger circles except for the area within the circle along the baseline (hatched areas). The radar beam intersects at 90° along the central circle. The beam intersects at 60° at the dashed circles. The useful data can be obtained by enlarging the circles, so the beams intersect at 30°. The intersection angles used in the range of 20° to 30° depend on the target location. As a result, the selection of crossing angle is essential to allow the minimization of variation of the cross-baseline component of wind, and the distance between two radars should be less than 100 km (Friedrich and Hagen, 2004). The data from a dual-Doppler must also consider from a different point of view to be an indeed useful observation. If the two radars are looking at the storm in the same direction, they will both measure the same component of velocity, then, there is no information available, especially on the baseline that connects the two radars. Thus, the radars need to view the storms from a different direction, and the ideal situation is when the two radars are exactly 90° apart.

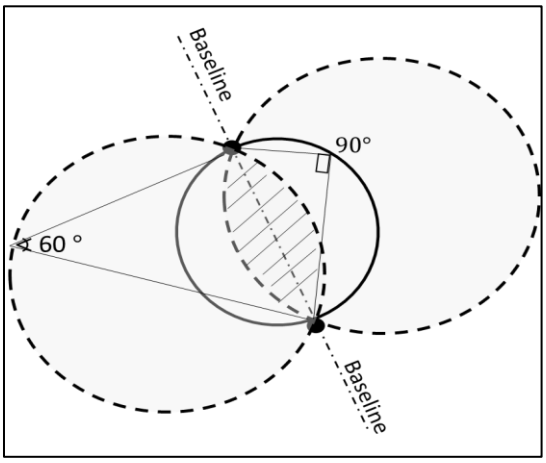

Figure 2.5 Schematic illustration of the location of dual-Doppler lobes for two Doppler radars (Ronald E., 2004).

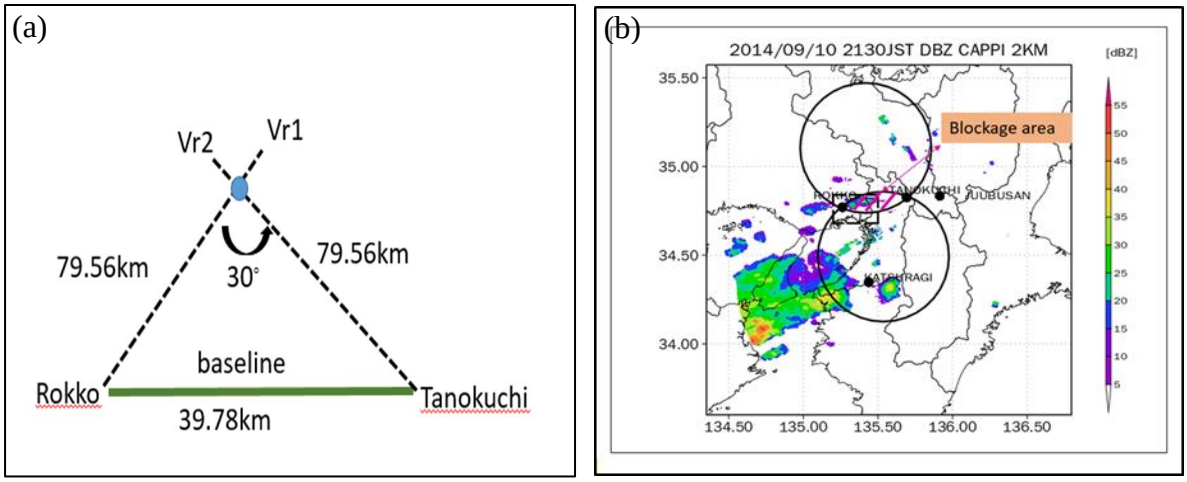

Figure 2.6 (a) The illustration of the calculated baseline from two radars with a crossing angle of 30 degrees. (b) The blockage area is shown at the target area when used two radars as mentioned in (a).

As illustrated in Figure 2.6(a), the calculated baseline from Tanokuchi to Rokko radar is 39.78 km, and by using a crossing angle of 30°, the estimated maximum radar coverage from each radar is 79.56 km, which this coverage is suitable for the observation range of 80 km that is operated in this region. The radar was also observed in the different views of the storm. However, the selection of radars is essential in analyzing the target location and the crossing-angle that should be utilized. For example, in Figure 2.6(b), the target area of study for event one (September 10, 2014) is not covered by the dual-Doppler analysis from Rokko and Tanokuchi radar stations as it is located at the baseline. Therefore, the other radar stations should be considered in this case study.

The Tanokuchi and Katsuragi stations were used for the DDA in this study, as shown in Figure 2.7(a) for the analysis of September 10th, 2014. The distance between the two radars is 58 km with the crossing angle used being 30°. In addition, the case study for event 2 (August 13th, 2018) and event 3 (July 25th, 2019) are presented in Figure 2.7(b). The selected two radars use for this events analysis are Tanokuchi and Rokko owing to the shortest distance to the target areas. The target analysis was carried out within the area denoted by the dashed red box. The crossing angle used is 20° to minimize the hatched areas between two radars. The Doppler radar data and radar reflectivity (Z_h) are interpolated into a Cartesian coordinate system with a horizontal grid spacing of 1.0 km and a vertical grid interval of 0.5 km Constant Altitude PPI before using the

dual-Doppler radar program (CAPPI dataset). To accurately estimate 3D wind vectors, spatially and temporally discontinuous and anomalous data were removed as noise from the Doppler velocities.

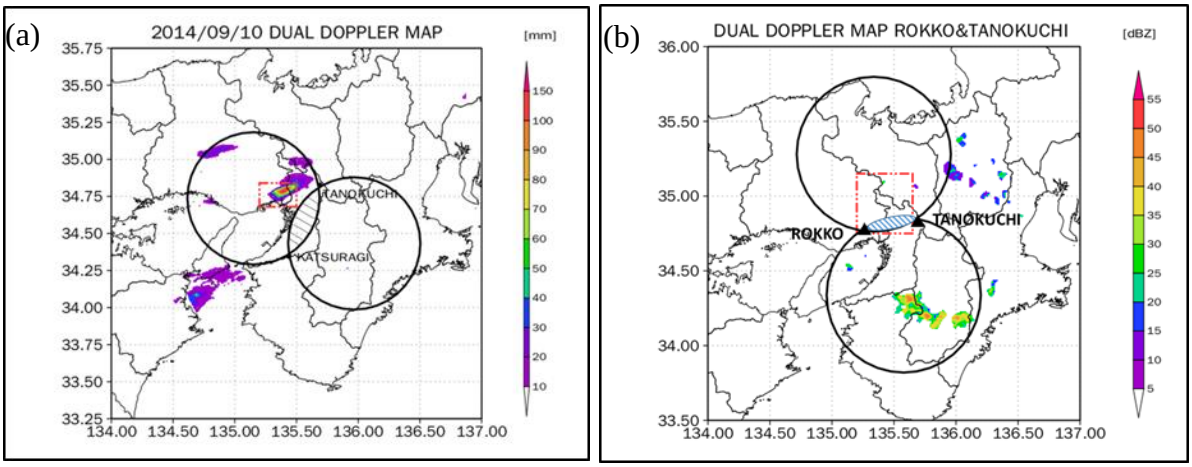

Figure 2.7 The observation domain for the dual-Doppler radar study was conducted within the two solid circles, but not within the hatched area, as shown on the map for (a) event 1 and (b) event 2.

2.2 Vertical Vorticity Analysis

2.2.1 Dual-Doppler Analysis

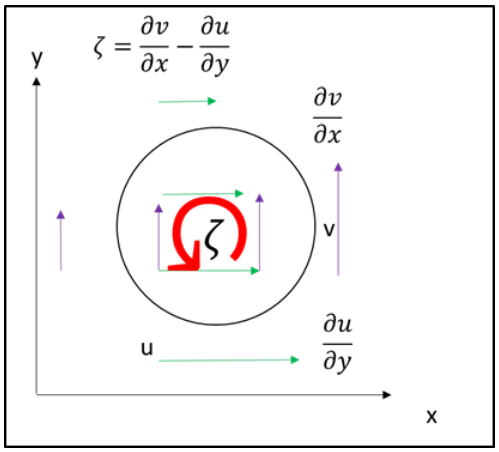

Figure 2.8 Schematic illustration of DDA vertical vorticity analysis.

Referred to Figure 2.8, the illustration of the estimation of DDA vorticity is shown. In the Cartesian coordinate system, the vertical vorticity is expressed as Equation (2.10):

$$\zeta = \frac{\partial v}{\partial x} - \frac{\partial u}{\partial y} \qquad (2.10)$$

where u is the zonal wind component, and v is the meridional wind component in the x and y direction, respectively.

The core vorticity of the DDA is defined as the maximum intensity of the positive and negative vorticities, which was obtained from the 5 min data for each CAPPI height. Table 2.3 described the advantages and disadvantages of the aforementioned methods. Each method has its advantage, therefore, in the final analysis, we expect to distinguish the limitation of pseudo-vorticity rather than DDA vorticity.

Table 2.3 Advantages and disadvantages of vertical vorticity methods

	Pseudo-Vorticity	DDA Vorticity
Advantages	• High spatial resolution • High temporal resolution	• High-quality estimation • Provide a 3D wind field
Disadvantages	• Not able to provide 3D wind fields	• Low temporal resolution • Low spatial resolution
Radar used	• Only one	• Two radars

2.2.2 Pseudo-Vorticity Analysis

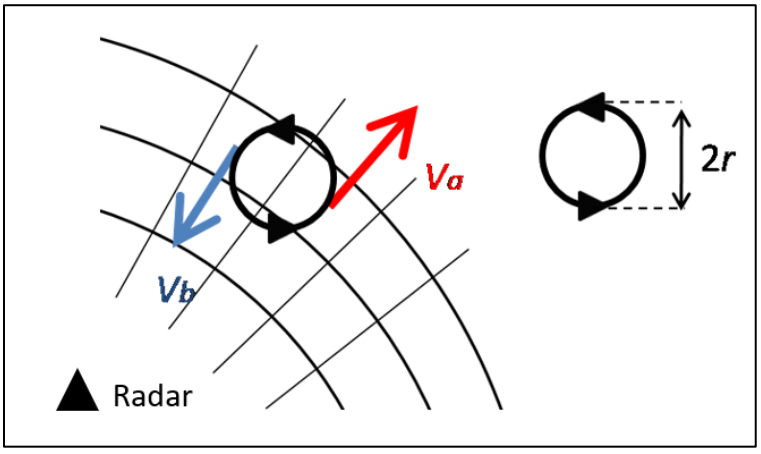

Figure 2.9 Illustration of pseudo-vorticity estimation using single radar.

The pseudo-vorticity is observed at a single radar, and the selection of radar is dependent on the distance from the radar to the target area. The selection also considers the data is not affected by radar noise errors such as blockage and data contamination. For the extraction of vorticity distribution from Doppler velocity, it was converted directly from raw data in the polar coordinate system without interpolation to analyze the vortex tube analysis.

The pseudo-vorticity was estimated by applying the method proposed in Nakakita et al. (2017) with a spatial resolution of 50 m × 50 m in each elevation angle at 1 min intervals. Using the radial velocity speed, the vorticity can be calculated by using Equation (2.11),

$$\zeta = 2 \times \frac{V_a - V_b}{2r} \qquad (2.11)$$

where V_a and V_b are the radial velocities moving toward and away from the radar in the Cartesian coordinates, respectively, and 2r is the total distance of radar pulse between the mesh's center. The illustration of pseudo-vorticity estimation is illustrated in Figure 2.9.

In this study, the core vorticity is defined as the maximum intensity of the positive and negative vorticities at each plan position indicator (PPI), which was extracted from the 1-min data for each elevation angle of PPI. In addition, the moving average method (150 m and 550 m) was used in this study for more enhancement of the vertical vorticity structure.

2.3 Study Area and Synoptic Conditions

In this study, we observed the storm cluster in the Kinki region and chose only events with heavy precipitation that occurred due to the atmospheric instability with the condition of multicell formation. The environmental condition of instability condition can be evaluated using Convective Available Potential Energy (CAPE) and Bulk Richardson Number (BRN) using radiosonde data observation. The low value of CAPE is not sufficient to support the multicell formation. According to a study, a typical multicell (or supercell) environment over the Great Plains (e.g., 2022 J kg^{-1} for a multicell, Stalker and Knupp 2022; 2542 J kg^{-1} for an Oklahoma supercell, Bluestein and Jain 1985). However, the frequency distribution of CAPE in the Tokyo region has been recorded at a value of 1000 J kg^{-1} at Tateno, in May between 1990 and 1999 (Shimizu et al., 2008). In general, BRN > 45 is favorable for multicell formation from a study (Weisman and Klemp 1982, 1984, 1986; Peterson 1984; Bluestein and Jain 1985). We will consider these two types of atmospheric

instability indicators as well as the environment condition derived from the JMA Mesoscale Model (MSM).

2.3.1 Event 1 - September 10, 2014

In this event, this study focused on the broken areal-type formation related to the development of an unstructured area relative to moderate-to-intense cells that merged into a line of convective storms. According to Bluestein and Jain (1985), this type of multicell has a longevity of 30–90 min without repetition, with the cluster storm.

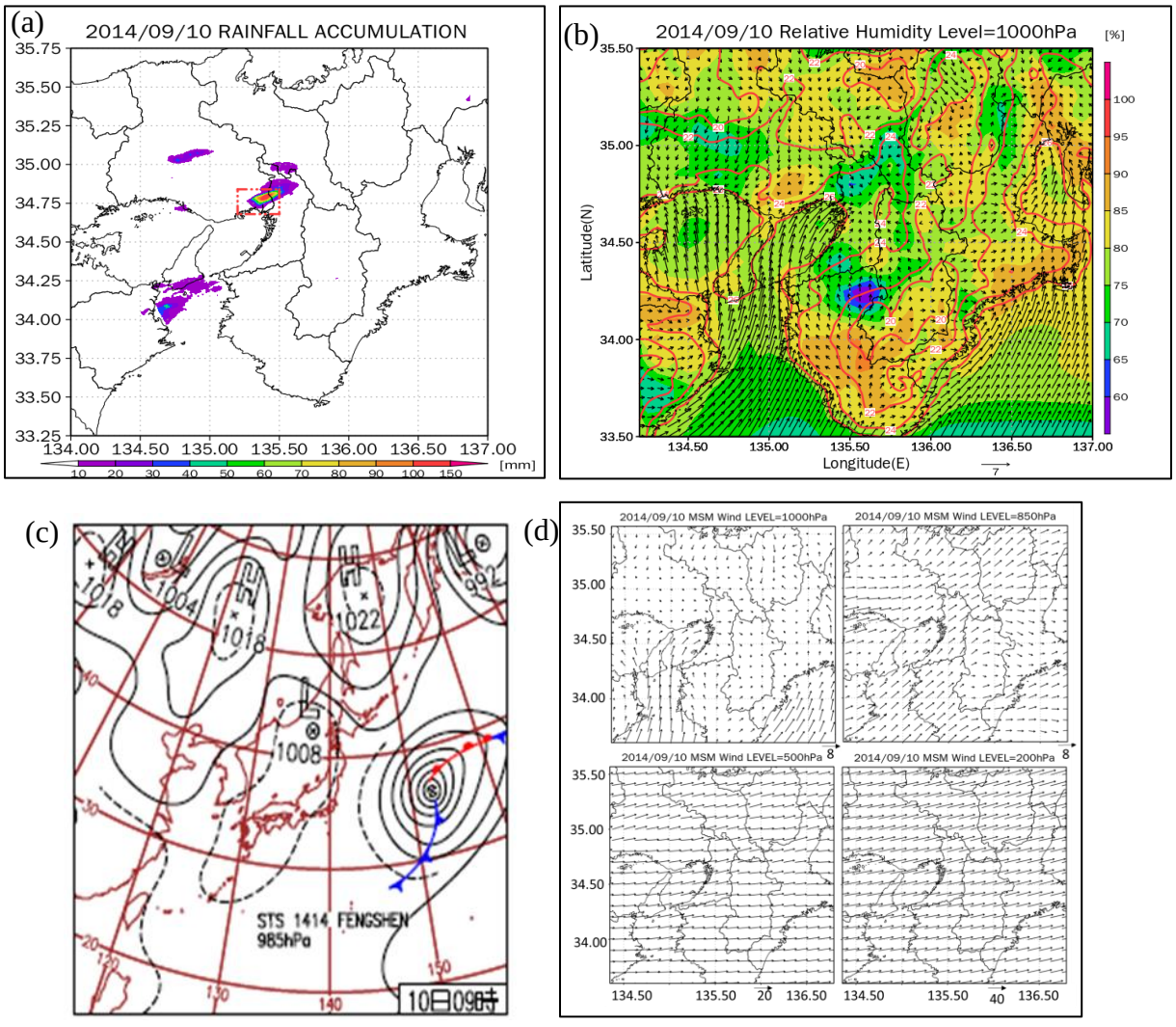

Figure 2.10(a) Rainfall accumulation map with red box indicated target area (b) MSM relative humidity (shaded), red contour (surface temperature) (c) Surface weather map of Japan at 9:00 JST (d) MSM wind level analysis. Images are based on data obtained on 10 September 2014.

The nearly $2^{1/2}$ hours of observation showed the maximum accumulated rainfall was 150 mm, as shown in Figure 2.10(a). There was a report of a flood that occurred in Ikeda city due to a downpour of heavy rainfall that reach 100 mm for one hour. The observed atmosphere in this region was sufficiently unstable for multicell formation. Relative humidity (RH) at 1000hPa and the surface wind vectors (Figure 2.10(b)) were obtained from the JMA MSM. RH in Kinki region was > 80% and over the ocean to the north was > 90%, while the ocean surface temperature was >26℃. The surface weather map presented the confluence on the target area and indicated the rising motion. Consequently, warm and humid air flowed towards the observation areas from the ocean south of Osaka bay, and a cold northerly flow prevailed over the northern part of the Kinki region. CAPE and vertical shear values from the surface to 6 km (866 J/kg and 0.003 s^{-1}, respectively) were calculated based on data observed at the Shionomisaki Station, approximately 150 km away from the target area at 2100 JST. BRN was calculated to be 60, indicating a multicell similar to the storm type classification. Figure 2.10(c) shows the surface weather map obtained at 0900 JST, observed that the Fengshen low-pressure tropical storm at 38° N and 152° E is far away from the study area. Therefore, the tropical storm did not affect this event. However, the event was locally affected by southwesterly winds from Osaka Bay, as shown in Figure 2.10(d). The storm-relative wind motion was dominated by the upper level of 500hPa since the storm moved northeastward during the analysis.

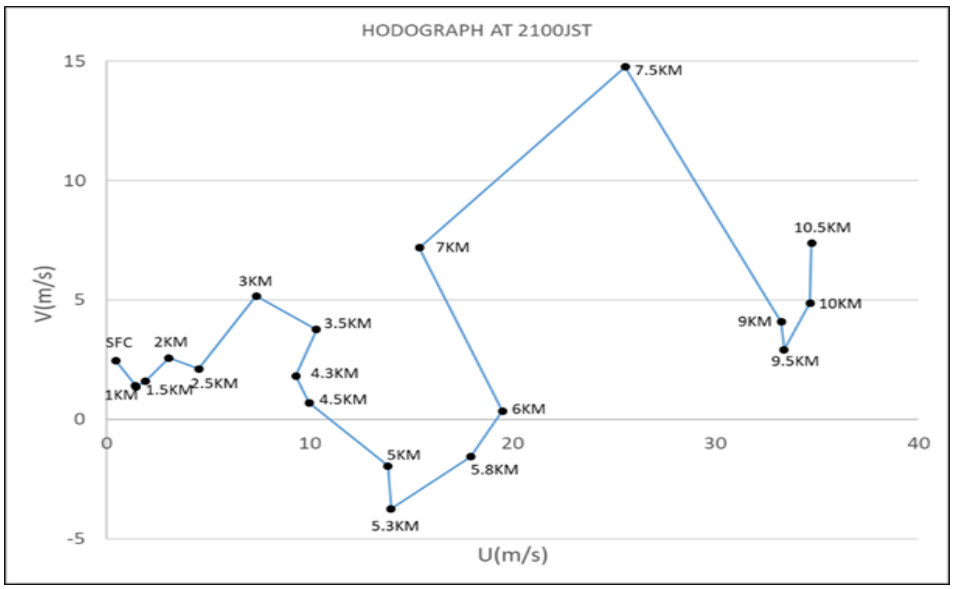

Figure 2.11 Hodograph obtained at Shionomisaki Station at 21:00 JST on 10 September 2014

As shown in the wind hodograph in Figure 2.11, the southwesterly wind was predominant up to an above ground level (AGL) of 11 km, with a maximum speed of 15 m s^{-1} at an AGL of 7.5 km. The vertical wind shear between the surface and AGL of 3 km was oriented east- to northeastward, with a magnitude of 2.2 m s^{-1} km^{-1}. The atmospheric conditions at 2100 JST were characterized by weak vertical wind shear, abundant water vapor at the surface, and warm moist air inflow from Osaka Bay.

2.3.2 Event 2 – August 13, 2018

The target area of this event is presented in Figure 2.12(a). The CAPE and vertical shear values from the surface to 6 km (2413 J/kg and 0.0012 s^{-1}, respectively) were calculated based on data observed at the Shionomisaki Station at 0900 JST. The BRN was calculated to be 865, indicating a multicell similar to the storm type classification. The observed atmosphere in this region was sufficiently unstable for multicell formation. As presented in Figure 2.12(b), RH at 1000hPa in the Kinki region was > 90%, and over the ocean to the north was > 80%, while the ocean surface temperature was >30℃. The surface wind vectors showed strong southerly wind toward Osaka bay, and the speed convergence wind observed at the target area leads to the rising motion. Consequently, warm and humid air flowed towards the observation areas from the ocean south of Osaka bay.

The surface weather map in Figure 2.12 (c) shows the surface weather map obtained at 0900 JST. The map shows that the Leepi low-pressure tropical storm at 25° N and 140° E is far away from the study area. Therefore, the tropical storm did not affect this event. However, the event was locally affected by southerly winds from Osaka Bay at the surface and southwesterly wind at 850hPa, as shown in Figure 2.12(d). The storm-relative wind motion was dominated by the upper level of 500hPa and 200 hPa since the storm moved southward during the analysis. As shown in the wind hodograph in Figure 2.13, the northerly wind was predominant up to an AGL of 10 km, with a maximum speed of 8.5 m s^{-1} at an AGL of 10 km. The vertical wind shear between the surface and AGL of 3 km was oriented north- to westward, with a magnitude of 0.167 m s^{-1} km^{-1}. The atmospheric conditions at 0900 JST were characterized by weak vertical wind shear, abundant water vapor at the surface, and warm moist air inflow from Osaka Bay.

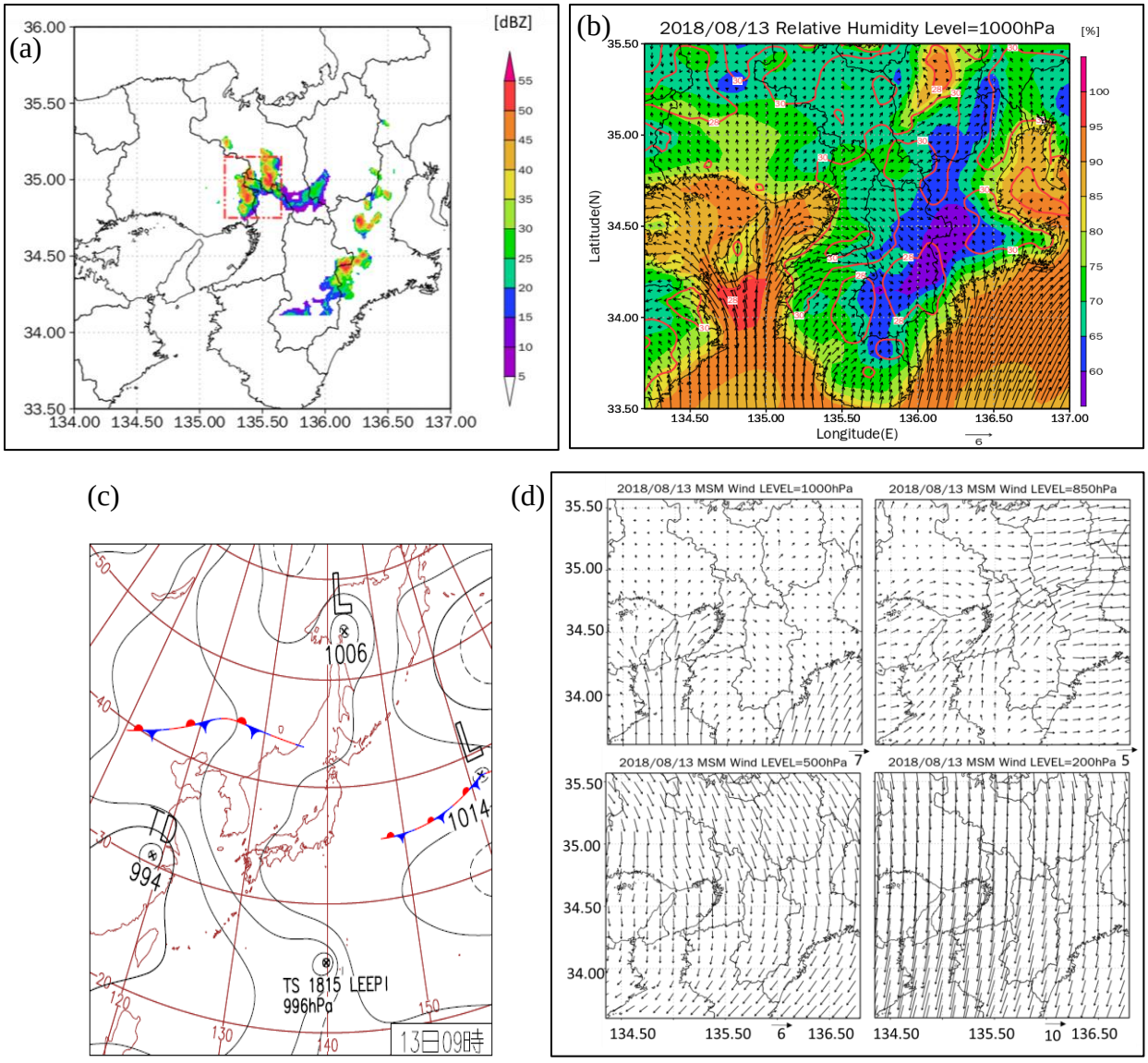

Figure 2.12 (a) Horizontal distribution of radar reflectivity at 1700JST with red box indicated target area (b) MSM relative humidity(shaded), red contour (surface temperature) (c) Surface weather map of Japan at 9:00 JST (d) MSM wind level analysis. Images are based on data obtained on 13 August 2018.

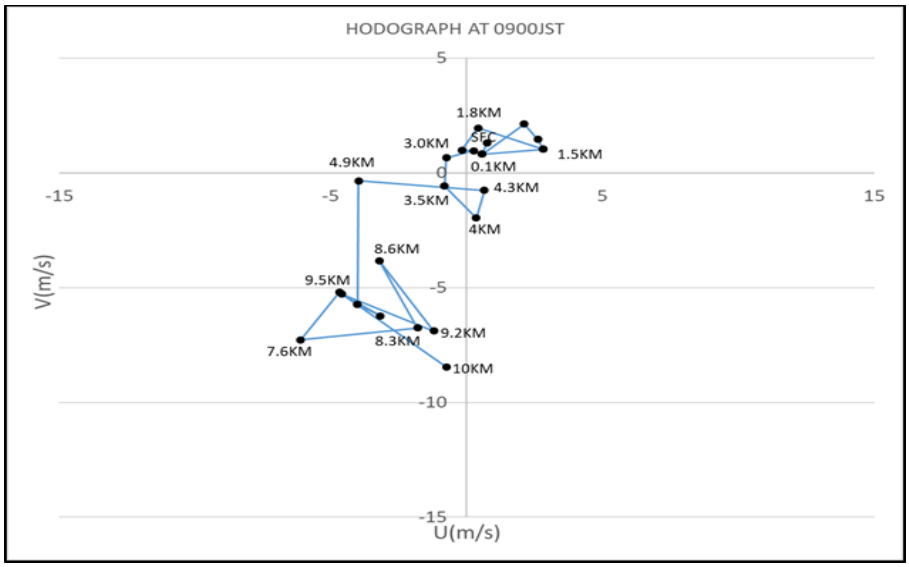

Figure 2.13 Hodograph obtained at Shionomisaki Station at 0900 JST on 13 August 2018.

2.3.3 Event 3 – July 25, 2019

The CAPE and vertical shear values from the surface to 6 km (706 J/kg and 0.0003 s^{-1}, respectively) were calculated based on data observed at the Shionomisaki Station at 0900 JST. The BRN was calculated to be 225, specified a multicell formation could be developed. The target area of analysis was designated in the red box in Figure 2.14(a). RH at 1000hPa and the surface wind vectors shown in Figure 2.14 (b) were observed and RH in Kinki region was > 90% and over the ocean to the north was > 80%, while the ocean surface temperature was >28℃. Consequently, warm and humid air flowed towards the observation areas from the ocean south of Osaka bay. The surface weather map at 0900JST in Figure 2.14(c) shows that the tropical depression at 28° N and 138° E is far away from the study area. Therefore, the tropical storm did not affect this event. However, the event was locally affected by southwesterly winds at 850 hPa from Osaka Bay, as shown in Figure 2.14(d). The storm-relative wind motion was dominated by the middle level of 850hPa since the storm moved northeastward during the analysis.

As shown in the wind hodograph in Figure 2.15, the northerly wind was predominant, with a maximum speed of 15 m s^{-1} at an AGL of 10 km. The vertical wind shear between the surface and AGL of 3 km was oriented west- to eastward, with a magnitude of 0.167 m s^{-1} km^{-1}. The atmospheric conditions at 0900 JST were characterized by weak vertical wind shear, abundant water vapor at the surface, and warm moist air inflow from Osaka Bay.

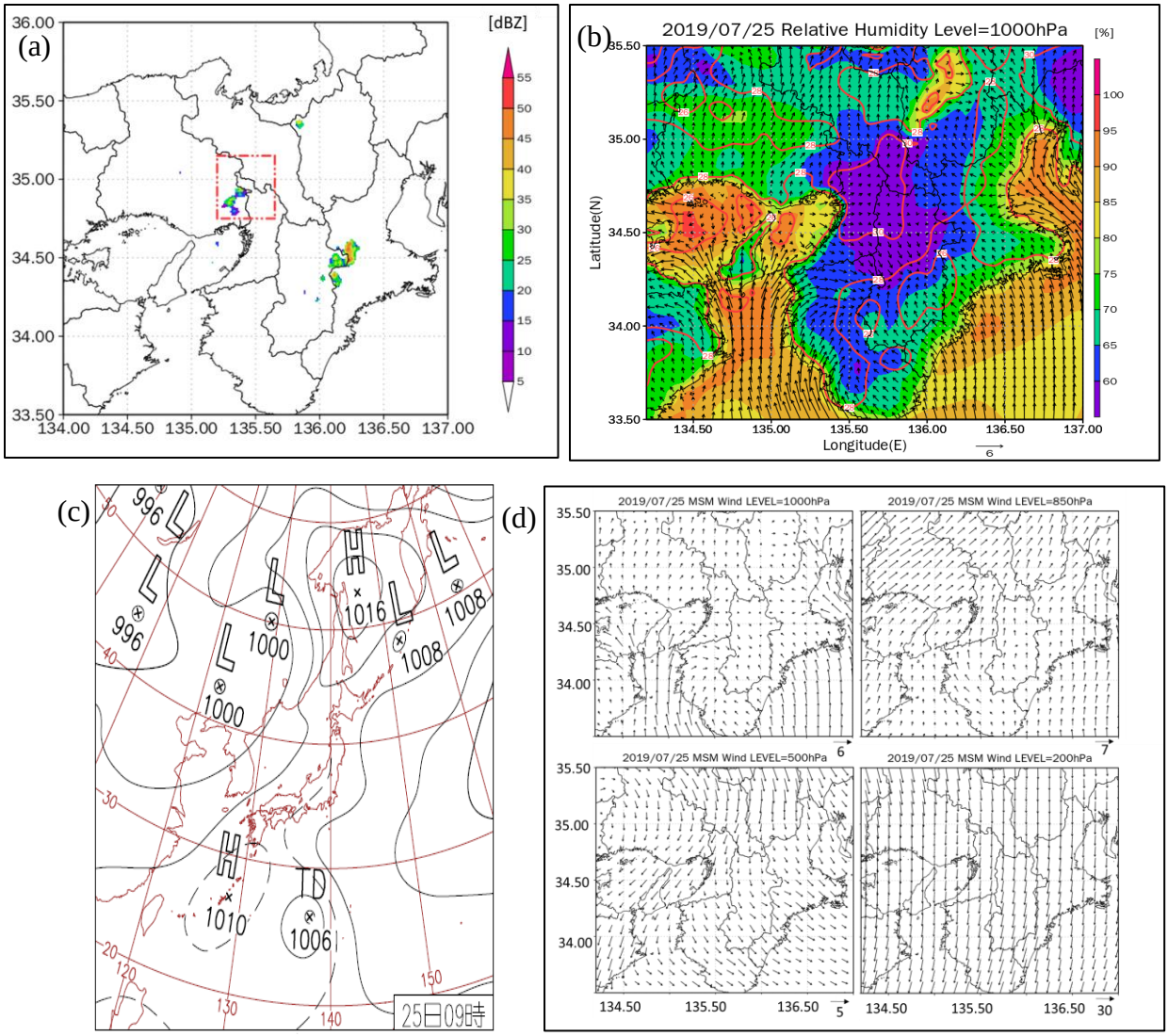

Figure 2.14 (a) Horizontal distribution of radar reflectivity at 1200JST with red box indicated target area (b) MSM relative humidity(shaded), red contour (surface temperature), (c) Surface weather map of Japan at 0900 JST, and (d) MSM wind level analysis. Images are based on data obtained on 25 July 2019.

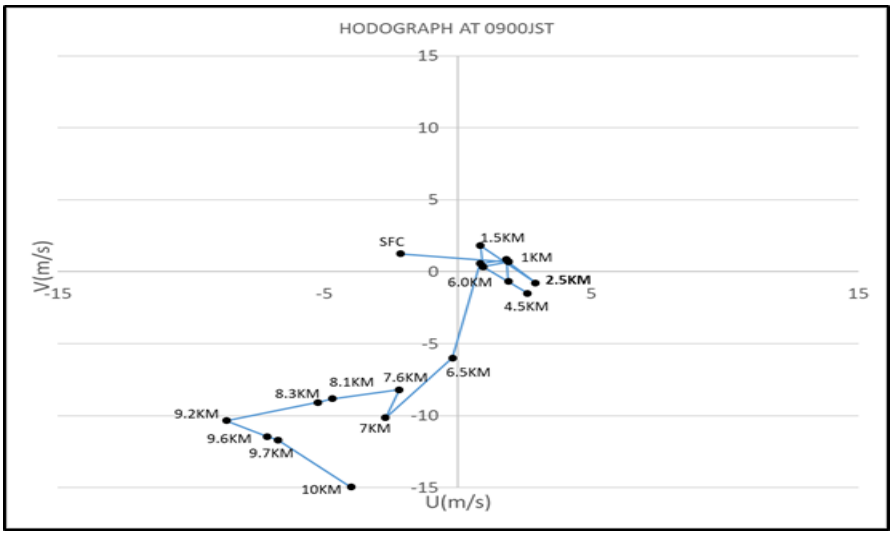

Figure 2.15 Hodograph obtained at Shionomisaki Station at 0900 JST on 25 July 2019.

CHAPTER 3

3 Preliminary Investigation of Single-cell to Multicell in the Cluster Thunderstorms using Pseudo-Vorticity Analysis

Abstract

The preliminary investigation of single-cell to multicell in the cluster thunderstorms using pseudo-vorticity analysis is proposed in this study. The techniques of vortex tube structure and identification of initial stage values of the first radar echo are applied to rainfall events with unstable atmospheric conditions in the Kinki region, Japan. Cluster thunderstorm cases of two events are selected and the analysis of single-cells to multicell is performed by investigating the initial stage of vorticity values and their structures. The vertical vortex tube of vorticity analysis is shown to examine the transition signals of cells merging from single-cells to multicell. In the case of two events, the positive vorticity greater than 0.015 s^{-1} possibly prolonged the duration of the lifetime by more than one hour, and less than 0.0025 s^{-1} might shorten the lifetime of single-cells in the multicell clusters. However, a strong correlation is not observed between the initial stage of vertical vorticity with the lifetime. The external factors that might affect the lifespan of cells should be studied, in combination with the evolution of cells investigated. The characteristic patterns for cells merging from single-cell to multicell are difficult to discover due to the change of core vorticity at upper-level height before single-cells merge into multicell. It is suggested to examine the reason for fluctuation by inspecting the mechanism's effect on the pattern.

3.1 Overview

The vertical vorticity is commonly analyzed in the supercell thunderstorm, tornadogenesis, and tropical cyclones. In the supercell thunderstorm, a study of vortex tube tilting characteristics was conducted in the initial and splitting stage due to its larger-scale areas of development. In the early stage, a pair of positive and negative vorticity generated depends on the vertical wind shear of the environment condition. The vertical vortex tube then appeared in the rain cell when the horizontal vortex tube meets an updraft. In the splitting stage, two vortex pairs were produced by the downdraft that existed between the updraft cells (Klemp, 1987). Moreover, an investigation on the first radar echo aloft that was described as "baby-rain-cell" in a single cumulonimbus cloud using vertical vorticity was established (Nakakita, E., et al. 2017). According to the studies, the criteria threshold of vertical vorticity values should be greater or equal to 0.03 s^{-1} to identify the hazardous rain-cell in the initiation stage before it developed to the cumulus stage. The study focused on the vertical vortex tube of a single-cell that connected at different altitudes and did not evolve into a multicell. Therefore, in the present study, the analysis of the transition from single-cell to multicell was adapted from the supercell and single-cell studies using the techniques of vertical vorticity analysis.

A novel approach is developed by utilizing vertical vorticity that can be used to characterize the transition from single-cells to multicell in the multicell environment condition. It is well known that the counter-rotating couplet plays an important role in cloud dynamics, affecting the entrainment of ambient air into convective clouds as well as the pressure field on the cloud. Therefore, vorticity is an essential parameter for the study of cloud dynamics. In addition, the study of detection of a lifetime for single-cell development using the initial stage of vertical vorticity intensity is not proven yet. It is assumed that the highest positive vorticity will be indicated the longest lifetime due to a stronger magnitude of rotation. Consequently, the purpose of this study is to examine the availability of vertical vorticity to characterize the merging of cells and to develop the signature values for the longevity of storm clusters using the vertical vorticity criterion.

3.2 Methodology

3.2.1 Classification of cells

In this study, the radar reflectivity from the composition of four radars into 0.25 x 0.25 x 0.25 km of Constant Altitude PPI (CAPPI) by Cressman interpolation (Masuda et al.,2014) was utilized to compare with the vertical vorticity in the evolution of single-cell development to multicell. The radar reflectivity can show the behavior of merging cells in the cluster thunderstorm. The study from (Westcott, 1994) indicated the ages of two cores of Z_h in the merging cells were the dominant factors that influence the growth of merging cells under different environmental conditions. For analysis of radar data, "single-cell", "multicell" and "cluster cell" were defined to identify the early development of echoes. A single-cell was defined when the value of reflectivity (Z_h) more than 10 dBZ with the closed contour existed at the 2-km above ground level (AGL).

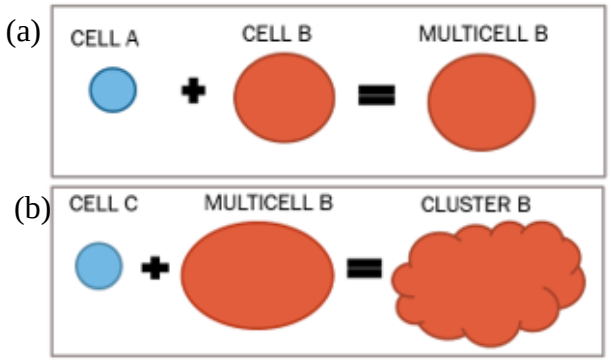

Figure 3.1 The schematic illustrations of (a) merging single-cell A and B to multicell B and (b) merging single-cell C with multicell B to cluster B.

The schematic illustration for merging single-cell A and single-cell B to multicell B is described in Figure 3.1(a). At first, single-cell A (blue color) was assumed to appear, then single-cell B (orange color). The different colors are used to differentiate the echoes with the maximum values of Z_h. When single-cell A merged with single-cell B (greater Z_h), it is labeled as multicell B. Figure 3.1(b) shows the schematic illustration for the merging of single-cell C with multicell B to cluster B. If another new single-cell developed, we named it cell C. If single-cell C merged with existing multicell B whose larger Z_h, the new label will be used such as cluster B. The naming procedure for single-cell is named A, B, C, etc. in formation order. The merged echoes take the name depending on the radar echoes with the strongest reflectivity before merging (Nishiwaki, et al. 2013). The merging of single-cell to multicell was determined by observing the edge contour line of merging echoes which is more than 10 dBZ.

3.2.2 Radar reflectivity and vertical vorticity analysis

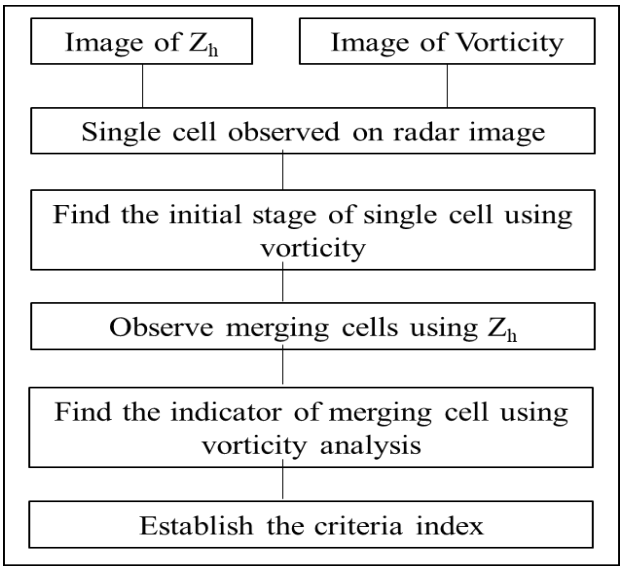

Figure 3.2 The methodology used in the analysis.

The details diagram for this method is presented in Figure 3.2. The first echo in the radar images was characterized as single-cell before it merged with another single-cell. After the identification of the single-cell, the vertical vorticity analysis was compared and checked 30 minutes before its development to find out the characteristics of cells merged in terms of vorticity values and structure. This method was employed to investigate the longevity of the lifetime of cells developed. Then, the merged cells were observed on the radar images using contour analysis of Z_h until the dissipation of the core possessed by the cells. The vertical vortex tube structures were examined as an indicator for the merging of two cells. Core vorticity implied the maximum positive and minimum negative vorticity values in the areas. A pair of positive and negative vorticity (hereinafter referred to as "pair") was referred to as the structure of vertical vorticity. The procedure for estimating the pseudo-vorticity has been explained in Section 2.2.1. The core positive and negative vorticity for the vertical vortex tube was selected qualitatively by finding the absolute value of vorticity (Nakakita, E., et al. 2017) at 0.01 s^{-1} and the updraft location in the target cell (Rotunno 1981). The criteria for the initial stage to evaluate the lifespan of cells and indicator of merging cells are developed. Figure 3.3 showed the comparison of vorticity at an elevation angle of 3.7 degrees, with the height of the cell observed located at 3 km height. From this figure, the investigated cell at the black solid circle color showed the propagation of cell after 10-minutes of the formation of the initial stage of vorticity, and the intense of Z_h strength could be observed.

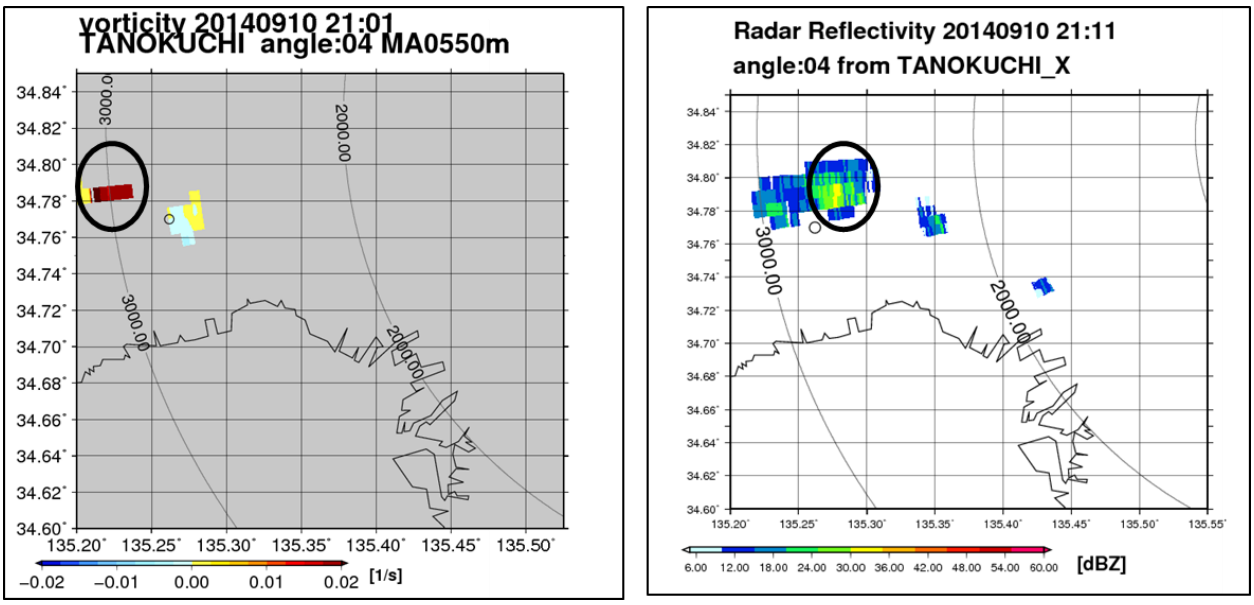

Figure 3.3 The comparison of the initial stage of vorticity and after 10-minute development using radar reflectivity. A black solid circle indicates the example of the investigated cell.

3.3 Results and Discussion

This section discusses the details of the development of merging from single-cell to multicell in cluster thunderstorms. CAPPI height of 2 km AGL composed of all four radar stations were utilized for the analysis of radar reflectivity to prevent the blockage from the topography. The PPI images of vertical vorticity at every elevation angle and structured to the vertical vortex tube were constructed for the analysis of cells merging. The radar station used for the vertical vorticity analysis was the Tanokuchi radar station due to the closer distance from the radar to the target areas.

3.3.1 Event 1 - 10th September 2014

The complete history of the entire storm is described in Figure 3.4(a). The duration of the analysis was shown only from 2100JST to 2200JST for the analysis. Cell A was generated after 1-hour observation started from 2000JST and it was still developed until a new single-cell B was generated at 2130JST. At 2131JST, single-cell B merged with cell A to become multicell A. Since the reflectivity of cell A was greater than cell B, the multicell was labeled as multicell A. Another single-cell C was generated at 2133JST and the intensity of multicell A become more intensified after the merging stage. At 2150JST, single-cell D appeared meanwhile the area of cell C became

larger and more developed. Cell C and cell D respectively merged into multicell A at 2150JST and 2153JST. At this time, we labeled it as cluster A because multicell A showed the maximum intensity of Z_h and it contained several single-cells that merged. The single-cell C was observed to move northeastward and started to separate with cluster A at 2200JST. Cluster A remained intensified by the combination of single-cell B, C, and D at 2200JST and the maximum radar reflectivity detected was 55 dBZ at this time. The detail of cells merging of single-cells A and B using radar reflectivity images is shown in Figure 3.4(b). Single-cell A remained developed until single-cell B appeared and merged into multicell A at 2131JST. The core of reflectivity merged at 2134JST, increased at 2135JST, and the areas of maximum reflectivity on single-cell B become widened at 2137JST. Cell B is more developed after merging into multicell.

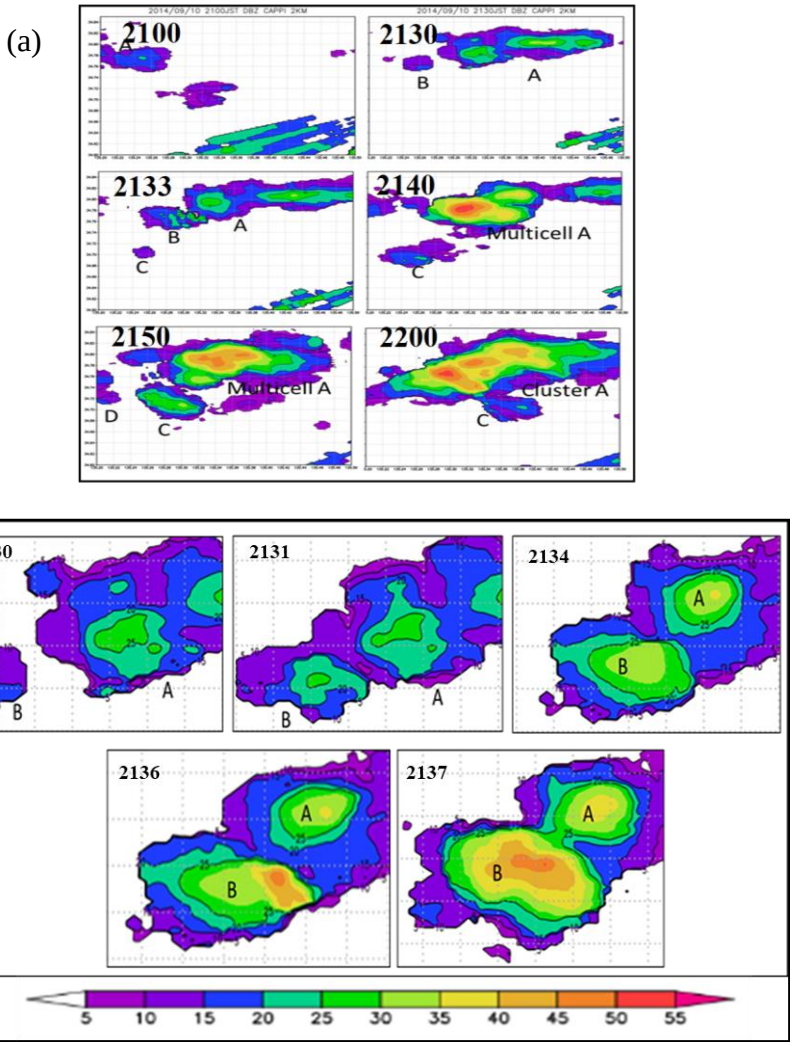

Figure 3.4 (a) The storm cluster history of Z_h at 2 km CAPPI height (b) One illustrative example of radar reflectivity images when single-cell A merge with single-cell B.

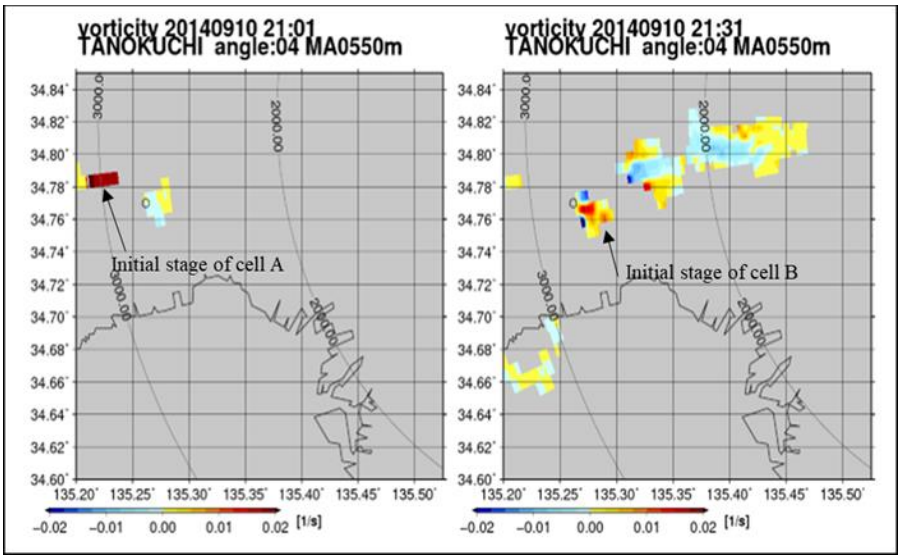

Figure 3.5 One illustrative example of the selection of the initial stage of cells A and B.

The vertical vorticity analysis was conducted to investigate these case studies. We extracted the vorticity values and observed the structure of the initial stage of each cell. The example of a vorticity image is presented in Figure 3.5. The initial stage of cell A and cell B were detected at 2101JST and 2131JST respectively from an elevation angle of 3.7 degrees. The highest intensity of core pair vorticity was identified in this stage. The summary of the initial stage and lifetime duration of each cell is presented in Table 3.1. The duration in each cell was examined from the early stage until the dissipating stage by observing the echoes of Z_h. We discovered that the lifetime of single-cells A and D indicated more than 1 hour, which the initial stage of vertical vorticity in the range of 0.005 s^{-1} to 0.04 s^{-1} for positive vorticity. The structure of pair vorticity was found mostly in the investigated cells.

Table 3.1 Initial stage of single-cell

Cell	Vertical Vorticity (s^{-1})		Structure	Duration (minutes)
	Positive	Negative		
A	+0.0400	-	Positive	100
B	+0.0181	-0.0242	Pair	50
C	+0.0200	-0.0100	Pair	40
D	+0.0051	-0.0029	Pair	110

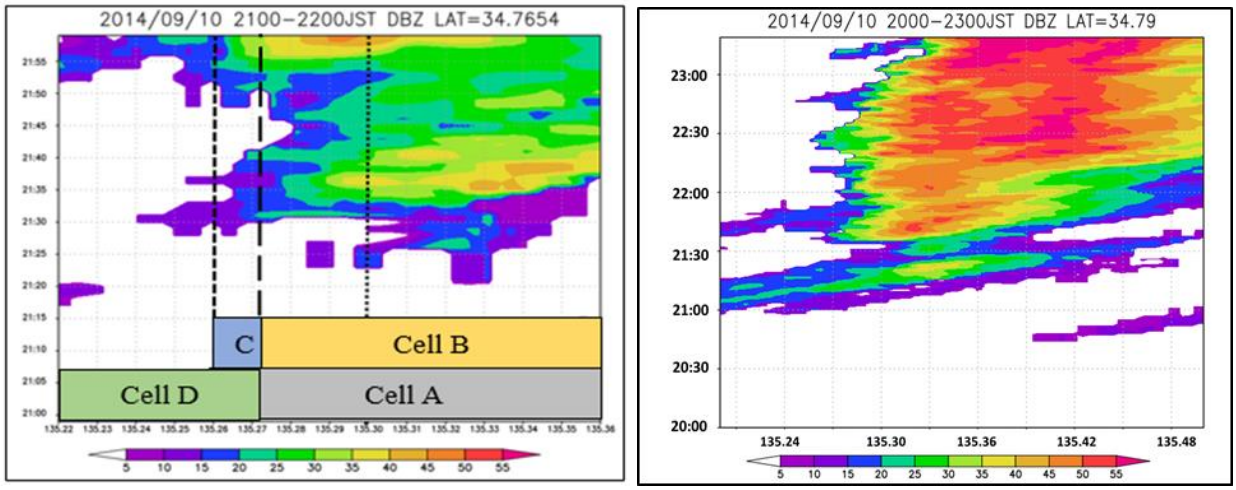

Figure 3.6(a) The time-longitude distribution of (a) each cell in cluster A at latitude 34.7654°N, (b) selected latitude at 34.79°N.

In recognizing the lifespan duration of each single-cell, the time distribution at selected latitude was constructed. We selected 34.7677°N as the level of analysis because the core of maximum reflectivity existed. As described in Figure 3.6(a), cell A was the dominant cell due to its development until 2200JST, and cell B which merged with cell A, was more developed until this period. Cell C merged into cluster A for 10 minutes only and it started to dissipate and separate from cluster A. Meanwhile, cell D showed the least intensity when combined into this cluster for this period although its lifetime revealed the highest compared to others. Then, time-longitude at the latitude of 34.79°N where the maximum vorticity is located was established until 2300JST as shown in Figure 3.6(b). The intensity of Z_h remained at the highest strength until the 2-hours analysis.

Subsequently, the vertical vortex tube structure was investigated to discover the transition signals of cells merging. For comparison between two cells, the vertical vortex tube analysis was established by choosing the core vorticity and their signature of merging before and after the merging. The example of vorticity analysis of vertical tube structure before merging for single-cell A and cell B was shown in Figure 3.7 and Figure 3.8, respectively. In Figure 3.7, the vorticity for each respective height was plotted and the core vorticity of positive (red color) and negative (blue color) was selected. After plotting at each height, we constructed the vertical dashed line for positive and negative vorticity to represent the vortex tube structure. From the analysis of vertical vorticity for cell A, the core of vorticity changed its position at heights 3 km and 4 km AGL. The possibility of changing the position of core vorticity in the complex distribution of multicell for

each cell might be happened before and after merging. As presented in Figure 3.8, cell B changed its position at a height of 3.5 km AGL and it was difficult to identify the vortex tube structure after merging. We examined the single-cell C and cell D merged with multicell A at 2151JST and 2154JST, respectively and the vertical vorticity showed the shift of core vorticity at 4.0 km AGL and 3.5 km AGL sequentially. The case study of another event will be analyzed to confirm this signature pattern of cells merging.

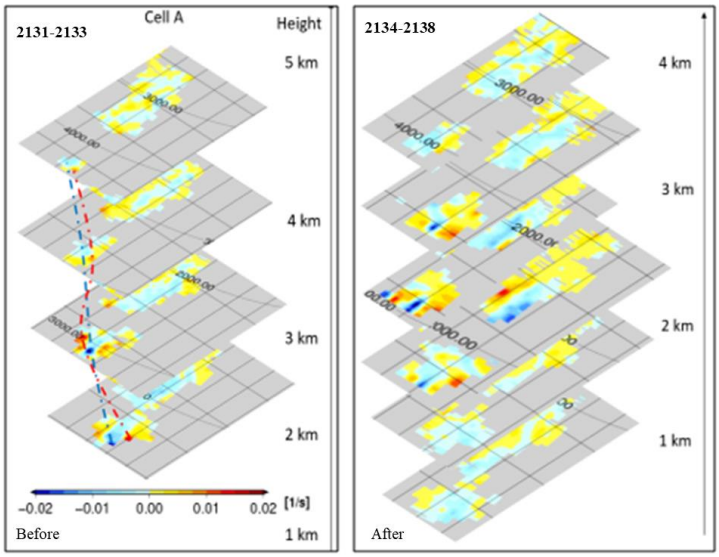

Figure 3.7 The vertical vortex tube structure of single-cell A.

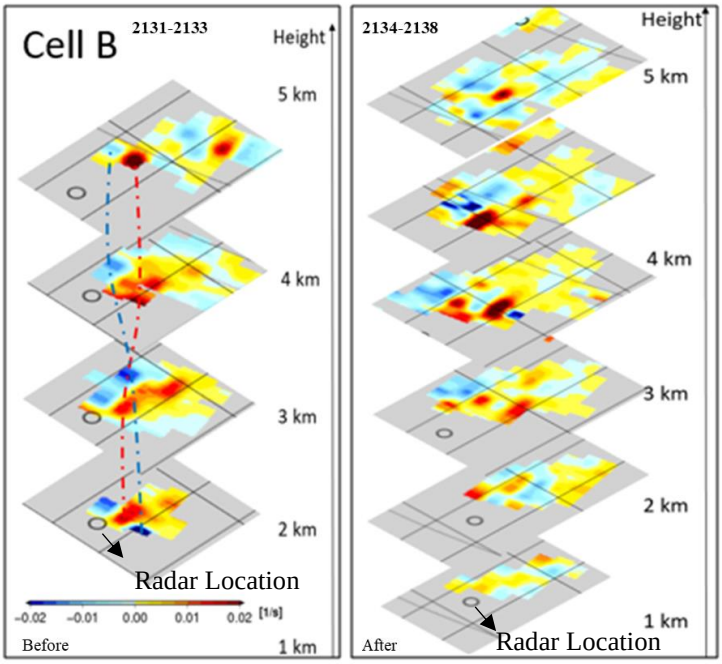

Figure 3.8 The vertical vortex tube structure of single-cell B.

3.3.2 Event 2 - 13th August 2018

To confirm our assumption of the vertical vorticity structure distribution, and the relationship between initial stage and lifetime, we selected another event with the same condition of multicell type from event one. The target area for this event and a complete history of the entire storms for the analysis at 2 km CAPPI height are presented in Figure 3.9(a). The area of cluster storms was large and sustained for more than one-hour duration. In this case study, 5 single-cells merged into cluster A since the Z_h of cell A remained the strongest until 1300JST.

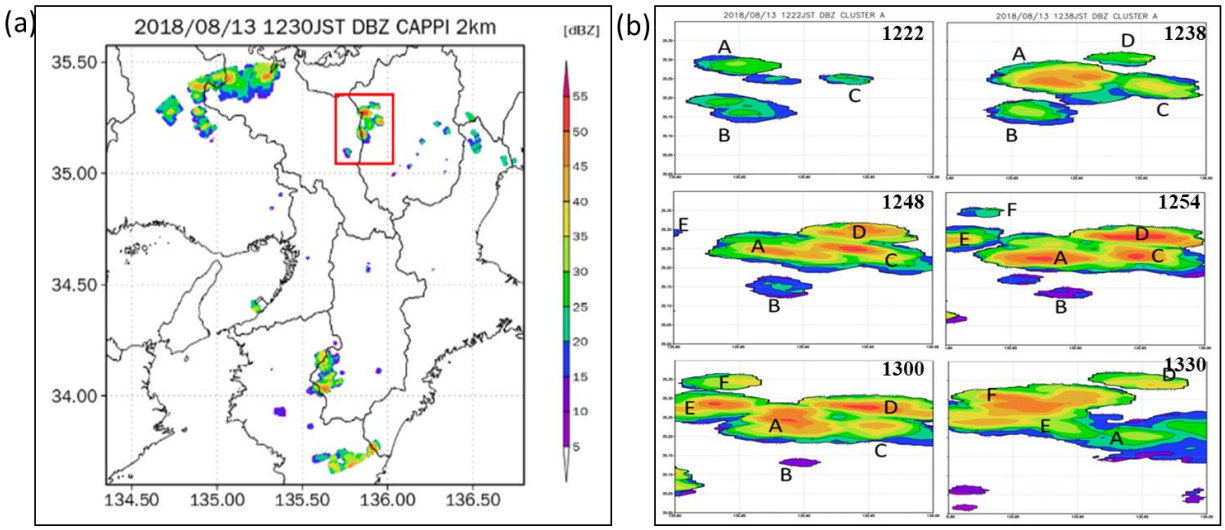

Figure 3.9(a) The target area in the Kinki region, Japan (b) The storm cluster Z_h history at 2 km CAPPI height.

As shown in Figure 3.9(b), we observed that single-cell A was intensified at 1222JST and single-cell B and C appeared near the single-cell A. However, cell B not merged with cell A until it dissipated at 1300JST. Cell C merged with cell A and we renamed it multicell A since the reflectivity of A higher than cell C. At the same time, cell D developed near multicell A. At 1248JST, cell D merge into multicell A and this multicell A had three cores of stronger reflectivity that initiated from each merging of single cells. Then, cell E propagated to multicell A and combined at 1301JST. From the detection of radar echoes, cell F was developed at 1254JST, merged at 1300JST, and deepened 20 minutes after its combination which the maximum radar reflectivity owned by cell F. Then, the analysis of the initial stage of vertical vorticity was examined for each cell and compared with the lifetime observed in the previous observation.

Table 3.2 Initial stage of each cell

Cell	Vertical Vorticity(s^{-1})		Structure	Duration (minutes)
	Positive	Negative		
A	+0.0150		Positive	130
B	+0.0020	-0.0102	Pair	45
C	+0.0025	-0.0043	Pair	50
D	+0.0085	-0.0028	Pair	100
E	+0.0058	-0.0030	Pair	40
F	+0.0045	-0.0040	Pair	120

The results of the initial stage of vorticity values and lifetime duration for each cell were presented in Table 3.2. In this event analysis, the lifetime of each cell showed more than 1 hour for single-cells A, D, and F. When we evaluated the initial stage of vertical vorticity, the intensity showed less than the threshold proposed by (Nakakita et al, 2017). However, the highest positive vorticity referred to cell A at 0.015 s^{-1} with the positive structure only. The comparison for each cell for examining the duration of each lifetime, the time distribution from 1200JST until 1500JST at location 35.2486°N was illustrated as shown in Figure 3.10. We found out that cell A was the main developing cell because of its existence until 1300JST. Meanwhile, cell C dissipated earlier than other cells. Cell B did not include in this area of analysis because it did not merge into cluster A. Cell D developed until it started to less intensity at 1330JST. Cell E started to develop from 1300JST until 1500JST, and cell F showed dominance after 1300JST.

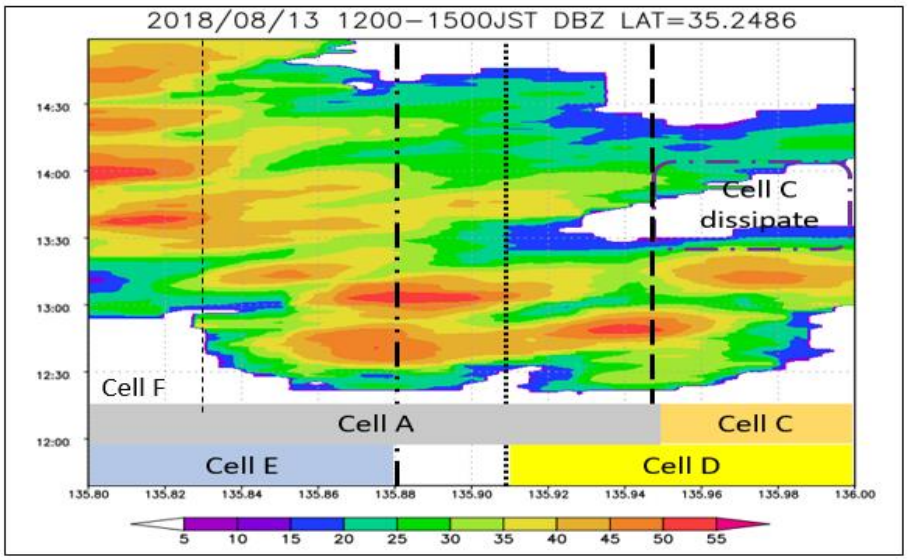

Figure 3.10 The time distribution of each cells in cluster A.

Consequently, we analyzed the vertical vortex tube pattern before and after the merging of single-cells for this event. The change of position happened in cell A at a height of 2.5 km before it merged as shown in Figure 3.11. Similarly, with cell C, the position of core vorticity in the vortex tube changes at level 2.5 km as described in Figure 3.12. The complex distribution in multicell resulting in the construction of vortex tube could not be done. From the observation of radar images, cell B did not combine with other cells and its lifespan remained until 1300JST which its duration was less than one hour. Cluster A merged with cell D and cell E at 1242JST and 1301JST respectively and the core of vorticity changed at the position of 4.5 km AGL. Cell F then combined with cluster A had the same signature as other cells and the position of core vorticity shifted at 4 km AGL.

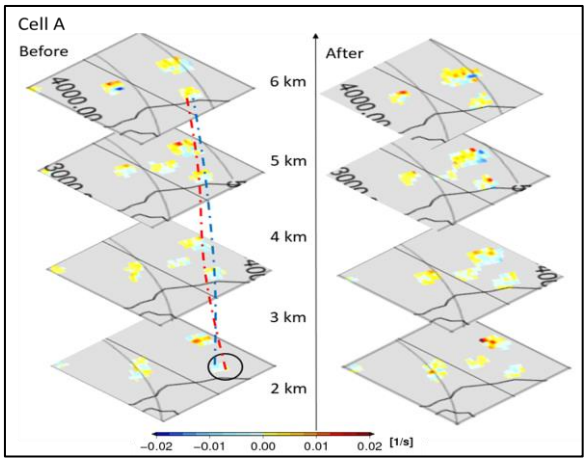

Figure 3.11 The vertical vortex tube structure of single-cell A.

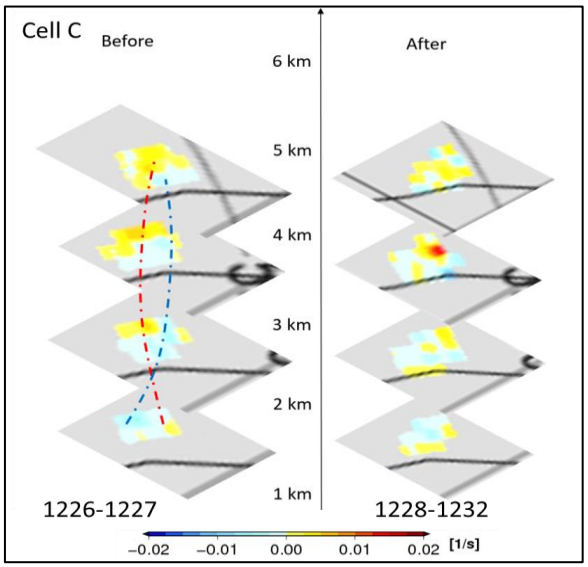

Figure 3.12 The vertical vortex tube structure of single-cell C.

3.3.3 Discussion

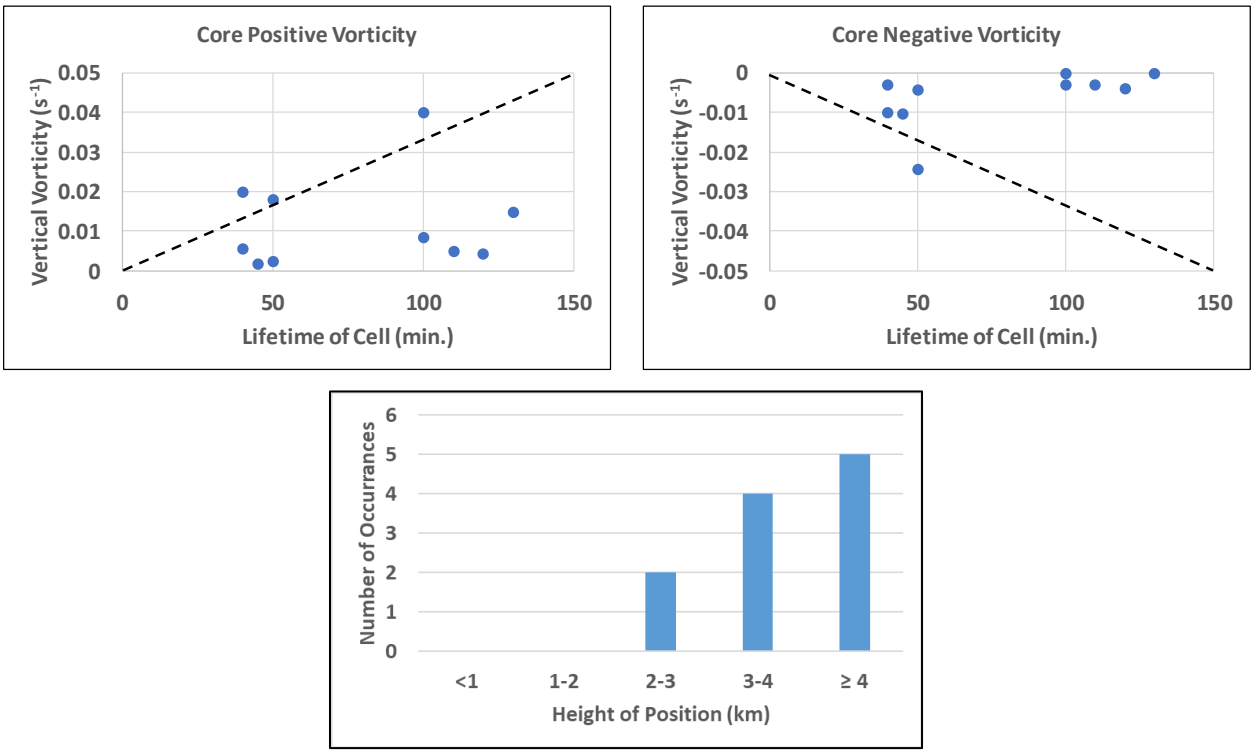

Figure 3.13 The relationships between the lifetime of cells and (a) core positive vorticity and (b) core negative vorticity. (c) Distribution of height of changing the position of single-cells before merged.

In our assumption, the greatest vertical vorticity intensity showed the longest lifespan of cells developed. Therefore, the relationship between lifetime and initial stage of core vorticity is investigated. The summary of the analysis is presented in Figure 3.13(a) and Figure 3.13(b) for core positive and core negative, respectively. For all investigated cells, there was a very low correlation observed between the cell's lifetime and core positive vorticity. In contrast, the intensity of core negative vorticity was observed a moderate correlation with the lifetime. The indicator of the initial stage of vertical vorticity could not be referred to as a factor in the longevity of the cells because the evolution of vertical vorticity is changed from the early stage of cloud development until its dissipating stage. However, we could observe that the greatest initial stage of vertical vorticity referred to the lifetime of cells more than 100 minutes. More statistical analysis has to be implemented to confirm the lifetime distribution. In addition, the fluctuating of core vorticity in the single-cells analysis before merged into multicell was observed at various height. As illustrated in Figure 3.13(c), the majority of single-cells showed the height of changing position

occurred at more than 4 km AGL, while after merged, the multicell distribution was hard to identify its core vorticity. Is the fluctuating position of vertical vorticity truly indicative of merging cells?

As a consequence, it is suggested to study the time-series of vertical vorticity to discover the characteristics of single-cells in the multicell environment condition. Furthermore, it is recommended to identify the reason for the changing position from the preliminary results by examining the vertical vortex tube structures. The bridge formation was discussed and found as the signature of cell mergings using radar reflectivity (Westcott, 1994) which was aided by the convergence line that commonly extended between the major clouds that initiated the development of the new cell. The schematic illustration of the bridge formation is described in Figure 3.14. As a result, convergence and downdraft are the key mechanisms in the initiation of new cell formation in the multicell environment.

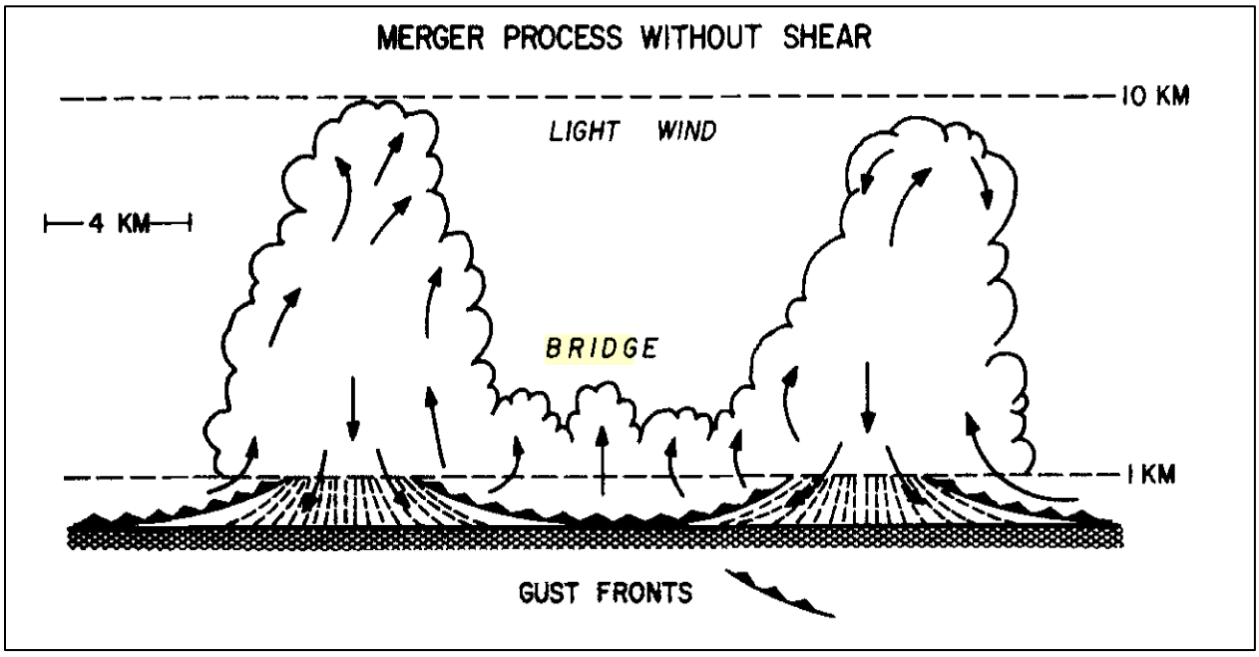

Figure 3.14 Schematic illustration relating downdraft interaction to bridging and merger in case of light wind and weak shear (Adapted from Simpson et al.,1980).

In addition, from a study by Kim et al., (2012), the average formation height of precipitation cores that was retrieved from liquid water content (LWC), revealed the height of single-cell and multicell at 4.6 km and 4.7 km, respectively, which the strength of updraft and downdraft for comparable cells were not the primary factors in facilitating the development and maintenance of precipitation cells over long periods. They mentioned that the position of updraft

or downdraft and its interaction with adjacent inflows were the most important mechanisms in multicell development. Therefore, we will further investigate the factors' effect on multicell development using dual-Doppler analysis because dual-Doppler synthesis is a widely used method for determining the air motions within precipitating cloud systems (Kim et al., 2012; Robert A.Houze, 2014).

3.4 Conclusions

The analysis of the initial stage of first radar echoes from vertical vorticity analysis is established and, the information about the lifespan duration for cells investigated could not be confirmed using this method. However, from the study of two events, the criteria index positive vorticity for the lifespan of cells more than one hour is greater than 0.015 s^{-1}, meanwhile, the criteria index positive vorticity for lifespan duration of cells less than one hour to indicate the dissipating stage is smaller than $0.0025s^{-1}$. This criteria index is less than the criterion threshold proposed by Nakakita et al (2013,2017). Further investigation is needed to identify the appropriate method to determine the lifespan of cells in the multicell cluster thunderstorms. We also have to consider the factors that contribute to the development of cells because there are many interactions that should be investigated in this complex multicell environment such as the strength of vertical wind shear, the instability of environment conditions, and others.

By utilizing the techniques of vertical vortex tube structure analysis, the availability of vertical vorticity to detect the transition signal of cells merging was examined before and after the occurrence of merging cells. We identified that the changing position of core vorticity happened before the combination. This indicator can be seen in all single-cells that were analyzed in these case studies. The probability of shifting of core vorticity before merging could contribute to the complex distribution of multicell when analyzing the merging of the vertical vortex tube. The study of vortex formation simulation in the shear-free environment showed that in the multicell cloud interactions, the tilting mechanism was the essential factor mechanism and it stated that positive and negative tubes of vertical vorticity were generated on either side of the updraft (A.Shapiro and Y.L.Kogan, 1994).

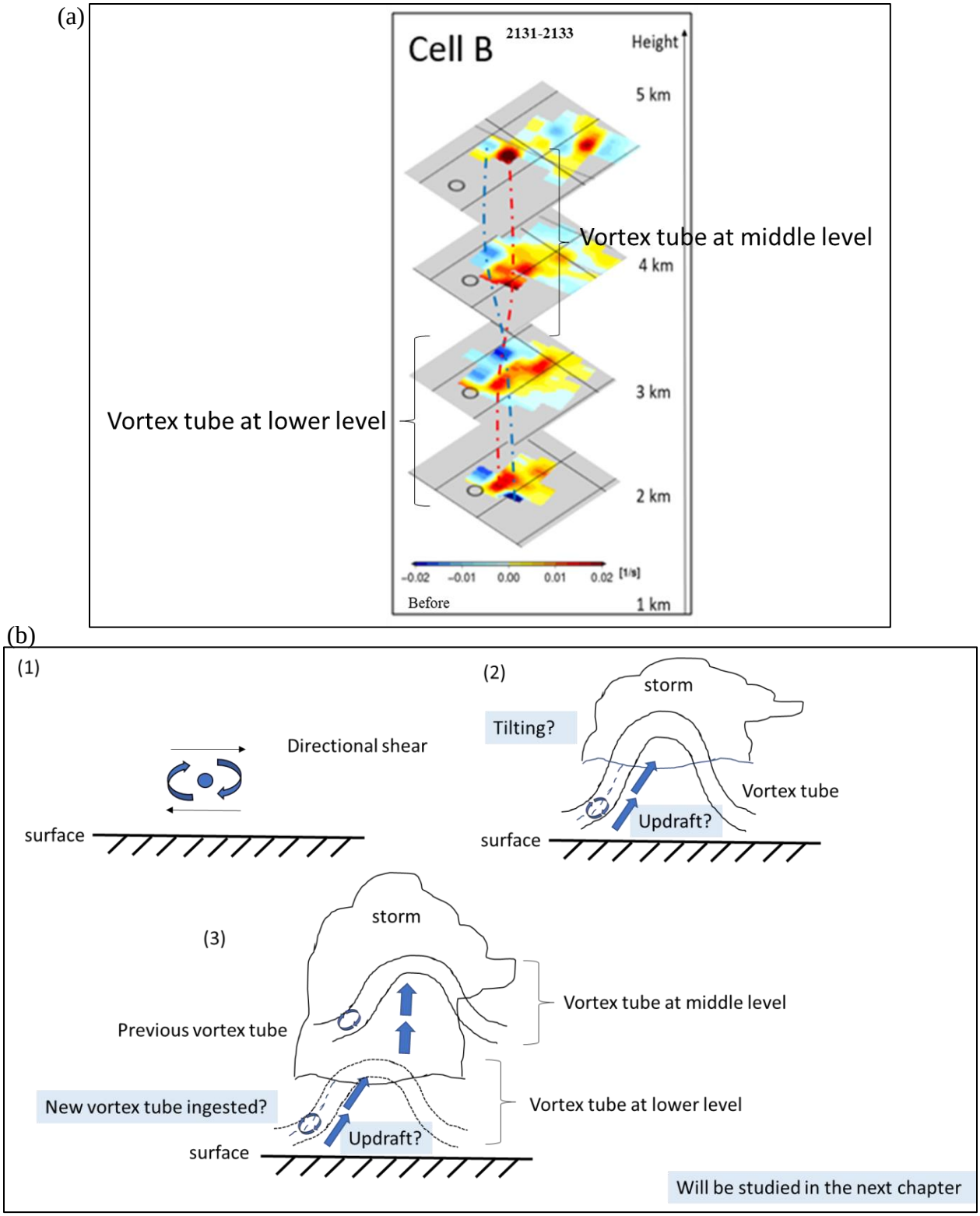

Figure 3.15 (a) The probability of changing the position of the vortex tube might be indicated the existence of a vortex tube at the middle-level and a new ingested vortex tube at the lower-level. The schematic illustration is shown in (b).

As shown in Figure 3.15(a), the vertical vortex tube distribution probably indicated the existence of a new vortex tube at the low-level and an existing vortex tube at the middle-level height with the presence of an updraft that contributed to the tilted vortex tube. The schematic illustration of the mechanism that affected the vortex tube is presented in Figure 3.15(b). Therefore, the dynamic vorticity is also crucial in the vertical vorticity analysis, and we will investigate the characteristics of single-cells transformed into multicell by emphasizing the dynamic and kinematic of cloud development.

In future work, we will further investigate the transition signals and characteristics from single-cell to multicell by developing new techniques for identifying the core vorticity position and its intensity. The effects of this fluctuating position of vertical vorticity in the next chapter will be more discovered and, the new characteristic patterns to distinguish the single-cell and multicell development will be developed. In the meantime, the kinematic and dynamic mechanisms that influence the core vorticity patterns using dual-Doppler analysis will be quantified for more understanding of multicell development.

CHAPTER 4

4 Investigation of Transition Signals from Single-cell to Multicell Thunderstorms Using Pseudo-Vorticity, Dual-Doppler Vorticity, and Mechanism Analysis

Abstract

In this study, the pseudo-vorticity and dual-Doppler vorticity analyses were established for the case study that occurred on September 10, 2014, in the Kinki region, Japan, by using X-band multi-parameter radar. The characteristic trends of the intensity, time series, and height of the core vorticity were determined to discover the signals of the transition from single-cells to multicell thunderstorms. The single-cell revealed the peak intensity of the core vorticity during the early stage of time series analysis, whilst the multicell presented the greater strength at the latter stage of development. The average peak core vorticity intensity of a single-cell calculated from pseudo-vorticity was 0.004 s^{-1}, and 0.04 s^{-1} was observed at DDA vorticity. The formation height of peak core positive vorticity calculated from DDA vorticity was 3.8 km and 3.9 km for single-cell and multicell, respectively. In contrast, both cells were observed at 4.4 km and 3.6 km from the pseudo-vorticity analysis. The formation height of peak vorticity was mostly related to the strength of the updraft. The frequent distribution of maximum updraft for multicell was revealed at a height of 4 km for intensity larger than 5 m s^{-1} and maximum downdraft with a strength greater than -1 m s^{-1} was observed at 1 km AGL. The stretching of the vortex tube, updraft, and convergence played substantial roles in the increment of core vorticity intensity, especially at the lower level, whereas the tilting of the vortex tube had more impact on the increment at the middle-level height. The distance between single-cells and multicell with the same sign of core vorticity was calculated and their intensities were compared. Only DDA vorticity showed the relationship between multicell to single-cell. The calculated distance was separated into five ranges, ranging from 5 to 25 km. The optimal distance was discovered to be in the range of 5–10 km. The results revealed that in the short range distance, the multicell affected the intensity of the single-cell due to the adjacent downdraft, and divergence occurred in the pre-existing multicell. The pseudo-vorticity was able to detect the peak rainfall after merging with the lead time of 17 minutes, compared with the DDA vorticity which presented a lead time of 13 minutes.

4.1 Overview

The disaster occurrences mainly such as floods and landslides are induced by the severe thunderstorms that are generated from the rain cloud. The single-cell typically has its lifetime of about one hour and the area of occurrence is basically in a small area. However, the multicell could also produce a higher intensity of precipitation which contributes to severe disaster due to its lifetime of more than an hour and the scale of areas are larger than a single-cell. Heavy precipitation from multicell thunderstorms can induce more severe disaster occurrence. The study of the transition from single-cell to multicell using the vertical vorticity analysis technique was established and it was difficult to examine the transition signal due to change of core vorticity at upper-level height (Ahmad. F, et al., 2020). From this previous study, the changing position of single-cells was observed as the signal of cells merging and the complex distribution was found in the multicell formation. We investigate the reliability of this pattern and observe the existence of lower-level vortex tubes of vorticity and mid-level vortex tube of vorticity depending on the vertical wind shear at the environment condition. For example, from a study of (Montgomery. MT, et al., 2006), in the numerical simulation of tropical genesis, the vertical shear profile will generate negative (positive) vertical vorticity when tilted upward by an updraft, on the radially inward side of the updraft below (above) z= 4 km as described in Figure 4.1.

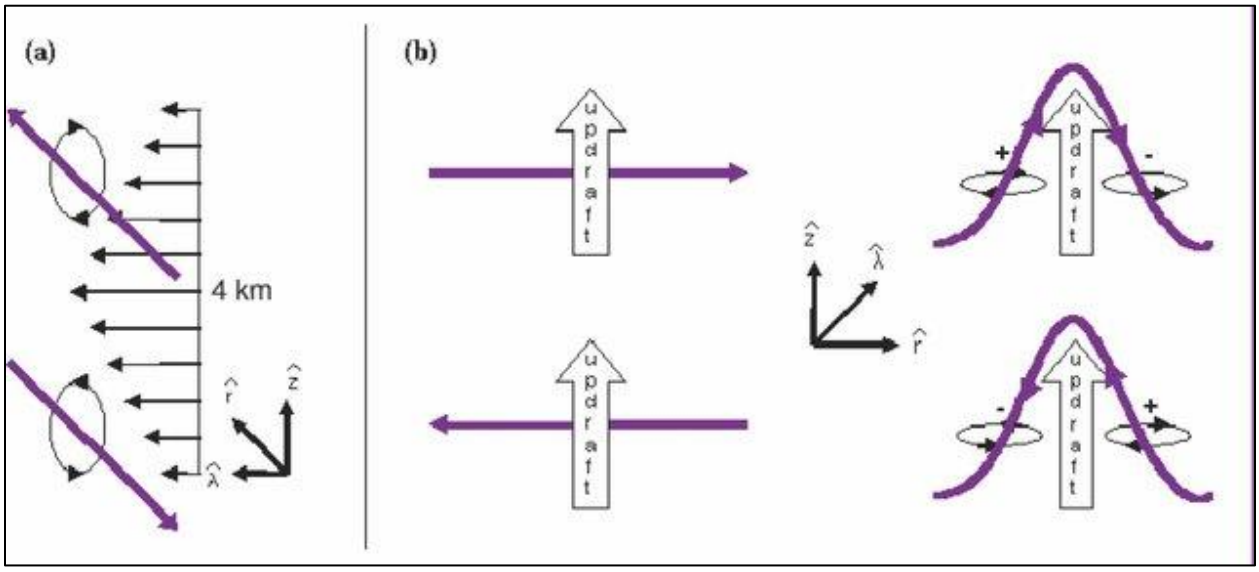

Figure 4.1 Schematic of vortex tilting at the early stage of initiation of the meso-convective vortex with purple lines representing vortex filaments. Adapted from (Montgomery. MT, et al., 2006).

This information also could be confirmed in the study of a supercell in which the low-level updraft enters the cloud with streamwise vorticity, then connected with the mid-level vorticity that was produced by tilting of the environmental crosswise vorticity to form a rotation of updraft extending from middle level to lower levels of the clouds (Robert A.Houze, 2014). Therefore, the changing position of vertical vorticity as analyzed in sections 3.3.1 and 3.3.2 might be indicated the combination of vertical vortex tubes from existing cells and other new single-cell development. As a result, we will examine this hypothesis in this analysis, and establish the new method in the construction of vertical vortex tube structure by examining the core vorticity at the same location for each positive and negative vorticity from the lower-level until the middle-level.

The methodology used in this chapter utilized methods from pseudo-vorticity analysis and dual-Doppler vorticity analysis. Since we conducted the dual-Doppler analysis, this new method also involved comparing with the previous study. The vertical vorticity analysis was suggested by focusing on the strength and formation height of core vorticity. Kim et al. (2012) distinguished the characteristics of single-cell and multicell in terms of height formation of LWC of precipitation cores and emphasized that the position of updraft and downdraft were the most important in facilitating the development and maintenance of precipitation cells over long periods. Therefore, the distance analysis will be proposed in this study to determine the effect of position on the development of precipitation cells. The distance analysis using vertical vorticity is a new approach analysis to discover the optimal distance of the cell merger process and its pattern. Moreover, the interest in the cell merging process exists because of the possible opportunities to increase precipitation via cloud seeding, and visualize the damaging effects of severe thunderstorms phenomena such as strong surface winds and lightning occurrence (Stalker et al.,2003).

The kinematic and dynamic mechanisms are essential to further investigate the cause and effect of vertical vorticity. In the meantime, understanding the mechanism that influences multicell development is essential by considering the environmental condition. Hence, by employing dual-Doppler analysis, this objective could be realized. We already explained the dual-Doppler analysis in section 2.1.2. For the above-stated reasons, this study aimed to discover the transition signals from single-cell to multicell based on pseudo-vorticity and dual-Doppler vorticity analysis. The investigation of characteristics of cells merging also included the analysis of the mechanisms, in which the goal is to quantify the factors affecting the characteristics of vertical vorticity.

4.2 Methodology

4.2.1 Classification of cells

In this chapter, the event analysis of 10th September 2014 was investigated with the additional analysis and new proposal of definition from the aforementioned Chapter 3. A single-cell was defined that cells develops within a range of 20 km from the center of the storm. As stated by Browning et al. (1976), the new cells that were developed from the parent cell should be 30 km from the core of Z_h. Hence, in this range, we determined the development of single-cell whether it was developed adjacent to the pre-existing cells by investigating the cross-section of radar reflectivity of dual-Doppler analysis. Therefore, the cross-section of each cell was constructed to identify its early stage and merging stage development. Since we were interested to distinguish the evolution of single-cell and multicell, the categorization of cells was divided with different labels of cells inspected. The classification of the single-cells label followed the cells' appearance (starting from A, B, and C), in contrast, the multicell label followed the cells merged starting from α, β, and γ in the order of formation.

4.2.2 Pseudo-vorticity analysis

The detailed formula used for the vertical vorticity is clarified in Section 2.2.1. The examination of PPI images of Z_h as described in Figure 4.2(a) was established to identify the case of the merged cell. A single-cell was defined with Z_h > 10 dBZ at a height of 2 km from the radar, and a multicell was defined as the existence of more than one core of Z_h > 10 dBZ at the same height. The merging of the echoes between the single-cell and multicell could be determined by monitoring the edge of the contour line of > 10 dBZ echoes at a height of 2 km and the increase in Z_h 5 min after merging. The core vorticity of the pseudo-vorticity method was defined as the maximum intensity of the positive vorticity intensity and the minimum values of the negative vorticity intensity at each plan position indicator (PPI), which was extracted from the 1-min data with a spatial resolution of 50 m × 50 m for each elevation angle. It was ensured that the locations of the core vorticities were consistent such that the vertical vortex tube could be constructed, as shown in Figure 4.2(b). The example of the time evolution of cells A and α is presented in Figure 4.3.

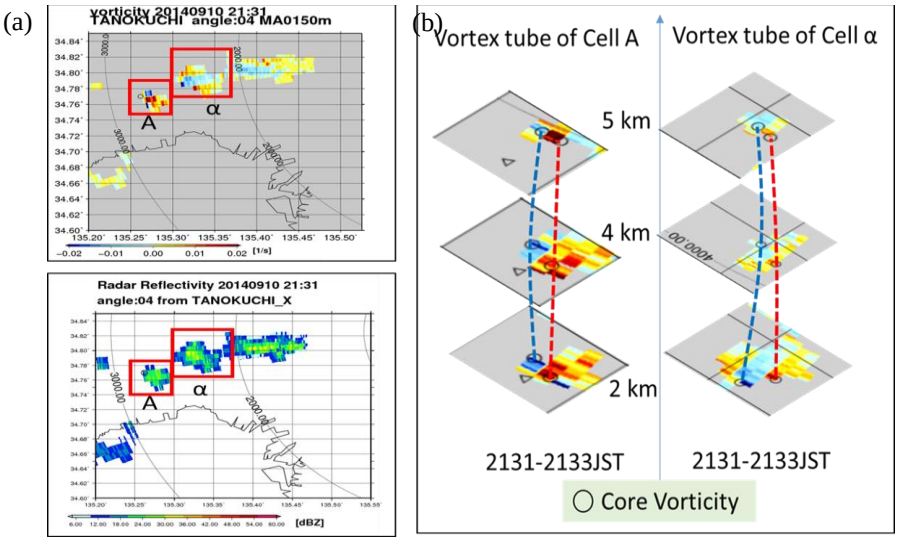

Figure 4.2(a) The comparison of PPI images of pseudo-vorticity and radar reflectivity. The red box referred to the boundary of single-cell and multicell. (b) The vertical vortex tube construction which circle indicated the core vorticity position. The red and blue lines referred to the vertical vortex tube of core positive and negative.

4.2.3 DDA vorticity analysis

The detailed formula used for the vertical vorticity is clarified in Section 2.2.2. The target event as discussed in Section 3.3.2 could not be analyzed using dual-Doppler analysis because the target area is not suitable to conduct the dual-Doppler analysis which, and the location is out of the observation. The dual-Doppler map to the target events is described in Figure 4.3. Therefore, we focused on the target on September 10, 2014, owing to the lifetime of storms more than 2 hours, and the target area could be analyzed with the dual-Doppler analysis.

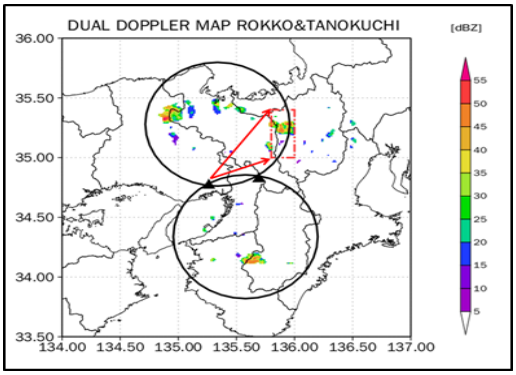

Figure 4.3 Dual-Doppler radar analysis map on 13th August 2018 with the target area shown on the red dashed line

In the DDA vorticity estimation, two Doppler radars namely Tanokuchi and Katsuragi radar stations were used. The spatial and temporal resolutions of this analysis were 1 km × 1 km × 0.5 km and 5 min intervals, respectively. The core vorticity of the DDA was defined as the maximum intensity of the positive vorticity and the minimum intensity of the negative vorticity intensity, which was obtained for each CAPPI height. The classification of the single-cells was determined with a closed contour of Z_h > 10 dBZ at a height of 2 km. The multicell was defined when more than one core of Z_h > 10 dBZ at the height of 2 km was observed. The merging of the echoes between the single-cell and multicell could be determined by monitoring the edge of the contour line of > 10 dBZ echoes at a height of 2 km and the increase in Z_h 5 min after merging, as shown in Figure 4.4(a). The schematic illustrations for the construction of a vertical vortex tube of core vorticity are presented in Figure 4.4(b). The maximum values of the positive and negative vorticities were identified to calculate the core vorticity at each cell boundary. The locations of the positive and negative core vorticities were ensured to be consistent so that the vertical vortex tube could be constructed.

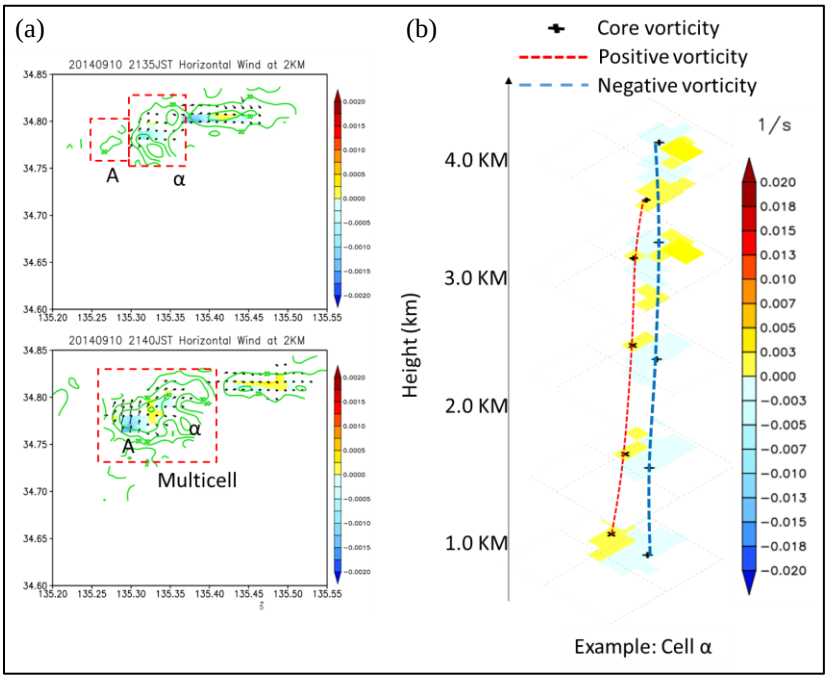

Figure 4.4(a) Storm-relative horizontal wind at 3 km height. The color scale determined the vertical vorticity from DDA, the contoured line indicated radar reflectivity in the interval of 10 dBZ. (b) In the vertical vortex tube construction, plus indicated the core vorticity position, red and blue lines referred to the vertical vortex tube of core positive and negative. All red color boxes referred to the boundary of cells.

4.2.4 Analysis of transition signals and mechanisms effect

The characteristic patterns of transition from single-cell to multicell in the multicell thunderstorm environment were determined by examining the intensity, and height of each core vorticity. We focused on the inspection of the peak intensity during the analysis period with respect to height and time. For the pseudo-vorticity, the height of cells developed was calculated using the equation below, by considering the height of the center of the radar beam h is given at a distance r by the equation adapted from Rinehart (2010).

$$h = \left[\sqrt{\mathrm{r}^2 + (k_e a)^2 + 2\mathrm{r}\,(k_e a + H_0)\,sin(\theta_e)}\right] - k_e a \qquad (4.1)$$

where a is the earth's radius, k_e is the ratio between a and the equivalent earth's radius, θ_e is the antenna elevation angle, and r is the distance between from radar to the point of target, and H_0 is the height of the radar above sea level. Atmospheric propagation conditions can be identified in k_e which can be written in terms of refractivity gradient as

$$k_e = \frac{1}{1 + a\left(\frac{dN}{dh}\right)} \qquad (4.2)$$

In this study, k_e was assumed as the standard refraction with the value of k_e is approximately 1.3333. A schematic illustration of the height determination is displayed in Figure 4.5(a) for the pseudo-vorticity analysis. The height of DDA vorticity could be retrieved based on the CAPPI height formation.

The distance calculated for the same sign of core vorticity was used by applying the Haversine formula as in Equation (4.3). The haversine formula is used to calculate the distance between two points on Earth's surface specified in longitude and latitude.

$$d = 2r\sin^{-1}\left(\sqrt{\sin^2\left(\frac{\phi_2-\phi_1}{2}\right) + \cos(\phi_1)\cos(\phi_2)\sin^2\left(\frac{\psi_2-\psi_1}{2}\right)}\right) \qquad (4.3)$$

where d is the distance between two points with longitude and latitude (ψ,ϕ) and r is the radius of the Earth. A schematic illustration of the distance analysis is displayed in Figure 4.5(b).

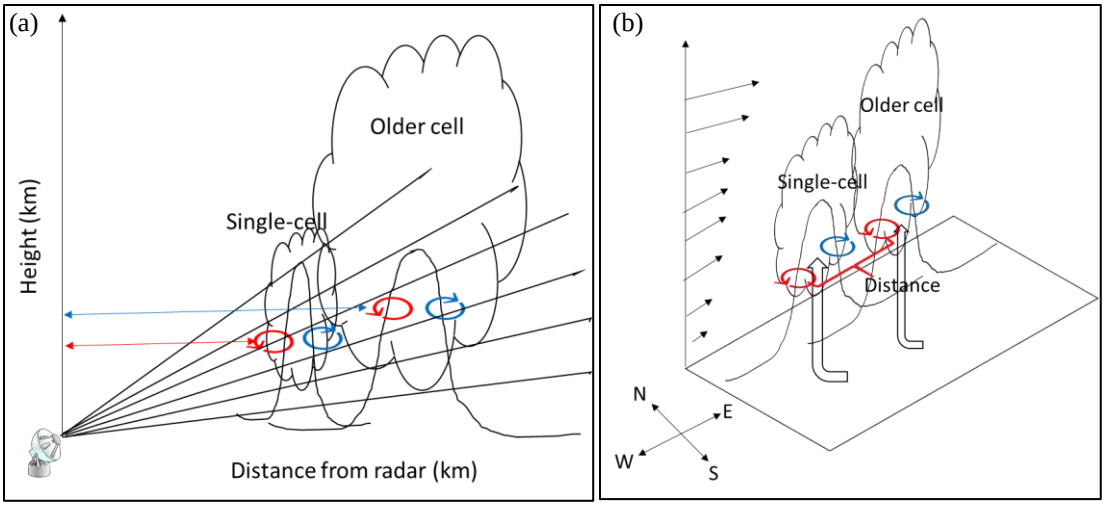

Figure 4.5 Schematic illustration of (a) height calculation from the pseudo-vorticity analysis and (b) distance analysis for the same sign of core vorticity for both methods. The red anticlockwise arrow indicates positive vorticity; the blue clockwise arrow specifies negative vorticity.

It has been discovered in numerous studies that tilting and stretching mechanisms are required for the dynamic formation of vorticity (Rotunno, 1981; Shapiro and Kogan, 1994; Boyer and Dhal, 2020), especially for supercell. Therefore, both mechanisms will be further investigated to analyze the vortex tube structure associated with the single-cell merged into multicell.

The rate of change in the vertical vorticity can be described by Equation (4.4), where the first and second terms on the right side of the equation represent the tilting of the horizontal vorticity and the third term represents the stretching of the vortex tube.

$$\frac{d\zeta}{dt} = \xi \frac{\partial w}{\partial x} + \eta \frac{\partial w}{\partial y} + \zeta \frac{\partial w}{\partial z} \qquad (4.4)$$

where (ξ, η, ζ) are vorticities in the (x,y,z) direction, respectively, and w is the z-component of velocity. The tilting term is important for the mesoscale process such as tornadoes which tilt the horizontal vorticity to vertical vorticity. The stretching term exponentially increases the vertical vorticity that is co-located with the horizontal convergence of air.

The convergence in the updraft and the divergence in the downdraft affect the vortex pair intensity at the lower and middle levels (Rotunno, 1981). Therefore, both factors will be examined in this study. Divergence as a property of the flow field is shown in Equation (4.5). Negative divergence is considered to be convergence in this study.

$$\text{Divergence} = \frac{\partial u}{\partial x} + \frac{\partial v}{\partial y} \qquad (4.5)$$

where u is the zonal wind component, and v is the meridional wind component in the x and y direction, respectively. These equations (4.4) and (4.5) use the wind fields obtained by dual-Doppler analysis at 5-minute intervals.

4.3 Results and Discussion

The transition from single-cell to multicell with the vertical cross-section through the storm will be explained in Section 4.3.1. The detailed analysis of vertical vorticity will be discussed in Section 4.3.2 for pseudo-vorticity and DDA vorticity analysis. The comparison of both methods in characterizing the signal patterns will be explained in Section 4.3.3 with the mechanism analysis. The evaluation of the kinematic and dynamic mechanisms will be presented in Section 4.3.4.

4.3.1 Detailed kinematic and cells distribution

The evolution of multicell formation is illustrated in Figure 4.6, which presents the horizontal section of radar echoes and wind motion at altitudes of 2 km at 5-minute intervals. Apparently, this cluster storm was a multicell thunderstorm that composed several cores of radar reflectivity in almost 2-hour observation. The storm propagated from the southeast to the northeast which started from a single-cell and combined with other cells that were newly generated at the left flank (relative to the direction of the cell motion) of the storm, and parent cells decayed on the right flank. The lifetime of the storm was more than 2 hours. It is noted that cell A developed very strongly at 2150JST. The multicell ε and η then developed with the strongest intensity and expanded in the large area.

Shown in Figure 4.7 are the changes with time of maximum radar reflectivity, vertical vorticity, and updraft velocities within the storm. During the one-hour observation, maximum reflectivity was increased from 30 dBZ to 50 dBZ and, it gradually rose until 70 dBZ. The maximum updraft speed increased from <1.5 ms^{-1} to >5 ms^{-1}, and rapidly increased after 1-hour observation. The peak of vertical vorticity occurred at the early development of multicell, then gradually increased after 2200JST. The rapid increment could be observed on the peak vorticity at 4 km height compared with 2 km AGL. Mostly the peak of updraft was consistent with the peak

of vertical vorticity. These changes indicate the storm gradually developed with the merged of single-cell and adjacent cells, therefore, a detailed investigation in terms of vertical vorticity and kinematic mechanism will be developed in the next section.

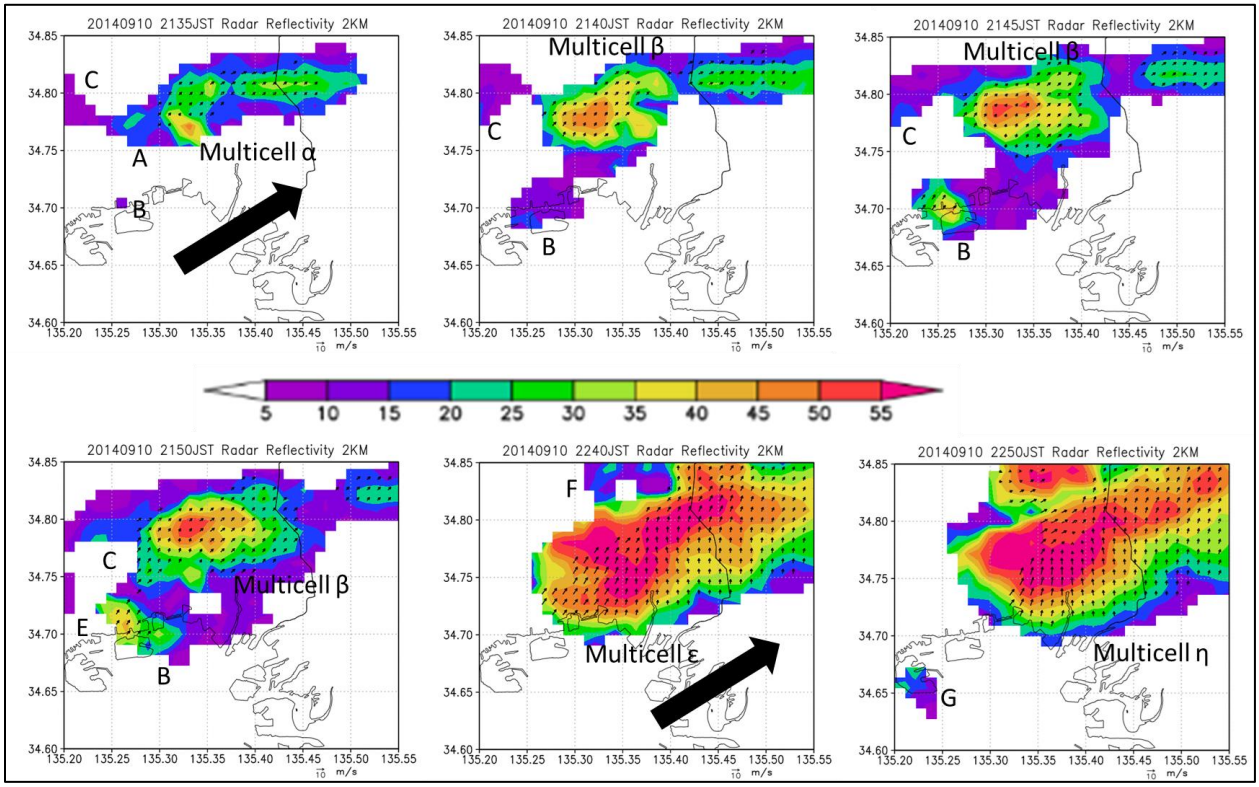

Figure 4.6 Storm propagation including the labels of the single-cells and multicell at a height of 2 km above the ground level. The black arrow indicates the storm motion movement.

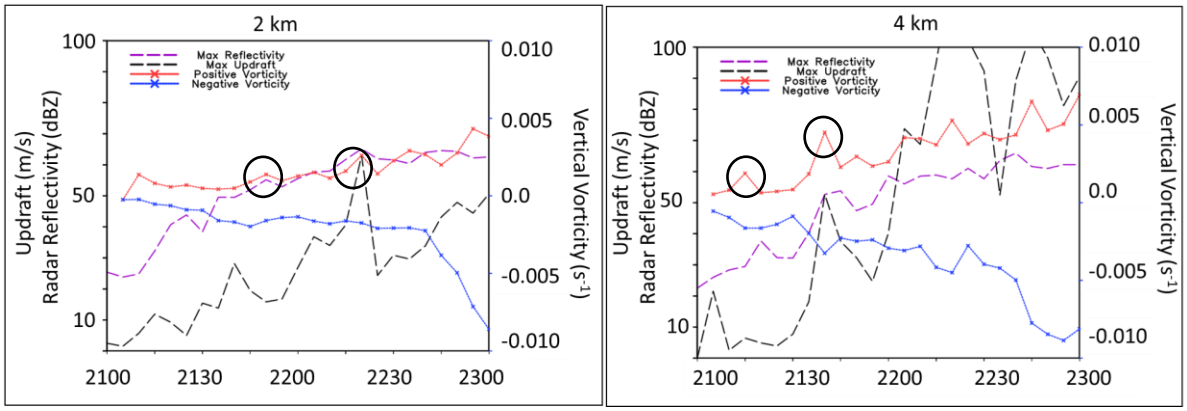

Figure 4.7 Core vorticity, maximum reflectivity, and updraft during the entire storm at 2 km and 4 km. The circle indicated the peak of vorticity that happened in the multicell development.

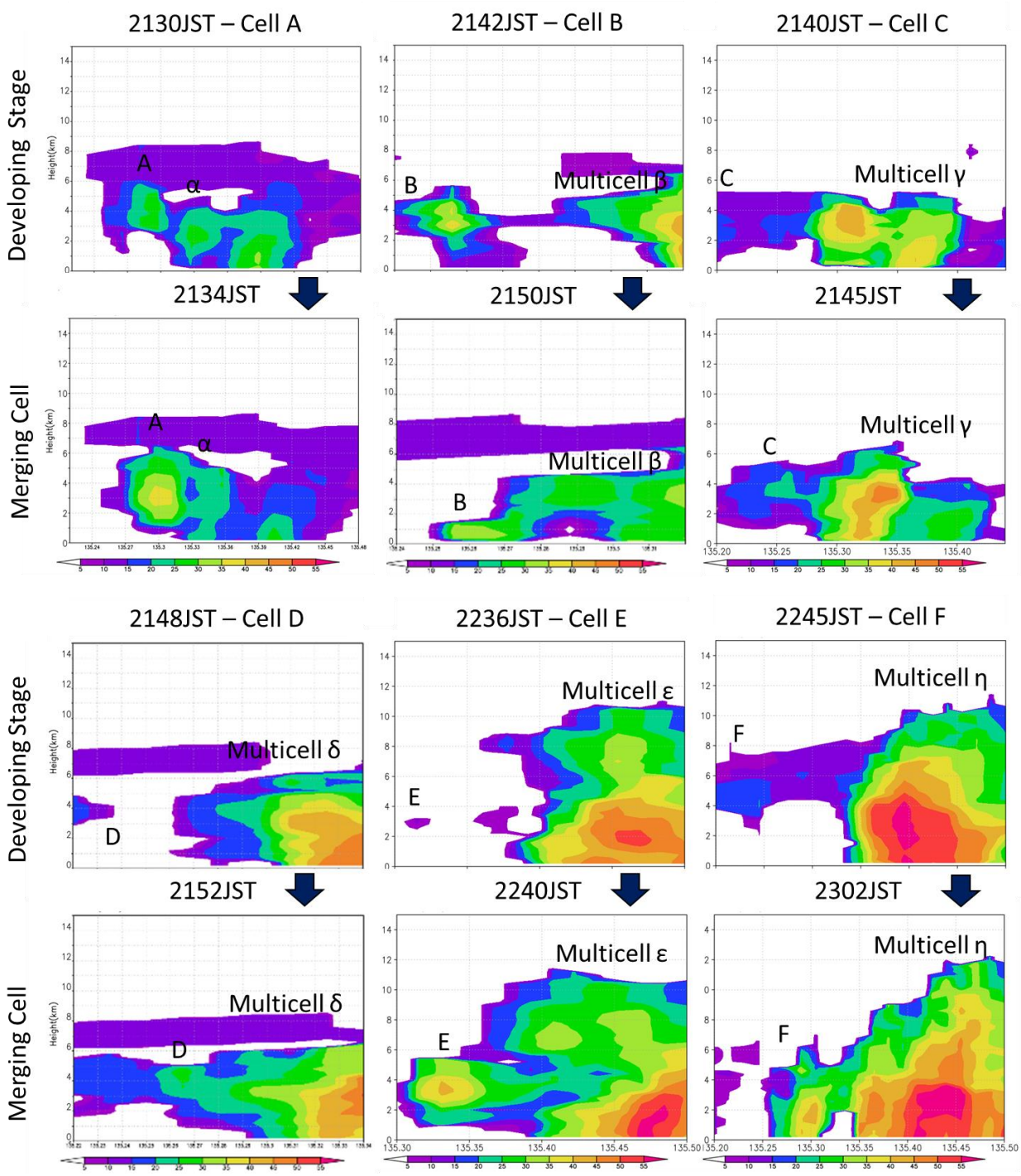

Figure 4.8 Vertical cross-section images of single-cell transformed into multicell respected with the time of developing stage and merged cells.

The vertical cross-section images of each single-cell that was investigated in this analysis were constructed as shown in Figure 4.8. It was clearly observed that all single-cells merged with the existing multicell, and combined to become a more intense multicell. From these figures, all single-cells developed after fully merging with the multicell, except cell B which was partially merged and dissipated earlier than those single-cells. The distribution of DDA vertical vorticity (shaded) and, the radar reflectivity (contoured) are described in Figure 4.9. Observations from 2135 to 2145 JST revealed the presence of three single-cells (Cells A, B, and C). Then, cell A merged with a cell α that generated multicell β, which is of interest because it was sustained during the storm for 60 minutes after its appearance. Only cell B partially merges with the multicell γ. After 15 min, a new single-cell (D) appeared and merged with the multicell δ. During the 30-minute observation, the intensity of Z_h increased, and the other new cell was not observed until cell E appeared close to the storm. A new single-cell (F) developed in the southwest of the storm, moved northeast, and merged with the multicell η.

In terms of horizontal distribution analysis, the vertical vorticity showed in the intensity in the range from 0.001 s^{-1} to -0.001 s^{-1}. At the early stage of formation, the developed cell disclosed the lowest intensity, then gradually increased after the multicell merged with single-cell A. In the first 1 hour-observation, the highest intensity could be observed at ±0.0015 s^{-1}, and several cores of vorticity were detected at the storm. After 1-hour observation, the storm revealed a high intensity in the multicell development compared with the developed single-cell F. Flow within the storm apparently converged between cell and multicell ε; the wind direction was northwest and southwest that converge at the center of the core vorticity in the multicell ε. The propagation of the vortex was following the wind motion, and its intensity remained the highest compared with single-cell which hereafter referred to as the “vorticity lobe”. Therefore, we are interested to discover the characteristics between single-cell and multicell in terms of vertical vorticity and kinematic mechanisms in this study and investigating the transition signals of single-cell to multicell formation. At first, the analysis of vertical shear will be implemented to categorize the existence of lower-level vorticity and mid-level vortex tube by using dual-Doppler analysis as discussed in section 4.3.2.

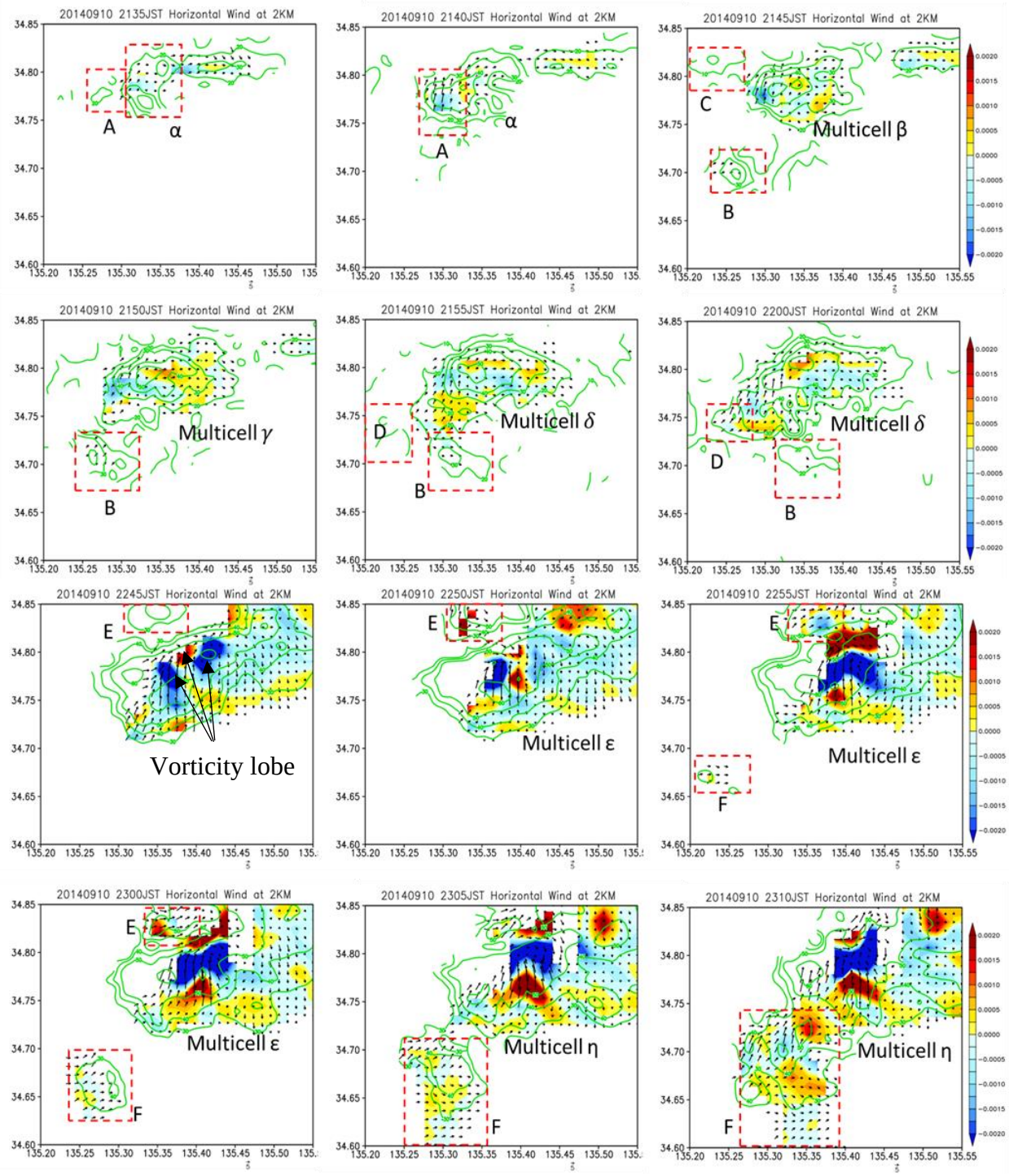

Figure 4.9 Storm-relative horizontal wind distribution at a height of 2 km in the interval of 5 minutes from the dual-Doppler analysis. In the horizontal distribution, the wind vectors denote 5 m s^{-1}. The color scale showed the vertical vorticity derived from DDA. The green contours indicate radar reflectivity at an interval of 10 dBZ. The data from 2205 until 2220 was excluded due to the non-existence of single-cells developed near the storm.

4.3.2 Vertical vorticity analysis

The analysis of vertical shear was firstly investigated to prove our hypothesis which was already discussed in section 3.3.3. The study of the existence of lower-level vorticity and mid-level vortex tube by using dual-Doppler analysis. As described in Figure 4.10, the existence of low-level vertical vortex tube and middle-level vertical vortex tube existed due to the vertical wind shear as analyzed in cell A from DDA. Therefore, we confirmed that the previous section 3.3.3 indicated the changing position of core vorticity happened owing to the existence of vertical shear in the cloud development. Since the single-cell developed near to the multicell, is the downdraft effect on the vertical vortex tube? Therefore, the new technique to identify core vorticity will be implemented as discussed previously in sections 4.2.2 and 4.2.3. Then, the examination of core vorticity of single-cells was retrieved as listed in Table 4.1.

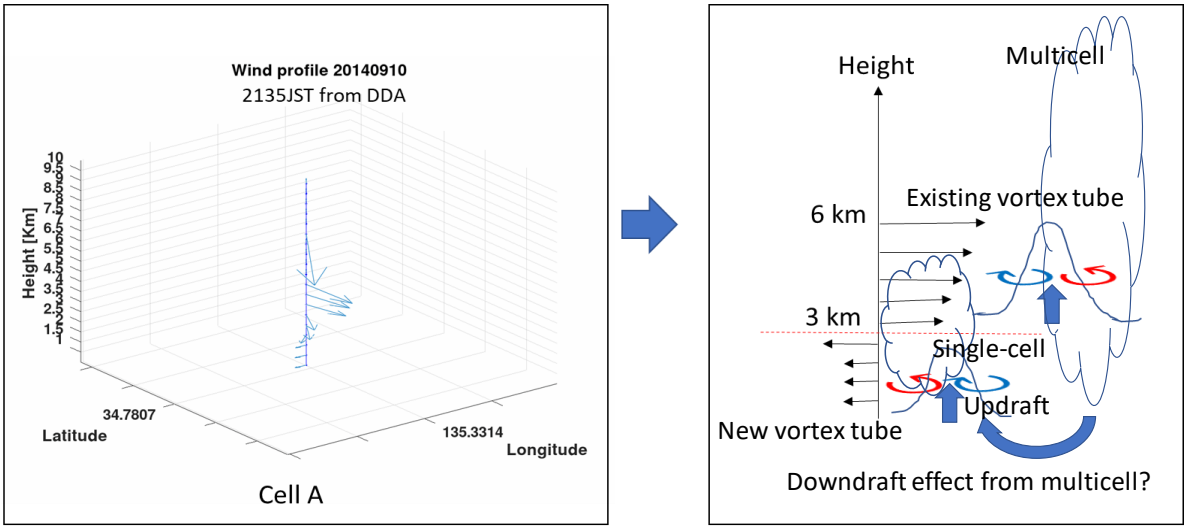

Figure 4.10 The wind profile from DDA for cell A investigated with the schematic illustration of the position of the vortex tube existed at low-level and middle-level.

Table 4.1 Peak of core vorticity intensity before merging into multicell

Single-Cell	*Pseudo-Vorticity (s^{-1})*		*DDA Vorticity (s^{-1})*	
A	***0.033***	***-0.075***	***0.0023***	***-0.0020***
B	***0.022***	***-0.027***	***0.0008***	***-0.0003***
C	***0.017***	***-0.008***	***0.0019***	***-0.0014***
D	***0.021***	***-0.012***	***0.0014***	***-0.0007***
E	***0.020***	***-0.032***	***0.0029***	***-0.0020***
F	***0.016***	***-0.008***	***0.0014***	***-0.0017***
Average	***0.022***	***-0.027***	***0.0018***	***-0.0014***

a) Pseudo-Vorticity

Firstly, an analysis of the time series for the pseudo-vorticity scenario was performed and, the peak core vorticity intensity was selected from 10-minutes period analysis. In order to identify the time of cells merged, the radar reflectivity was compared with the vertical vorticity as illustrated in Figure 4.11. Could vertical vorticity forecast the cells merged before the radar reflectivity appeared? How about the lead time of detection of peak rainfall after merging with the other cell? We will attempt to discover these above-mentioned research questions.

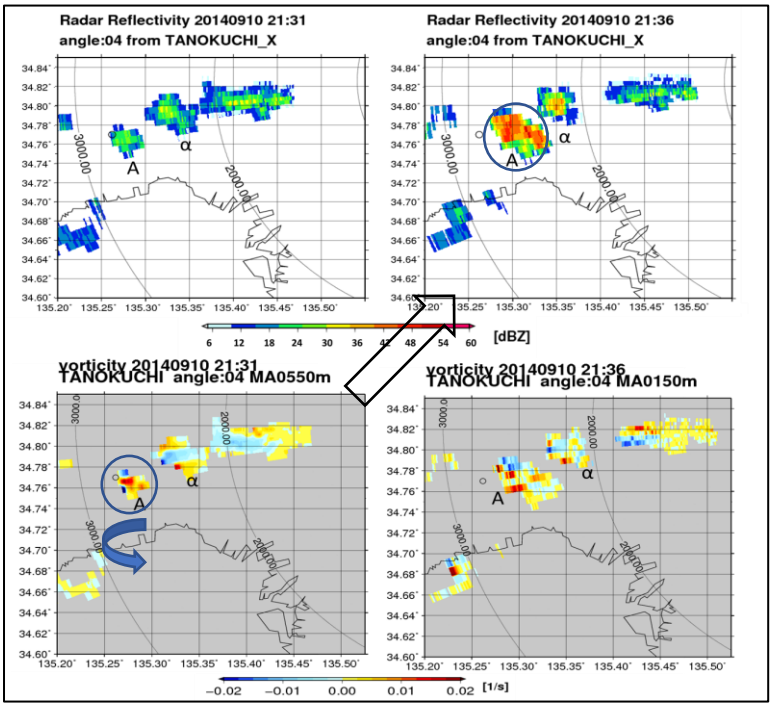

Figure 4.11 Horizontal distribution of radar reflectivity and vertical vorticity from pseudo-vorticity

i. Time-Series Analysis

At the early stage of multicell formation, it was found that single-cell A indicated the greatest intensity of vertical vorticity compared with multicell α as shown in Figure 4.12(a) after the merging occurrence at time 2134JST. The core vorticity of boundary cell A rapidly increased after the merging at 2134 JST, and the intensity of the core vorticity peaked at 2137 JST, that was, 3 min after the merging. The maximum intensities of cell A were 0.076 s^{-1} and –0.110 s^{-1}. The intensity of the core vorticity of cell α did not rapidly increase after merging. The maximum values (0.023 s^{-1}, –0.020 s^{-1}) could be observed at 2131 JST.

Meanwhile, single-cell E as shown in Figure 4.12(b) indicated less intensity compared with multicell ε during the 10-minute observation. After merged, there was a rapid increase and sudden decrease of the multicell, then remained steadily at the end of the analysis. The maximum intensities of cell E were 0.036 s^{-1} and –0.037 s^{-1} at 2243JST. The intensity of the core vorticity of cell ε rapidly increased after merging. The maximum values (0.069 s^{-1}, –0.070 s^{-1}) could be detected at 2243 JST. Other single-cell B, D, and F showed a pattern similar to the single-cell E, in which the intensity of multicell was higher than single-cells. However, in the time-series analysis, the peak of core vorticity was mostly observed for both cells. Therefore, the peak of core vorticity is indicated as the transition signals of vertical vorticity that merged into the multicell. Later, these transition signals will be analyzed in conjunction with their formation height.

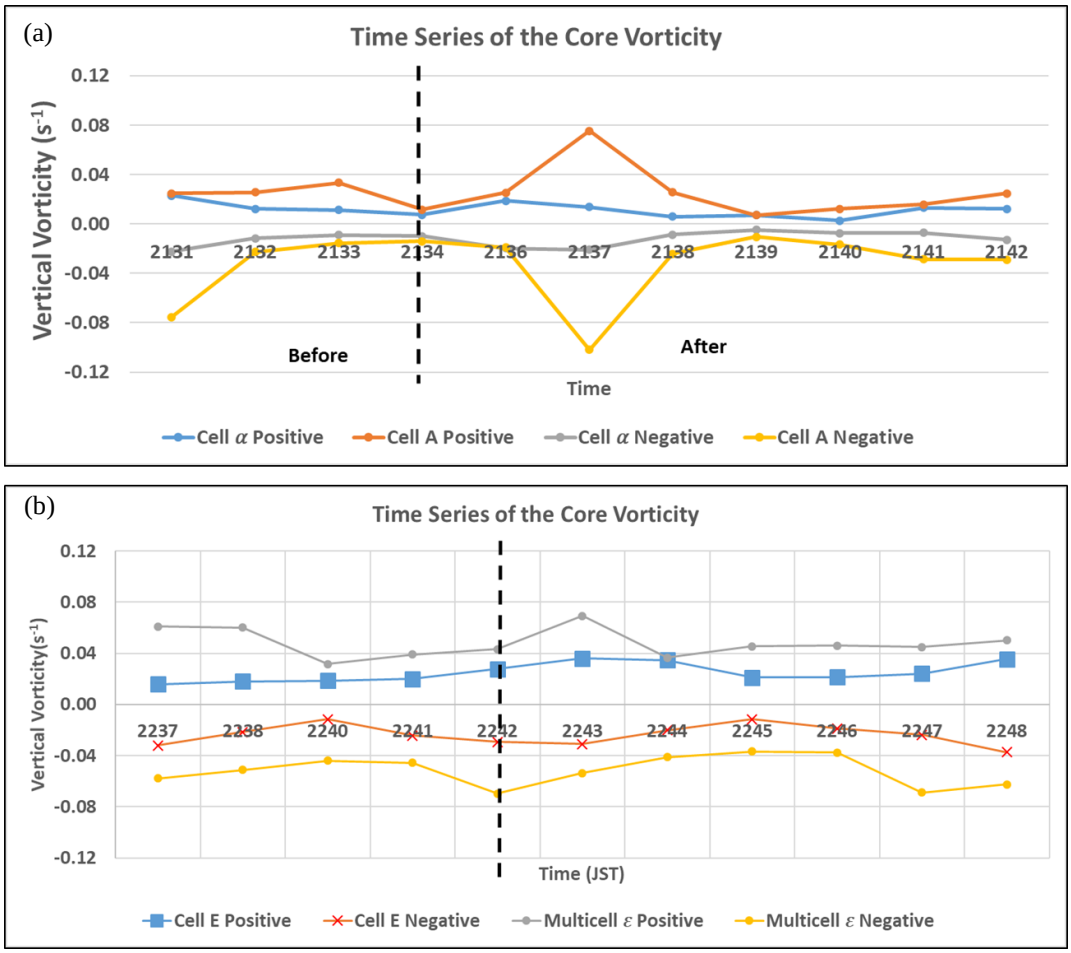

Figure 4.12 Time series of the core vorticity between (a) single-cell A and multicell α and (b) single-cell F and multicell ε for positive and negative vorticity for pseudo-vorticity at each elevation angle. The black dashed line indicates the cell merging before and after cells merging.

ii. Peak of core vorticity intensity and height formation

The peak of core vorticity at each boundary of the cell is summarized in Table 4.2. The peak of core vorticity showed that single-cell B was the largest intensity at both pair vorticities followed by the single-cell E. Multicell ε indicated the highest intensity for this period and multicell α displayed less strength intensity during the analysis. Consequently, at the early stage of multicell formation with two cores of Z_h, the intensity of core vorticity at the early stage of multicell formation revealed the single-cell showed greater strength, compared with the existing cell which presented lower intensity of vertical vorticity. After merging several single-cells, the multicell revealed a higher intensity of vertical vorticity. As a result, the evolution of vertical vorticity showed its maximum magnitude depended on the stage of multicell formation. The decaying cells always refer to the dissipating stage, which the less magnitude of vorticity inside the cell. On the other hand, the cells that are newly and continuously developed always referred to as the developing stage showed a high magnitude of vorticity.

Table 4.2 Peak of core vorticity intensity and its formation height.

Single-cell	**Peak Core Positive Vorticity (s^{-1})**	**Height of Peak (km)**	**Peak Core Negative Vorticity (s^{-1})**	**Height of Peak (km)**
A	0.08	4.1	-0.11	4.1
B	0.02	5.0	-0.03	5.0
C	0.02	3.5	-0.02	3.5
D	0.03	3.5	-0.03	3.5
E	0.04	3.9	-0.04	3.9
F	0.02	6.2	-0.02	6.2
Multicell				
α	0.02	2.4	-0.02	2.4
β	0.04	4.1	-0.03	2.8
γ	0.03	4.2	-0.03	2.5
δ	0.03	5.0	-0.03	3.4
ε	0.07	4.3	-0.07	4.0
η	0.05	1.4	-0.06	1.3

From Table 4.2, the height of peak core vorticity from single-cell indicated the similarity in the height of core positive and negative vorticity. In addition, their positions are located at the height in the range of 3.5 km to 6.2 km. The multicell revealed the different pattern of location of core vorticity with the height of core positive vorticity presented at a higher height compared with the core negative vorticity. With the exemption of cell α, this cell showed at the same height of 2.4 km for core pair vorticity. The average formation height of single-cell was 4.4 km for both pair core vorticities. In contrast, the average formation height for multicell was 3.6 km for core positive vorticity and 2.7 km for core negative vorticity. The different heights of peak core vorticity might be influenced by the strength of the updraft for single-cell, whilst downdraft affects mostly the position of core negative vorticity. Using Z_{dr} column as an indicator for the updraft, we could observe the updraft located at the center of pair vorticity that influenced the height of peak vorticity as shown in Figure 4.13. Later, we will investigate more using DDA analysis in terms of convergence and updraft.

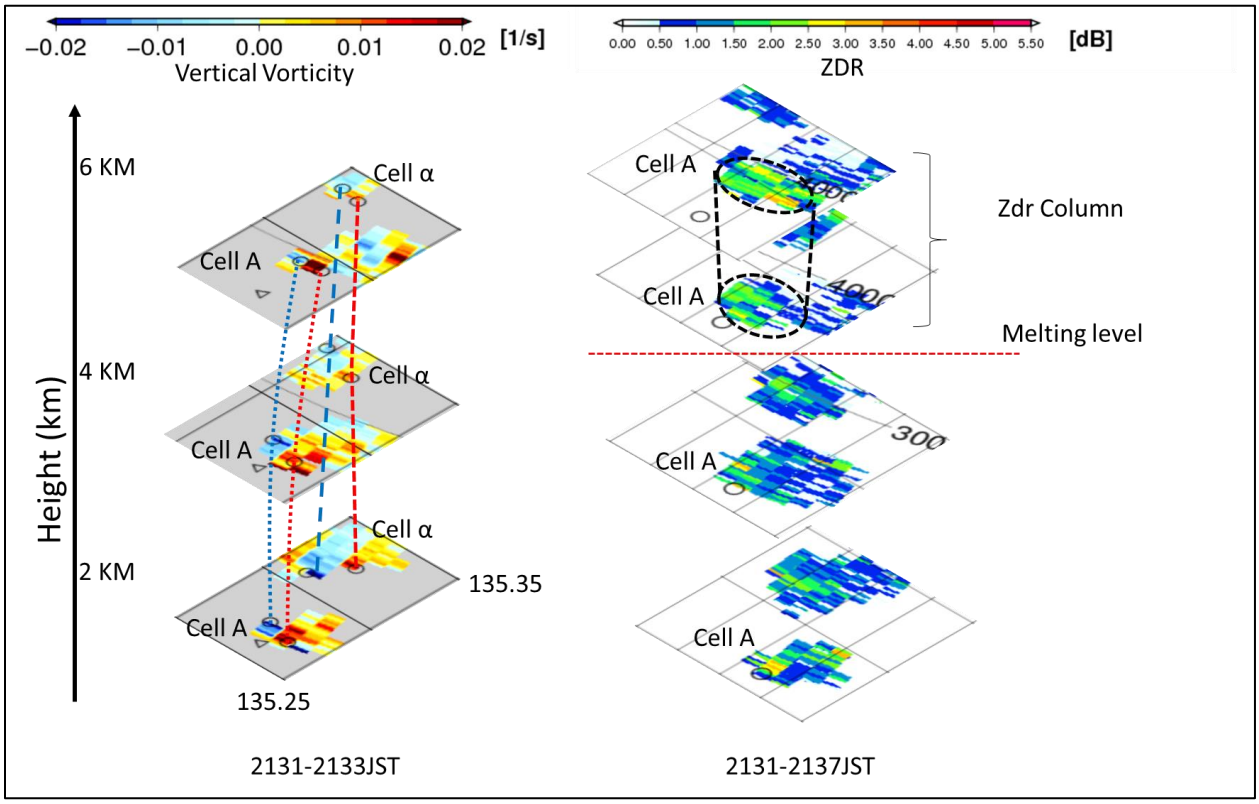

Figure 4.13 The vortex tube of single-cell A and multicell α at the early stage of multicell formation before merging (left figure), and updraft position and strength using the Z_{dr} column (right figure).

iii. Distance Analysis

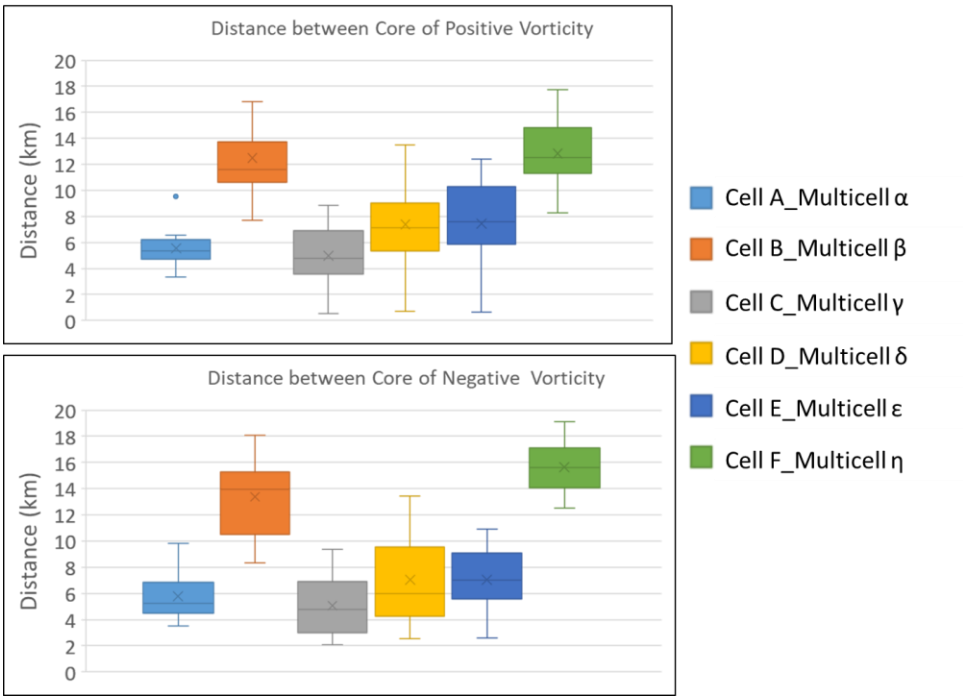

Figure 4.14 Core vorticity analysis in terms of the distance and correlation between the core vorticity and distance.

An additional analysis was conducted for all cells to determine the correlation between the distance and core vorticity before and after merged. Figure 4.14 summarizes the results, in which the shortest distance of the core vorticity occurred on the single-cells A and C. We discovered that the core vorticity intensity was the strongest between 5 and 10 km although the distance and core vorticity were not correlated. In order to investigate the correlation between the core vorticity intensity and distance in more detail, the separation of core vorticity intensities of the single-cell and multicell was verified. The Pearson correlation indicated that there is no relationship between the single-cells ($r = 0.28$)[1] and ($r = 0.05$)[2] and multicell ($r = 0.04$)[1] and ($r = 0.28$)[2]. Why does the distance analysis for pseudo-vorticity is not showing a significant relationship? We will compare it with the DDA vorticity analysis to identify whether the distance analysis could be indicated as a characteristic pattern of cell merging analysis. Furthermore, the distance of 5-10 km disclosed the frequent occurrence of the threshold of core vorticity greater than ± 0.03 s^{-1}. The shortest

[1] Core positive vorticity
[2] Core negative vorticity

distance affects the increment of core vorticity because the merged of the same sign of core vorticity results in the enhancement and maintenance of the intensity of vertical vorticity. To confirm this hypothesis, the horizontal distribution of vertical vorticity is analyzed in Figure 4.15.

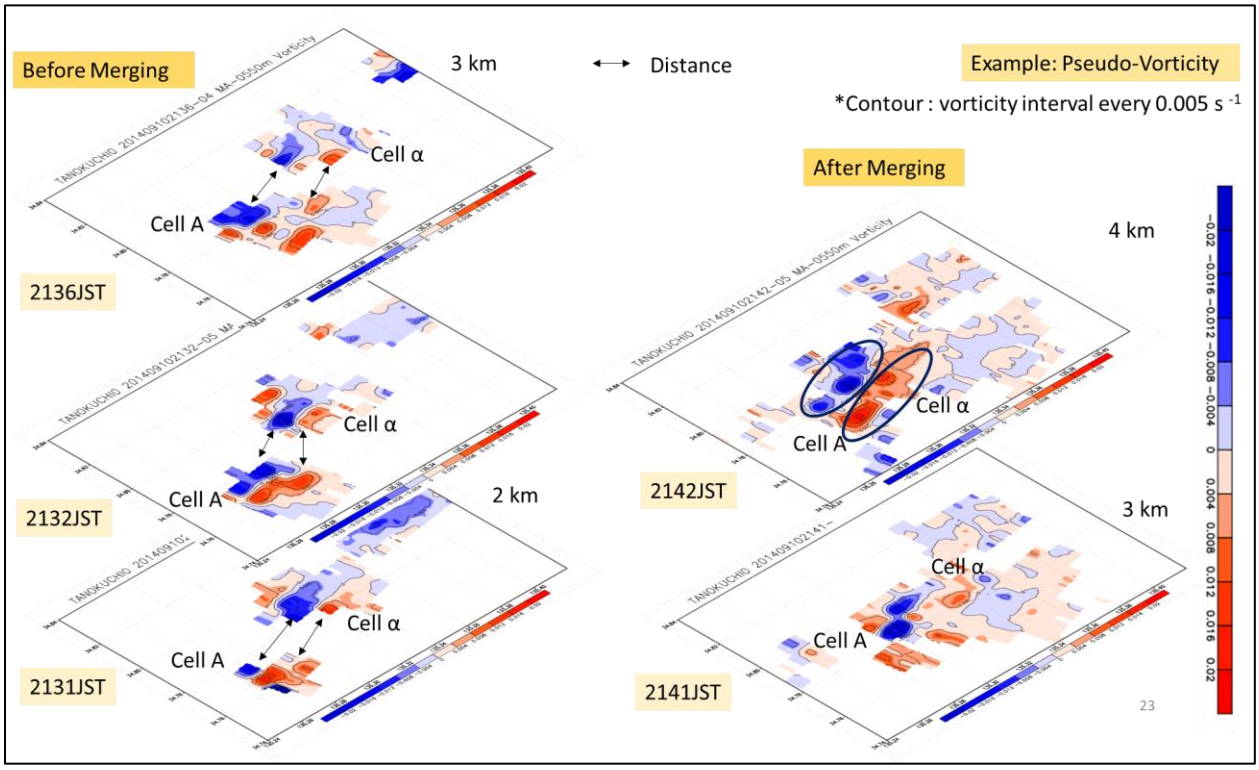

Figure 4.15 The distribution of merged cells at the shortest distance.

The horizontal distribution of cell A and cell α at a period before merged (2131JST-2136JST) showed each boundary of the cell possessed its own vortex with a different magnitude of positive and negative vorticity. Previously, the time-series analysis revealed that the peak of core vorticity of cell A happened at 2137JST. It is indicated that during the merger of multiple vortices, the intense vortices are further enhanced especially at the early stage of their lifetime. After merged, we discovered that cell A presented the highest intensity after combining with the vortex from the existing cell and the area of merged cells became larger with three cores of the negative vortex and two cores of the positive vortex after 1-min merged. In the same sign of rotation, the merged vortex effect more on the areas in which the merged vortices changed from small-scale to large-scale area. Therefore, we could find the large area of vortex mostly in the multicell development.

b) DDA vorticity

Based on our pseudo-vorticity analysis, the core vorticity intensity disclosed the increment of core vorticity at the early stage of multicell formation and the height of formation of peak core vorticities could be distinguished between single-cell and multicell. Since DDA provided the highest quality estimation, we will further analyze the characteristics of vertical vorticity and the transition signals using this method.

i. Time-Series Analysis

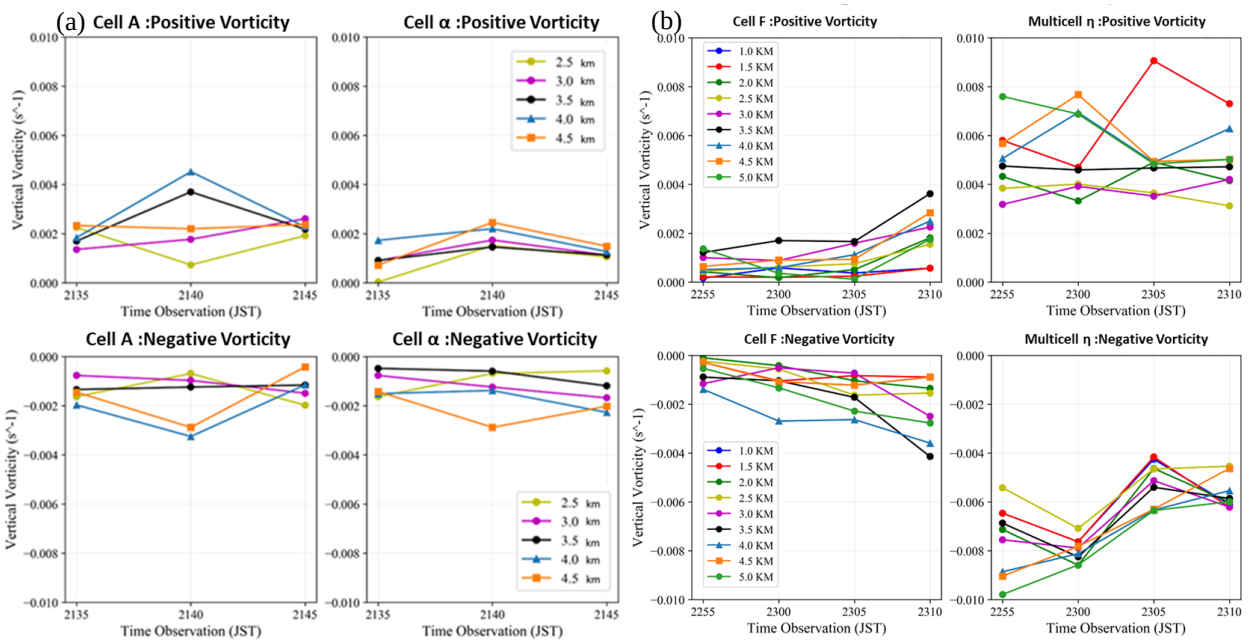

Figure 4.16 Time series of the core vorticity between (a) single-cell A-multicell α, and (b) single-cell F-multicell η for positive and negative vorticity at each CAPPI height.

The time series of cell A merged with cell α, is shown in Figure 4.16(a). The peak of core vorticity intensity patterns occurred in both cells, with cell A (0.005 and –0.003 s^{-1}) being significantly more than cell α (0.003 and –0.003 s^{-1}). Since the temporal resolution is a 5-min interval, mostly the peak of core vorticity occurred after merged. Meanwhile, cell F as shown in Figure 4.16(b) indicated less intensity compared with multicell η during the 10-minute observation. The maximum intensities of cell F were 0.004 s^{-1} and –0.004 s^{-1} at 2300JST. The intensity of the core vorticity of cell ε rapidly increased after merging at 2300JST. The maximum values (0.009 s^{-1}, –0.010 s^{-1}) could be detected at 2305 JST. Other single-cells B, C, D, and E

showed a pattern similar to the single-cell F, in which the intensity of multicell is higher than single-cells. However, in the time-series analysis, the peak of core vorticity was mostly observed for both cells. The peak of core vorticity will be analyzed in conjunction with its formation height.

ii. Peak of core vorticity intensity and height formation

The peak intensity of core vorticity of the cells investigated is summarized in Table 4.3. Based on the early formation of multicell from 2100 to 2200 JST, multicell (α, β, γ, δ) indicated the persistence of the core vorticity intensity (0.003 s^{-1} and –0.003 s^{-1}). The core vorticity of cells B, C, and D ranges from 0.003 to –0.002 s^{-1}. At the latter stage of multicell formation, the intensity of the core vorticity of the multicell increased after it merged with the single-cells E and F. The positive and negative vorticities range from 0.008 to 0.009 s^{-1} and from –0.010 to –0.012 s^{-1}, respectively, revealing the core vorticity maxima of the multicell. The intensities of the core vorticity of cells E and F are 0.005 and –0.012 s^{-1} and 0.004 and –0.004 s^{-1}, respectively. All single-cells that merged with the multicell showed lower core vorticity, except for cells A, E, and F. These characteristic patterns revealed similarities with the pseudo-vorticity analysis method. We will discuss this in detail in Section 4.3.3.

Table 4.3 Core vorticity intensity and its height formation

Single-cell	**Peak Core Positive Vorticity (s^{-1})**	**Height of Peak (km)**	**Peak Core Negative Vorticity (s^{-1})**	**Height of Peak (km)**
A	0.005	4.0	-0.003	4.0
B	0.003	3.5	-0.002	2.5
C	0.002	3.0	-0.002	4.5
D	0.003	3.5	-0.002	2.0
E	0.005	5.5	-0.012	5.5
F	0.004	3.5	-0.004	3.5
Multicell				
α	0.003	4.5	-0.003	4.5
β	0.003	4.0	-0.003	4.0
γ	0.003	4.0	-0.003	4.5
δ	0.003	4.0	-0.003	4.0
ε	0.008	6.0	-0.012	5.5
η	0.009	1.0	-0.010	5.0

From Table 4.3, the height of peak core vorticity from single-cell indicated the similarity in the height of core positive and negative vorticity only for cells A, E, and F. In addition, their positions were located at the height in the range of 3.5 km to 5.5 km. The multicell revealed the same location of core vorticity with the height of core vorticity existing in the range of 4.0 km until 4.5 km for cells (α, β, γ, δ). The average formation height of single-cell was 3.8 km and 3.7 km for core positive and negative vorticity, respectively. In contrast, the average formation height for multicell was 3.9 km for core positive vorticity and 4.6 km for core negative vorticity. The different heights of peak core vorticity might be influenced by the strength of the updraft in single-cell and updraft-downdraft in the multicell which will be further discussed in Section 4.3.3.

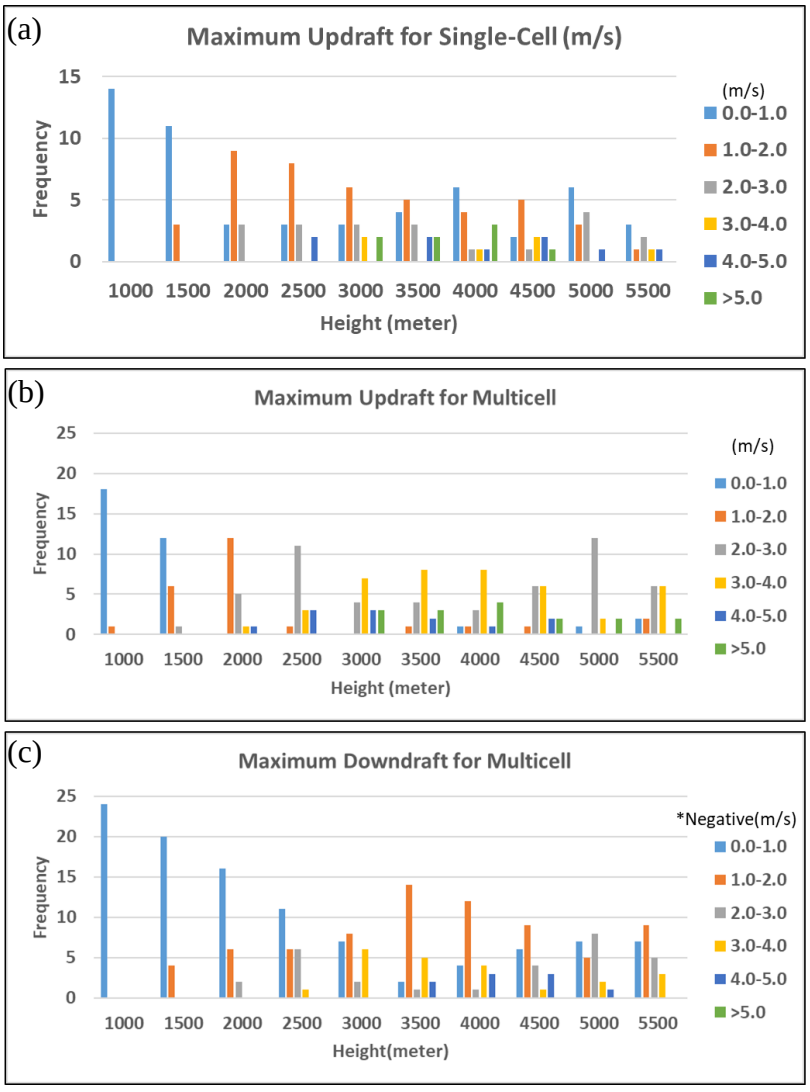

Figure 4.17 Distribution of maximum updraft for each height for (a) single-cell (b) multicell, and (c) distribution of maximum downdraft in multicell.

From Figure 4.17(a), maximum updraft greater than 5 m/s in single-cell showed the dominant height from 3 km until 4.5 km, which the most frequently occurred at level 4 km. The position of maximum updraft is almost identical to the average formation height of single-cell for core vorticity as analyzed in Table 4.3. Meanwhile, the maximum updraft as presented in Figure 4.17(b) was greater than 5 m/s located between 3 km and 5.5 km, and the most frequent height was located at 4 km height. In addition, the maximum downdraft greater than -1 m/s, revealed the height was positioned at 1 km height, but the maximum downdraft still occurred until 5.5 km height, as illustrated in Figure 4.17(c). From these analyses, we could have confirmed that the peak of vertical vorticity is correlated with the position of maximum updraft for single-cell, and updraft-downdraft in the multicell.

iii. Distance Analysis

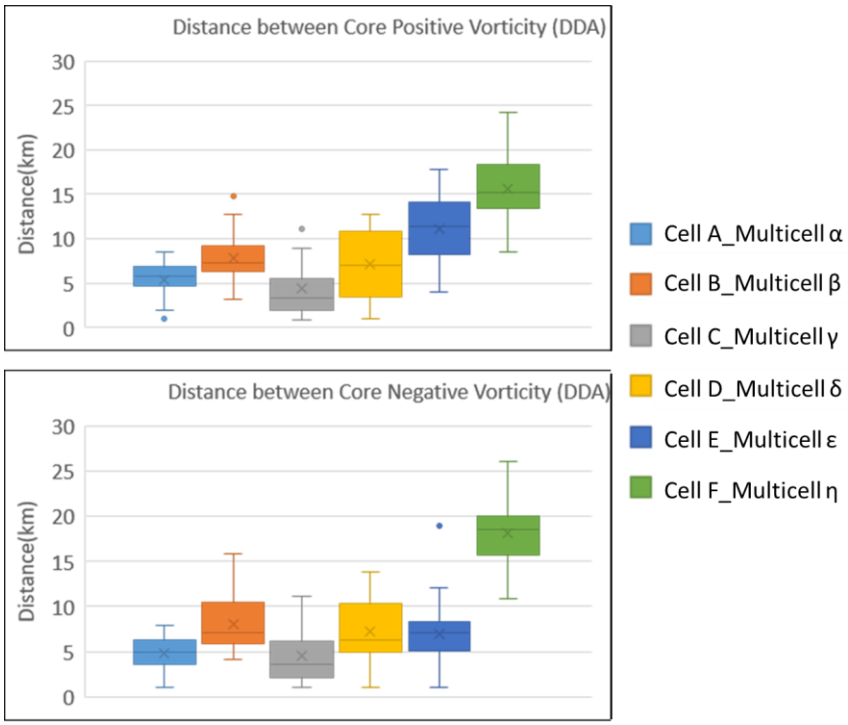

Figure 4.18 Analysis of the core vorticity in terms of the distance and correlation between the core vorticity and distance.

Based on our analysis of the distance during the merging of each cell, the single-cells A and C showed a range of distance that occurred at <10 km. In contrast, the distance of cells B, E, and F, ranged from 5–25 km, as shown in Figure 4.18. It remains unclear what is the optimal distance affects the strength of the core vorticity. The distance and core vorticity did not strongly

correlate, similar to the pseudo-vorticity method. However, we observed that the strongest core vorticity (±0.003 s^{-1}) primarily occurs at a distance ranging from 5–10 km. The short distance during merging contributes to the enormous strength of the core vorticity. This pattern is identical to the pseudo-vorticity method. Moreover, the Pearson correlation between the distance of single-cell and multicell, and the intensity of each core vorticity was compared. The results indicated a moderate correlation between the distance of the multicell and intensity of the positive and negative vorticity (r = 0.57 and 0.48), respectively, whereas a correlation was not observed for the single-cell (r = 0.13 and 0.15). Our assumption in the distance analysis is, that at the shortest distance, the multicell behavior affects the increment or decrement of core vorticity because of the interaction between updrafts or downdrafts that influenced the vertical vorticity intensities. We could not obtain this relationship using the pseudo-vorticity method, owing to the low quality of estimation compared with DDA vorticity which is a high-quality estimation.

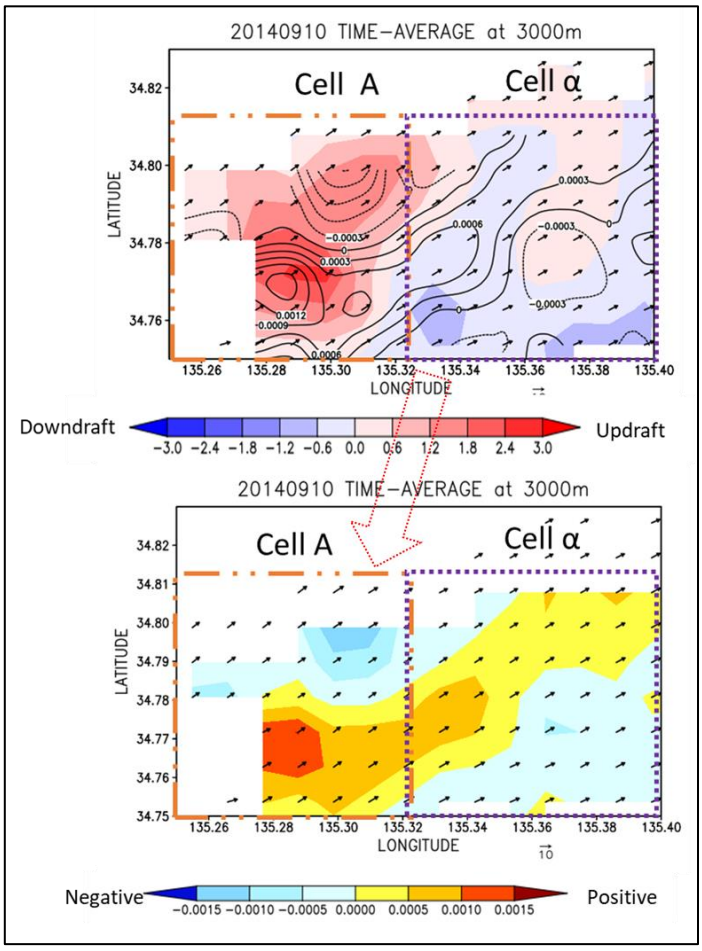

Figure 4.19 Downdraft effect from cell α to single-cell A on the vertical vorticity intensity increment. This figure showed at a height of 3 km AGL.

The horizontal distribution of vertical vorticity is also analyzed as shown in Figure 4.19 for cell A and cell α, which showed the shortest distance. The results of time average formation (2120JST-2150JST) revealed the downdraft influenced the increment of positive vorticity located at 3 km height. As noted by Jason et al. (2014), the downdraft could produce positive near-surface vertical vorticity via transportation to the surface in the tornadogenesis studies. In this analysis, the position of downdraft near to the development of a new single-cell, that merged into a multicell. The intense of positive vorticity is due to the merged of vortices and the strength of updraft that primarily mechanism in the vertical vorticity.

4.3.3 Mechanisms analysis

In this section, we will discuss more on the analysis of transition patterns of core vorticity in terms of intensity, formation height, and distance analysis with the additional mechanism analysis.

i. Time-Series Analysis

The time-series analysis showed similar transition patterns for single-cell and multicell with the increment intensity after merging for both pseudo-vorticity and DDA vorticity methods at the early stage and later stage of multicell development respectively. As a result, in this section, we will show the analysis of single-cell A-multicell α, and single-cell F-multicell η for further discussion in terms of kinematic and dynamic analysis.

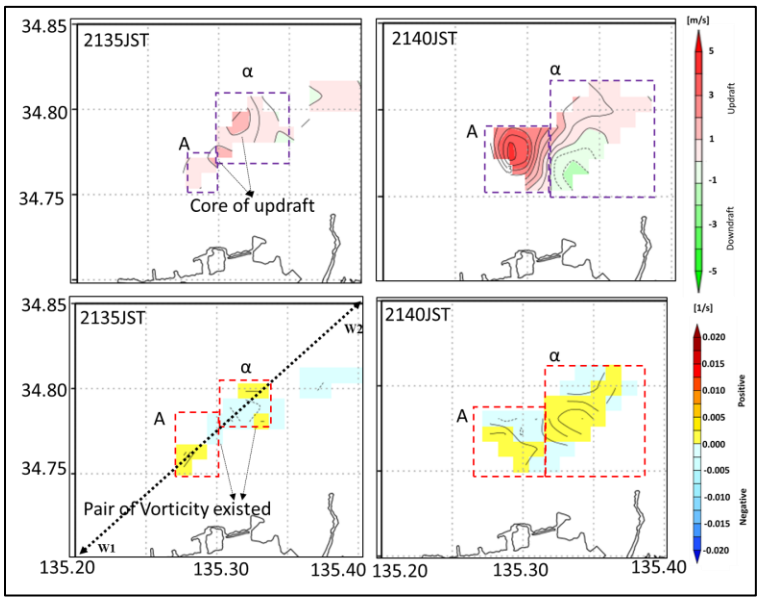

Figure 4.20 The horizontal distribution of updraft (top figure) and vertical vorticity (below figure) at 2 km height CAPPI.

At the horizontal distribution of updraft and DDA vorticity, as shown in Figure 4.20, the core of the updraft is located between the pair vorticity at the boundary of cells A and α at 2135JST. This result is similar to the findings of Franklin et al. (2006), which identified that the core of the updraft is located between the pair vorticity. Single-cell A specified the peak intensity of the updraft compared with multicell α at a height of 2.5 km, at 2140 JST.

Figure 4.21(a) and Figure 4.21(b) present the vertical cross-section along the lines shown in Figure 4.20. In the W1-W2 section, at 2135JST, the single-cell A was developed at the middle level (2 km – 4 km) with the maximum updraft of 2.13 ms^{-1} at 3 km height. The inflow could be observed at the left flank of the downdraft (LFD) of the storm typically generated at this middle level. At this period, the maximum downdraft at the multicell developed at the lower level with the maximum intensity of 0.35 ms^{-1} at 2 km AGL. The single-cell A that was developed adjacent to multicell α, was influenced by the downdraft of the parent cell. With the existence of warm and moist inflow from the environment at the lower level and the convergence at the lower level, the updraft was generated at the boundary of cell A. The pair vorticity was discovered that developed at the middle-level height.

After 5-min observation (2140JST), the Z_h intensity of single-cell A increased, with the increment of convergence, updraft, and vertical vorticity during the cell merging development. The multicell α was observed at the lowest intensity, and single-cell A become more dominant at this time. The vertical vortex tube of single-cell presented a pair of peak vortices at the middle height, meanwhile multicell showed the pair of vorticity at the upper-level. The convergence intensity slightly increased with the updraft strength resulting in the dominance of single-cell A. In comparison, the divergence at the lower level indicated the descending air motion of multicell α to dissipate. These mechanisms proved that convergence and updraft are an important mechanisms for the intensification and maintenance of core vorticity. The single-cell A currently showed the core of Z_h at 48 dBZ at 4 km height.

After cells merged at 2145JST, we could observe the widening areas of all mechanisms investigated whilst the core of Z_h (>40 dBZ) was observed near the ground. Therefore, the downpour of rainfall is mostly expected during this time in this area. It was found that another inflow started to develop at 4 km height yield to the advection of position for vortex tube in single-cell A. The convergence at the lower level and updraft remained happened in single-cell, but not in the multicell.

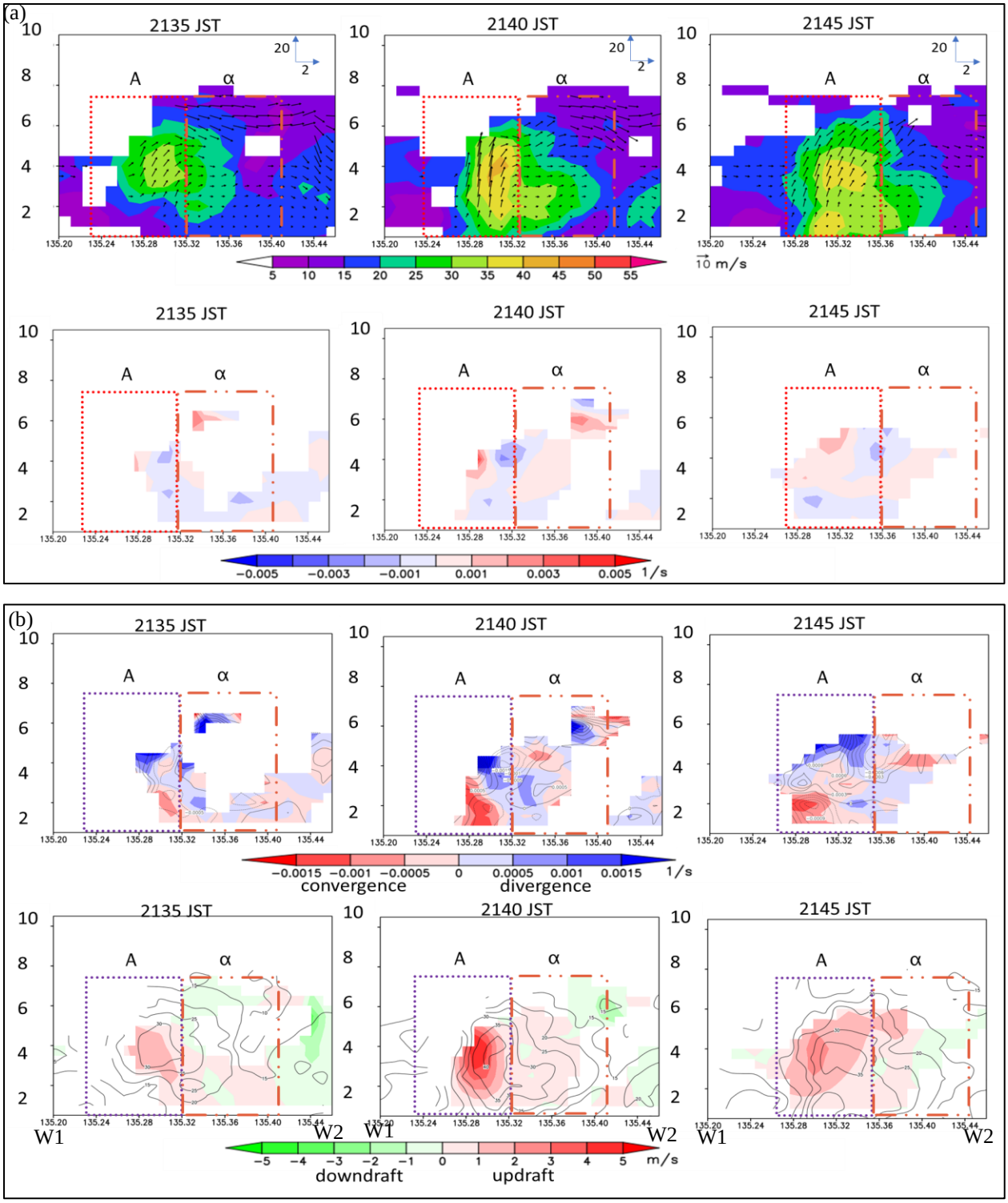

Figure 4.21 Kinematic analysis of cell A and multicell α. (a) Top figure indicates radar reflectivity with wind vector, below figure shows vertical vorticity. (b) Top figure indicates convergence (red color), and divergence (blue color), below figure shows updraft (red shaded color) and downdraft (green shaded color). See Figure 4.20 for the cross-line.

To evaluate the dynamic mechanism of vertical vorticity, the vertical cross-section through both cells is presented in Figure 4.22(a) for stretching vortex tube and Figure 4.22(b) for tilting of vortex tube. We observed that the stretched vortex tube remained happened at the middle-level height which intensified the core vorticity in single-cell A. The tilting of the vortex tube produced a similar pattern of height, with the change in sign from left to right indicating that the tilting of horizontal vorticity associated with the gradient of vertical vorticity produces a couplet of counterrotating vortices that crossed the updraft.

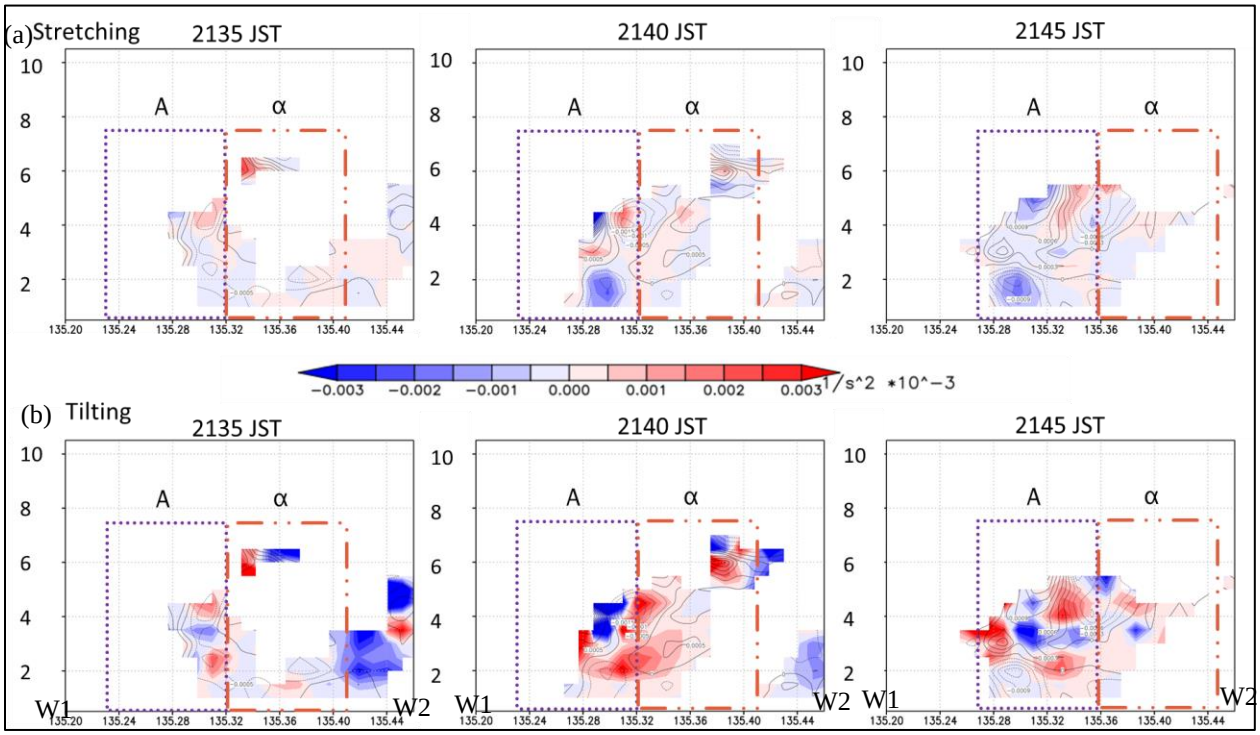

Figure 4.22 Dynamic analysis of cell A and multicell α. (a) Top figure indicates stretching term (b) below figure shows the tilting term.

At the horizontal distribution as presented in Figure 4.23, the maximum updraft remained high intensity at the center of the storm at 2300JST and 2305JST. The downdraft was observed at the rear flank of the storm, and single-cell F propagated northeastward to merge with the existing multicell. The vertical vorticity is also located at the center of the updraft with the positive vorticity on the right and negative vorticity on the left flank of the storm.

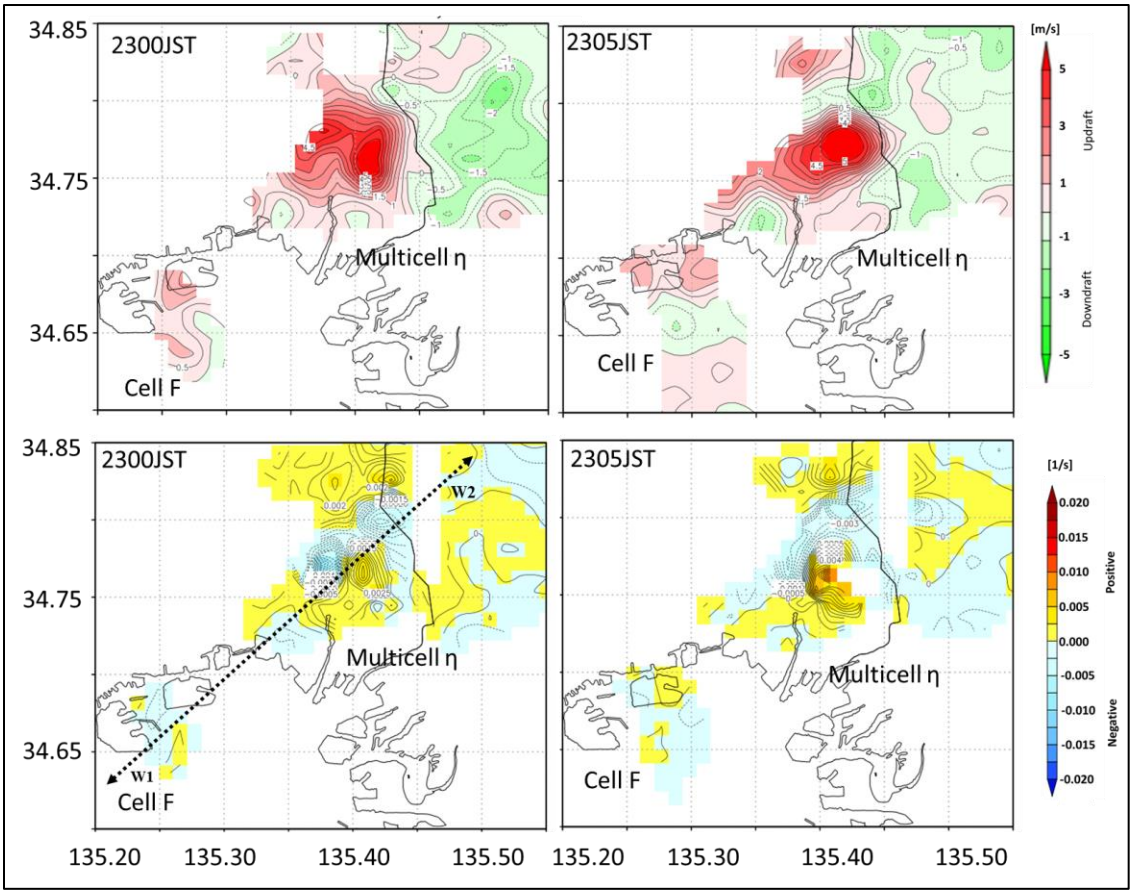

Figure 4.23 The horizontal distribution of updraft and vertical vorticity at 2 km height CAPPI.

Figure 4.24(a) and Figure 4.24(b) present the vertical cross-section along the lines shown in Figure 4.23. In the W1-W2 section, at 2255JST, the cell F was developed at a longer distance and started to merge with the existing multicell with the inflow could be observed at the left flank of downdraft (LFD) at the middle level (2 km–4 km) with the maximum updraft 3.03 ms^{-1} at 4.5 km height. During this period, the maximum downdraft at the multicell steadily developed with a maximum intensity of 4.72 ms^{-1} at 3.5 km AGL. The single-cell F that was developed far from the existing cell, was not influenced by the downdraft of the parent cell. However, with the existence of wind shear from the environment at the lower level (refer to hydrograph), this cell merged and combined into one multicell. We discovered that the intensity of convergence at the lower level was small, the vertical vorticity showed the lowest intensity compared with the multicell. The pair vorticity in the vertical vortex tube was discovered that developed until the middle-level height.

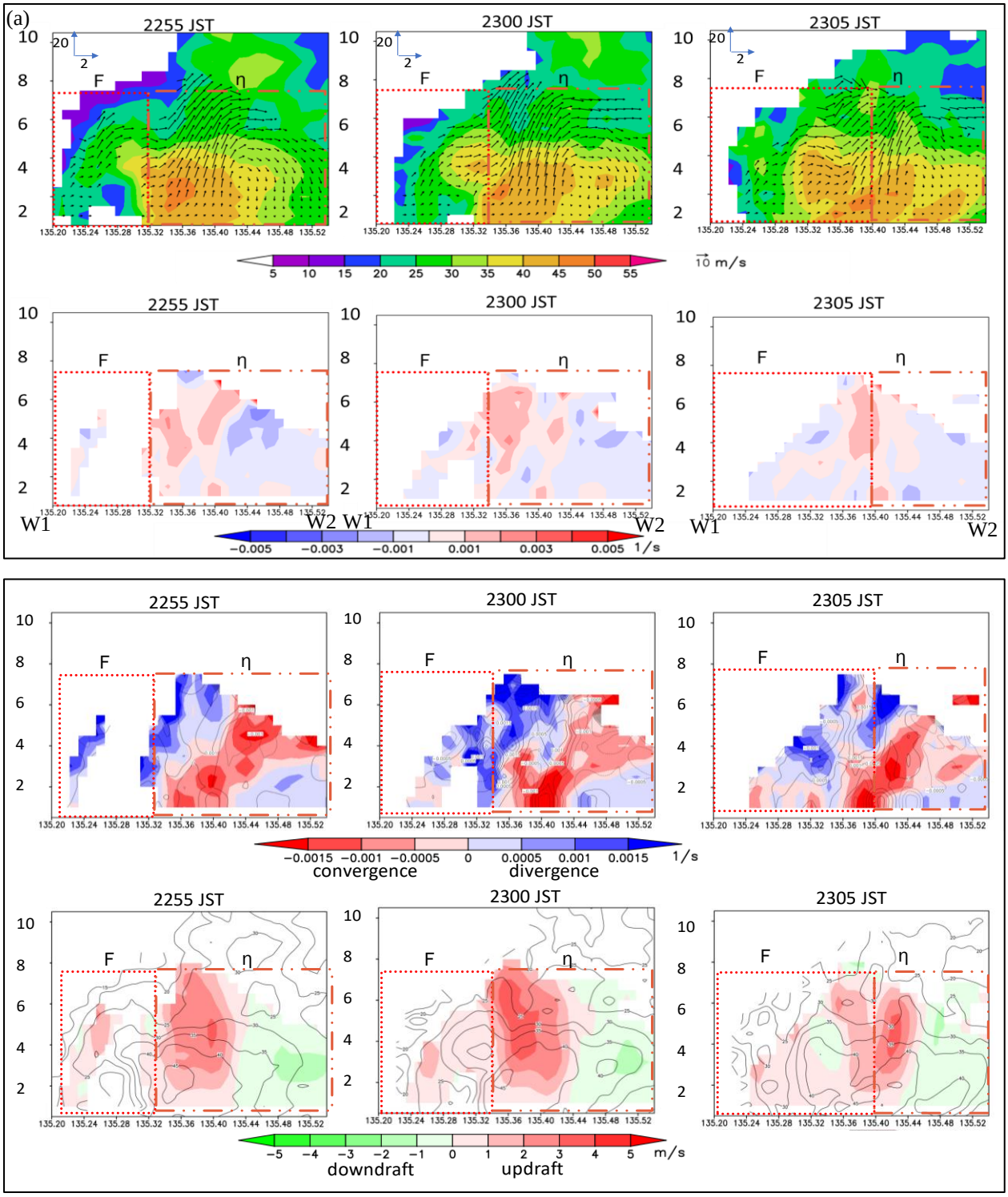

Figure 4.24 Kinematic analysis of cell F and multicell η. (a) Top figure indicates radar reflectivity with wind vector, below figure shows vertical vorticity. (b) Top figure indicates convergence (red color), and divergence (blue color), below figure shows updraft (red shaded color) and downdraft (green shaded color). See Figure 4.24 for the cross-line.

After 5-min observation (2300JST), the Z_h intensity of cell A increased, with the increment of convergence, updraft, and vertical vorticity during the cell merging development. The vertical vorticity of single-cell presented at the middle height, meanwhile multicell showed the pair of vorticity at a low level. The results indicate that the position of updraft and downdraft influence the location of pair vorticity after merged. The multicell always showed the core of Z_h at 45 dBZ at 2-4 km height. After cells merged at 2305JST, we could observe the widening areas of all mechanisms investigated whilst the core of Z_h was observed near to the ground, and single-cell merged observed the widening area of the core of Z_h at more than58 dBZ. Therefore, at this latter stage of multicell formation, the downpour of rainfall occurred near the ground, and with the merged of singe-cell, the intensity increased and covered more areas.

To evaluate the dynamic mechanism of vertical vorticity, the vertical cross-section through both cells is presented in Figure 4.25(a) for stretching vortex tube and Figure 4.25(b) for tilting of vortex tube. We observed that the stretched vortex tube was influenced by the convergence at the lower level, and it remained happened at the multicell boundary, resulting in the increment of vertical vorticity intensity in the multicell compared with single-cell. The tilting of the vortex tube also provided the intense value at the middle height indicating the vertical wind shear that remained happened at the multicell storm.

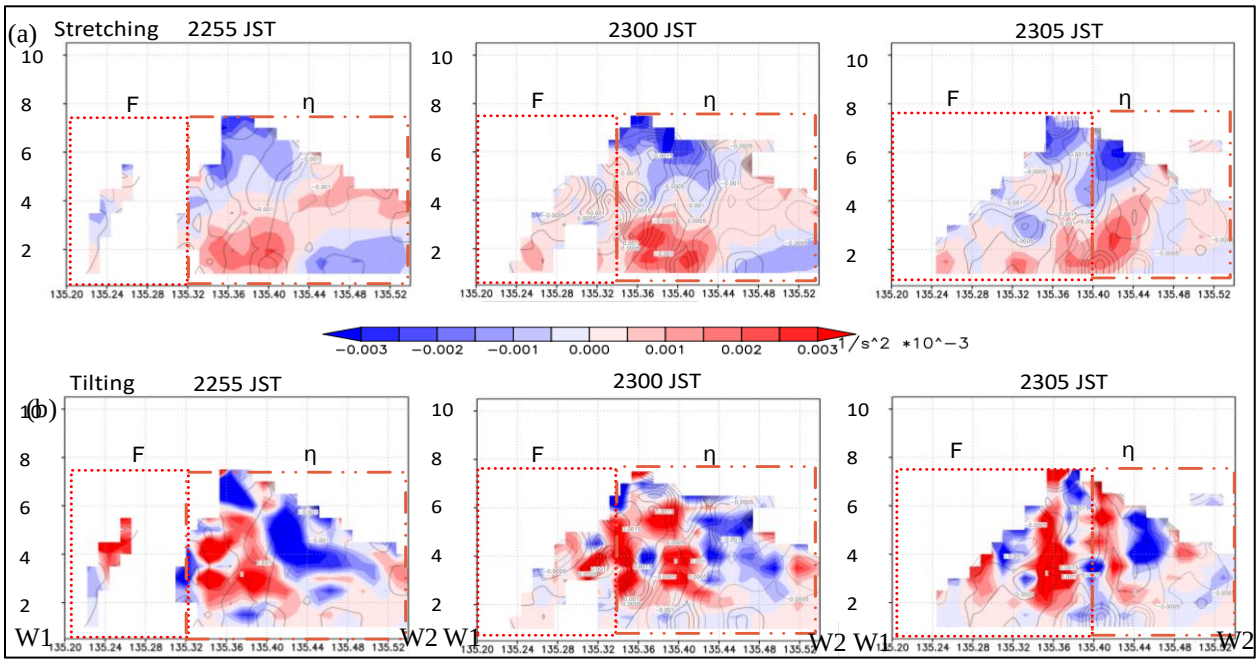

Figure 4.25 Dynamic analysis of cell F and multicell η. (a) Top figure indicates stretching term (b) below figure shows the tilting term.

From both analyses of single-cells A and F, the increment of core vorticity mainly happened because of the merger of two cores with different ages, which the single-cell specified the developing stage, meanwhile the multicell showed the maturing or dissipating stage. Although the vertical vorticity was indicated upon 5-minutes after cells merged, the peak of core vorticity indicated the transition of single-cell to multicell. In addition, the first detection of vertical vorticity could be used as an indicator of maximum rainfall after cells merged. As discussed in Section 4.3.2, we discovered that all single-cells investigated showed the rapid increment of core vorticity after cells merged. This new finding indicated the potential of cell merged could be observed in the time-series of core vorticity analysis before and after merging by observing the first detection of vertical vorticity.

In order to prove the new findings, the lead time detection of peak rainfall was quantified as described in Figure 4.26. The outcome proved that the first detection of vertical vorticity before merged could be utilized to forecast the peak of rainfall after cells merged with the average of 13-minute for DDA vorticity and 17-minutes from pseudo-vorticity analysis from this case study. Therefore, the vertical vorticity method is proved beneficial in the analysis of cells merging, and the potential of heavy rainfall occurrences.

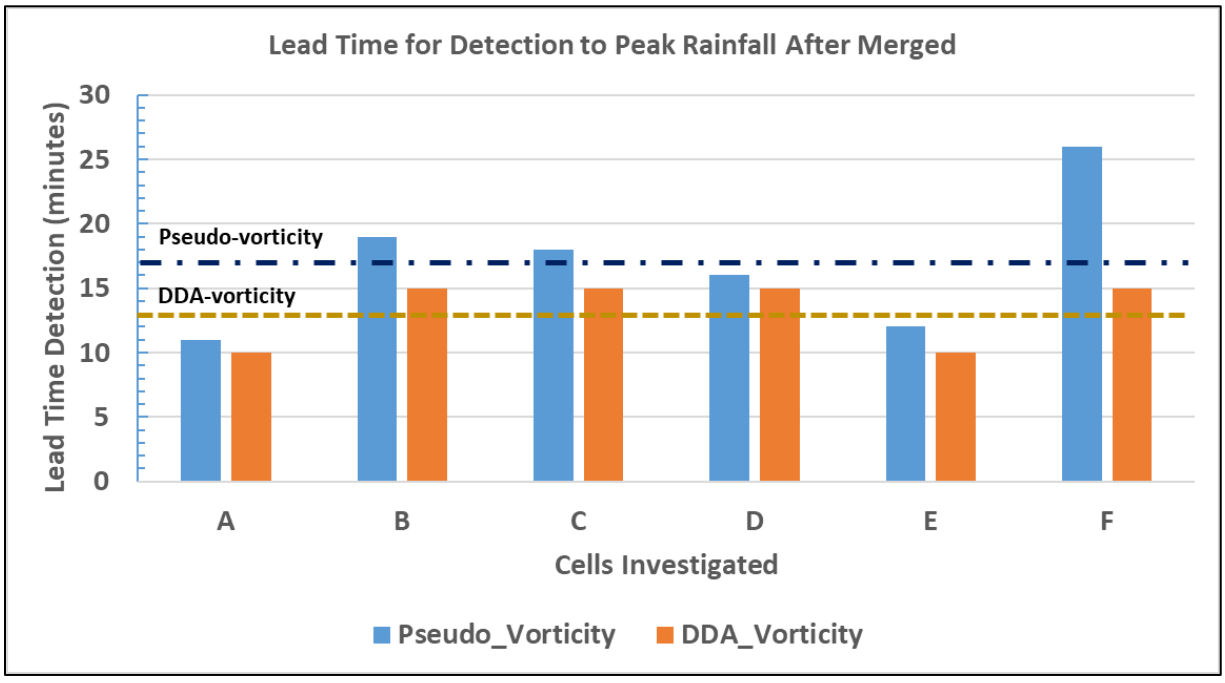

Figure 4.26 Lead time detection of the first detection of vertical vorticity between the peak of core Z_h after cells merged.

ii. Peak of core vorticity intensity and height formation

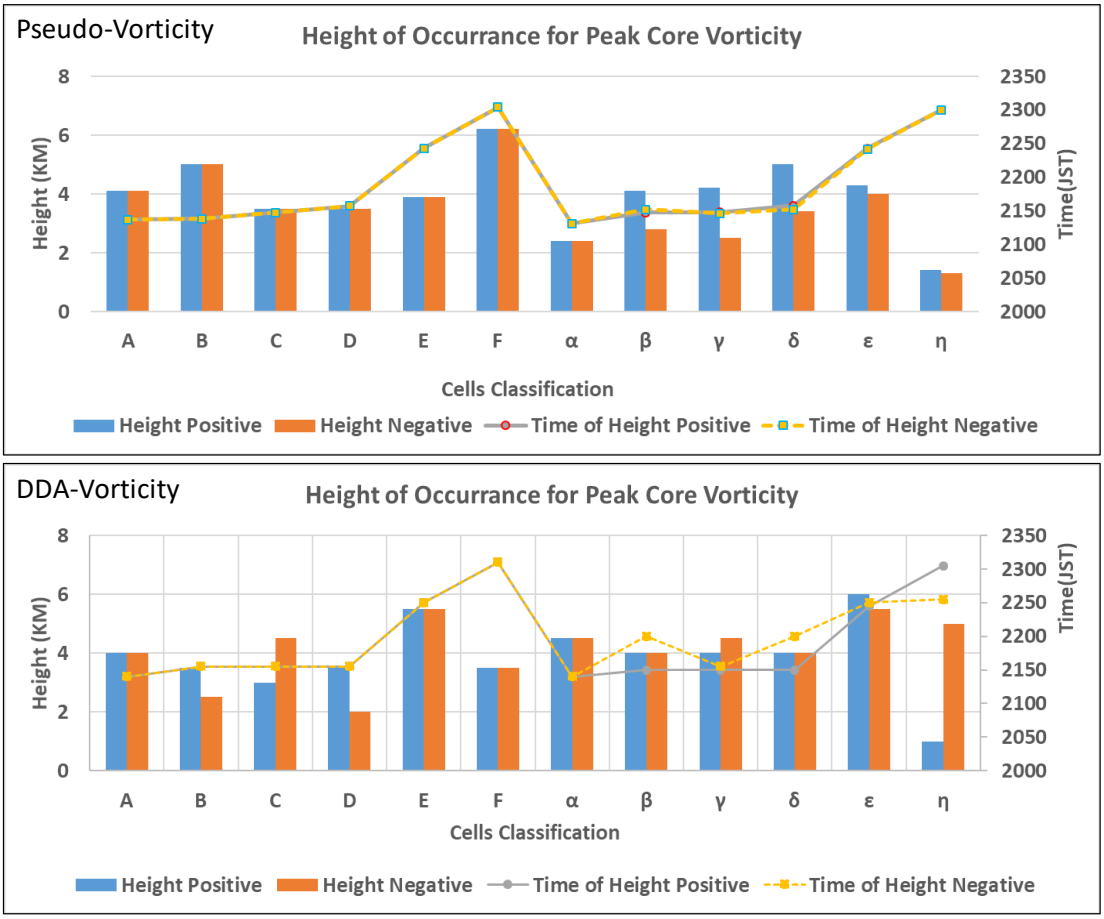

Figure 4.27 The time investigation of formation height and time occurrence of peak core vorticity.

In order to identify the characteristics patterns between single-cell and multicell, we quantify the height formation of peak core vorticity and calculated the average height of peak core vorticity for both methods. The mechanisms that influenced the formation height of peak vorticity will be discussed in this section.

As shown in Figure 4.27, the pseudo-vorticity method could distinguish the height of peak core vorticity between single-cell and multicell. The height of peak core vorticity of positive and negative for single-cells showed a similar height approximately in the range of 3 to 4 km except for cell F. In contrast, the height of peak core vorticity was discovered at various heights which the height of the multicell showed in the range of 2-6 km AGL. The average formation height of single-cell was 4.4 km for both pair core vorticities. In contrast, multicell showed the average formation height was 3.6 km for core positive vorticity and 2.7 km for core negative vorticity.

In the DDA vorticity method, the height of peak core vorticity was observed at a similar height for single-cells A, E, and F, together with multicell α, β, and δ, in the range of 4 to 6 km. There was various height of peak core vorticity that were observed in the single-cell and multicell. The average formation height of single-cell was 3.8 km and 3.7 km for core positive and negative vorticity, respectively. In contrast, the average formation height for multicell was 3.9 km for core positive vorticity and 4.6 km for core negative vorticity. The calculated average formation height for the maximum updraft for single-cell and multicell were 3.9 km, and 4.0 km, respectively. These patterns of formation height of updraft are similar to the height of core vorticity from the DDA method. Thus, the relationship between the height of peak core vorticity intensity and maximum updraft existed in this study.

In terms of the occurrence time of peak core vorticity, the pseudo-vorticity method presented the equivalent period of peak intensity. We could conclude that the pseudo-vorticity can differentiate the characteristics of single-cell and multicell in terms of height and developing time of peak core vorticity intensity due to the high spatial and temporal resolution of estimation. In terms of occurrence time of peak core vorticity, this method revealed a similar period of the developed peak at single-cell only, but not in the multicell. These characteristic patterns are dissimilar to the pseudo-vorticity method. DDA vorticity is not capable to distinguish the pattern of single-cell and multicell owing to the low temporal and spatial resolution. However, we assumed that the peak of core pair vorticity in the single-cell developed at the same period due to the updraft development, meanwhile, in the multicell, it presented the different occurrence peak of pair vorticity due to the updraft and downdraft influenced in the multicell.

As described in Figure 4.28, the time-average of single-cell developed into multicell, which occurred from 2120JST until 2130JST involving single-cells A, B, C, and D, revealed that the vertical vortex tube with the highest positive vorticity magnitude remained happened at the longitude of 135.28°E from 3.5 km until 4.5 km. It was also found that the maximum updraft was positioned adjacent to the position of maximum positive vorticity, and occurred at a similar time at each height. The location of maximum updraft was also identified as located adjacent to the core of positive vorticity, which concluded that the pair of vorticity existed in the multicell development similar to the supercell formation. The magnitude of rotation for multicell was found less than supercell which supercell mainly observed at the highest magnitude of positive vorticity at 0.1 s^{-1}, compared with the multicell attained at 0.005 s^{-1} in this study.

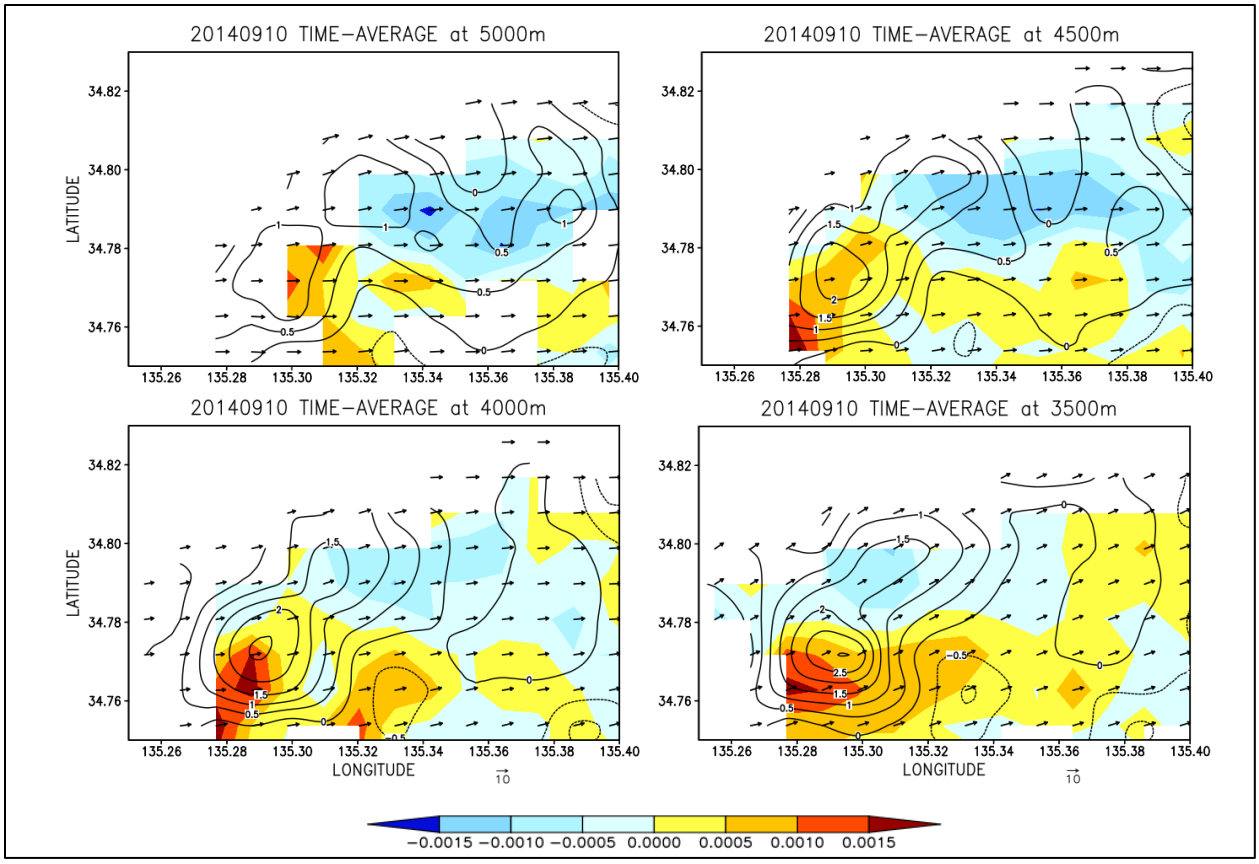

Figure 4.28 The spatial changes of vertical vorticity from 3.5 km to 5.0 km with positive vorticity(red color), and negative vorticity (blue color) shaded region. The solid black contour indicated updraft with an interval of 0.5 m s^{-1}. The dashed black contour specified the downdraft.

iii. Distance Analysis

As discussed in Section 4.3.2, the pseudo-vorticity method could not be utilized in the distance analysis due to its low resolution of estimation. As a result, we evaluated the distance analysis using the DDA vorticity method with respect to the core vorticity intensity, using distance intervals of 5–10 km, 10-15 km, 15-20 km, and 20–25 km. As shown in Figure 4.29(a), the scatterplot show there was a relationship between multicell that affect the intensity of single-cell. Figure 4.29(b) illustrated the pattern of maximum core positive vorticity intensity for single-cells occurring in the range of 5–10 km, however, the intensity of core vorticity showed the lowest value at the furthest distance. The gradually decreasing pattern could be observed in the single-cell over the distance analysis. The minimum intensity values were performed mostly at distance ranging from 20 to 25 km. As a result, in the distance analysis, the core vorticity of a single-cell was

influenced by the multicell at the shortest distance due to the effect of downdraft existed in the multicell as shown previously in Figure 4.19 at 3 km height. For further investigation, the mechanism study is analyzed for the shortest distance (Cell A), and farthest distance (Cell G).

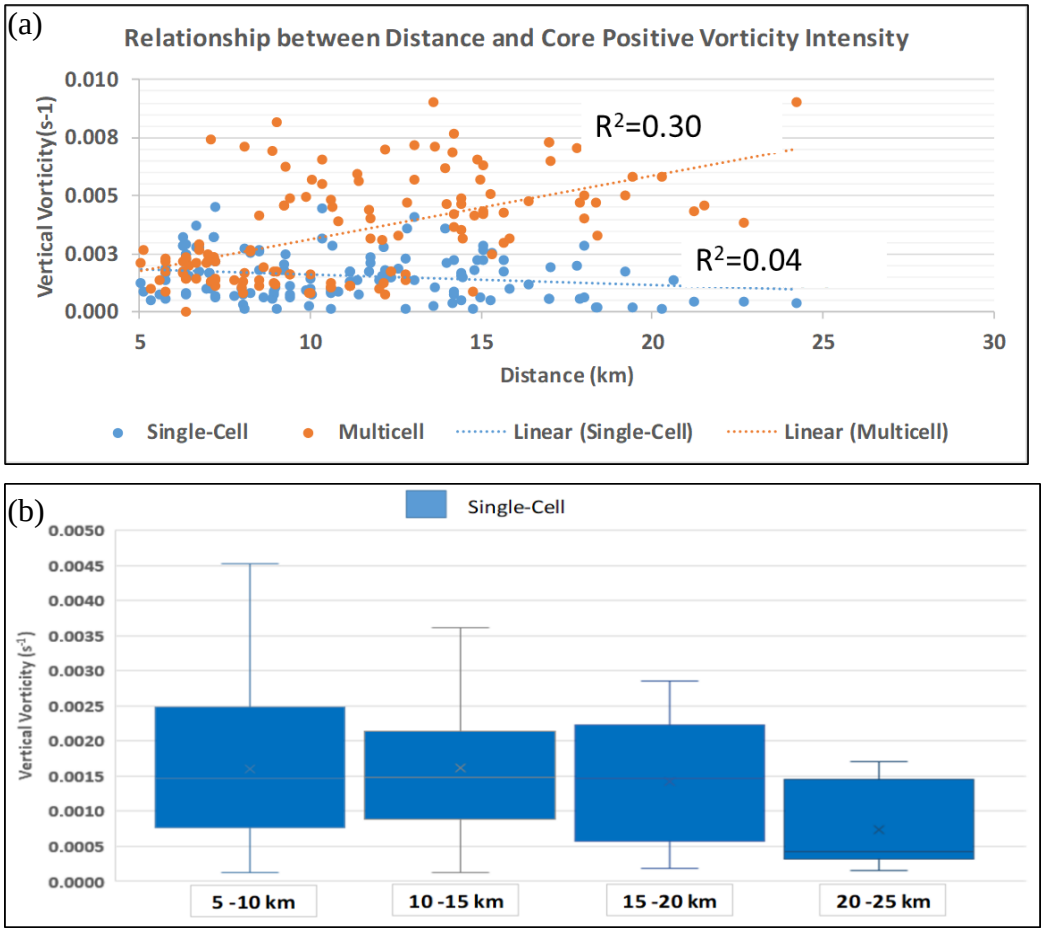

Figure 4.29 (a) Scatterplot relationship between distance and single-cell(blue color) and multicell (orange color). (b) Box-and-whisker plots of core vorticity intensity for new cells and multicell at each distance interval for positive vorticity.

The mechanisms analysis is conducted to investigate the influence of the relationship between multicell and single-cell. It is assumed that the downdraft is mainly the primary factor for the correlation. As noted by Jason et al. (2014), the downdraft could produce positive near-surface vertical vorticity via transportation to the surface in the tornadogenesis studies. In multicell formation, the cell merging process was mostly linked to the increased updraft and downdraft of moist air in the presence of precipitation (Wescott, 1994). The interactions of cells in multicell formation with regard to differential movement and outflow collisions could initiate new cloud

formation (Stalker and Knupp, 2002). Therefore, we discussed the investigation employing the downdraft and divergence in relation to the increment of core positive vorticity intensity.

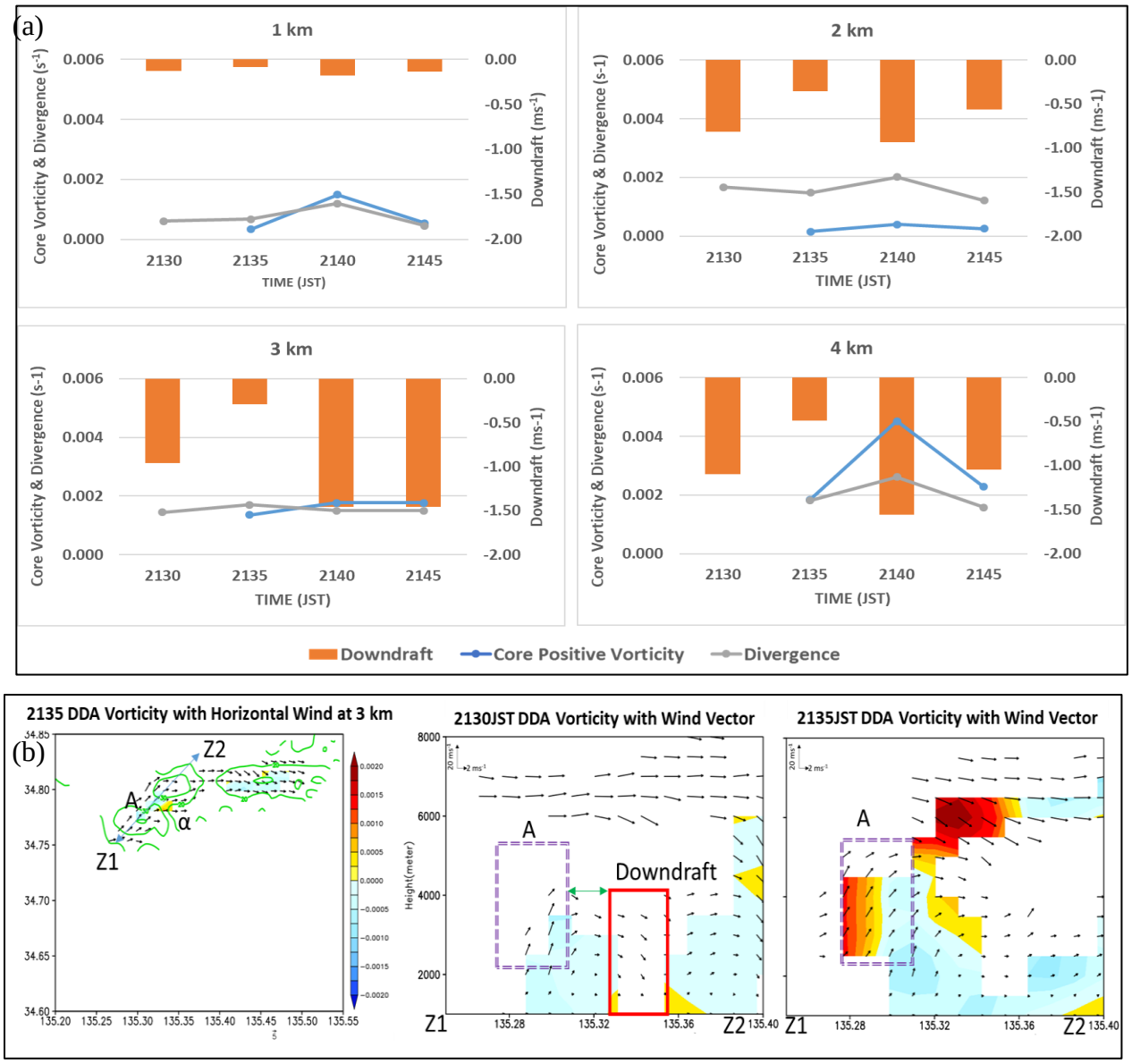

Figure 4.30 (a) The time-series of new cell A for positive vorticity (blue line color) related to the downdraft (orange color column) and divergence (grey line color) from cell α. (b)Vertical cross sections of DDA vorticity with wind vector taken along line Z1-Z2 for single-cell A (dashed purple color) and cell α. The red box indicated the downdraft happened in cell α. Radar reflectivity in interval 10 dBZ is in the green contour line.

From the time-series as shown in Figure 4.30(a), we observed at 2130JST that the maximum downdraft of cell α occurred at the height of 2-4 km, and the divergence that happened slightly at the height of 2 km before the development of the core vorticity. The vertical vorticity of cell A started at 2135JST with the highest intensity at 4 km (0.002 s^{-1}). The peak intensities of core vorticity in the single-cell A indicated that the influence of downdraft position and its interaction with the divergence outflow in the cell α could be an indicator of the influence of the increment of core vorticity in the short distance range as illustrated in Figure 4.30(b).

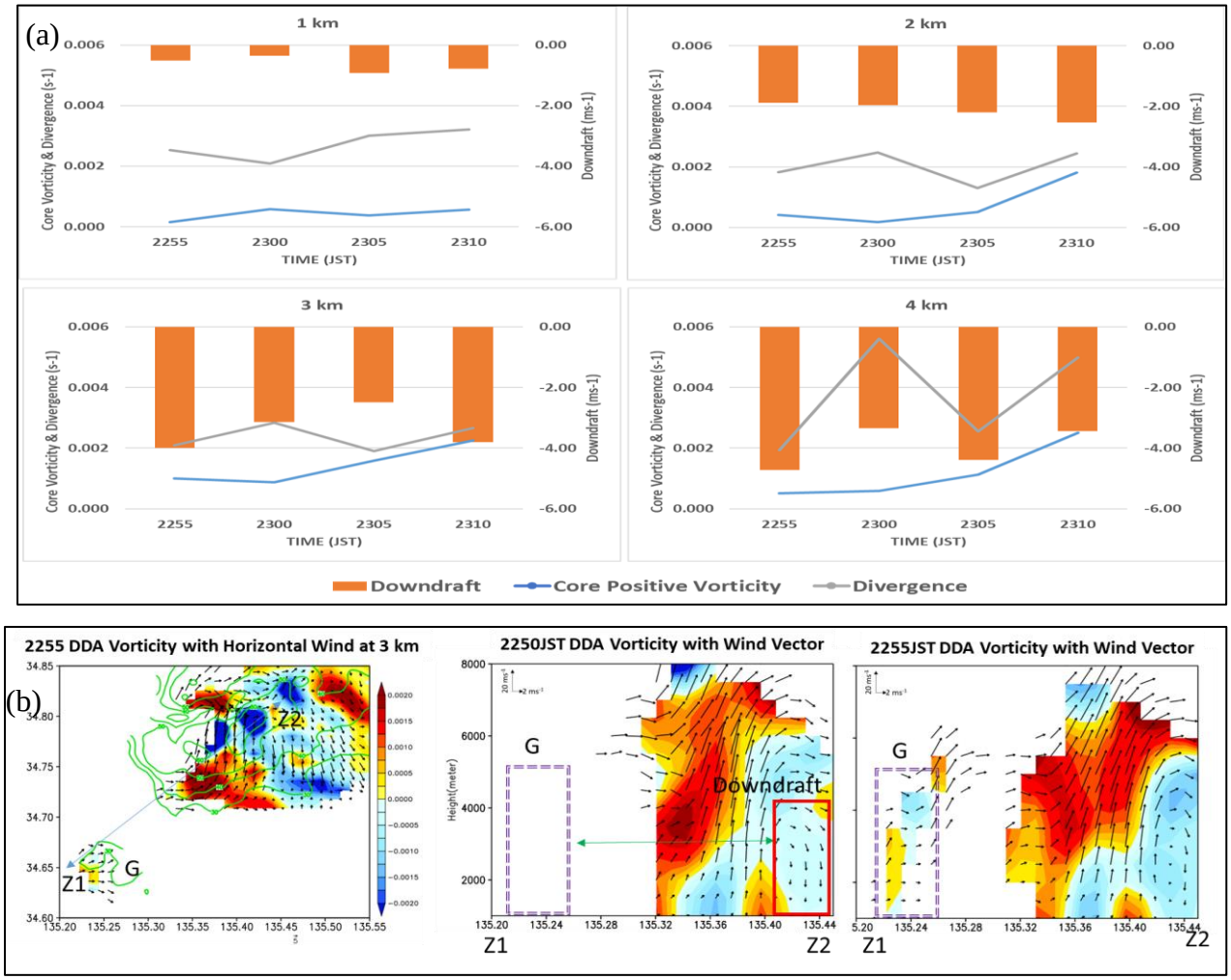

Figure 4.31 (a)The time-series of single-cell F for positive vorticity (blue line color) related to the downdraft (orange color column) and divergence (grey line color) from cell η. (b) Vertical cross sections of DDA vorticity with wind vector taken along line Z1-Z2 for new cell F (dashed purple color) and cell η. The red box indicated the downdraft happened in cell η. Radar reflectivity in interval 10 dBZ is in the green contour line.

As shown in Figure 4.31(a), the downdraft and divergence occurred in cell η at 2255JST, in which the maximum intensities occurred at 3 and 4 km height. The single-cell F that was developed itself, was specified at 0.0014 s^{-1} and -0.0017 s^{-1} at 2255JST, and slightly increased in 15 minutes of observation. Although the downdraft occurred in the older cell, the vertical vorticity revealed less intensity in the longest distance as described in Figure 4.31(b). These new findings are useful to study the vertical vorticity evolution in the multicell formation, in which downdraft and divergence outflow could influence the core vorticity intensity which the most influential distance occurred in the optimal distance of 5 -10 km. The position of the downdraft is the most important in facilitating the development and maintenance of precipitation cells over long periods.

Table 4.4 Correlation coefficient (R^2) between the core vorticity intensity and mechanisms

Mechanisms	Positive Vorticity
Updraft	0.52
Stretching	0.56
Convergence	0.45
Divergence	0.48
Tilting	0.37

Apart from this, we investigated the correlation between the mechanisms and core vorticity intensity using DDA vorticity only because DDA vorticity showed a high estimation compared with pseudo-vorticity as described in Table 4.4. The results showed that updraft and convergence were the main factors in the increment of vorticity intensity with the dynamic mechanism of stretching was the contribution of effect in the vortex tube. The tilting mechanism has a lesser impact on the intensity of the core vorticity because it assists in the position of pair vorticity and remained tilted in the updraft. Figure 4.32 shows the correlation coefficient at each height level for positive vorticity. It showed that stretching and convergence primarily affect the lower level (1–1.5 km). Tilting and updraft lead to an increase in the intensity of the core vorticity in the middle level (2–5 km). Divergence only affects the upper level, which agrees with the rising motion of cloud development.

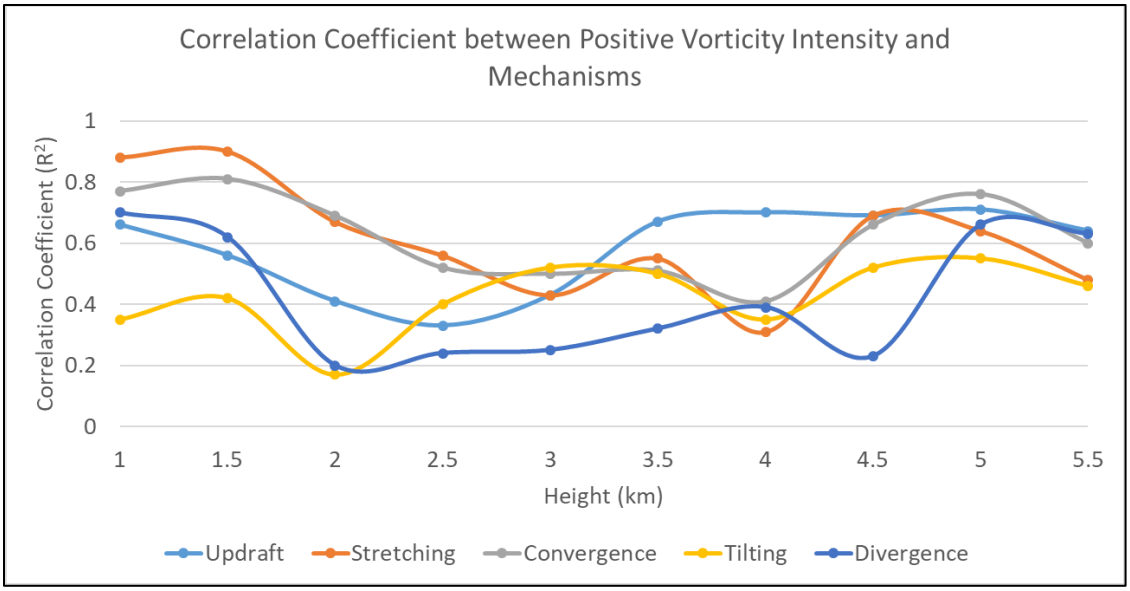

Figure 4.32 The correlation coefficient of core positive vorticity intensity to the height between mechanisms using DDA vorticity.

4.3.4 Theoretical discussion on vortex merger in the transition from single-cell to multicell

In the analysis of single-cell merged into multicell, the study using vertical vorticity was proposed to discover the transition signals from single-cell to multicell thunderstorms. The purpose of our study is to discover the transition signals and characteristics between single-cell and multicell and their mechanism influence. The new single-cell clouds which were developed adjacent to the pre-existing multicell were observed developed in the middle height with the existing pair of vorticities. Meanwhile, the multicell also signified the pair of vorticity inside the clouds. The results revealed the steady increment of core vorticity intensity that happened during the transition and reached the peak after merging. During the transition from single-cell to multicell, the intensity of vertical vorticity intensified steadily before it reached its peak. The study discovered that the average core vorticity intensity before merging indicated a double peak after merging for both pseudo- and DDA vorticity analysis.

In the qualitative analysis in Section 4.3.3, the analysis revealed the low-level convergence to be mainly the result of the increment of the magnitude of vertical vorticity. As for the relationship between vertical vorticity and low-level convergence, the vortices observed in our study intensifies along with the low-level convergence within them intensified. This is probably associated with intensifying convergence and thus intensifying of the vortex tube. With the

convergence, the stretched vortex tube was identified as a contributing factor in the increase of the vertical vorticity intensity as illustrated below:

Consider a column with pre-existing cyclonic relative vorticity,

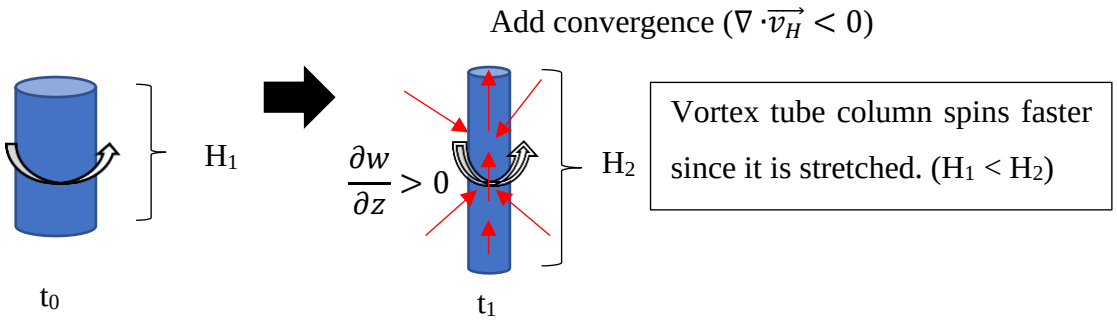

Furthermore, the tilting term analyzed in this study revealed the gradient of vertical velocity happened mostly at the middle-level height. The tilting term might be contributed to the increment of core vorticity from time to time since the horizontal vortex tube that was generated at the lower-level height remained tilted to the vertical. The merged updraft might be influencing the tilting of the vortex tube probably influenced in the transition from single-cell to multicell. The cyclonic vorticity was generated at the left side of the updraft and remained located near the updraft position resulting in the enhancement of vorticity intensity. Therefore, in this section, we will discuss the theoretical underpinnings of characteristics of single-cell that merged into multicell thunderstorms based on the vertical vorticity equation.

The local change of the vertical vorticity in the single-cell research by Nakakita et al., (2017) used the equation of tilting term and stretching term in their study to identify characteristics of single-cell with the sign of pair vorticity. The equation used was:

$$\frac{d\zeta}{dt} = \underbrace{\left(\frac{\partial w}{\partial y}\frac{\partial u}{\partial z} - \frac{\partial w}{\partial x}\frac{\partial v}{\partial z}\right)}_{\text{tilting}} - \underbrace{\zeta\left(\frac{\partial u}{\partial x} + \frac{\partial v}{\partial y}\right)}_{\text{stretching}} \qquad (4.6)$$

where ζ is the vertical vorticity, and u, v, and w are the velocity components retrieved from DDA.

This equation is basically used to understand the dynamics of low-level mesocyclones and tornadoes. Firstly, by considering the tilting term, the horizontal vorticity is generated by the vertical wind shear tilted into the vertical by a horizontal gradient of w. The schematic illustration is as follows:

a) Suppose *v* is increasing with height ($\frac{\partial v}{\partial z} > 0$) and *w* is varying with *x* ($\frac{\partial w}{\partial x} > 0$), the wind becomes increasingly southerly with height

1)

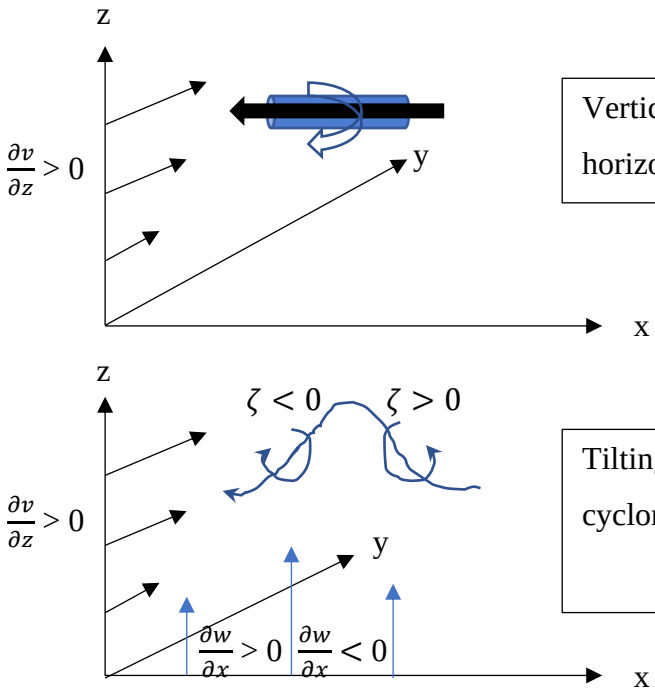

Vertical wind shear creates horizontal vortex tube

Tilting of vortex tube creates cyclonic or anticyclonic vorticity

b) Suppose *u* is increasing with height ($\frac{\partial u}{\partial z} > 0$) and *w* is varying with *y* ($\frac{\partial w}{\partial y} > 0$), the wind becomes increasingly westerly with height

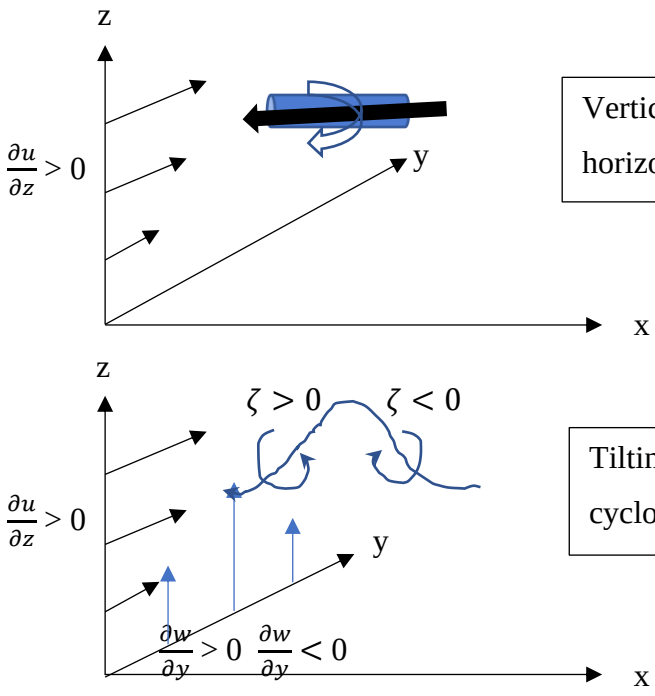

Vertical wind shear creates horizontal vortex tube

Tilting of vortex tube creates cyclonic or anticyclonic vorticity

Next, we consider the stretching term. The stretching term is composed of the divergence term and the vertical vorticity.

From the continuity equation,

$$\frac{1}{\rho}\frac{dp}{dt} = -\nabla \cdot \vec{v} = -\left(\frac{\partial u}{\partial x} + \frac{\partial v}{\partial y} + \frac{\partial w}{\partial z}\right) \qquad (4.7)$$

where ρ is the density and p is the pressure.

For incompressible flow, $\frac{dp}{dt} = 0$

$$-\nabla \cdot \overrightarrow{v_H} = -\left(\frac{\partial u}{\partial x} + \frac{\partial v}{\partial y}\right) = \frac{\partial w}{\partial z} \qquad (4.8)$$

$$\left(\frac{\partial u}{\partial x} + \frac{\partial v}{\partial y}\right) = -\frac{\partial w}{\partial z} \qquad (4.9)$$

The stretching term showed that the spin-up of vorticity is proportional to the convergence. This might explain the rapid development of many strongly rotating cyclonic systems. The rate of vorticity growth is proportional to the vorticity itself. With the horizontal convergence of air, the enhancement of spin due to the conservation of angular momentum when fluids are compressed can further amplify aloft vortices. In summary, for an incompressible fluid,

$$\nabla \cdot \overrightarrow{v_H} < 0 \rightarrow \frac{\partial w}{\partial z} > 0 : stretching$$

$$\nabla \cdot \overrightarrow{v_H} > 0 \rightarrow \frac{\partial w}{\partial z} < 0 : shrinking$$

Consequently, we will verify the theoretical used as discussed above in the vortex merger between the single-cell and multicell related to the stretching and tilting of the vortex tube. The mechanisms that amplify the intensity of vertical vorticity were mainly studied and agreed that low-level convergence is the primary mechanism in vertical vorticity (Shapiro et al., 1999; Markowshi and Hannon, 2006; Dahl et al., 2017). The stretching term is composed of the divergence term and the vertical vorticity. Furthermore, the increment of core vorticity from time to time might be influenced by the tilting term. The horizontal vortex tube will be tilted to the vertical vortex tube with the sign of pair vorticity depending on the environmental wind shear.

For example, in our analysis, single-cell A showed a higher increment than other single-cells. At the time of 2135JST, the peak of vertical vorticity for single-cell A at 2.5 km was 0.0023 s^{-1}, and the existing multicell α was 0.0017 s^{-1} at a height of 4.0 km. The tilting and stretching of the vortex tube for single-cell A was 2.49 x 10^{-6} s^{-2} and 2.94 x 10^{-6} s^{-2} at 2135JST compared with multicell α was 1.7 x 10^{-6} s^{-2} and 7.9 x 10^{-6} s^{-2}, respectively. At 2140JST after merging, single-cell A exhibited 0.005 s^{-1} at a height of 4.0 km and multicell α showed the peak of vertical vorticity intensity at 0.003 at the height of 4.5 km. The single-cell A showed the tilting of the vortex tube was 5.14 x 10^{-6} s^{-2} and 1.49 x 10^{-6} s^{-2} for stretching of the vortex tube. Meanwhile, multicell α was 7.99 x 10^{-6} s^{-2} and 3.26 x 10^{-6} s^{-2} for tilting and stretching of the vortex tube.

While comparing the convergence values, at the time at 2135JST, the value of single-A was 0.0017 s^{-1} at a height of 2.5 km and for multicell was highest at 6 km height at 0.0011 s^{-1} indicating the convergence aloft and divergence at the lower-level. From the convergence value at every height, the existing cells could be known as be maturing stage, developing stage, and maturing stage. At 2140JST, the convergence of single-cell A showed higher at 3.5 km with a value of 0.0023 s^{-1}, and multicell at 2.0 km with a value of 0.0021 s^{-1}. At this time, the merged vortices revealed that the existing multicell which is in the dissipating stage could be increased a little due to the small convergence that affected the stretched vortex tube. Meanwhile, the cell which was newly developed will be largely increased in which the convergence intensity could be one of the factors increment in the merged vortices.

The local change of vertical vorticity could be influenced by the stretching and tilting of vortex tube in the transition from single-cell to multicell and inside the multicell too needed to be understood. Therefore, in this study, we want to understand the theoretical in terms of stretching and tilting despite many researchers found that low-level convergence influenced in the stretched of the vortex tube. From this analysis of vortices merger, we could see the increment of core vorticity due to the existence of convergence that stretched the vortex tube. Two vortices at the same sign (orientation) with (almost) parallel axes, within a certain distance, mix (merge) a substantial portion of their core vorticity into a single vortex (P.Meunier et al., 2005).

In addition, we could observe the height of peak core vorticity also changed from time to time. The transition signals in terms of height could be observed when checking the peak of vertical vorticity. The peak of vortices could be related to the increase of rotation owing to the stretched of vortex tubes due to the existence of convergence. This process is well-understood in the supercell

thunderstorm, and we could apply it in the single-cell that transformed into a multicell. Since the local change of vorticity is related also to the tilting term, we will examine the contribution of the tilting term in the merging vortices.

According to equation (4.6), the tilting term can express the vertical wind shear that produces the sign of positive and negative. The results discovered that the tilting of the vortex tube always presented with the highest intensity at the middle-level height. It might be represented the core of positive and negative vorticity remained at the middle-level height due to the development and merging of the updraft. The updrafts caused the tilting of the horizontal vortex tube resulting in the increase and maintenance of vertical vorticity (Markowski and Hannon, 2006). The multicell formation commonly did not need the strong vertical wind shear such as supercell, therefore, the weak vertical shear was able to trigger the development of multicell development.

From our study, we also discovered that the cells developed adjacent to the multicell thunderstorms were influenced by the horizontal vorticity that was developed from the downdraft in the multicell. However, the most significant results obtained from our study was the optimal distance that influenced the vertical vorticity at single-cell that merged into multicell in the range of 5 km – 10 km. The downdraft as mainly analyze in the tornado study, signified that the downdraft could advect the vertical vorticity to the surface and contributed to the largest intensity. Therefore, we could conclude that the downdraft in our study also influences in the merging vortices of single-cell and multicell, in which the shortest distance influence the more intensifying of core vorticity intensities.

In addition, the finding that we obtained from the merging analysis showed that the positive vorticity always merged with the same sign of vorticity, which the sign of positive vorticity located at the left side of updraft and negative vorticity situated at the right side of updraft as shown in the schematic analysis in Figure 4.33. We observed that the sign of positive and negative vorticity always showed equal signs of vortices for single-cell and multicell thunderstorms when cells started to merge. The vortex with the largest magnitude of vorticity will be advected faster than the smallest magnitude of vorticity. These transition signals quantified that the existence of vertical wind shear might be determined from this signal.

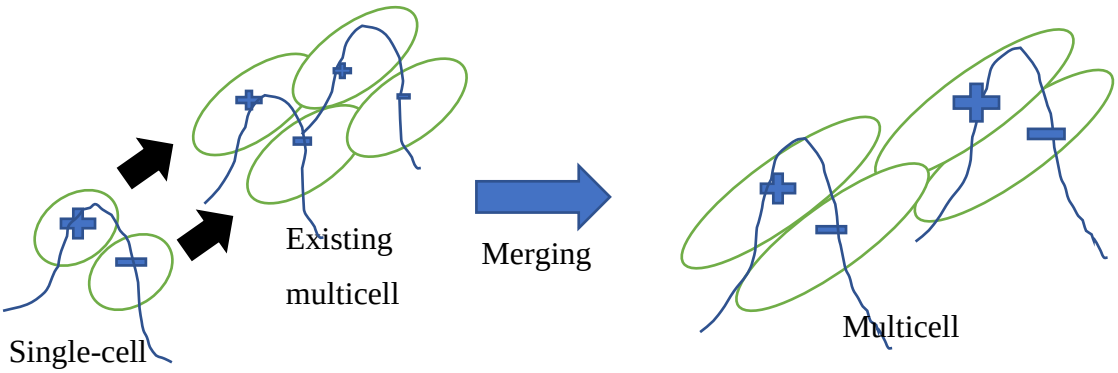

Figure 4.33 Schematic illustration of the same sign of vorticities between single-cell and multicell.

From the sign of vorticity, we could know the vertical wind shear from the tilting term of the vorticity equation as follow:

$$\frac{d\zeta}{dt} = \underbrace{\xi\frac{\partial w}{\partial x} + \eta\frac{\partial w}{\partial y}}_{\text{tilting}} + \underbrace{\zeta\frac{\partial w}{\partial z}}_{\text{stretching}} \qquad (4.10)$$

where (ξ, η, ζ) are vorticities in the (x,y,z) direction, respectively and w is the z-component of velocity. The first two terms of the right-hand side of the equation indicate the tilting motion of a horizontal vortex tube by a vertical shear of the horizontal wind.

If we assume the horizontal vorticity is zero, then

$$\xi = \frac{\partial w}{\partial y} - \frac{\partial v}{\partial z} = 0 \Rightarrow \frac{\partial w}{\partial y} = \frac{\partial v}{\partial z} \;\; and \;\; \eta = \frac{\partial u}{\partial z} - \frac{\partial w}{\partial x} = 0 \Rightarrow \frac{\partial w}{\partial x} = \frac{\partial u}{\partial z}$$

where u is the zonal wind which is positive when blows from the west and negative if from the east, and v is the meridional wind which is positive when blows from the south and negative if from the north.

From our study, we concluded that the local change of vertical vorticity in terms of tilting term and stretching term could be specified in the merging process of the vortices. Consequently, the single-cell that was developed adjacent to the multicell showed its characteristics with the presence of a pair of vorticity, developed inside the cell and the multicell showed the existence of a vertical vortex tube with the pair of vorticity. With the same sign of vorticity, we discovered that the single-cell will be merged into the multicell which the highest intensity will remain longer into the intensifying thunderstorms. In addition, the height of peak core vorticity changed from time to time indicating the stretched and tilted vortex tube that influenced the merging process.

4.3.5 Comparison between DDA and pseudo-vorticity analysis

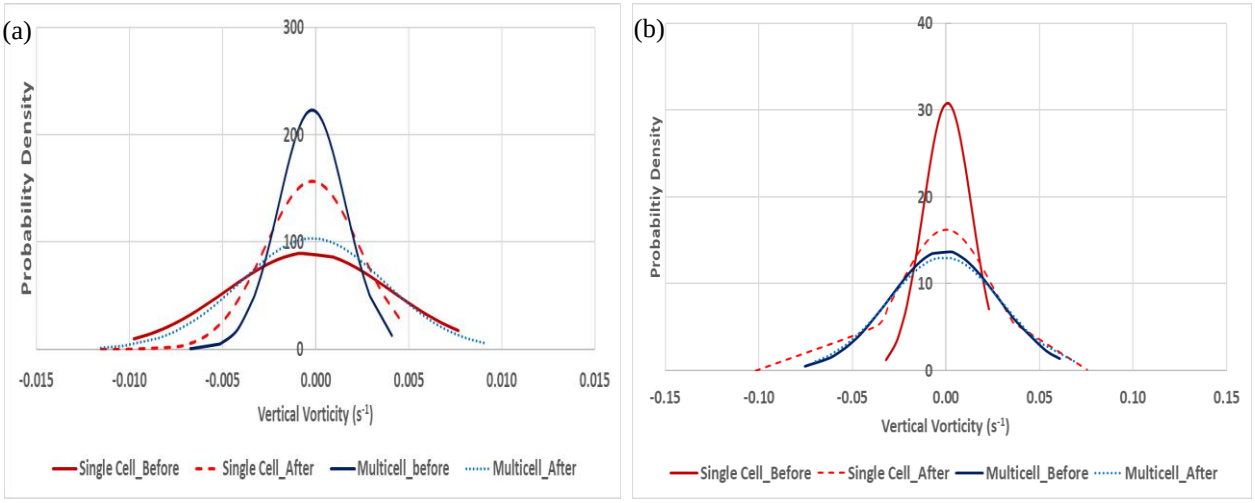

Figure 4.34 Probability density distribution of single-cell and multicell core vorticity intensity for (a) DDA vertical vorticity (b) pseudo vertical vorticity.

The intensity values of core vorticity from pseudo-vorticity are approximately ten times higher than that derived from DDA vorticity. From Figure 4.34(a), DDA showed the probability density of single-cell compared with the multicell. The results revealed that the probability density of positive vorticity of single-cell was not larger than 0.005 s^{-1}, whilst the multicell specified almost 0.09 s^{-1}. Here, we emphasized on the positive vorticity (cyclonic rotation) due to the significance of the inflow of air mass into the storm rather than negative vorticity (anticyclonic rotation). A study by Geng et al., (1997), in the meso-β-scale convective system (MCS), they found the maximum magnitude of the vorticity was 7.6 x 10^{-3} s^{-1} at the mid-level during the development stage of the system using dual-Doppler analysis in the spatial resolution of 0.5 km x 0.5 km x 0.25 (height of 0.25 km-2 km, 0.5 km at the altitude above 2 km). Therefore, we assumed that the threshold of DDA vorticity of multicell could be attained to 0.005 s^{-1}, slightly below than the maximum magnitude of the MCS system. The outcomes discovered that after the merging process, both intensities of single-cell and multicell increased.

In Figure 4.34(b), the pseudo-vorticity presented a different pattern of probability density, with the highest intensity value owned by the single-cell, and multicell showed the lowest core vorticity intensity. This pattern is different from the outcome of DDA vorticity, which clarified that the pseudo-vorticity able to detect the precise of single-cell development due to its highest spatial and temporal resolution. Moreover, the analysis using pseudo-vorticity did not show

significantly on the multicell before and after merged. The single-cell exhibited the pattern of increment mostly similar to the multicell distribution, indicating that the intensity of vertical vorticity will be increased and its characteristics almost similar to the multicell.

Additionally, the DDA intensity exhibited the average core vorticity of single-cell at 0.004 s^{-1} and multicell at 0.005 s^{-1}. Meanwhile, in the pseudo-vorticity analysis, the average core vorticity intensity for single-cell and multicell was revealed at 0.04 s^{-1}. As listed in Table 4.1, the average intensity of core vertical vorticity before single-cells transformed into multicell was 0.002 s^{-1} and 0.02 s^{-1} for DDA and pseudo-vorticity, respectively. From these findings, it is reasonable to assume the transition signals from single-cell to multicell between 0.002 s^{-1} until 0.004 s^{-1} which this new criterion index applied in DDA analysis, and 0.02 s^{-1} until 0.04 s^{-1} for pseudo-vorticity. In contrast, the findings showed the average magnitude of vertical vorticity for multicell formation was 0.005 s^{-1}, which was lower than the MCS system using dual-Doppler analysis, and 0.04 s^{-1} based on pseudo-vorticity analysis as discussed previously.

Table 4.5 The comparison of vertical vorticity analysis from pseudo-vorticity and vertical vorticity

Patterns	Pseudo-Vorticity	DDA Vorticity	Reason
A	✓	✓	All methods showed the same pattern of peak intensity after merged
B	✓	✓	First detection of vertical vorticity available to predict the peak rainfall after merged
C	✓	✓	Vertical vorticity able to characterize the feature of single-cell and multicell
D	✓	✗	The coarse temporal and spatial resolution effect on the selection height of peak intensity
E	✗	✓	Lower estimation from pseudo-vorticity effect on the distance analysis between single-cell to multicell

A:	the transition signals showed the peak of vorticity intensity after merged
B:	predict the peak of rainfall after merged in lead-time of 10 minutes
C:	characterize the single-cell and multicell based on time of occurrence
D:	characterize the single-cell and multicell based on height of peak intensity
E:	analyze the distance effect of single-cell to multicell

Based on these results, we could conclude that DDA vorticity is able to discriminate the intensity of vertical vorticity between single-cell and multicell owing to the highest estimation from the exact formula itself. Pseudo-vorticity, on the other hand, has the best temporal and spatial resolution for describing single-cell and multicell storms based on height and time of occurrence. We determined that in the comparison of pseudo-vorticity and DDA vorticity analysis, where each method has its own advantages, the vertical vorticity is solely utilized in the short-term precipitation forecast as an analysis of the transition from single-cell to multicell development. The summary of the comparison using two methods of vertical vorticity is listed in Table 4.5.

4.4 Conclusions

In this study, the analysis of transition signals from single-cell to multicell was investigated based on a two-hour observation on 10 September 2014 using pseudo-vorticity and dual-Doppler vorticity analyses. The kinematic and dynamic mechanisms that controlled the characteristic patterns of the core vorticity intensity, its peak, and formation height including the distance analysis were determined by investigating the updraft or downdraft, convergence or divergence, stretching, and tilting of the vortex tube.

In terms of core vorticity intensity distribution, the core vorticity of single-cell increased after the merging process with the single-cell intensity is higher than that of the older cell at the early stage. In the meantime, the multicell revealed the highest intensity at the latter stage of multicell formation. The DDA intensity exhibited the average core vorticity of single-cell at 0.004 s^{-1} and multicell at 0.005 s^{-1}. Meanwhile, in the pseudo-vorticity analysis, the average core vorticity intensity for single-cell and multicell was revealed at 0.04 s^{-1}. From this new finding, and the highest resolution of DDA estimation, the threshold of core vorticity intensity suggested for single-cell transformed into multicell at the range of 0.002 s^{-1} to 0.004 s^{-1}. The magnitude of vorticity for the multicell cluster storms was indicated approximately at 0.005 s^{-1}. The new threshold discovered from this analysis could be utilized in the detection of hazardous cells and the potential of merging cells since the indicator was not larger than 0.010 s^{-1} which was indicated as supercell thunderstorms. However, another supplementary factor such as vertical wind shear of the cells should be considered.

The study discovered that single-cells revealed a peak of core vorticity intensity after merging with pre-existing cells. The results of the height and time occurrence formation of peak core vorticity using pseudo-vorticity could distinguish the characteristic between single-cell and multicell due to its finest temporal and spatial resolution. The average formation height of single-cell for pair vorticity was 4.4 km calculated from the pseudo-vorticity method, compared with DDA, which showed the different heights of formation (3.8 km and 3.7 km) for positive and negative vorticity respectively. In addition, the pseudo-vorticity method indicated the average formation height of multicell was (3.8 km for positive vorticity, 2.7 km for negative vorticity), and (3.9 km for positive vorticity, 4.6 km for negative vorticity) based on DDA. From this finding, we could conclude that on average the single-cell showed the formation height of peak vorticity intensity at 4 km, and multicell slightly above 4.0 km. The results revealed the height of peak vorticity is mainly affected by the strength of the updraft. The frequent distribution of maximum updraft for multicell was revealed at a height of 4 km for intensity larger than 5 m s^{-1} and maximum downdraft with a strength greater than -1 m s^{-1} was observed at 1 km AGL. From our analysis, the average updraft velocities for the single-cell and multicell were 1.9 and 3.9 m s^{-1} respectively, and the average downdraft velocities were 0.7 and 1.4 m s^{-1}, respectively.

However, DDA vorticity showed similarities in time occurrence in single-cell, and differences in multicell. The time of peak was investigated related to the updraft strength and the height of the maximum updraft. The peak of these vorticities related to the convergence at the lower level influenced the updraft position, updraft strength, and wind motion. The convergence at a lower level also influenced the stretched of the vertical vortex tube and the amplification of vorticity intensity that occurred. The lead time forecast for the detection of peak rainfall could be developed by employing the peak of core vorticity. It was observed that the average of time detection of peak rainfall with the peak of core vorticity intensity was approximately 17 minutes, and 13 minutes for pseudo-vorticity and DDA vorticity, respectively.

In this study, the distance analysis of the same sign of core vorticity using DDA vorticity presented the best analysis compared with pseudo-vorticity owing to the high resolution of estimation. The results discovered that the existence of a relationship between multicell to single-cell at the shortest distance with the optimal distance was in the range of 5-10 km resulting in the strongest core vorticity intensity. The mechanisms analysis quantified that the downdraft and divergence affect the core vorticity strength at the shortest distance compared to the longest

distance. The distance and position of updraft and downdraft were the most important in facilitating the development and maintenance of precipitation cells over long periods.

From the mechanism analysis, with the existence of the updraft, the horizontal vorticity would be tilted into the vertical vorticity. We found that the vertical vorticity mostly developed at the middle level for the new cells, parallel to the position of the updraft and generation of wind motion in the clouds. Due to the strength of the updraft and convergence, various heights were observed for the core vorticity of the new cells. The tilting of the vortex tube was influenced mostly at the middle level, similarly to the updraft position. These findings help us for a better understanding of the characteristics of single-cells that developed in multicell thunderstorms. In conclusion, the vertical vorticity is able to present the transition of cell merging process between single-cell and multicell, in terms of occurrence of peak, height, and time development of core vorticity. The transition signals help us to forecast the peak of rainfall after cells merged, and the threshold of single-cell merged discovered at the range of 0.002 s^{-1} to 0.004 s^{-1} with the optimal distance in the range of 5-10 km could be more influenced by the multicell characteristics. It is recommended to differentiate the criteria of transition from the first development of single-cell to multicell and compared with the cells that are not merged to facilitate forecasts of the severity of thunderstorms and cell merging in the multicell environment conditions.

For future works, it is suggested to integrate the multi-polarimetric radar analysis with vertical vorticity analysis because of the advantages of multi-parameter radar analysis in the detection of hazardous clouds and the signature patterns of supercell characteristics. In the meantime, these radar parameters also specified the updraft strength. Basically, the vertical vorticity is associated with the updraft intensity. Therefore, this integration could be beneficial in the understanding of kinematic mechanisms and microphysical studies in the cells merging. The characteristics of the single-cell-to-multicell case, and single-cell not merged case using multi-parameter radar analysis are expected to improve the short-term precipitation forecast in the determination of the transition signals from single-cell to multicell.

CHAPTER 5

5 Polarimetric Characteristics of Transition from Single-cell to Multicell Thunderstorms with Vertical Vorticity Analysis

Abstract

The development of characteristic patterns of a single-cell to multicell thunderstorms was developed by using a multi-parameter radar analysis. The differential reflectivity (Z_{dr}) column and specific differential phase (K_{dp}) column were further investigated, including the analysis of vertical vorticity from a dual-Doppler method. The kinematic mechanism analysis using a dual-Doppler radar was also examined in this study. From the evolution of cells investigation, the convergence was observed before the initiation of the updraft. The peak of updraft and core vorticity intensity were identical in their stage of development, whereby radar reflectivity indicated the increment after the cells merged. During the transition, the characteristic patterns were observed on the increment of positive core vorticity and K_{dp} at 2 km and 5 km of Constant Altitude Plan Position Indicator (CAPPI) height, respectively, at the same position. The Z_{dr} column was not observed after the cell merging; however, it was identified 5 min after the cell had merged. In contrast, the K_{dp} column was always identified after the cell merging, and the column showed an increment of intensity 5 min after the cells had merged. The positions of both Z_{dr} and K_{dp} columns were located parallel with the location of the updraft. The results indicated a strong correlation of a maximum K_{dp} column depth above the melting height with the core positive vorticity, especially in the single-to-multicell case. Analysis of K_{dp} columns depth revealed the signatures of changing of updraft in the multicell development. The increased updraft intensity was mainly associated with an increase in vertical vorticity. With precipitation, the maximum K_{dp} column depth is a good indicator for deep convection updrafts, as the life phases of multicell development were controlled by updrafts, and the warm moist inflow from low-level.

5.1 Overview

The investigation of the transition from single-cell to multicell studies is crucial in flood forecasting and severe warnings dissemination. The localized heavy rainfall from the multicell storms can contribute to catastrophic disasters such as floods and landslides. Commonly, the lifetime of a multicell is more than one hour, and a single-cell typically less than one hour. Therefore, it is important to predict the severity before the initiation and peak detection of hazardous clouds as early as possible for the flood warning systems. In a previous study (Adachi et al., 2013), the detection of hazardous clouds was investigated by utilizing dual-polarization radar parameters such as differential reflectivity (Z_{dr}) and specific differential phase (K_{dp}). Using Z_{dr} column, it was clearly revealed the high Z_{dr} column formed 10 min prior to the onset of heavy rainfall on the ground. In addition, both Z_{dr} columns and K_{dp} columns successfully in the detection of the updraft (Kumjian et al. 2014; van Lier, et.al, 2016). The study of supercell characteristics mostly investigated the existence of Z_{dr} arc, Z_{dr} column, and K_{dp} column. It was observed that the Z_{dr} column appeared one hour before the formation of the Z_{dr} arc in the tornadogenesis, and Z_{dr} signatures of supercell storm persisted for half and an hour (Suzuki et al., 2018).

The research is motivated by the advantages of multi-parameter radar analysis in the detection of hazardous clouds and signature patterns of supercell characteristics. As a result, the multicell characteristics based on Z_{dr} and K_{dp} columns will be examined in this study. This study aimed to discover the polarimetric transition signals from single-cell to multicell by adapting the methodology of multi-parameter radar analysis. To quantify the effect of mechanisms influenced on the cells' development, the kinematic mechanisms and vertical vorticity analysis will be compared for investigating the relationship with the potential of cell merging induced heavy precipitation. The analysis of the DDA method from the previous chapter revealed that the potential of single-cell to multicell for core positive vorticity was discovered in the range of 0.002 s^{-1} to 0.004 s^{-1}. Therefore, this study will verify in the case of single-cell not merged into multicell. To differentiate the characteristics and factors that influence the merged of cells, the environment condition, and polarimetric characteristics will be investigated. Therefore, the study on polarimetric for detection of potential heavy rainfall in multicell thunderstorms could provide insight into the understanding of the transition patterns to multicell characteristics from the initiation stage to the development stage of occurrence of heavy rainfall for single-cell.

5.2 Methodology

5.2.1 Classification of cells

In this study, the events were divided into three cases to investigate the polarimetric characteristics of single-cells merged, multicell, and single-cell not merged in the multicell environment condition. The selection events were chosen on the 13th of August 2018 and the 25th of July 2019. The detail of the environmental condition could be referred to in Section 2.3.2 and Section 2.3.3. Firstly, the images of Z_h at 2 km CAPPI height were compared to define the characteristics of the development of the single-cell (hereinafter referred to as "SC"), multicell (hereinafter referred to as "MC") and single-cell not merging (hereinafter referred to as "SCNM"). In this study, we focused on the first development of single-cell and observed whether the cell was more developed and merged into multicell or not. The criteria of cells investigated will be discussed as follow.

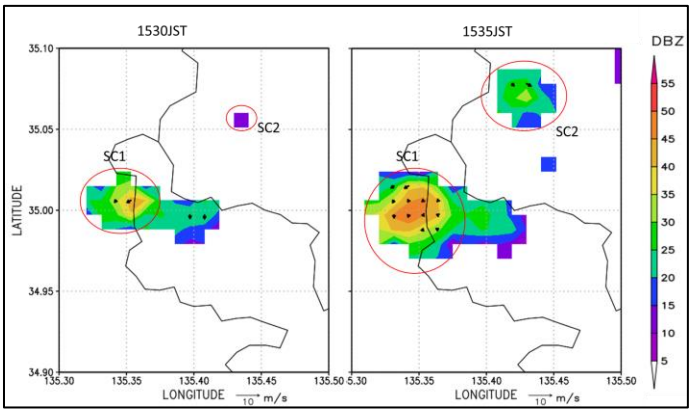

Figure 5.1 The development of SC1 and SC2 were observed at 1530JST and 1535JST.

For the case of a single-cell transition to multicell, the single-cell was determined by evaluating one core of Z_h more than 45 dBZ which was developed less than 30-min before it transformed into the multicell. The multicell was characterized when observing the two or more cores of Z_h greater than 25 dBZ. Different criteria were introduced due to the emphasis on the core of Z_h in the maturing stage and the developing stage. The study event on 13th August 2018 was selected, whereby SC1 and SC2 started to develop at 1530JST and 1535JST, respectively (Figure 5.1). They transformed into multicell since the two cores were observed in Figure 5.2(a) at 1600JST and these cores remained detected at 1605JST as presented in Figure 5.2(b). The illustration of multicell development was also confirmed by the cross-section of SC1 at line AA' as described in Figure 5.2(c).

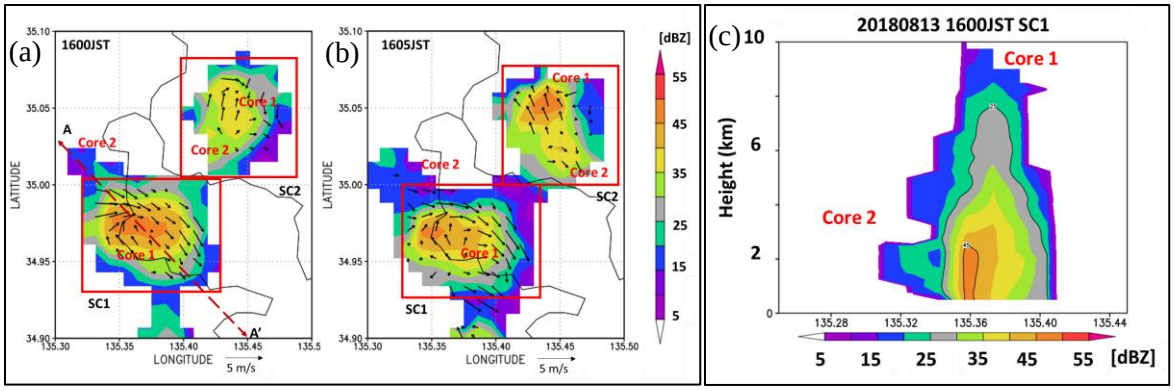

Figure 5.2 The horizontal wind distribution of (a) Target area of cells investigated for SC1 and SC2 after the transition to multicell (b) After 5-min cells merged into multicell (c) Illustration of multicell development with a cross-section of at line AA'.

The probability of a single-cell not merging into the multicell still existed in the weakly shear environment. To evaluate this study, the case of none merging was compared by observing a single-cell with the core of Z_h more than 45 dBZ and developed in less than 1 hour. This case was observed at the region and time as presented in Figure 5.3. SCNM1 referred to event 1, meanwhile, SCNM2 and SCNM3 represented event 2.

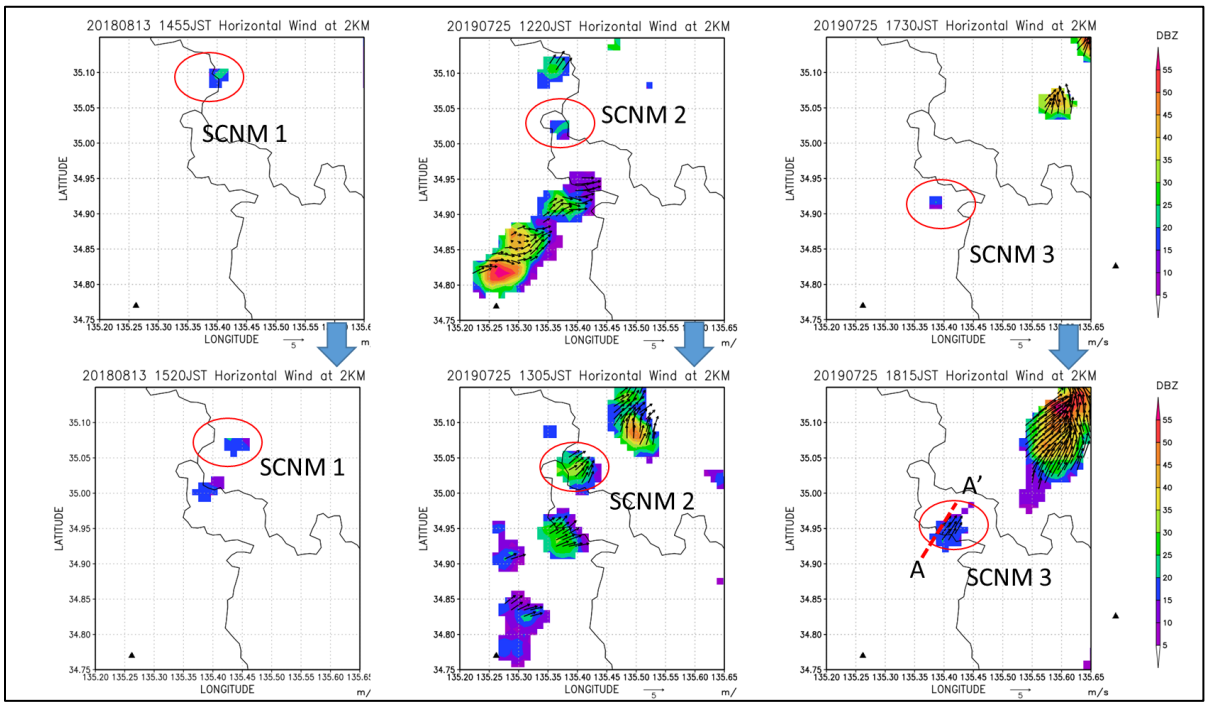

Figure 5.3 Horizontal distribution of radar reflectivity at 2 km CAPPI height for single-cell not merged (SCNM) at the target location and time of the first cell developed. Time is shown in JST.

5.2.2 Kinematic mechanism analysis

A Dual-Doppler radar analysis was performed for retrieval of the three-dimensional (3D) wind fields to examine the kinematic mechanisms of cloud development by using two components of the Doppler velocity by two radars simultaneously (Kim et al., 2012). In this study, we selected Tanokuchi radar and Katsuragi radar stations as already discussed in Section 2.1.2. the kinematic mechanism analysis was also investigated to quantify the relationship of polarimetric characteristics. The vertical vorticity from Dual-Doppler Analysis (hereafter referred to as "DDA") method was included in the investigation since vertical vorticity is associated with the updraft intensity. The core vorticity was defined as the maximum of positive vorticity and the minimum of negative vorticity. The formula used for extraction of vertical vorticity is shown as equation (5.1) where *u* and *v* are the horizontal wind obtained from the dual-Doppler analysis. The spatial and temporal resolution in this parameter is 1 km x 1 km x 0.5 km in the interval every 5 minutes.

$$\zeta = \frac{\partial v}{\partial x} - \frac{\partial u}{\partial y} \qquad (5.1)$$

where *u* is the zonal wind component, and *v* is the meridional wind component, which are these components of velocity in the *x* and *y* directions, respectively, retrieved from dual-Doppler radar analysis.

5.2.3 Multi-parameter radar analysis

The X-band multi-parameter radar stations from XRAIN radar networks in the Kinki region, Japan (Juubusan, Rokko, Katsuragi, and Tanokuchi) were used in this study. The radar parameters such as Z_h, Z_{dr}, and K_{dp} were analyzed using composite four stations due to the advantages in providing useful information in hydrological applications and microphysical analysis (Dong et al., 2012). The radar parameters obtained from each radar were converted to compose together into 0.25 x 0.25 x 0.25 km of Constant Altitude PPI (CAPPI) by Cressman interpolation (Masuda et al., 2014) using four radars in every 5 minutes.

The dual-polarization radar parameters such as Z_{dr} and K_{dp} column were mainly used to investigate the strength and location of the updraft to examine the severity of thunderstorms (van Lier, et.al, 2016). Therefore, the characteristic patterns of transition to multicell focused on the Z_{dr}

column and K_{dp} column depth were investigated as illustrated in Figure 5.4(a) and Figure 5.4(b) respectively**.** The column depth was defined when the Z_{dr} (>2 dB) and K_{dp} (>1.5 deg/km) were above the melting height level. We proposed the new method of analysis by emphasizing that the maximum of both columns to be calculated after the melting height because these columns reflected the considerable amounts of supercooled water were being lifted if the updraft occurs. The above-mentioned polarimetric characteristics in this study will be further analyzed. The melting level was observed at 5 km above ground level (AGL) for both events, which retrieved from the radiosonde data at Shionomisaki station.

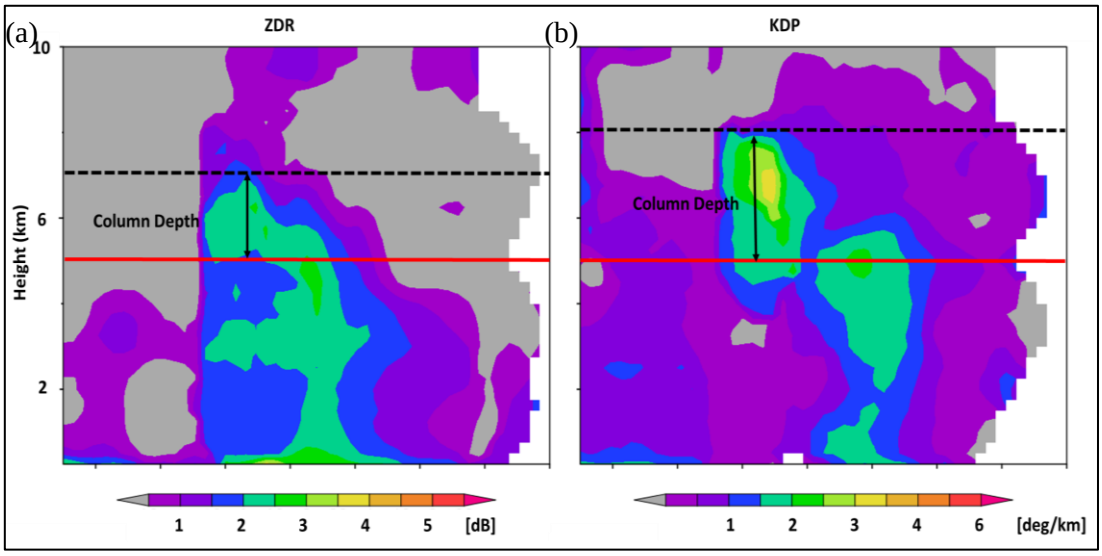

Figure 5.4 Illustration of **(a)** Z_{dr} column depth **(b)** K_{dp} column depth referred to solid arrow, above the melting level indicated by red solid line.

5.3 Results and Discussion

5.3.1 Kinematic mechanism analysis

a) Single-cell merged into multicell

The analysis of Z_{dr} and K_{dp} images at 5 km CAPPI height were described in Figure 5.5(a) and Figure 5.5(b) for both cells investigated at 1555JST before developing into multicell. From these images, SC1 and SC2 showed the highest intensity for K_{dp} and not presented at Z_{dr} indicated that K_{dp} detected the deep convection updraft (van Lier, et al., 2016). To confirm the development of cells, a cross-section of SC1 is constructed before the transition as shown in Figure 5.6. At

1545JST, a strong downdraft was observed in the cells indicating the cell was in the maturing stage. 5-min after the transition, the new cell developed adjacent to the existing SC1 with the existence of convergence and the updraft mainly observed in the SC1. The downdraft and updraft remained happened in the multicell development.

The horizontal wind distribution with radar reflectivity and vertical vorticity at 2 km CAPPI height are presented in Figure 5.5(c) and Figure 5.5(d). Both the cells SC1 and SC2 revealed that one core of Z_h was greater than 45 dBZ at 2 km CAPPI height and the vertical vorticity showed the highest peak at SC1 than SC2. This characteristic could indicate the transition to the multicell as the new cell started to develop at the southwest of the SC1. This can be referred to as the position of a new cell developed at the same location of K_{dp} and vertical vorticity. However, this signature pattern for SC2 could not be identified due to the lowest intensity of vertical vorticity. To confirm the transition of a single-cell to multicell, the time-series of kinematic mechanisms and vertical vorticity were developed.

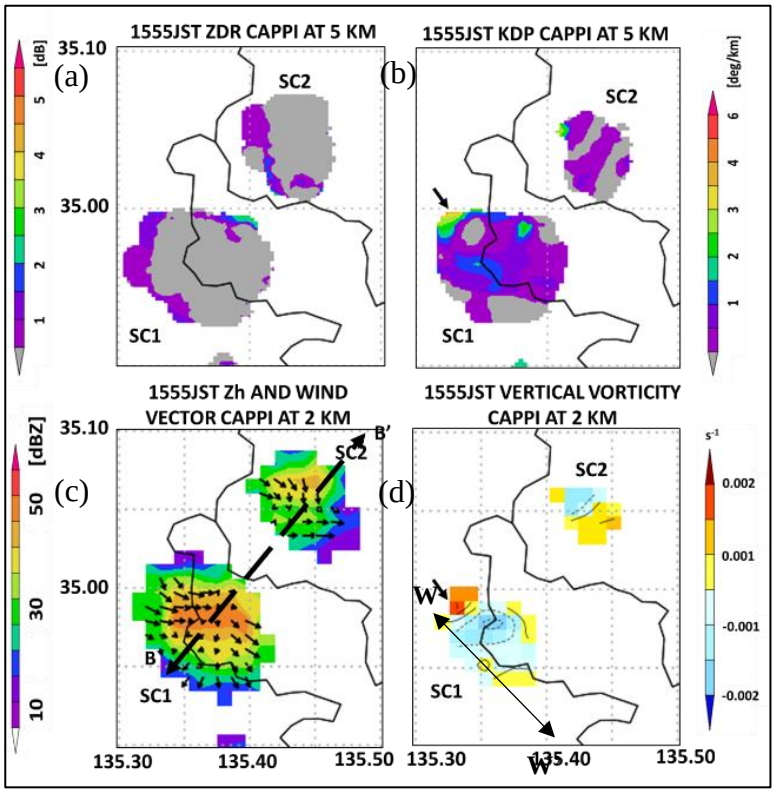

Figure 5.5 Horizontal distribution at 1555JST for SC1 and SC2 for **(a)** Z_{dr} **(b)** K_{dp} at 5 km height, and **(c)** Z_h **(d)** Vertical vorticity at 2 km height. Line BB' gives the location of the vertical cross-section shown in Figure 5.10.

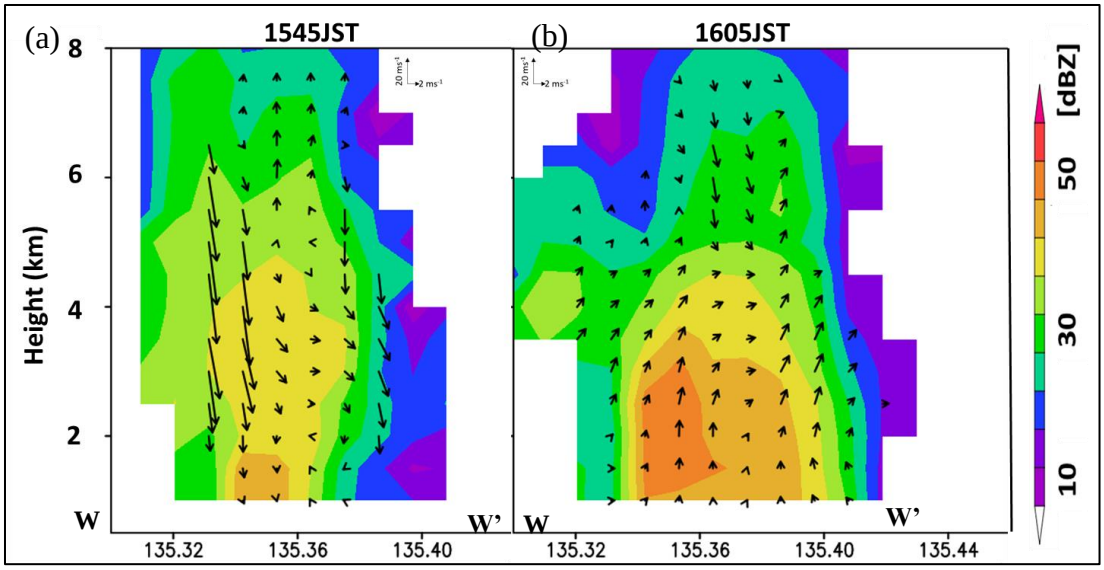

Figure 5.6 Vertical cross-section of SC1 at (a) 1545JST before transition into multicell (b) at 1605 JST after the transition. See Figure 5.5(d) for location.

The evolution of SC1 and SC2 were examined on the average of Z_h, updraft, and convergence maxima that were retrieved from the entire storm volume; and core vorticity was chosen at the height of 3.5 km (SC1) and 3 km (SC2), respectively. The evolution of SC1 from a single-cell to a multicell is illustrated in Figure 5.7(a). During nearly one hour of observation for SC1, a maximum reflectivity had increased from 10 dBZ to 60 dBZ, a maximum convergence had increased from <0.001 s^{-1} to 0.003 s^{-1}, a maximum updraft had increased from <10 m s^{-1} to 50 m s^{-1}, and a maximum vertical vorticity had increased from < 0.001 s^{-1} to 0.008 s^{-1}. The maximum Z_{dr} column (3 km – 4 km) existed at similar time of updraft indicated that SC1 developed more intense as the peak updraft occurred 10-min after the development. The maximum K_{dp} column existed after 5-min of peak updraft, but a signature pattern that could be observed during the transition with the maximum K_{dp} column of 1 km existed at 1555JST.

For the time-series analysis of SC2 as described in Figure 5.7(b), a maximum reflectivity had steadily increased from 30 dBZ to 50 dBZ, a maximum convergence rose from 0.002 s^{-1} to 0.004 s^{-1}, a maximum updraft peak until 50 ms^{-1}, and a maximum vertical vorticity peak to 0.004 s^{-1}. The maximum column depth of Z_{dr} existed at similar time with the peak updraft, with the highest column discovered at 1615JST, 15-min before the peak of updraft in the multicell. The K_{dp} column always existed in the single-cell and multicell, however, the signature patterns during the transition was similar to SC1, whereby a maximum K_{dp} column of 1 km discovered in this analysis.

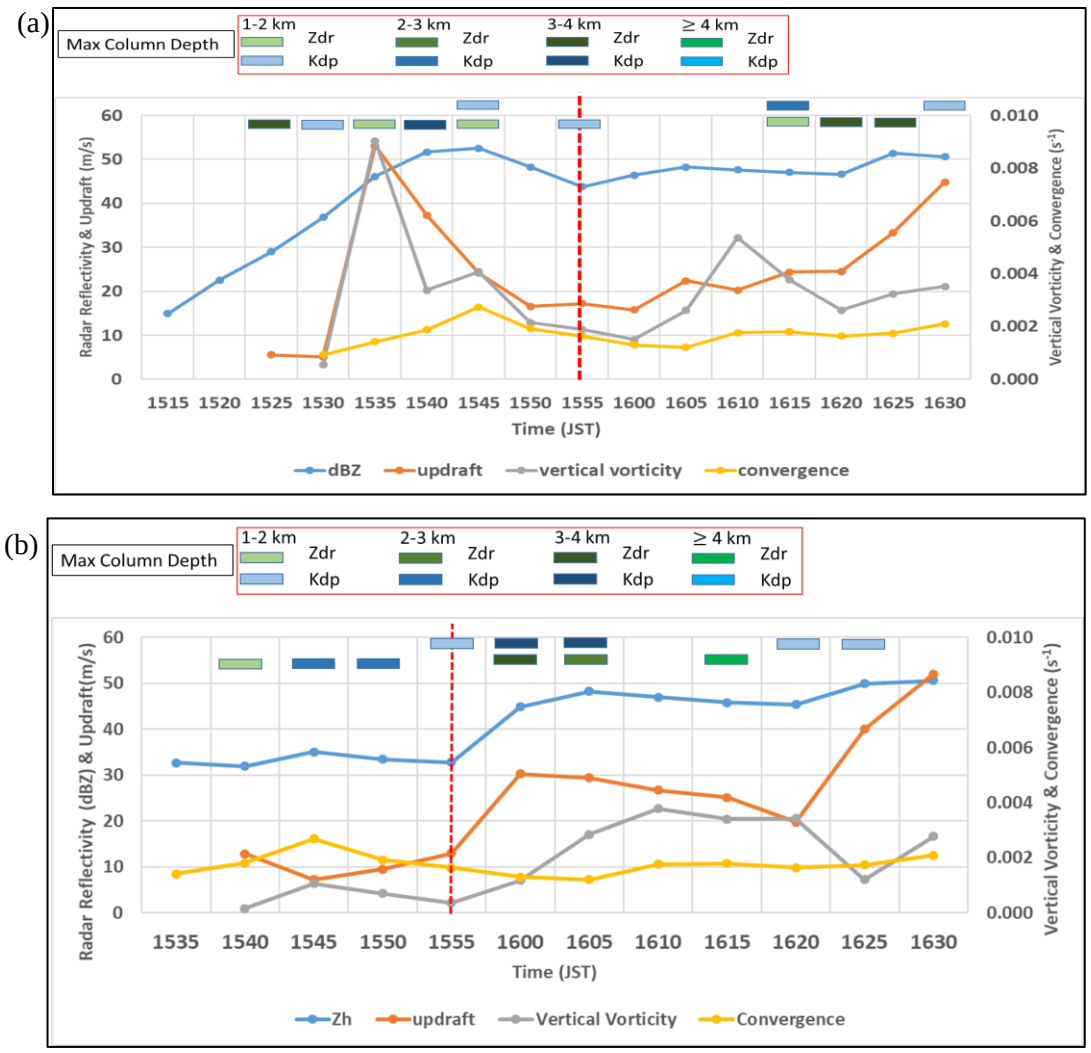

Figure 5.7 Time-series of averaged maximum reflectivity, updraft, and convergence for entire storm volume and of maximum vertical vorticity **(a)** for SC1 **(b)** for SC2.

b) Single-cell not merged

Figure 5.8 showed the example of a time-height distribution of SCNM2 with radar reflectivity and wind vectors. In the 30-minutes lifespan of single-cell not merged, we could observe the intense of Z_h with the strong upward motion at middle height and top of the cloud. The height of the cloud was approximately 6 km height. However, this cell is not merged although it was observed the multicell formation is shown in Figure 5.3. Therefore, the kinematic mechanism will be studied and compared with the position of columns for Kdp and Zdr. As shown in Figure 5.9(a) and 5.9(b), the peak of convergence, updraft, and core vorticity occurred in the cell, but with less intensity compared with SC1 and SC2.

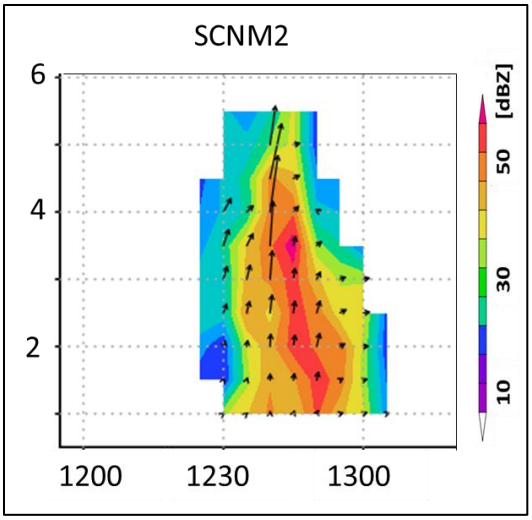

Figure 5.8 Example of time-height distribution of SCNM2 indicated the duration of cells investigated.

(a)

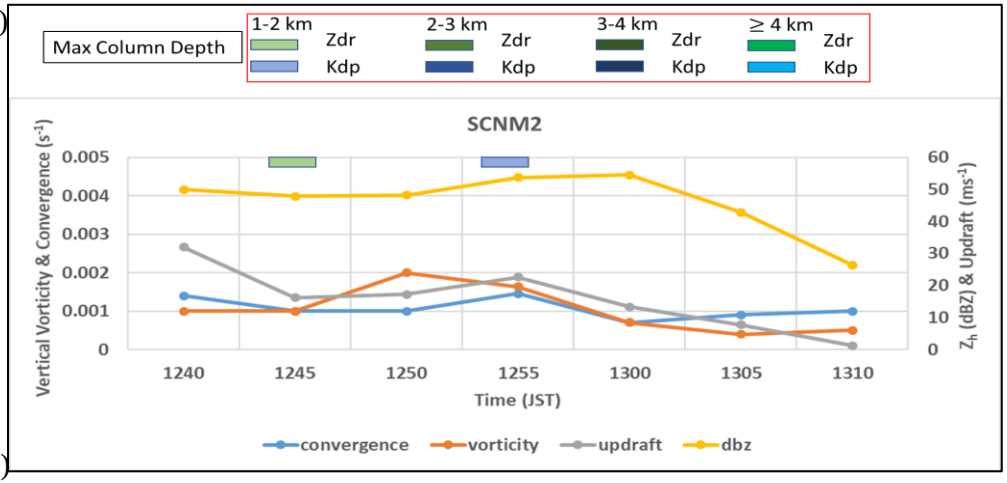

(b)

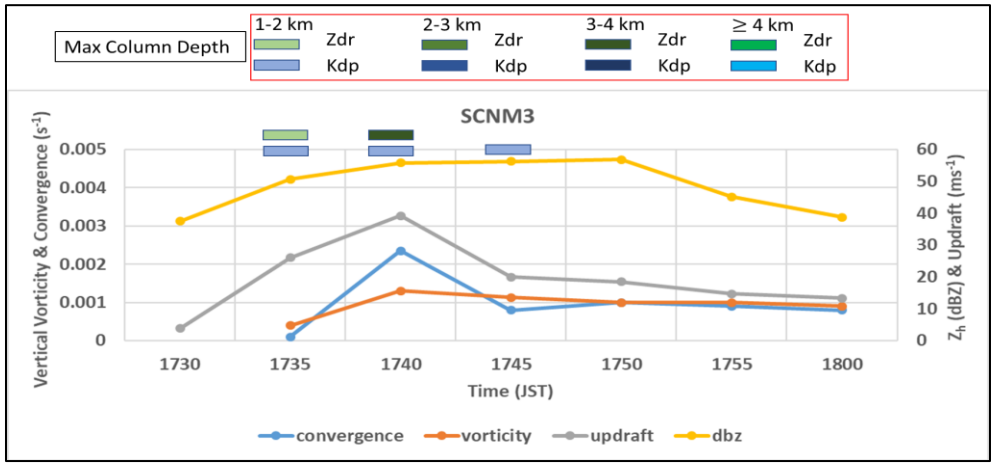

Figure 5.9 Time-series of averaged maximum reflectivity, updraft, and convergence for entire storm volume and of maximum vertical vorticity **(a)** for SCNM2 **(b)** for SCNM3.

5.3.2 Z_{dr} column and K_{dp} column analysis

a) Single-cell merged into multicell

For further investigation in detecting the Z_{dr} and K_{dp} columns, the cross-section for SC1 and SC2 was employed as shown in Figure 5.7(a) and Figure 5.7(b). The maximum Z_{dr} column (3 km – 4 km) existed at similar time of updraft indicated that SC1 developed more intense as the peak updraft occurred 10-min after the development. The maximum K_{dp} column existed after 5-min of peak updraft, but a signature pattern that could be observed during the transition with the maximum K_{dp} column of 1 km existed at 1555JST. The maximum column depth of Z_{dr} existed similar time with the peak updraft, with the highest column discovered at 1615JST, 15-min before the peak of updraft in the multicell. The K_{dp} column always existed in the single-cell and multicell, however, during transition, the characteristic was observed similar with SC1, which maximum K_{dp} column of 1 km discovered in this analysis.

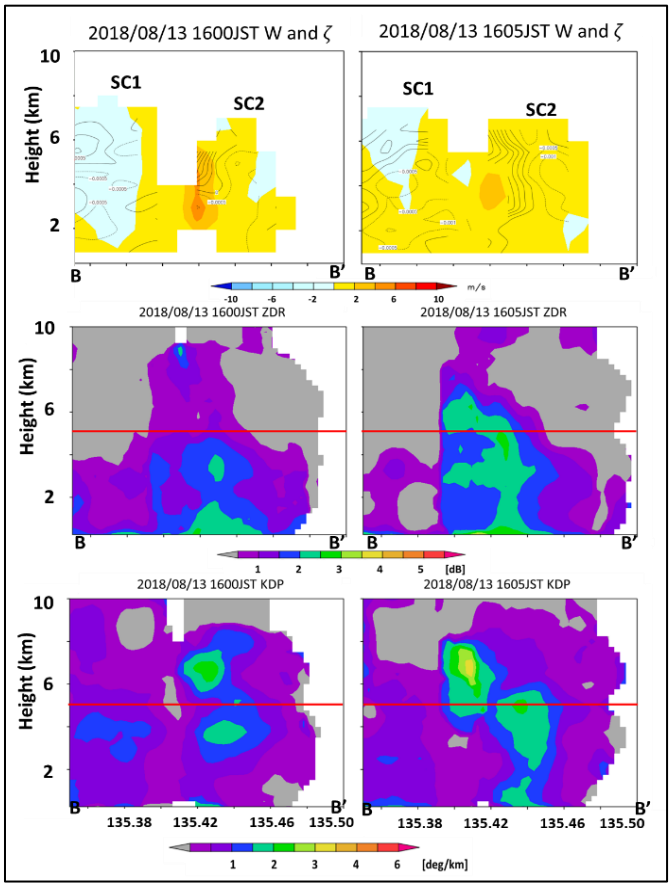

Figure 5.10 Vertical cross-section of updraft (shaded) and vertical vorticity (contoured line), Z_{dr}, and K_{dp} through SC1 and SC2 at 1600JST and 1605JST. The red solid line showed the melting height (See Figure 5.5(c) for location).

Moreover, the cross-section for SC1 and SC2 was employed as shown in Figure 5.10. The cells merged at 1600JST indicated the highest of updraft strength between 2 km until 6 km of AGL. The Z_{dr} column was not found at this time, however Z_{dr} with intensity between 2 dB - 3 dB existed at below of melting height. This indicated that the graupel existed at the location of updraft, indicated the regions of deep convection updrafts (van Lier, et.al, 2016). The K_{dp} column occurred at the same location and time of development of updraft. After 5-min, the intensity of updraft decreasing, and Z_{dr} and K_{dp} columns existed at this time. The identical position of both columns was found in comparison to the updraft location. The extended Z_{dr} and K_{dp} columns showed mainly the above melting level height with the similar position of the updraft formation. These results were similar to the previous study (van Lier, et.al, 2016), which proved that both Z_{dr} and K_{dp} columns could be utilized in identifying the updraft and correlated well with the intensity.

b) Single-cell not merged

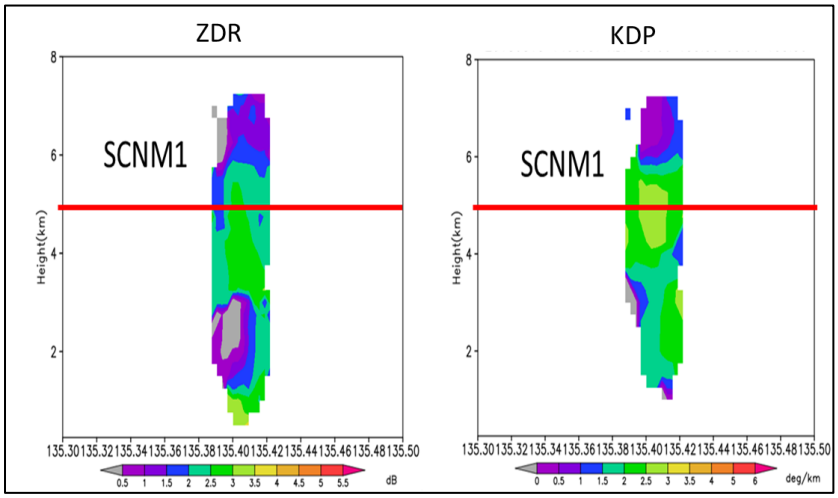

Figure 5.11 The maximum column depth of Z_{dr} and K_{dp} for SCNM1.

As presented in Figure 5.11, SCNM presented the maximum column depth of Z_{dr} and K_{dp} in the range of 1 km - 2 km. In the case of single-cell to multicell, it showed the frequent of K_{dp} column depth in the interval of 1 km - 2 km, and Z_{dr} column at interval of 1 km - 2 km and 3 km - 4 km. Maximum Z_{dr} and K_{dp} column revealed the highest column during the formation of updraft and before peak of updraft in multicell, but lower column observed at SCNM. With the highest strength of vertical vorticity and column depth, this finding suggested us to identify the relation-ship between both indicators. The new approach of discovering the relationship between maximum Z_{dr} and K_{dp} column depth with the maximum intensity of core vorticity are suggested in this study.

5.3.3 Discussion of characteristics and mechanisms

Table 5.1 Characteristics of cells investigated

Cells	Max Z_{dr} Column Depth (km)	Max K_{dp} Column Depth (km)	Max Updraft (ms^{-1})	Core Vorticity (s^{-1}) DDA Vorticity
SC1	*3 km*	*3 km*	*7.8*	*0.009*
SC2	*3 km*	*3 km*	*5.8*	*0.001*
MC1	*3 km*	*2 km*	*9.8*	*0.008*
MC2	*4 km*	*3 km*	*9.7*	*0.004*
SCNM1	*1 km*	*1 km*	*5.0*	*0.003*
SCNM2	*1 km*	*1 km*	*1.1*	*0.002*
SCNM3	*3 km*	*1 km*	*3.9*	*0.001*

The analysis was continued by examining the updraft and core vorticity intensities for each cell as listed in Table 5.1. The strength of updraft in SC and MC showed the largest at approximately 10.0 m s^{-1} with the core vorticity intensity could be attained until 0.01 s^{-1}. SCNM showed the average intensity of updraft at 4 m s^{-1}, and the core vorticity observed was less than 0.003 s^{-1}. A good correlation was observed between the formation height of maximum updraft with the core vorticity intensity, and also between the strength of updraft and vertical vorticity (r=0.80) for all cells investigated. Therefore, core vorticity intensity was mainly influenced by the strength of the updraft in the multicell development. The results indicated that the transition signals of single-cells did not merge showed the strength of vorticity below 0.004 s^{-1}. This new finding of peak core vorticity intensity could be referred to as an indicator of transition signals of single-cell to multicell by considering the factor of environmental conditions. Moreover, a good correlation was observed between the formation height of maximum updraft with the core vorticity intensity, and also between the strength of updraft and vertical vorticity (r=0.80) for all cells investigated. Therefore, core vorticity intensity was mainly influenced by the strength of the updraft in the multicell development.

As presented in Figure 5.12, for the cells not merged, they presented the maximum column depth of Z_{dr} and K_{dp} in the range of 1 km - 2 km. In the case of a single-cell to multicell, it showed the frequent of K_{dp} column depth in the interval of 1 km - 2 km, and Z_{dr} column at an interval of 1 km - 2 km and 3 km - 4 km. The maximum Z_{dr} and K_{dp} columns revealed the highest column during the formation of updraft and before the peak of updraft in multicell, but a lower column

was observed at SCNM. With the highest strength of vertical vorticity and column depth, this finding suggested to identify the relationship between both indicators. The new approach of discovering the relationship between the maximum Z_{dr} and K_{dp} columns depth with the maximum intensity of core vorticity were suggested in this study.

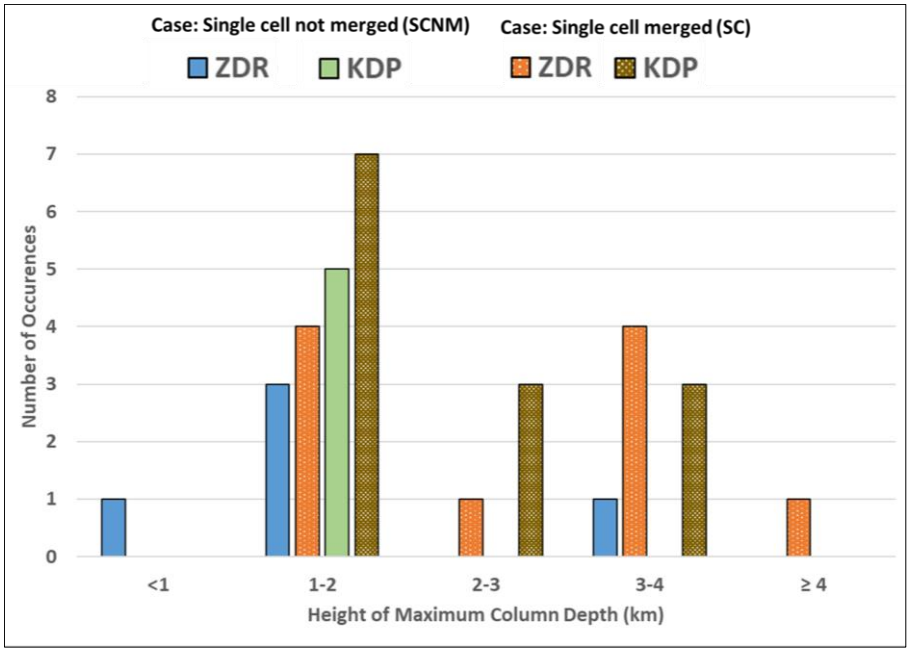

Figure 5.12 Distribution of the calculated height of maximum column depth of Z_{dr} and K_{dp}.

The Pearson correlation coefficient showed that the maximum K_{dp} column depth for core vorticity intensity for DDA vorticity showed the highest at 0.88 and moderate correlation (0.58) for Z_{dr} column. The relationship of core vorticity with the maximum K_{dp} column depth for case of merged cells was discovered at the average of 3 km with core vorticity could be attained until 0.01 s^{-1}. In comparison, the none-merged cells cases had revealed the lower strength of core vorticity and maximum column depth at 1 km. As the transition signals might be varied from case to case, the K_{dp} column was always discovered during the cells merging and it quantified the best relationship with vertical vorticity. These new findings revealed that K_{dp} was the main consideration that indicated the transition signals of cells merging because in the multicell development, the updraft continued to develop with the existence of warm and moist inflow at lower level that supported the formation of new cells. In this study, the continuous of updraft development could be evaluated using the K_{dp} column, rather than Z_{dr} column.

Moreover, the additional factor throughout the cells might influence the cells merging, such as vertical wind shear. The zonal vertical wind shear that was calculated from 1 km until 6 km using a dual-Doppler radar, showed the non-existence of wind shear occurred for the case of none-merged cells as presented in Figure 5.13. The magnitudes of vertical shear at single-to-multicell cases were found to be the highest intensity at 5 m/s. This explanation was well-reasonable for the none-merged cells, although in the multicell environment conditions.

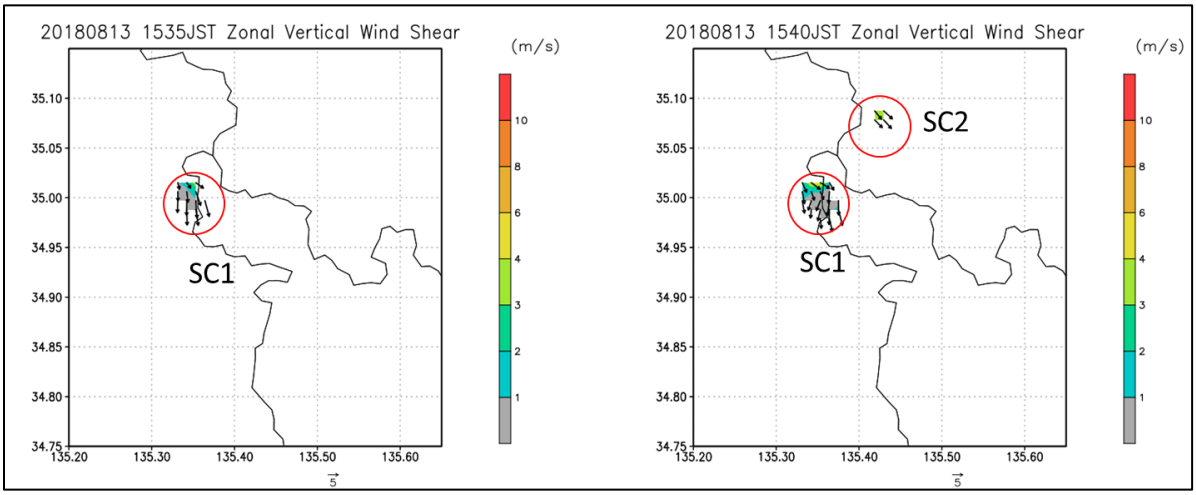

Figure 5.13 Calculated zonal vertical wind shear existed on the case of cells merged.

5. CONCLUSIONS

This study presented the analysis of transition from a single-cell to multicell formation utilizing Z_{dr} column, K_{dp} column, updraft and vertical vorticity intensity. From the two events study, the merged cells indicated the vertical wind shear of about 5 m/s, meanwhile none-merged cells showed the none-existence of wind shear at the cells. From the analysis of time-series, the results presented that the convergence mostly developed before the initiation of the updraft, and the peak of updraft intensity occurred consistent with the period of core vorticity for both cells. The convergence and updraft strength mainly affected the core vorticity intensity. The investigation of Z_{dr} and K_{dp} columns revealed that the position of updraft was collocated with both columns. The K_{dp} columns were existed during the cells merging and an increment was observed 5-min after the cells merged. In contrast, Z_{dr} column showed the extended of column 5-min after the cells merged to the multicell. These signature patterns could be observed during the analysis of merged cells.

The maximum of column depth for Z_{dr} and K_{dp} to examine their relationship with the core vorticity intensity is suggested. The good correlation between the maximum column depth of K_{dp} and the core vorticity was discovered in comparison with Z_{dr}. This finding proved that K_{dp} is a useful proxy for deep convection updrafts (van Lier, et.al, 2016), since the life stages of multicell formation is controlled by the updraft and cells merging mainly related to the stronger updraft and downdraft of moist air in the presence of precipitation. In particular, Z_{dr} above the melting height is a useful indicator at the early appearance of deep convection (Kumjian et al. 2014; van Lier, et.al, 2016). The schematic illustration of both the maximum of Z_{dr} and K_{dp} columns depth in the process of transition before merging and after merging is described in Figure 5.14. The K_{dp} column existed during the transition, and an increment was after the cells merged. In contrast, the Z_{dr} column showed the extended column after 5-minutes of transition to the multicell.

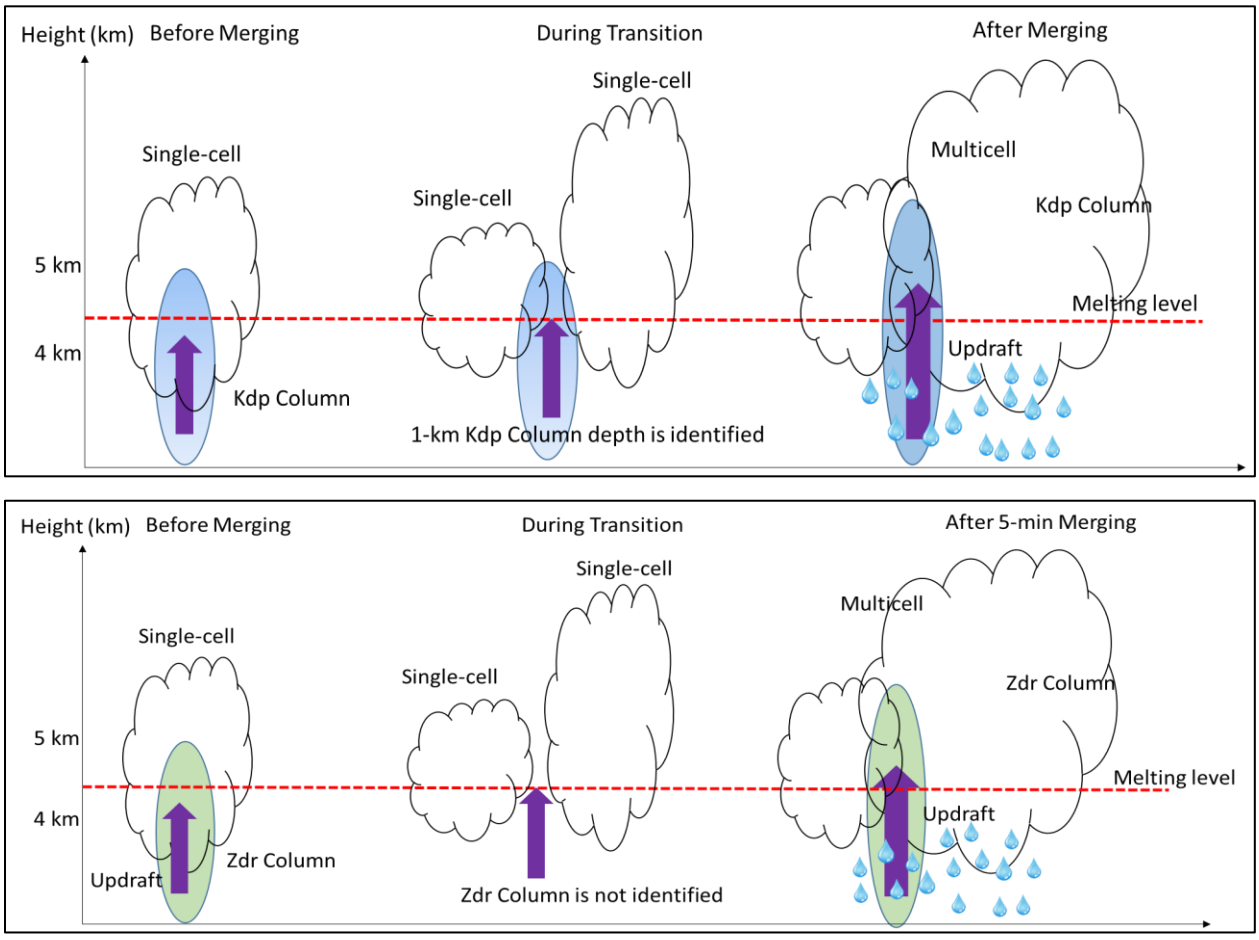

Figure 5.14 Schematic illustration of (a) K_{dp} column depth (b) Z_{dr} column depth in the process of transition stage from single-cell to multicell formation.

CHAPTER 6

6 Conclusions and Future Work

6.1 Conclusions

The main objective of this study is to examine the availability of vertical vorticity as the short-term precipitation forecast estimation for the transition signals from single-cell to multicell in the multicell thunderstorms environment. The vertical vorticity is proved could forecast the severity of hazardous cells before the maximum rainfall to the ground. Therefore, the preliminary analysis of single-cells that were developed adjacent to pre-existing cells and single-cells that developed on their own formation were investigated. The case study was selected depending on the instability condition and not influenced by the synoptic disturbance such as a frontal system or typhoon. By utilizing a single Doppler radar to estimate the vertical vorticity from the pseudo-vorticity method, the radar station was chosen subject to the target location.

For the first case study, the broken-type of multicell formation was analyzed with four single-cells developed in one-hour development using pseudo-vorticity analysis for two events. The initial stage of vertical vorticity for all cells was evaluated to discover the relationship with the lifetime. In the meantime, the vertical tube structure was examined to identify the transition pattern from single-cell to multicell. The core pair vorticity was defined as the maximum and minimum values of intensity at the absolute greater than 0.01 s^{-1}. The preliminary results showed that the pattern of changing position occurred in the single-cells development. On the other hand, in the analysis of the multicell formation, it was difficult to identify the core pair vorticity due to the complex distribution among the multicell. A previous study by Rotunno (1981) showed that in a thunderstorm, a pair of clockwise-anticlockwise vorticity is generated by tilting of the horizontal vortex. Nakakita et al (2017) utilized this pair of vorticity to identify hazard rain cells before they generated into a single thunderstorm. Both studies did not discuss about the pair of vorticity during the transition from single into multicell.

Here, we presented the investigation of the pair of vorticity in more detail during the transition. In Chapter 3, we showed the pattern of the changing position of core vorticity before the merge. Here we showed that in the lower height (2 km in cell B & cell C), the unbalanced pair vorticity will tend to wrap another core vorticity. Rottuno (1981) already observe from his model

in solution at a lower level. The updraft tends to move towards the certain direction which will tilt one vorticity and subsequently stretched. Meanwhile, another core is speculated by Rotunno (1981) to be wrapped (diminished). That is why from our result showed that the pair of vorticities in the lower height tends to have a different orientation compared with the pair vorticity condition in the upper level.

Furthermore, the study revealed that there was no strong correlation between lifetime and initial stage owing to the evolution of vorticity in single-cell development. Therefore, the analysis of the mechanisms should be considered to quantify the development of vertical vorticity from single-cell to multicell formation. The dual-Doppler analysis (DDA) was capable to study the kinematic mechanisms throughout the cells' development. The transition pattern of changing position was discovered at a different level because of the probability of another vortex tube development from other cells. Therefore, the analysis had been continued by introducing the new definition in the selection of the core pair vorticity using pseudo-vorticity analysis and a new approach of using dual-Doppler analysis. With the method of estimating the vertical vorticity from DDA, the two Doppler radars were deployed which the radar locations were influenced in this study. The new definition of core vorticity was introduced by focusing the core vorticity intensity at the same location, and the vertical vortex tube could be constructed by aligning these core vorticities. Therefore, the core vorticity position remained during the period of analysis.

In Chapter 4, we discussed more detail on the intensity of the core on each pair of vorticity during the transition from single-cell to multicell. The characteristics of transition signal were newly developed in this analysis, with focus on the time series-analysis, the formation height of core vorticity, and distance analysis. The time-series analysis of vertical vorticity was conducted to identify the temporal change of cells before and after single-cells merged with the multicell. The result showed that the intensity of the core vorticity reached its peak during the transition. In this study, the calculated average of vertical vorticity before merging was perceived at 0.002 s^{-1} (DDA vorticity) and 0.02 s^{-1} (pseudo-vorticity). The peak of core vorticity intensity of single-cell was revealed larger at the early stage when compared with the multicell. However, at the later stage of multicell development, the multicell showed greater intensity than single-cells developed. In this study, pseudo-vorticity presented the average vertical vorticity at 0.04 s^{-1} for both single-cells and multicell. In contrast, the average of core vorticity for the transition from single-cell to multicell was attained in the range of 0.002 s^{-1} to 0.004 s^{-1}. The mature vortex in the multicell was

always discovered at the later stage defined as core vorticity maxima boundary at the threshold intensity of more than 0.005 s^{-1} for DDA. These characteristic patterns could be observed by both methods using pseudo-vorticity and DDA although the intensity of pseudo-vorticity was ten-times higher than DDA vorticity analysis.

Table 6.1 The summary of methods used for the transition signals analysis based on positive vorticity

Characteristic Patterns	**DDA Vorticity**		**Pseudo-Vorticity**	
	Single-cell	Multicell	Single-cell	Multicell
Time-series analysis	Peak after merged		Peak after merged	
Average of core vorticity before merging	0.002 s^{-1}		0.02 s^{-1}	
Average of peak core vorticity intensity	0.004 s^{-1}	0.005 s^{-1}	0.04 s^{-1}	0.04 s^{-1}
Average formation height of peak core vorticity for positive (top) and negative vorticity (below)	3.8 km 3.7 km	3.9 km 4.6 km	4.4 km 4.4 km	3.6 km 2.7 km

Furthermore, the peak intensity and the formation height of core vorticity were evaluated using vertical vorticity analysis to distinguish the characteristics between single-cell and multicell. These patterns revealed that the time occurrence and formation height of single-cells for both positive and negative vorticity were always referred to at the same period. The peak of core pair vorticity happened at 4.4 km height for pseudo-vorticity, and in DDA vorticity showed a slight difference which was located at 3.8 km, and 3.7 km for positive and negative vorticity, respectively. In contrast, the multicell showed the different characteristics of height formation and time of occurrence of peak vorticity for both methods. The comprehensive characteristics pattern for single-cell and multicell for both methods are described in Table 6.1.

In these findings, the mechanism analysis was proved to the crucial in the transition from single-cell to multicell formation affecting the evolution of vertical vorticity. The convergence, updraft, and stretching of vortex tube were discovered as the main proxy of intensification of peak core vorticity, especially at the lower level. In addition, the tilting of the vortex tube was always observed at the middle height, which influenced the tilted of the vertical vortex tube to remain developed in the single-cell and multicell development. The merged vortices presented the height

of peak also changed from time to time due to the stretched vortex tube which the existence of convergence. The local change of vertical vorticity which is composed of tilting term and stretching term could be used in determining the vortices merger and transition signal from single-cell and multicell. Two vortices at the same sign (orientation) with (almost) parallel axes, within a certain distance, mix (merge) a substantial portion of their core vorticity into a single vortex (Meunier et al, 2005). Therefore, the distance also affects the intensity of merged vortices.

The maximum updraft in the developing of single-cell was discovered to impact the formation height and period of occurrence of the core vorticity. The maximum updraft greater than 5 m s^{-1} was frequently observed at 4 km. Since the multicell is commonly at the maturing stage in which the updraft and downdraft occurred within the cloud, both mechanisms were evaluated in terms of their height based on their intensity. Consequently, the frequent distribution of maximum updraft for multicell was revealed at a height of 4 km for intensity larger than 5 m $s^{-1,}$ and maximum downdraft with the strength greater than 1 m s^{-1} was observed at 1 km AGL. From our analysis, the average updraft velocities for the single-cell and multicell were 1.9 and 3.9 m s^{-1} respectively, and the average downdraft velocities were 0.7 and 1.4 m s^{-1}, respectively. These results of the present statistical properties of the peak core vorticity will improve nowcast and short-time forecast models of localized severe rainfall based on vertical vorticity analysis.

The distance analysis was established to discover the relationship of core vorticity intensity between single-cell and multicell. The distance of the same sign of core vorticity was calculated, and by applying the pseudo-vorticity method, no correlation was obtained due to the low estimation resolution. In comparison with the DDA vorticity method, the intensity of core vorticity from the single-cell was affected by the multicell, especially in the range of 5-10 km. Therefore, the optimal distance was discovered at this range that effects the core vorticity intensity of single-cells owing to the downdraft and divergence mechanisms which were frequently acquired in the multicell. Consequently, the distance also affects the intensity of core vorticity which the cell merger potential for the critical distance should be further investigated to determine the success of merging vortices to identify the potential of hazardous cells after merging.

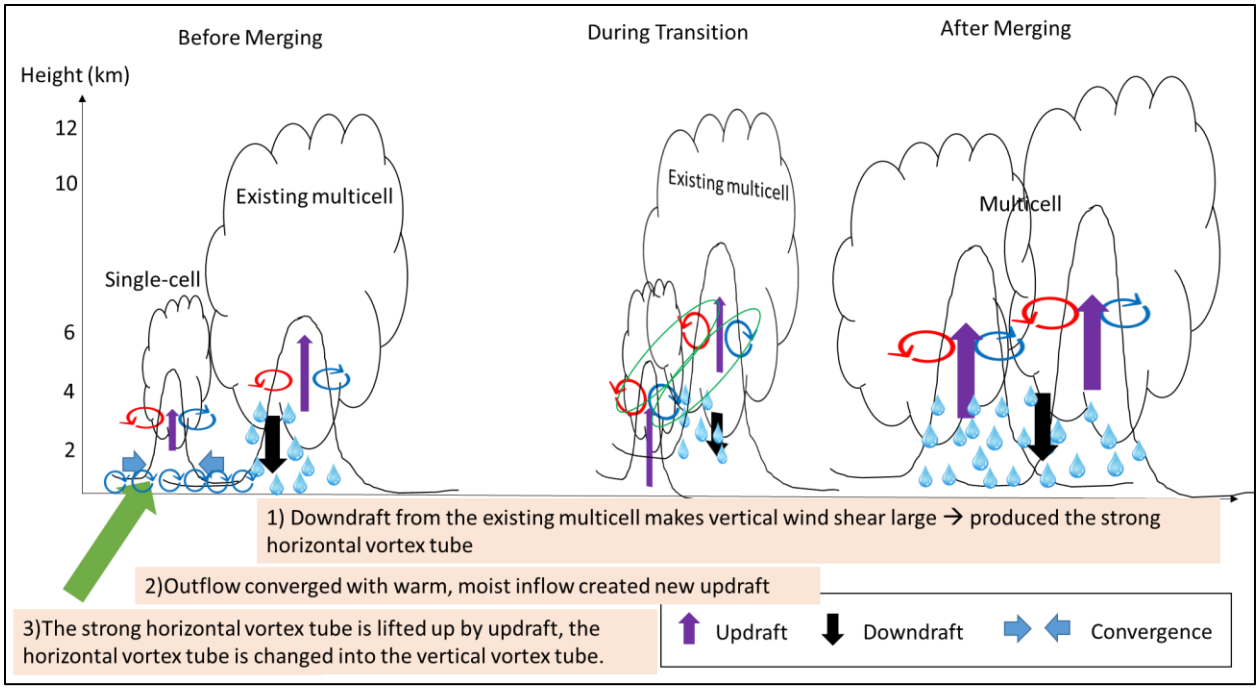

Figure 6.1 Schematic illustration of transition stage from single-cell to multicell in terms of vertical vorticity and mechanisms influence such as updraft, convergence, and downdraft.

At the transition stage from single-cell to multicell, the older cell tends to dissipate stage, in which descending air motion is the most dominant. The variation of the horizontal wind component with height, also known as vertical wind shear, is considered to determine the horizontal vorticity. The downdraft from the multicell produces the large vertical wind shear which produced the strong horizontal vortex tube. Horizontal gradients of vertical velocity, which are greatest on the updraft flanks, accomplish the tilting. The tilting effect is visible on the upward-bent black line of the vortex tube. The positive and negative terms of the tilting term indicate that the tilting of horizontal vorticity associated with wind shear generates a pair of counterrotating vortices that straddle the updraft, with cyclonic rotation to the left and anticyclonic rotation to the right as observed for older cell and also single-cell.

With the downdraft of cool air, and supply of warm and moist air, the new single-cell generated at the adjacent older cell which the convergence mostly occurred at lower-level. The single-cell is currently in the developing stage, and we assumed the characteristics of vertical vorticity are also influenced by the updraft that tilted the vortex tube until its peak vorticity happened mainly at 4 km height. With the horizontal convergence of air, the enhancement of spin due to the conservation of angular momentum when fluids are compressed can further amplify

aloft vortices. After merging to become multicell, the merged updraft remained intensified in the multicell cloud with the convergence influencing the stretched vortex tube to become more amplified resulting in the increment of rotation in the cloud.

The most important findings were discovered during the detection of maximum rainfall before it reaches the ground. It was quantified that the first detection of vertical vorticity in the single-cell could be referred to as an indicator of the peak of radar reflectivity after cells merged into multicell. In these new outcomes, the pseudo-vorticity quantified the lead time as an average of 17 minutes, and the DDA specified an average of 13 minutes before the peak of rainfall reaches the ground. These new findings could assist the forecasters in disseminating the early warnings to prevent more damage to infrastructure and casualties.

From this analysis regarding the utilization of pseudo-vorticity and DDA vorticity analysis, we will explain the comparison using these methods. The pseudo-vorticity, which has a good temporal and spatial resolution, could detect the precise development of a cloud, compared with the DDA vorticity, which is only a good quality estimation. Using pseudo-vorticity, the first detection of vertical vorticity was able to forecast the peak rainfall after cells merged in 17 minutes. This method also could detect the development of single-cell and peak of core vorticity intensity 5-minutes and 3-minutes earlier than DDA, respectively. In the detection of formation height of peak intensity, pseudo-vorticity is able to distinguish between the characteristics of single-cell and multicell, which were observed almost similar to the frequent height of maximum updraft/downdraft. However, both pseudo- and DDA vorticity methods show similarities in the peak intensity pattern after cells merged, and the time occurrence of peak intensity for single-cell almost identical to each other. The peak of core vorticity intensity of single-cell and multicell indicated the similarities albeit the pseudo-vorticity intensity is ten times higher than DDA. The distance analysis could be evaluated using DDA only due to its high quality of estimation.

The limitation still existed in this research because since the DDA analysis is in 5 minutes intervals, it is expected that the vorticity in the storm can increase during those few minutes. The real storms are often too complex to draw a definitive conclusion (Markowski and Hannon, 2006) however, using the vertical vorticity in the merging process, provides new insight into the cells merger process. It is recommended to add supplementary information such as thermodynamic observations which appears to be a connection with the multicell formation.

In Chapter 5, further investigation of the transition from single-cells to multicell in the multicell environment condition by selecting another event that was focused on the first single-cell development and transition into the multicell. The single-cells that were not merged in this environment were also included to compare the transition signals and their characteristics. The multi-parameter radar analysis was focused by examining the Z_{dr} and K_{dp} columns that are beneficial in evaluating the stage of multicell development. In addition, the peak of vertical vorticity analysis was investigated to verify the criterion index from the previous study. In this study, the new approach was established by quantifying the maximum Z_{dr} column and K_{dp} column that were calculated from the melting level because these columns reflected the considerable amounts of supercooled water were being lifted if the updraft occurs. Results indicated that the maximum K_{dp} column was always identified before and after cells merging and the intensification of intensity occurred after 5-minutes of transition from single-cell to multicell. Meanwhile, a maximum of Z_{dr} column was discovered after 5-minutes of the transition. On average, the maximum height of both columns revealed at most of 3 km height from the melting level. The analysis proved that in the transition of single-cell to multicell, updraft frequently developed in the multicell formation with strong strength. Apart from that, single-cells that were not merged usually reveal the maximum of Z_{dr} and K_{dp} column of 1 km height which this characteristic pattern could be indicated as the non-merging of cells including the inspection of vertical wind shear at those cells.

In the meantime, the peak intensity of single-cell before transition into multicell was varied according to the influence of convergence and updraft that supplied into the single-cells development. However, the peak of core vorticity was discovered could be attain to 0.04 s^{-1} that could be indicated as the transition from single-cell to multicell in this study. Therefore, future investigation is needed to identify the threshold statistical index for the transition from single-cell to multicell. Furthermore, the correlation analysis between the maximum K_{dp} column with the peak intensity of core vorticity was studied, and a good correlation was identified. This new finding revealed that K_{dp} is a useful proxy for deep convection updrafts since the life stages of multicell formation are controlled by the updraft and cells merging mainly related to the stronger updraft and downdraft of moist air in the presence of precipitation. In particular, Z_{dr} above melting height is the useful indicator of the early appearance of deep convection.

In conclusion, the vertical vorticity and polarimetric methods were able to produce the signals of transition from the single-cell to multicell thunderstorms that were discovered as the novelty in this study. The development of single-cell by comparing with the radar reflectivity, could not forecast early on the cells merging, however, the intense rotation in the single-cell before merging could be the indicator of signal the hazardous cell after merging. In identifying the hazardous storms that generated the severe weather that will contribute to flood disasters, the single-cell storms which merged into multicell were identified in the range below 0.005 s^{-1} which was appropriately used when comparing the supercell's vertical vorticity commonly could be attained at 0.01 s^{-1}. The characteristics of single-cell were identified as the development of peak vorticity always located at the same height and time of occurrence which could be distinguished from the characteristics of multicell. In contrast, using the polarimetric characteristics, the K_{dp} column was discovered as the transition signal from single-cell to multicell which a 1-km column depth generated during the transition. The differentiation of the Z_{dr} column and K_{dp} column between the cells merged and none-merged revealed that the maximum column of K_{dp} developed in the range of less than 1 km for the cells none merged. These findings were identified as vital in the understanding of the transition from single-cell to multicell by examining the vertical vorticity and polarimetric characteristics.

6.2 Future Work in Malaysia

Malaysia is typically exempt from natural disasters such as earthquakes, volcanic eruptions, and typhoons, but it is nonetheless susceptible to floods, man-made catastrophes, and landslides. Currently, flooding is the most common hazard in Malaysia. Malaysia experiences two types of flooding: flash floods and monsoonal floods. Flash floods are typically caused by severe rainfall linked with localized heavy rainfall lasting less than six hours, whereas monsoon floods are triggered by persistent high rainfall that causes widespread inundation. When the northeast monsoon prevails from November to January, the monsoon flood always happens in accordance with a seasonal pattern. Large flooding regions are affected by these monsoon floods due to a high concentration of runoff that exceeds the capacity of streams and rivers. Using numerical weather prediction (NWP) analysis, it is possible to forecast the onset of heavy rainfall during the northeast monsoon. However, the localized heavy rainfall's initial development cannot be predicted. To issue

thunderstorm warnings, forecasters must assess radar echoes, satellite imagery, and six-panel upper charts, and identify heavy rainfall areas.

Recently, the flood and landslide disaster events become more gradually increase in number because of the rapid development of urbanization on the upper hill that can change the surface characteristics and alter the hydrological cycle. For instance, the flash flood occurred in Klang valley, on the 7th March 2022 due to the localized heavy rainfall in addition to the drainage system that cannot cope with the amount of rainfall runoff. Figure 6.2 describes the images of a flood that occurred in Kuala Lumpur lately.

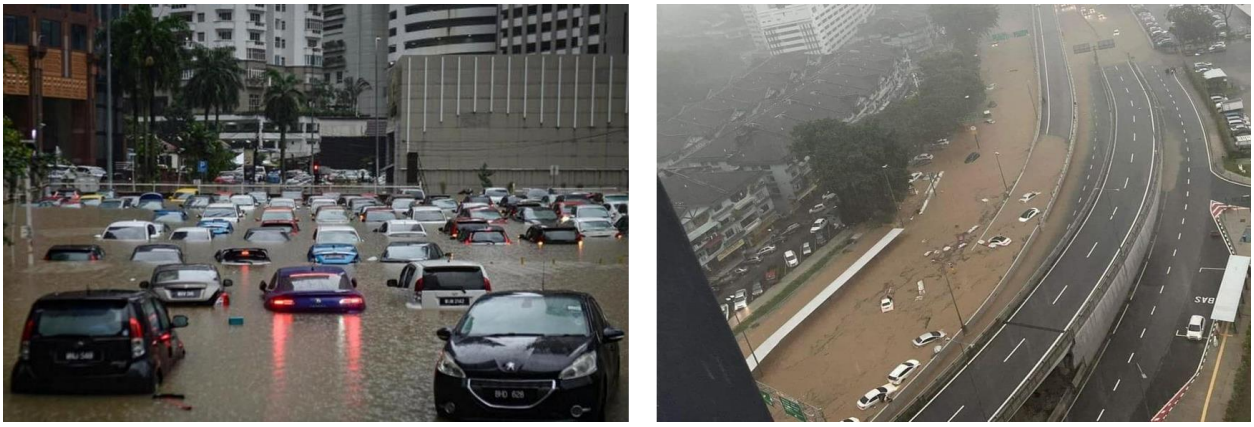

Figure 6.2 The floods inundated at the city center of Kuala Lumpur on March 7, 2022. (Source: Berita Harian)

The flood disaster has resulted in the potential of greater flood damage, and it contributes to a lot of disruption to socio-economic activities. Climate change also influences the pattern of weather to become more intense in terms of the total rainfall such as abnormal severe floods hit over the east coast of Peninsular Malaysia during the northeast monsoon in the period of 15-17 November 2014 which was labeled as “Yellow Flood” as presented in Figure 6.3. These flood events cause millions of damages in three states namely, Terengganu, Kelantan, and Pahang. Moreover, the tropical depression made landfall on the eastern coast of Peninsular Malaysia in December 2021, bringing three days of severe downpours across the whole peninsula. More than 300mm of rain fell in 24 hours, which led to floods and flash floods in different parts of Malaysia. As a result, 54 people died and 2 people are still missing. Figure 6.4 shows the flood-prone areas extracted from the Department of Drainage and Irrigation (DID) for the Peninsular and East Coast of Malaysia.

Figure 6.3 The prolonged heavy rainfall hit east coast of Peninsular Malaysia in 2014.

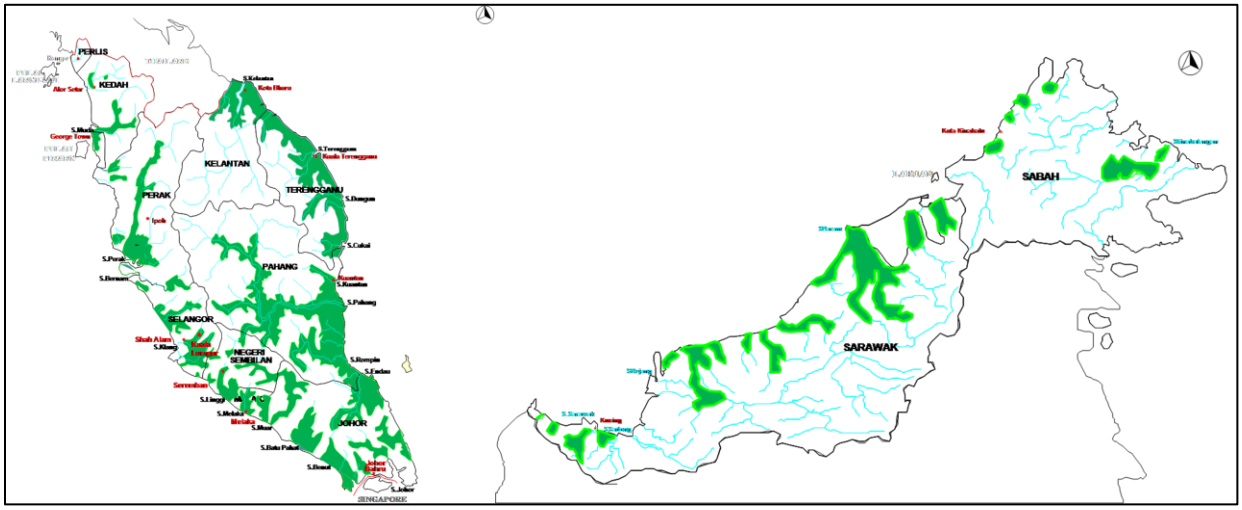

Figure 6.4 Green shaded areas indicate the flood prone areas in Peninsular Malaysia, and Sabah Sarawak (Source: DID)

Consequently, the Malaysian Meteorological Department (MMD) proposed the upgrading and new installation of weather radars to improve the radar coverage for achieving accurate and timely issuance of warnings, especially in urban areas. In collaboration with DID, flood forecasting and warnings could be improved significantly to minimize flood losses and death. Figure 6.5 presented the weather radar maps including the new installation of dual-polarization radars.

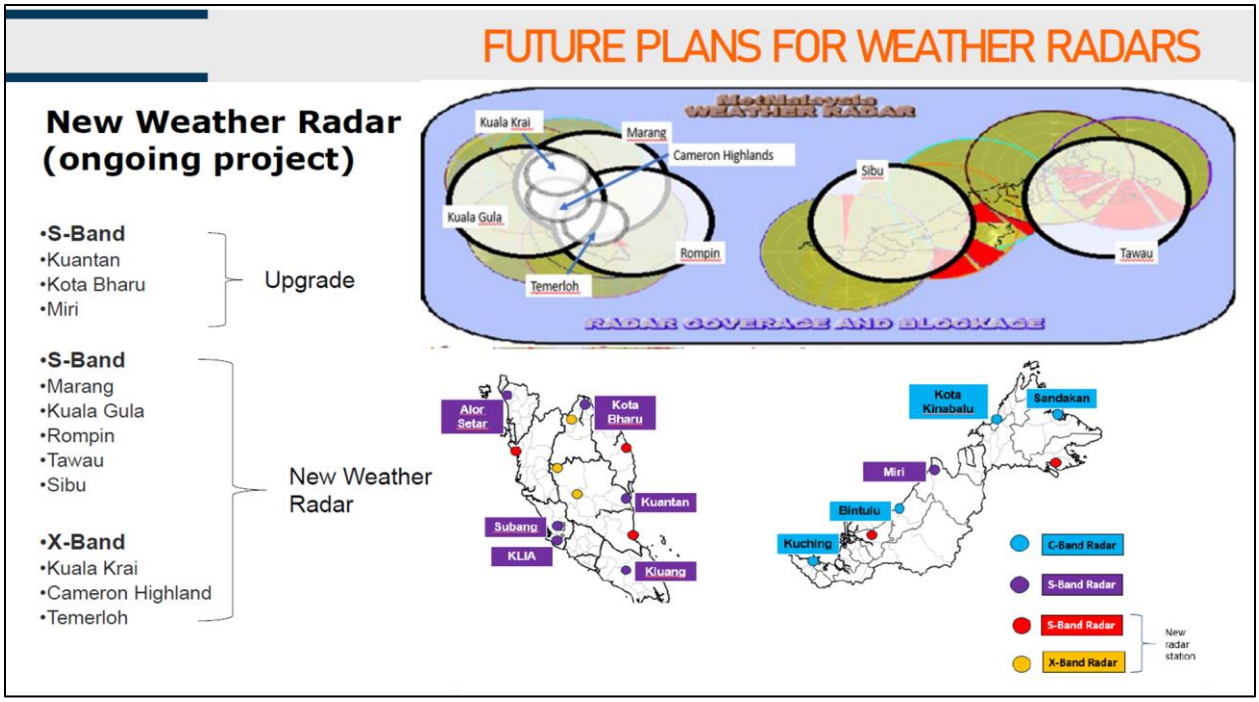

Figure 6.5 The weather radar observations in Malaysia region.

Adapting from Japanese experiences and methodologies, the author is motivated by the rapid development of dual-polarization weather radars in Japan. Numerous research on the short-term precipitation forecast utilized the dual-polarization radar parameters as already discussed in the previous chapters including the successful of detection hazardous cells using the vertical vorticity technique. Therefore, the preliminary analysis of flash floods will be investigated using dual-polarization radar parameters. This analysis will assist the forecaster in MMD to identify the early detection of severe weather and identification of potential heavy rainfall that will be occurred. This information also can assist DID to predict the flash flood that might be happened in the future.

REFERENCES

Adachi, A., Kobayashi, T., Yamauchi, H., & Onogi, S. (2013). Detection of potentially hazardous convective clouds with a dual-polarized C-band radar. Atmospheric Measurement Techniques, 6, 2741-2760.

Ahmad, F., Yamaguchi, K. and Nakakita, E., 2020: Investigation of Single-cell to Multicell in the Cluster Thunderstorms using Vorticity Analysis. Annual Journal of Hydraulic Engineering, JSCE, **76(2)**, 187-192.

Bluestein, H. B., and M. H. Jain, 1985: Formation of Mesoscale Lines of Precipitation: Severe Squall Lines in Oklahoma during the Spring. J. Atmos. Sci., 42, 1711–1732.

Boyer, C. H., and Dahl, J. M. L. (2020). The Mechanisms Responsible for Large Near-Surface Vertical Vorticity within Simulated Supercells and Quasi-Linear Storms. Monthly Weather Review 148, 10, 4281-4297.

Browning, K., Frankhauser, J., Chalon, J., Eccles, P., Strauch, R., Merrem, F., Musil, D., May, E., and Sand, W. (1976). Structure of an Evolving Hailstorm Part V: Synthesis and implications for Hail Growth and Hail Suppression. Monthly Weather Review 104, 5, 603-610.

Bringi, V. N., N. Balakrishnan, and D. S. Zrnić, 1990: An examination of propagation effects in rainfall on radar measurements at microwave frequencies. J. Atmos. Oceanic Technol., 7, 829–840.

Byers, H. R. and Braham, R., 1949: The Thunderstorm: Report of the Thunderstorm Project. Washington, D.C., U.S. Government Printing Office.

Dahl, J. M. L. (2017). Tilting of Horizontal Shear Vorticity and the Development of Updraft Rotation in Supercell Thunderstorms, *Journal of the Atmospheric Sciences*, *74*(9), 2997-3020.

Dong-Soon Kim, and Masayuki Maki, Validation of composite polarimetric parameters and rainfall rates from an X-band dual-polarization radar network in the Tokyo metropolitan area, Hydrological Research Letters, 2012, 6,76-81.

Doswell, Charles A. (1985). The operational meteorology of convective weather. Volume II. Storm scale analysis. NOAA technical memorandum ERL ESG,15.

E. Nakakita, R. Nishiwaki, H. Yamabe, and K. Yamaguchi, “Research on the prognostic risk of baby cell for guerilla-heavy rainfall considering by vorticity with doppler velocity,” *The Journal of Japan Society of Civil Engineers*, vol. 69, no. 4, pp. 325–330, 2013.

E. Nakakita, Sato, H., Nishiwaki, R., Yamabe, H., & Yamaguchi, K. (2017). Early Identification of Baby-Rain-Cell Aloft in a Severe Storm and Risk Projection for Urban Flash Flood. Advances in Meteorology, 2017(Article ID 5962356).

E.Westcott, N. (1994). Merging of convective clouds: Cloud Initiation, Bridging, and Subsequent Growth. American Meteorological Society, 122, 780-790.

Franklin, C. N., Holland, G. J. and May, P. T., 2006: Mechanisms for the Generation of Mesoscale Vorticity Features in Tropical Cyclone Rainbands. Mon. Wea. Rev., 134(10), pp. 2649-2669.

Friedrich, K., & Hagen, M. (2004). On the use of advanced Doppler radar techniques to determine horizontal wind fields for operational weather surveillance. *Meteorol.Appli.*, 155-174.

Gao, j., M. Xue, A. Shapiro, and K. K. Droegemeier, 1999: A variational method for the analysis of three-dimensional wind fields from two Doppler radars. Mon. Wea. Rev., 127, 2128–2142.

Geng, B., Fujiyoshi, Y. and Takeda, T., 1997: Evolution of a Multicell Thunderstorm in Association with Mid-Level Rear Inflow Enhanced by a Mid-Level Vortex in an Adjacent Thunderstorm, J. Meteor. Soc. Japan, 75, pp. 619-637.

Gunn, R. and D.G. Kinzer, 1949: The terminal velocity of fall for water droplets in stagnant air. J. Meteor., 6, 243-248.

Hirano, K., and M. Maki, 2010: Method of VIL calculation for X-band polarimetric radar and potential of VIL for nowcasting of localized severe rainfall -Case study of the Zoshigaya downpour,5 August 2008-, *SOLA*,6, 89–92, doi:10.2151/sola.2010-023.

Hirano, K., and M. Maki, 2018: Imminent nowcasting for severe rainfall using vertically integrated liquid water content derived from X-band polarimetric radar, *J. Meteor. Soc. Japan*,96, 201-220, doi: 10.2151/jmsj.2018-028.

Jonathan M. Wilkinson, Robert Neal, Exploring relationships between weather patterns and observed lightning activity for Britain and Ireland, Quarterly Journal of the Royal Meteorological Society, 10.1002/qj.4099, **147**, 738, (2772-2795), (2021).

Kato, T, 2020: Quasi-stationary band-shaped precipitation systems, named “Senjo-Kousuitai”, causing localized heavy rainfall in Japan, *J. Meteor. Soc. Japan*, 98, 485-509, doi:10.2151/jmsj.2020-029.

Kato, A., and M. Maki, 2009: Localized heavy rainfall near Zoshigaya, Tokyo, Japan on 5 August 2008 observed by X-band polarimetric radar: Preliminary analysis, *SOLA*, 5, 89-92, doi:10.2151/sola.2009–023.

Kim, D., Maki, M. and Shimizu, S., 2012: X-band Dual-Polarization Radar Observations of Precipitation Core Development and Structure in a Multicellular Storm over Zoshigaya, Japan, on August 5,2008. J. Meteor. Soc. Japan, 90(5), pp. 701-719.

Klemp, J. B., 1987: Dynamics of Tornadic Thunderstorms. Annu. Rev. Fluid Mech., 19, 369-402.

Kumjian, M. R., Khain, A. P., Benmoshe, N., Ilotoviz, E., Ryzhkov, A. V., & Phillips, V. T. J. (2014). The anatomy and physics of ZDR columns: Investigating a polarimetric radar signature with a spectral bin microphysical model. *Journal of Applied Meteorology and Climatology*, *53*(7), 1820–1843.

Kumjian, M. R., and Ryzhkov, A. V. (2008). Polarimetric Signatures in Supercell Thunderstorms. Journal of Applied Meteorology and Climatology 47, 7, 1940-1961.

Maesaka, T., Maki, M., & Iwanami, K. (2011). Operational Rainfall Estimation By X-Band Mp Radar Network In Mlit, Japan. Proceedings of 35th Conference on Radar Meteorology, July.

Maki, M., S.-G. Park, and V. N. Bringi, 2005: Effect of natural variations in rain drop size distributions on rain rate estimators of 3 cm wavelength polarimetric radar. J. Meteor. Soc. Japan, 83, 871–893.

Markowski, P. & Hannon, C., 2006. Multiple-Doppler Radar Observations of the Evolution of Vorticity Extrema in a Convective Boundary layer. *American Meteorological Society,* Volume 134, pp. 355-374.

Masuda, A., & Nakakita, E. (2014). Development of a technique to identify the stage of storm life cycle using X-band Polarimetric Radar. Journal of Hydraulic Engineering, 70, 493-498. (Japanese).

Ministry of Land, Infrastructure, Transport and Tourism, 2021: Summary of the white paper on land, infrastructure, transport and tourism in Japan, 2021, available online at https://www.mlit.go.jp/en/statistics/white-paper-mlit-index.html [accessed 19 May 2022].

Montgomery, M. T., Nicholls, M. E., Cram, T. A., and Saunders, A. B. (2006). A Vortical Hot Tower Route to Tropical Cyclogenesis. *Journal of the Atmospheric Sciences* 63, 1, 355-386.

National Oceanic and Atmospheric Administration (NOAA): Severe weather Thunderstorm Basics. Available online at https://www.nssl.noaa.gov/education/svrwx101/thunderstorms/ [accessed 19 May 2022].

Nishiwaki, N. et al., (2013). Behaviour and structure of convective clouds developing around a mountainous area observed by stereo photogrammetry and Ka-band and X-Band Radars: Case study of Northern Kanto, Japan. Journal of the Meteorological Society of Japan, 91(No.5), pp. 609-626.

Naylor, J., & Gilmore, M. S. (2014). Vorticity Evolution Leading to Tornadogenesis and Tornadogenesis Failure in Simulated Supercells, Journal of the Atmospheric Sciences, 71(3), 1201-1217.

Patrice Meunier, Stéphane Le Dizès, Thomas Leweke, (2005). Physics of vortex merging, Comptes Rendus Physique, Volume 6, Issues 4–5, 431-450.

Peterson, R. E., Jr., 1984: A Triple-Doppler radar analysis of a discretely propagating multicell convective storm. J. Atmos. Sci., 41, 2973–2990.

Protat, A. and Zawadzki, I., 1999: A Variational Method for Real-Time Retrieval of Three-Dimensional Wind Field from Multiple-Doppler Bistatic Radar Network Data. J. Atmos. Oceanic Technol., 16, pp. 432-449.

Robert A.Houze, J. (2014). Cloud Dynamics (Second Edition ed., Vol. 104). Elsevier Inc.

Ronald E. Rinehart (2004): Radar for Meteorologists, Rinehart Publication, ISBN: 0-9658002-1-0.

Rotunno, R., 1981: On the Evolution of Thunderstorm Rotation. Mon. Wea. Rev., 109(3), pp. 577-586.

Shapiro, A. and Kogan, Y. L., 1994: On vortex formation in multicell convective clouds in a shear-free environment. Atmos. Res., 33(1-4), 125-136.

Shapiro, A., Potvin, C. K. and Gao, J., 2009: Use of a Vertical Vorticity Equation in Variational Dual-Doppler Wind Analysis. J. Atmos. Oceanic Technol., 26(10), 2089-2106.

Simpson, J., et al.,1980: On Cumulus Mergers. Archiv Fur Meteorologie, Geophysik 7 Bioklimatologie, Serie A, vol. 29, no. 1–2, 1980, pp. 1–40.

Shimizu, S., H. Uyeda, Q. Moteki, and T. Maesaka, 2008: Structure and formation mechanism on the 24 May 2000 supercell-like storm developing in a moist environment over the Kanto Plain, Japan. Mon. Wea. Rev., 126, 2389–2407.

Shimizu, S., 2012: Multiple Doppler Radar Analysis for Retrieving the Three-Dimensional Wind Field Within Thunderstorms. In: Doppler Radar Observations-Weather Radar, Wind Profiler, Ionospheric Radar, and Other Advanced Applications. Croatia: Intech, pp. 231-246.

Stalker, J. R. and Knupp, K. R., 2002: A Method to Identify Convective Cells within Multicell Thunderstorms from Multiple Doppler Radar Data. Mon. Wea. Rev., 130(1), 188-195.

Stalker, J. R., and Knupp, K. R., 2003: Cell Merger Potential in Multicell Thunderstorms of Weakly Sheared Environments: Cell Separation Distance versus Planetary Boundary Layer Depth. Mon. Wea. Rev., 131(8), 1678-1695.

Shusse, Y., Tsuboki, K., Geng, B., Minda, H., and Takeda, T., 2005: Structure and Evolution of Deeply Developed Convective Cells in a Long-Lived Cumulonimbus Cloud under a Weak Vertical Wind-Shear Condition, J. Meteor. Soc. Japan, 83, pp. 351-371.

Suzuki, Shin Ichi, et al. ,2018: X-Band Dual-Polarization Radar Observations of the Supercell Storm That Generated an F3 Tornado on 6 May 2012 in Ibaraki Prefecture, Japan. Journal of the Meteorological Society of Japan, vol. 96A, 2018, pp. 25–33.

van Lier-Walqui, M., Fridlind, A. M., Ackerman, A. S., Collis, S., Helmus, J., MacGorman, D. R., North, K., Kollias, P., & Posselt, D. J. (2016). On Polarimetric Radar Signatures of Deep Convection for Model Evaluation: Columns of Specific Differential Phase Observed during MC3E, Monthly Weather Review, 144(2), 737-758.

Vasiloff, S. V., Brandes, E. A., Davies-Jones, R. P. and Ray, P. S., 1986: An Investigation of the Transition from Multicell to Supercell Storms. J. Appl. Meteor. Climatol., 25(7), pp. 1022-1036.

Weisman, M. L., and J. B. Klemp, 1982: The dependence of numerically-simulated convective storms on vertical wind shear and buoyancy. Mon. Wea. Rev., 110, 504–520.

Weisman, M. L., and J. B. Klemp, 1984: The structure and classification of numerically simulated convective storms in directionally varying wind shears. Mon. Wea. Rev., 112, 2479–2498.

Weisman M. L. and J. B. Klemp, 1986: Glossary of Meteorology. [Online] Available at: https://glossary.ametsoc.org/wiki/Bulk_richardson_number

APPENDICES

Appendix-A

The vertical vorticity equation in terms of the evolution of thunderstorms rotation (Rotunno et al.,1981)

The curl of vorticity is defined as

$$\underset{\omega}{\rightarrow} = \nabla \times \underset{u}{\rightarrow}$$

was twice the local rate of rotation of a fluid element. In a Cartesian coordinate,

$$\underset{\omega}{\rightarrow} = \nabla \times \underset{u}{\rightarrow} = \begin{bmatrix} \frac{\partial}{\partial x} \\ \frac{\partial}{\partial y} \\ \frac{\partial}{\partial z} \end{bmatrix} \begin{bmatrix} u \\ v \\ w \end{bmatrix} = \begin{bmatrix} \frac{\partial w}{\partial y} - \frac{\partial v}{\partial z} \\ \frac{\partial u}{\partial z} - \frac{\partial w}{\partial x} \\ \frac{\partial v}{\partial x} - \frac{\partial u}{\partial y} \end{bmatrix}$$

Therefore, the evolution of the vertical vorticity within thunderstorm updraft is well-governed by

$$\frac{\partial \zeta}{\partial t} = \xi \frac{\partial w}{\partial x} + \eta \frac{\partial w}{\partial y} + \zeta \frac{\partial w}{\partial z}$$

Initial development of vertical vorticity within the updraft by tilting of horizontal vorticity (ω_h) into the vertical

$$\omega_h = \xi \frac{\partial w}{\partial x} + \eta \frac{\partial w}{\partial y} = \left(\frac{\partial w}{\partial y} - \frac{\partial v}{\partial z}\right) i + \left(\frac{\partial u}{\partial z} - \frac{\partial w}{\partial x}\right) j$$

where the vertical wind shear $\left(-\frac{\partial v}{\partial z}\right) i + \left(\frac{\partial u}{\partial z}\right) j$ determines the horizontal vorticity. We can assume that $\eta = \left(-\frac{\partial v}{\partial z}\right)$ and $\xi = \left(\frac{\partial u}{\partial z}\right)$ where η is the environmental streamwise vorticity, defined as the vorticity around an axis parallel to the environment wind, and ξ is the environmental crosswise vorticity, defined as the vorticity around an axis normal to the environmental wind.

Appendix-B

The basic principles of classical dual-Doppler radar analysis (Adapted from Shimizu and Maesaka, 2006)

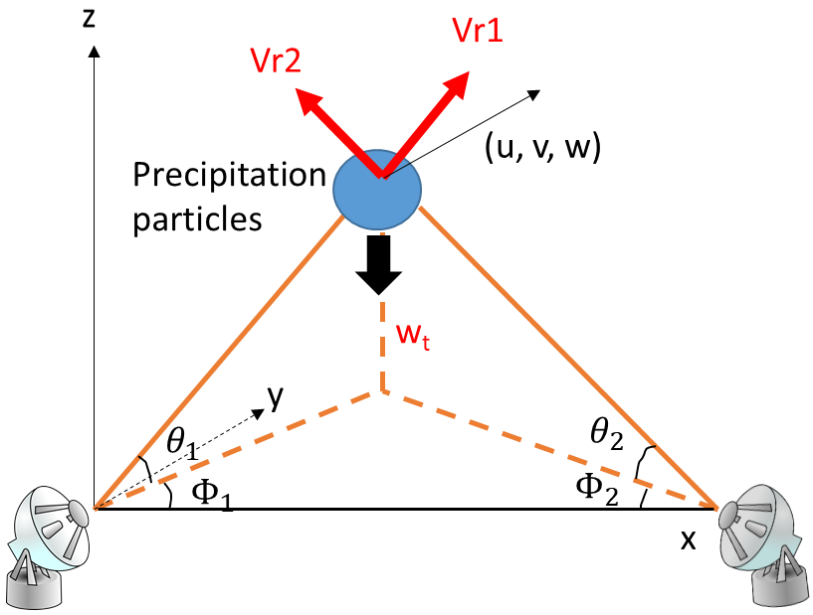

$$V_{r1} = u\cos\theta_1 cos\Phi_1 - v\cos\theta_1 sin\Phi_1 - (w + w_t)\sin\theta_1$$

$$V_{r2} = u\cos\theta_2 cos\Phi_2 - v\cos\theta_2 sin\Phi_2 - (w + w_t)\sin\theta_2$$

$$\frac{\partial(\rho w)}{\partial z} = -\rho\left(\frac{\partial u}{\partial x} + \frac{\partial v}{\partial y}\right)$$

where θ and Φ are elevation and azimuth angles. ρ is the air density on the horizontal layer and (u, v, w) are wind components in Cartesian coordinates (x, y, z).

The simplified Shimizu and Maesaka (2006) cost function is defined as below where J_o is the difference between observed and analyzed radial velocity, J_d is continuity equation error, J_s is a smoothness constraint, J_b is the measurement of the distance of variational analysis to the background fields, m is the numbers of radars, u, v, and w are velocity components of wind, x_m, y_m, and z_m are the distance between the target and the radar site, w_t is the target drop of velocity, $\overline{\rho}$ is the mean horizontal air density, and are reciprocals of the error variance.

$$J = J_o + J_d + J_s + J_b$$

$$J_o = \frac{1}{2}\sum_{i,j,k,m} \lambda_o (Vr_m - u\cos A - v\cos B - (w + w_t)\cos C)^2$$

$$J_d = \frac{1}{2}\sum_{i,j,k} \lambda_d D^2$$

$$J_s = \frac{1}{2}\left[\sum_{i,j,k} \lambda_s (\nabla^2 u)^2 + \sum_{i,j,k} \lambda_s (\nabla^2 v)^2 + \sum_{i,j,k} \lambda_s (\nabla^2 w)^2\right]$$

$$J_b = \frac{1}{2}\left[\sum_{i,j,k} \lambda_{ub} (u - u_b)^2 + \sum_{i,j,k} \lambda_{vb} (v - v_b)^2 + \sum_{i,j,k} \lambda_{wb} (w - w_b)^2\right]$$

$$A = \frac{x_m}{r_m}$$

$$B = \frac{y_m}{r_m}$$

$$C = \frac{z_m}{r_m}$$

$$D = \frac{\partial \bar{\rho} u}{\partial x} + \frac{\partial \bar{\rho} v}{\partial y} + \frac{\partial \bar{\rho} w}{\partial z}$$